FACTORS AFFECTING THE FRAGMENTATION OF PEPTIDE IONS: METAL CATIONIZATION AND FRAGMENTATION TIMESCALE

A Dissertation

by

KEVIN LEE KMIEC

Submitted to the Office of Graduate Studies of
Texas A&M University
in partial fulfillment of the requirements for the degree of

DOCTOR OF PHILOSOPHY

August 2012

Major Subject: Chemistry

Factors Affecting the Fragmentation of Peptide Ions:

Metal Cationization and Fragmentation Timescale

FACTORS AFFECTING THE FRAGMENTATION OF PEPTIDE IONS:

METAL CATIONIZATION AND FRAGMENTATION TIMESCALE

A Dissertation

by

KEVIN LEE KMIEC

Submitted to the Office of Graduate Studies of
Texas A&M University
in partial fulfillment of the requirements for the degree of

DOCTOR OF PHILOSOPHY

Approved by:

Chair of Committee,	David H. Russell
Committee Members,	Paul E. Hardin
	Simon W. North
	Emile A. Schweikert
Head of Department,	David H. Russell

August 2012

Major Subject: Chemistry

ABSTRACT

Factors Affecting the Fragmentation of Peptide Ions: Metal Cationization and Fragmentation Timescale. (August 2012)

Kevin Lee Kmiec, B.A., Hendrix College

Chair of Advisory Committee: Dr. David H. Russell

The factors affecting peptide fragmentation have been extensively studied in the literature in order to better predict the fragment ion spectra of peptides and proteins. While there are countless influences to consider, metal cation binding in the gas-phase is particularly interesting. Herein, a comparison of fragmentation patterns of a model peptide series with various charge carriers (H^+, Li^+, Na^+, K^+, and Cu^+) will assist in determining the location of the preferred binding site of the metal cation and in assessing differences in the fragmentation pattern as a result of this binding site. An interesting observation from these studies reveals abundant *x*-type fragment ions occurring from the fragmentation of alkali-metal cationized peptides. As these fragment ions have been observed in previous studies by others but not addressed, the factors affecting the formation of these *x*-type fragment ions are explored.

Additionally, a home-built 193-nm photodissociation tandem time-of-flight mass spectrometer is utilized to study how peptide fragmentation kinetics affect the fragmentation pattern observed. Initially, the fragmentation timescales of various peptides are investigated. Results indicate that longer fragmentation timescales (~10

microseconds) result in an increased number of identified peaks with internal and ammonia loss fragment ions being the most common in comparison to 'prompt' fragmentation timescales (~1 microsecond). Furthermore, *b*-type fragment ion formation is also favored at longer timescales for the arginine containing peptides investigated.

The fragmentation pattern of several proline containing peptides is examined by collision-induced dissociation and 193-nm photodissociation. Unique fragment ions are observed with each occurring at a proline residue. Few differences are detected between CID and 193-nm photodissociation spectra, indicating that the proline residues direct fragmentation rather than the dissociation method.

In an effort to improve the performance of the photodissociation tandem TOF instrument, the addition of a second source and a dual-stage reflectron are incorporated. The modifications result in improved mass range, signal-to-noise, and increased fragment ion collection efficiencies. High quality mass spectra are acquired across a range of mass-to-charge ratios from ~600 to 1900. Furthermore, the modifications continue to allow investigation of various fragmentation timescales with the addition of an additional timeframe of ~3 microseconds.

DEDICATION

This dissertation is dedicated first and foremost to my family, my parents Edward and Janis, and my brother Kyle. The values my parents have taught me throughout my life have made me into the person I am today. My mom has always listened whenever life has gotten me down, and without her advice those down times would have been much more numerous and extensive. My dad, more than anyone else, has taught me the value of a hard day's work and has always been there when I need a distraction from the sometimes tireless work of graduate school. Kyle is not just my brother; he is also one of my best friends and is still one of the few people in the world that can always make me laugh.

This work is also dedicated to the love of my life and my future wife Cassie. She is always there to encourage me even when life is at its worst and without her consistent support I would never have reached this point in my life. She truly makes every day brighter.

ACKNOWLEDGEMENTS

I would like to first thank my advisor Dr. David H. Russell for providing me with the opportunity to earn a Ph.D. degree. This has been both a financial contribution and a physical contribution through his assistance within the laboratory. As an instrument builder, the progress at times can be slow, but with Dr. Russell encouragement, I persevered through most of the trials and tribulations without much delay.

I am also thankful for the guidance and support of my committee members, Dr. Emile Schweikert, Dr. Simon North and Dr. Paul Hardin.

I am especially thankful to the machinists, Will Seward and Carl Johnson, who have helped to create the instrumentation utilized in these studies. Without their skill set, my instrument is just a simple block of metal with to purpose or function. Their work is further enhanced by that of Greg Matthijetz. Without Greg's consistent aid with electronics and Labview programming of the photodissociation time-of-flight instrument experiments would be far more difficult than could be imagined.

My first years in graduate school would not have been possible without the excellent guidance of Dr. Garrett Slaton and Dr. Jody May. Garrett was a tremendous help during my first summer of work in the Russell group as he showed me the ropes of one of the more difficult experiments in the Russell Group, photodissociation tandem time-of-flight mass spectrometry. Jody inspired me to become more interested in mass spectrometry instrument development and modification which through the years has led

me to construct an instrument far different from the version with which I originally began.

Finally, I would like to thank the other former and current members of the Russell research group who have helped me through graduate school both in and out of the lab, specifically, Dr. Kent Gillig, Dr. Bill Russell, Dr. Shane Tichy, Dr. Brad Williams, Dr. Ryan Blase, Dr. Stephanie Cologna, Roberto Gamez, Kyle Fort, Josh Silveira, Junho Jeon, Fred Zinnel, Kim May, and Dr. Chaminda Gamage. I would also like to thank Dr. Francisco A. Fernandez-Lima who performed all theoretical calculations included in this work which yields a perfect complement to the fragmentation data shown herein.

NOMENCLATURE

ADC	Analog-to-Digital Converter
CID	Collision-induced Dissociation
COM	Center-of-mass
DC	Direct Current
ECD/ETD	Electron Capture Dissociation/ Electron Transfer Dissociation
ESI	Electrospray Ionization
FTICR	Fourier Transform Ion Cyclotron Resonance
IVR	Intramolecular Vibrational Redistribution
KE	kinetic energy
LC	Liquid Chromatography
LDI	Laser Desorption Ionization
m/z	mass-to-charge ratio
MALDI	Matrix Assisted Laser Desorption/ Ionization
MS	Mass Spectrometry
MCP	Microchannel Plate
PSD	post source decay
PTMs	post translational modifications
QET	Quasi-equilibrium theory
RF	Radio Frequency
RRK	Rice, Ramsperger, Kassel

RRKM	Rice, Ramsperger, Kassel, Marcus
S/N	signal to noise
SID	Surface Induced Dissociation
TDC	Time-to-Digital Converter
TIS	timed ion selector
TOF	time-of-flight
UV	Ultraviolet

TABLE OF CONTENTS

CHAPTER Page

CHAPTER Page

LIST OF FIGURES

Page

LIST OF TABLES

Page

CHAPTER I

INTRODUCTION

Tandem mass spectrometry (MS) is an effective technique for determining gas-phase ion structure based on the fragmentation pattern of an ion of interest [1, 2]. This technique involves formation of the gas-phase ion followed by subsequent separation based on mass-to-charge ratio (*m/z*) within the first mass analyzer. Isolation of the ion of interest is obtained after this separation, and the excess internal energy of the ion, either from activation or from the ionization process, induces fragmentation. Mass analysis of fragment ions is then performed in the second stage. Differences in *m/z* between each fragment ion detected are utilized to correctly identify the structure of the precursor ion selected from the first mass analyzer. Tandem MS is an established method, capable of identifying small molecules and large macromolecules. A block diagram and schematic on tandem mass spectrometry is shown in Figure 1.

This dissertation follows the style of the International Journal of Mass Spectrometry.

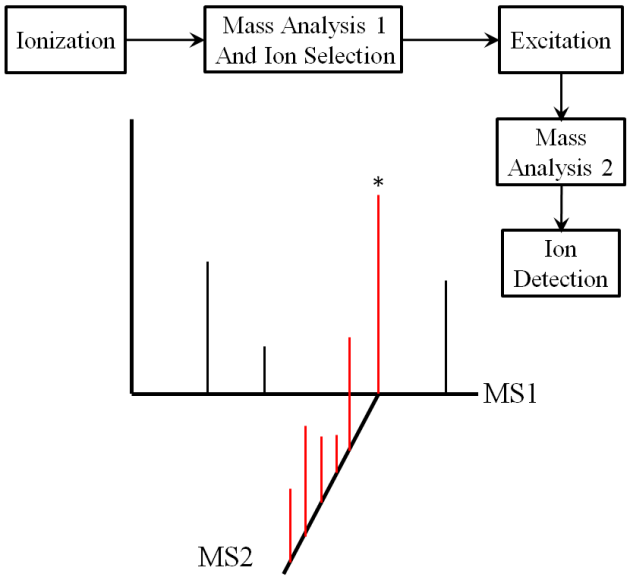

Figure 1: Illustration of a typical tandem MS experiment. After separation in MS1, the starred ion is selected for excitation and its fragments are analyzed in MS2.

Ionization Methods

As no mass spectrometry experiment can be performed without the presence of a charge on the molecule of interest, it is understandable to begin a mass spectrometry discussion with the ionization method. The charge in this sense is a tag for examining the mass of the ion. Countless methods of ionization exist, including electron impact ionization [3], chemical ionization [4], photoionization [5], fast-atom bombardment [6], electrospray ionization (ESI) [7], and matrix assisted laser desorption/ionization (MALDI) [8]. Some methods produce predominantly singly charged ions while others favor multiple charge states. Ionization methods can form deprotonated, protonated, cationized (metalated), and/or electron deficient/rich ions. Several ionization methods can be considered "hard" as they produce ions with high internal energies, while other

methods are softer ionization techniques. Although, all methods are useful depending on the molecule of interest, this discussion will focus on ESI and MALDI as these are currently the most common methods of analysis of biomolecules.

Electrospray Ionization (ESI)

The first documentation of the electrospray phenomenon was shown in 1914 by Zeleny [9]. However, Chapman in 1930 used electrospray ionization coupled with ion mobility showing that electrospray had analytical utility [10]. ESI in mass spectrometry analysis was performed in the early 60s by Malcolm Dole [11]; however, the notoriety for development of electrospray ionization for analysis of biomolecules is given to John Fenn who first performed the technique in 1984 [7], earning him the Nobel Prize in 2002.

ESI is performed by spraying a solution of the analyte molecule, typically in a water/methanol mixture, through a thin charged needle, creating a fine spray of charged droplets composed of the analyte of interest and solvent [12]. The sprayed droplets are dried using a dry gas or heat which rapidly desolvates the solvent leaving the charge on the molecule. ESI produces predominantly multiply charged ions and is considered "soft" ionization technique as the evaporating solvent removes excess thermal energy from the system producing "cool" ions. ESI is also a constant wave technique, meaning that continuous ion formation is possible making ESI an ideal match for liquid chromatography (LC). However, the constant spray does not make ESI easily adaptable

to pulsed mass analyzers such as time-of-flight, requiring the need for other methods of ionization.

Matrix Assisted Laser Desorption/Ionization (MALDI)

MALDI is considered a unique ionization method; however, the development of MALDI began with laser desorption/ionization (LDI) in the early 1960s [13]. LDI involves irradiating small molecules spotted on a surface with a high intensity pulsed laser which ionizes small molecules. Karas and Hillenkamp demonstrated that by the addition of a matrix, *i.e.* a small organic molecule, the ionization efficiency of large molecules could be dramatically improved [8]. Additionally, the contributions of Tanaka in 1988 in ionizing a wide range of biomolecules using a MALDI based process lead to him receiving part of the Nobel Prize in 2002 [14]. A schematic of the MALDI process is shown in Figure 2.

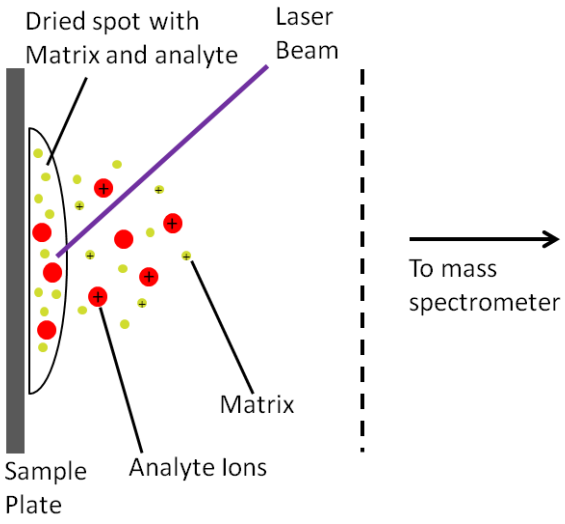

Figure 2: Schematic of the MALDI process. The dried spot on the sample plate consists of a mixture of predominately matrix molecules along with analyte molecules. The photons from the laser, usually in the UV range, bombard the sample spot forming both matrix and analyte ions.

The mechanism of MALDI is not completely understood and has been the subject of much debate in the literature [15, 16]. Such a topic is not main focus here, but one currently accepted hypothesis is that the matrix absorbs the incoming photons resulting in local heating which can result in desorption from the surface followed by ionization in the gas-phase [15].

The matrix serves many purposes in the MALDI process one of which is to absorb photons from the laser and transfer a portion of that energy to the analyte molecule. Careful selection of a proper matrix is vital to MALDI mass spectrometry experiments. First of all, the matrix must absorb the incoming photon wavelength and typically ultraviolet (UV) lasers are used in MALDI. Secondly, the matrix must be able to donate a proton to the analyte molecule, or in other words, it must be an acid.

Without a good source of protons, the protonated analyte molecule will not be observed; however, it must be noted that this is only valid for examining protonated molecules which is the primary use of MALDI. The matrix also must be able to co-crystallize with the analyte molecule. If the analyte is isolated from the photon absorbing matrix, the potential for energy transfer does not exist and desorption of the matrix will not 'carry along' the analyte molecules to the gas phase. Also, the matrix acts as a 'shield' for the analyte molecules against the photons which could cause the analyte molecules to be excited [15]. This occurs primarily because the matrix is mixed in large molar excess in comparison to the analyte molecules. The most common form of a matrix is a small organic acid such as α-cyano-4-hydrocinnamic acid, 2,5-dihydroxy benzoic acid, and sinapic acid.

MALDI has been shown to ionize biomolecules from a few hundred Daltons up to 100,000 Daltons giving it a very broad mass range [8, 14, 15] with primarily singly charged ions being formed. The pulsed nature of the MALDI experiment is also ideal for coupling to time-of-flight mass spectrometers. While applications for ESI have developed rapidly as this technique is easily adaptable to quadrupoles and ion traps, MALDI has grown more slowly but still has considerable application for biomolecule analysis.

Mass Analyzers

Countless methods of methods of *m/z* analysis exist including the double focusing sector [17, 18], time-of-flight (TOF) [19, 20], quadrupoles [21, 22],

Fourier-Transform Ion Cyclotron Resonance (FTICR) [23], and ion traps [21]. A brief discussion of several of these will be provided here for comparison against the time-of-flight mass spectrometer; the mass analyzer of chosen for the studies presented here.

Magnetic/Electrostatic Sectors

Sector mass spectrometers were the most commonly used mass spectrometers through much of the 20th century [24]. A magnetic sector involves the separation of ions of varying mass-to-charge through a magnetic field as depicted in Figure 3.

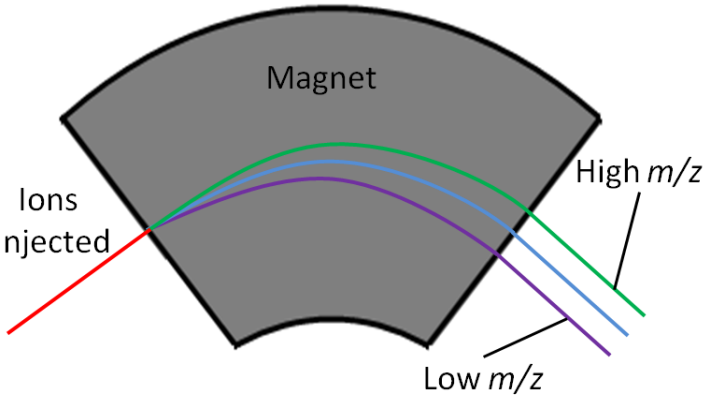

Figure 3: Depiction of ion trajectories in a magnetic sector mass spectrometer. Notice the high *m/z* ions have a larger radial path than the low *m/z* ions.

In a magnetic sector, the magnetic field will redirect lower mass-to-charge ions more than high mass-to-charge ions creating a separation of the differing species. However, magnetic sectors to not provide any kinetic energy focusing which decreases their maximum achievable resolution; therefore, they are usually combined with

electrostatic sectors. These mass analyzers have the same shape as the magnetic sector but instead of a magnetic field they have two plates with an electric potential across them. Ions with a larger kinetic energy will follow a path closest to the outer electrode (higher potential) while lower kinetic energy ions will transverse more closely to the inner electrode (lower potential). After traversing the focusing region, ions of the same *m/z* but differing kinetic energies should be focused at the exit.

The combination of the magnetic and electrostatic analyzers is the most common form of the sector instrument, known as a double-focusing sector mass spectrometer. This instrument originally debuted by Dempster [17] and Nier [18] offers *m/z* analysis with kinetic energy focusing. Even though the sector mass analyzer has high resolution (~30,000) and mass range (<20,000 *m/z*), their high cost, large size, and slow analysis speeds have diminished their use for many applications [24].

Quadrupoles

Quadrupoles offer the ability to separate ions as they travel through 4 parallel cylindrical (or hyperbolic) electrodes that have a fixed direct current (DC) voltage and an alternating radio frequency (RF) voltage. Generally, ions travel in a spiraling motion down the length of the rods and based on the applied fields, only those ions with a stable orbit transmit through the mass analyzer. A schematic of a quadrupole is seen in Figure 4.

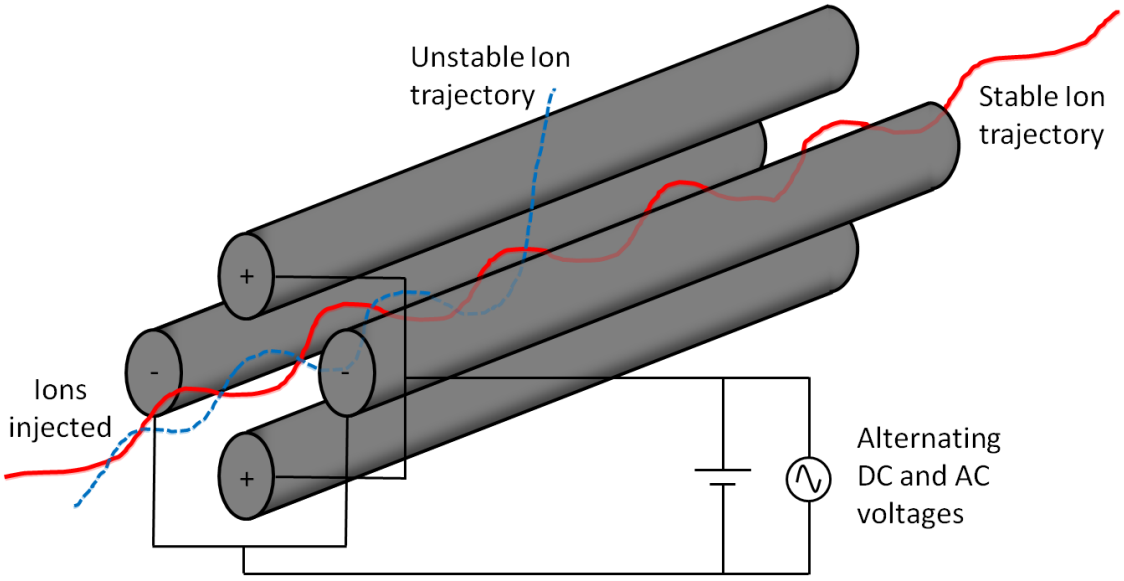

Figure 4: A model of a working quadrupole mass spectrometer. Note that the stable ion trajectory of the solid line is transmitted while the dashed ion trajectory is ejected from further analysis.

The first studies on quadrupoles for mass spectrometry analysis were undertaken by Wolfgang Paul [21] and many of the equations describing ion motion through a quadrupole were described by March [25]. Even though the mass range (<4000 *m/z*) and resolution (10,000) of a quadrupole can be limited, they are still considered one of the most widely applicable mass analyzers because of their small size and relatively low cost. Unfortunately a single quadrupole cannot be used to perform tandem MS experiments and as such they are usually combined with multiple quadrupoles [26], known as triple quads[27], or with time-of-flight mass analyzers[28].

Fourier Transform Ion Cyclotron Resonance

Fourier Transform Ion Cyclotron Resonance (FT-ICR) monitors the frequency of an ion's orbital motion while contained in a magnetic field [23]. This frequency can be mathematically treated by a Fourier Transform to obtain *m/z* information of the molecule. The longer the ion can be contained in the magnetic field, the better the resolution and mass accuracy of the measurement. Typically measurement times of 500 ms to 1 second are sufficient for generating high resolution mass spectra. A further advantage of FTICR mass spectrometers is their ability to isolate a single *m/z* ratio for sequential analysis allowing for multiple mass analyses to be undertaken.

The FTICR technique was originally developed by Hipple in 1949 [29] and it still continues to see many applications today [23, 30, 31]. The extremely high resolution (500,000 to 1,000,000) and mass accuracy are the instrument's primary advantages, but they come at a price. FTICR requires very low pressures so that the cycling ion will remain stable in is motion. FTICR also requires a significant amount of physical space owing to the high magnetic field and thus are highly expensive as a result of the maintenance required for the superconducting magnet.

Ion Traps

The ion trap mass spectrometer was developed simultaneous with the quadrupole mass analyzer by the same person, Wolfgang Paul [21]. There are varying electrode geometries of ion traps, but the basic principle involves using electrostatic potentials, both RF and DC, to isolate ions with a given volume [22]. Paul's design in 1953

consisted of two rounded end cap electrodes with a central ring electrode [21]. Ions would enter through a small aperture in the end cap electrode and exit through a similar aperture on the opposite side. Various other types of electrode geometries have been developed for similar uses in ion trapping experiments, but only two others will be highlighted here: the linear ion trap and the Orbitrap.

The linear ion trap [32, 33] initially appears quite similar to quadrupole mass analyzers except it contains two end cap electrodes at the ends of the quad. The end caps are held at a higher DC potential than the quadrupole which results in containment of ions with the quadrupole by the RF and DC potentials. Linear ion traps have larger storage capacities than their predecessor Paul traps as the total trapping volume is larger [33]. The Orbitrap mass analyzer [34, 35] operates similarly to the FTICR analyzer by measuring the frequency of the rotary motion of charged particles to generate a mass spectrum. The difference here is that no magnetic field is used; rather, the ions oscillate based on a balance between the attractive forces toward an inner barrel like electrode and the centrifugal forces created by the circular motion. While the resolution of the Orbitrap is very high (150,000), an ion's motion is not infinitely stable within the device and eventually ions will be lost. The Orbitrap is also not amenable to tandem experiments with in the trap itself; therefore, it may be more suitable to refer to the Orbitrap as an ion detection method rather than a true ion trap.

Most ions traps have a similar advantage as FTICR analyzers in that they can perform MS^n experiments. However, they suffer from the fact that only a given range of *m/z* ratios can be trapped simultaneously which leads to a mass discrimination effect.

Ion traps also do not have the resolution of FTICR instruments, but the small size and reasonable cost still make the ion trap useful for many applications.

Time-of-Flight

Each of these methods of mass analysis has distinct advantages and disadvantages, but the simplest of all the mass analyzers is time-of-flight (TOF) mass spectrometry [36]. TOF mass spectrometers only require a vacuum chamber, an ionization method, and a means of ion acceleration and detection. Additionally, TOF mass spectrometers have high sample throughput, excellent sensitivity, virtually limitless mass range, high *m/z* resolution (~50,000), and are perfectly compatible with pulsed ion sources and lasers. Although J.J. Thomson was the first to apply TOF principles to separate ions [19], Stephens is given credit for proposing the first TOF mass spectrometer [20] while Cameron and Eggers provided the first experimental evidence of a TOF instrument with their *ion velocitron* [37]. Since this time, advances in TOF technology to improve the resolution and sensitivity of the technique have been made and TOF continues to be a commonly used mass spectrometer today [38-40].

As mentioned previously the operation of a TOF mass spectrometer is quite simple. After ionization occurs, an accelerating voltage is applied to a plate nearby where the ion is formed, known as the source. This accelerating voltage imparts kinetic energy into the recently formed ion. The kinetic energy applied gives the ion a set velocity based on the equation:

$$(1) \qquad KE = \frac{1}{2}mv^2$$

where *KE* is kinetic energy, *m* is mass and *v* is velocity. This equation can be rearranged to solve for velocity and other terms imbedded in the *KE* term can be removed, including the voltage applied E_v, the charge of ion *e*, and the number of charges *z*:

$$(2) \qquad v = \sqrt{\frac{2KE}{m}} = \sqrt{\frac{2E_v ze}{m}}$$

Once the ion begins its motion, it will enter a field-free region usually defined by a ground grid. The field-free region is critical as it keeps the velocity constant over the drift length allowing for controlled separation of ions. All ions formed in the source region will acquire approximately the same overall kinetic energy and will have a flight time to the detector based on equation 3:

$$(3) \qquad t = d\sqrt{\frac{m}{2zeE_V}}$$

where *t* is time, and *d* is the field free distance traveled. This equation neglects the time spent in the ion source which can be approximated to be small relative to the drift time. As an example, a singly charged ion with a mass of 1000 Daltons traveling a distance *d* of 2.0 meters with a voltage applied of 15000 volts will have a time-of-flight of approximately 37 microseconds. With the same parameters, an ion with a mass of 2000 Daltons will travel the distance in 52 microseconds resulting in a separation of ions by their mass-to-charge ratios.

A time-of-flight spectrum can easily be converted to mass-to-charge spectrum by again rearranging equation 3:

$$(4) \qquad m/z = 2eE_v\left(\frac{t}{d}\right)^2$$

which can be simplified further by grouping together variables that are constant for a given set of instrument conditions:

$$(5) \qquad m/z = Kt^2 + k'$$

This is the standard equation used to calibrate TOF mass spectra and determine the masses of unknown variants. According to this equation, the mass accuracy is directly dependent on how well the peak centroid, or *t*, can be determined, a topic that will be discussed later in this chapter. Additionally, the mass resolution is directly related to the time resolution by equation 6:

$$(6) \qquad \frac{\Delta m}{m} = \frac{2\Delta t}{t}$$

It is initially obvious that the resolution can be increased by increasing the overall drift time *t*, either by decreasing the acceleration voltage, E_v, or increasing the drift length, *d*. However, adjusting these variables will not correct for several errors that are inherent to TOF mass spectrometry.

Several factors can influence the initial ion distribution in the source region which will contribute to the mass resolution with these factors are best described by examining two ions of the same *m/z* seen in Figure 5 [41, 42].

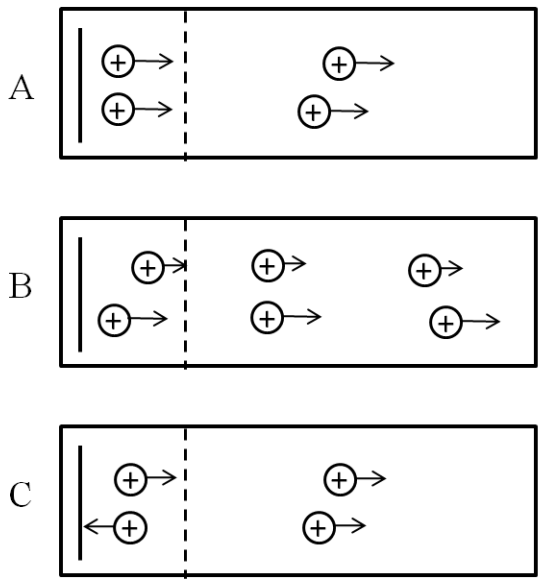

Figure 5: Several situations that exist in the initial ion distribution that will affect resolution in the TOF mass spectrometer. A) Ions formed in the same position and kinetic energies but at different times, B) Ions formed at the same time and with the same kinetic energies but at different distances from the source plate, C) two ions formed at the same time and position but with different initial kinetic energies.

In Figure 5A, the two ions are formed in same position with identical kinetic energies, but are formed at slightly different times. As the two ions are accelerated towards the detector, this initial difference in time will remain until the ions reach the detector resulting in a broad peak. If two ions are formed at the same time but at different positions, or distances from the source plate, they will obtain different kinetic energies and therefore have different velocities (Figure 5B). The difference in kinetic energy occurs because there is a field gradient between the source plate and the ground grid, and depending on where the ion is formed. Ions formed closer to the source plate will obtain a greater amount of kinetic energy than ions created closer to the ground grid.

This too will contribute to peak broadening as the two ions here will take different amounts of time to cross the distance *d*. Finally Figure 5C shows two ions formed at the same time and position but with differing initial kinetic energies, the most difficult discrepancy to correct. This kinetic energy difference can best be thought of as velocities in opposite directions. An ion initially traveling against the field will have to turn around while the other ion will not resulting in a broader ion signal at the detector. These three discrepancies are the major contributors to peak broadening and as such a significant amount of research was undertaken to correct these features and improve the maximum achievable resolution for TOF instruments.

Wiley and McLaren first introduced *time-lag focusing* in 1955 to correct an ion's initial time, spatial, and energy distribution to improve the mass resolution of TOF instruments [43]. Time-lag focusing is achieved by initially forming ions in a field free region and then adding a fast (~10 ns) voltage pulse to accelerate ions a given time after ion formation. A depiction of their instrument and its operation is seen in Figure 6.

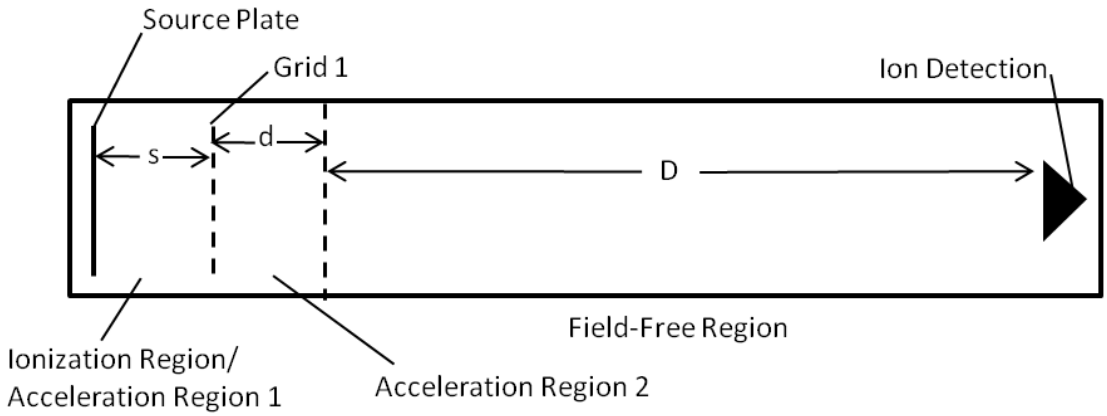

Figure 6: Depiction of the Wiley and McLaren's instrument utilizing time-lag focusing [43].

Ions were formed between a source plate and a grid that were both held at the same electric potential. A short distance from the grid 1, a ground grid was placed in order to define the field free region. A short time after ion formation, the voltage on the source plate was increased by a fast pulse accelerating ions across grid 1 and toward the detector. Upon implementation of this pulse, ions will experience two electric fields: the first in the region between the source plate and grid 1 which is usually a lower field than that between the second electric field located between grid 1 and the ground grid. All the factors shown in Figure 5 can be corrected to some extent by utilizing time-lag focusing or delayed extraction as it is commonly referred to today [44-47].

The improvement in resolution is initially obvious when considering the situation in Figure 5A where two ions form at slightly different times. The delay between ion formation and extraction will allow "slower forming ions" to form without accelerating the "fast forming ions" toward the detector. Once the pulse is applied, the ions will be

accelerated toward the detector and will arrive at the same time. The condition in Figure 5B, where ions are formed at two different positions, can be compensated by using low extraction fields which will minimize the difference in kinetic energy each ion receives based on its position. However, if low extraction fields are used the error resulting from two ions formed at the same time and position but with different kinetic energies (Figure 5C) is not corrected. Delayed extraction allows for partial correction of both of these situations. The low extraction field in the first acceleration region (see Figure 6) provides a correction for the different positions of the ions while the high acceleration field in acceleration region 2 accounts for ions with differing kinetic energies by minimizing the kinetic energy difference between these two. Delayed extraction can vastly improve the resolution of TOF instruments; however, further energy correction can be achieved by implementing other energy focusing devices.

The reflectron is another means of improving the resolution of TOF mass spectrometers by correcting for differences in kinetic energy. Originally debuted by Mamyrin in 1973 [48], a reflectron consists of a stack of large inner diameter lenses with an increasing electric potential. Ions that enter the reflectron will turn around 180° within the reflectron at a point defined by their initial kinetic energy. This is best described by two ions with the same *m/z* but different kinetic energies. The ion with a higher kinetic energy will penetrate deeper into the reflectron than the ion with lower kinetic energy. As the lower kinetic energy ion does not have to travel as far, it will exit the reflectron first and at some point, ideally the location of the ion detector, the higher kinetic energy ion will catch up to the lower kinetic energy ion. This will result in an

improved resolution for two reasons: 1) the decrease in Δt in the ion arrival time, and 2) the increase in the total time-of-flight t owing to the turn around and increased path length.

Mamyrin's original reflectron design is now referred to as a dual-stage reflectron [48], but the reflectron shown in Figure 7 is based on a single-stage design [49] and has advantages in simplicity compared to other reflectron designs.

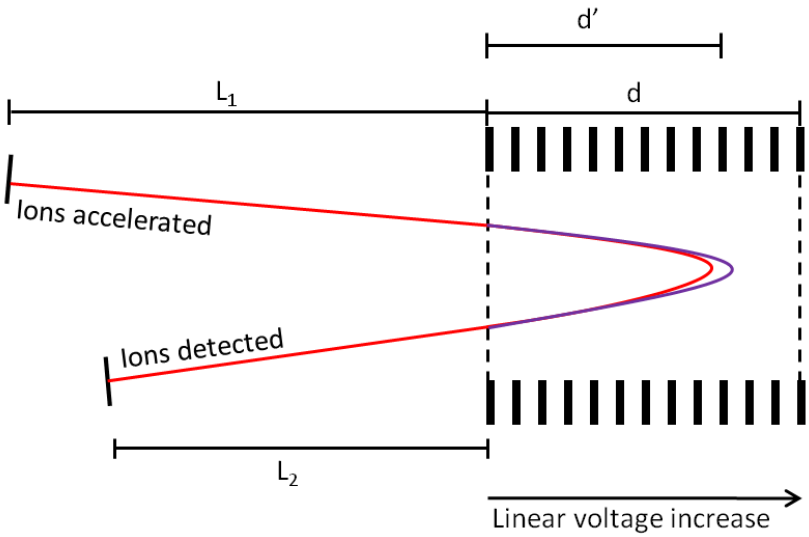

Figure 7: Diagram of a single-stage reflectron mass analyzer examining two ions of the same m/z. Note that one ion penetrates deeper into the reflectron owing to its higher kinetic energy than the other ion. Ideally, the two ions will arrive at the detector at the same time.

The parameters L_1 and L_2 are specific to a given mass spectrometer, and through several derivations of reflectron focusing parameters can provide the optimum length of the reflectron, d. This derivation will be examined in chapter 4 or can be seen in work

by Standing [49, 50] and others [51]; however, it must be noted that proper dimensions must be selected so that ions will focus properly at the detector.

Several other factors exist that could influence the maximum achievable resolution of TOF instruments [39]. The error in the time measurement owing to the detector response can decrease the overall resolution. Errors in the ion trajectory owing to non-uniform electric fields or penetrating fields from various sources can influence resolution. The use of grids is ideal for creating uniform electric fields, but studies have been done which show that ions can be lost when passing through a grid [52]. Finally, voltage variations from the power supplies used can decrease the maximum achievable resolution. Most of these effects are minimal compared to the kinetic energy and velocity problems that delayed extraction and the reflectron correct, but they are still worth consideration.

Time-of-flight has been around since the dawn of mass spectrometry but it did not see significant utilization until the advances in reflectron and delayed extraction technology. With the advent of MALDI, TOF mass analyzers will continue to be a commonly used instrument platform owing to their simplicity, low cost, and high performance capabilities.

Detectors and Signal Analysis Techniques

Likely the most common method of charge particle detection, the electron multiplier is one of the most efficient detection methods known to mass spectrometry. A variation of the electron multiplier commonly utilized in TOF mass spectrometers is the

microchannel plate detector (MCP) [53]. The operation of a double stacked MCP, chevron-style design is shown in Figure 8.

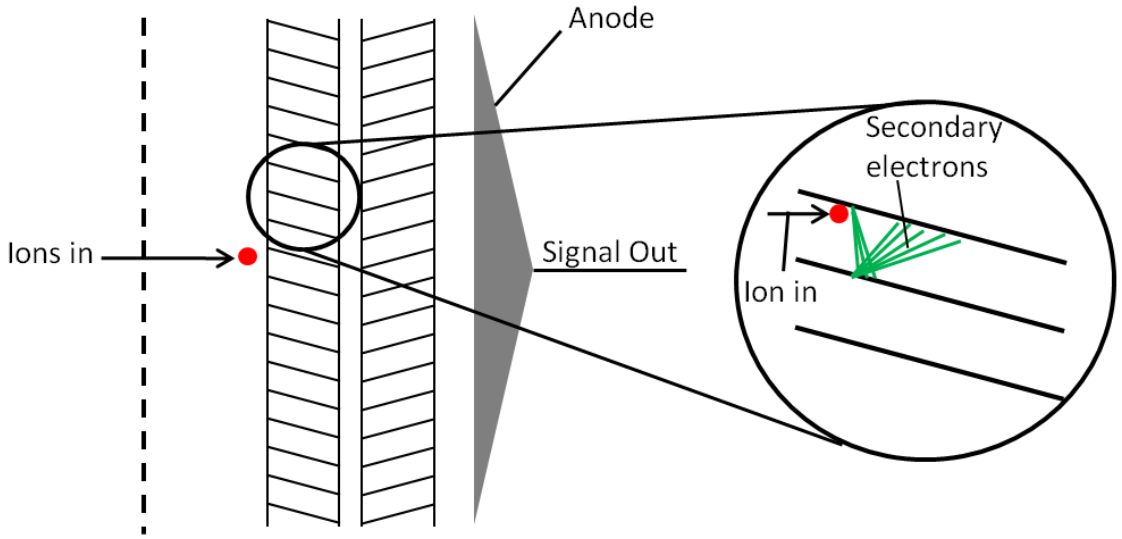

Figure 8: Dual microchannel plate assembly with Chevron style stacking. The inset clearly shows the secondary electrons that are created from the initial ion impact and the further secondary electrons created thereafter.

The performance of the MCPs is critical to charged particle detection. They are typically made of a glass material with a specific pore diameter and angle which are then coated with a conductive material. The electron cascade moves down each pore individually magnifying signals up to 10^6-10^8 fold at the anode. Without this magnification of signal, charge particle detection would not be as efficient and mass spectrometry experiments would be quite limited.

After the electrons exit the MCP pores, they move to the anode and generate a current which can be measured. How this signal is measured is dependent on the type of

experiments being performed, but typically analog-to-digital or time-to-digital conversion is utilized [42]. An Analog-to-Digital converter (ADC) utilizes a voltage measurement which is taken at a frequency defined by the internal clock of the ADC. The voltage at each point is measured and then recorded, and subsequent analyses are averaged together to provide an improvement ion in signal-to-noise ratio. ADC methods are excellent so long as there are a sufficient number of ions produced and the sampling rate of the ADC is fast enough to produce enough data points across a given Gaussian peak. ADC methods also have a high dynamic range since the current is measured and recorded for all values large and small.

Time-to-digital converters (TDC) operate by looking for a threshold voltage within a defined time *bin*. Usually this bin is on the order of a few nanoseconds depending on the separation capabilities of the instrument. A TDC does measure the amount of current generated, but it only records a 1 or a 0 in terms of output; that is, if sufficient ion signal is generated, the TDC will record a 1 and if there is no enough ion current, no count will be recorded. Multiple acquisitions are summed rather than averaged to provide a final spectrum. TDC methods are ideal for experiments where the ion yield is low since the signal can be continually summed while the noise is discriminated against (recorded as a 0). Typically, TDC are used in combination with amplifier/discriminators which can help control the amount of signal sent to the TDC. A disadvantage of TDCs is that they have a low dynamic range as high current signals will be recorded identical to low current signals.

The recording techniques employed can also have a dramatic affect on the mass resolution and accuracy of an instrument. At least 3 data points across a peak are required to accurately fit the Gaussian distribution as pictured in Figure 9 and low intensity or broad signals can make this more difficult. Initially it may seem beneficial to collect more points across a given peak; however, too many points can result in peak distortions.

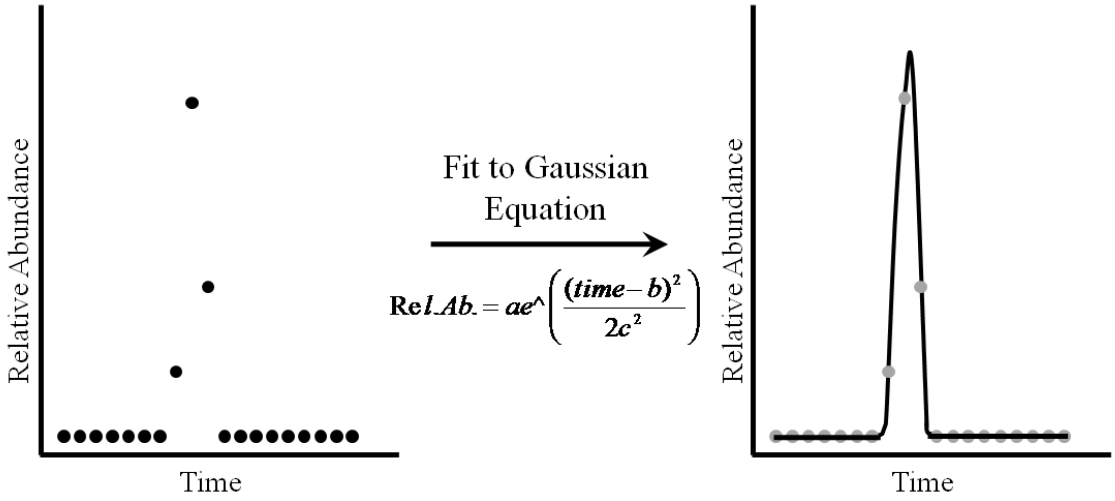

Figure 9: With the data points obtained to the left, a Gaussian fit can be applied in order to accurately determine the peak centroid, critical for high mass accuracy.

Proper sampling speed (ADC) or bin width (TDC) is necessary in order to accurately centroid a peak. Careful selection of ion detection and signal analysis methods are essential to obtaining correct data from a mass spectrometry experiment.

Gas-Phase Ion Fragmentation

Recall that tandem mass spectrometry requires two mass analyses with ion excitation in between (Figure 1). Various methods of excitation have utility for current mass spectrometers. Ions dispersed from the first *m/z* analysis must fragment in order to determine the gas-phase ion structure from the second time analysis. The thermodynamics and kinetics describing gas-phase ion fragmentation has been studied and can be predicted based on well known theories.

In general, gas-phase ion fragmentation can be explained using Rice, Ramsperger, Kassel (RRK) theory [54, 55] or equivalently the quasi-equilibrium theory (QET) [56]. This theory makes two assumptions: 1) that excess energy flows freely through all degrees-of-freedom with all states being accessible and 2) that intramolecular vibrational redistribution (IVR) occurs faster than the fragmentation rate. For most cases, these assumptions are valid [57]; however, there have been exceptions [58]. The results of these assumptions arrive at the RRK equation:

$$k(E) = \nu\left(\frac{E - E_0}{E}\right)^{S-1} \qquad (7)$$

where *k(E)* is the rate constant as a function of internal energy, *v* is the frequency factor, *E* is the internal energy of the molecule, E_0 is the energy required for the dissociation of a specific bond, and *s* is the number of oscillators in the system. This equation cannot accurately predict the correct rates of reaction, but two important conclusions can be made: (1) the rate has a strong inverse dependence on the degrees-of-freedom and (2) the rate increases rapidly as with excess internal energy. The rates predicted by this theory

are incorrect because the equation does not accurately account for the vibrational and rotational frequencies of the molecule; however, RRK theory does provide a good relative approximation. The modification to this theory by Marcus [59] to generate Rice, Ramsperger, Kassel, Marcus (RRKM) theory [60], can more accurately predict rates because it more explicitly accounts for the vibrational and rotational energies than RRK theory. However, for the discussions here the RRK theory is sufficient.

The relationship between the rate of dissociation (*k(E)*) and the internal energy dependence can be shown with a Wahrhaftig diagram as shown in Figure 10 [2].

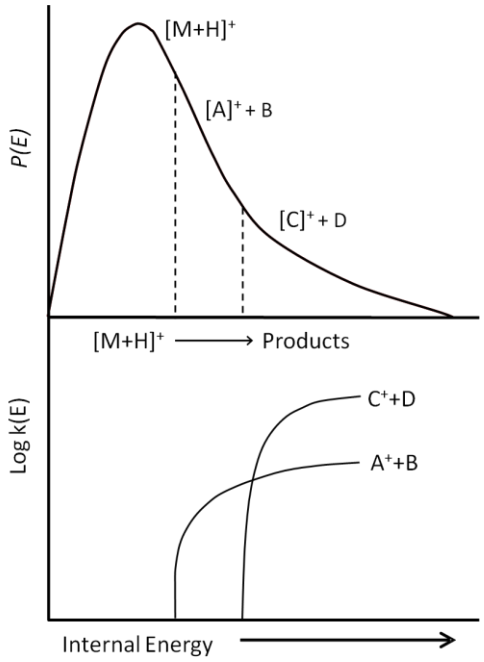

Figure 10: Wahrhaftig diagram illustrating the relationship between the precursor ion probability distribution (top panel) and rate of fragmentation (bottom panel) and the ion internal energy (x-axis). Note that at certain ion internal energies, formation of a given fragment will be favored over others.

A probability distribution of ions (*P(E)*) with a given internal energy is seen in the top portion of the diagram is the population of ions according to the internal energy. This probability distribution can be very narrow at low internal energies for thermal ions in a Boltzman distribution or it can be very broad for excited ions. However, at any given internal energy a specific fragment will be favored over another; for example, the fragmentation pathway $[M + H]^+ \rightarrow C^+ + D$ will be favored at higher internal energies. Overall, two important features are noted: 1) as the internal energy increases, different fragment ions will be kinetically favored (log *k(E)* is larger), and 2) at a given rate (*k(E)*), certain fragment ions may not form. It is this latter feature that will be a key point examined in the research herein. While these theories are valid for nearly all ion classes, including biomolecular ions, specifically peptides and proteins, fragmentation is of major interest to those that study proteomics topics.

Biological Mass Spectrometry: Proteomics

Proteomics has recently become a major focus of tandem mass spectrometry [61-63]. Proteomics in a general sense is the study of proteins, specifically their structure and function [64]. In mass spectrometry, proteomics is primarily focused on identifying the proteins within a given system, usually determining the primary sequence of a protein. Ideally the protein of interest can easily be ionized and introduced into the gas phase by ESI or MALDI, discussed previously; however, this is not always the case. If we consider a single protein of interest, there are two primary methods of analysis used today[65]: top-down [66] and bottom-up [67].

Top-down proteomics methods involve ionizing the intact protein and subjecting that protein to an excitation method in order to generate peptide fragments [66, 68]. The fragment ions will then be identified in order to attempt to determine the primary structure, amino acid sequence, of the protein. Since most proteins are large and the mass-to-charge range of most mass spectrometers may not be optimal for large species, ESI is typically used as the ionization method since multiply charged ions can be formed. Top-down has the advantage of minimal sample preparation when compared with bottom up techniques; however, it is quite difficult to fragment a modest sized protein of 100,000 Daltons and of course fragment interpretation can also be difficult, as fragment ions can have charge ranging from that of the precursor to unity.

Bottom-up proteomics methods are more traditional as they involve digesting the protein into smaller parts with an enzyme, typically trypsin, to generate small parts of the protein called peptides[67]. These peptides are modest in length, usually 8-15 amino acid residues and are therefore easier to examine and fragment within the mass spectrometer. However, no intact protein information can be obtained by this method and determining the complete amino acid sequence is dependent upon the efficiency of peptide ionization and fragmentation.

The fragmentation of peptides and proteins has been well studied since the first proposal for positive ion fragmentation nomenclature by Roepstorff in 1986 [69] which was eventually modified by Biemann the following year [61]. Originally, the nomenclature only treated fragmentation that occurred along the peptide backbone, but

Biemann's work in 1988 observed fragment ions that involved both the backbone and the side chains [70]. The notation as it is commonly used today is shown in Figure 11.

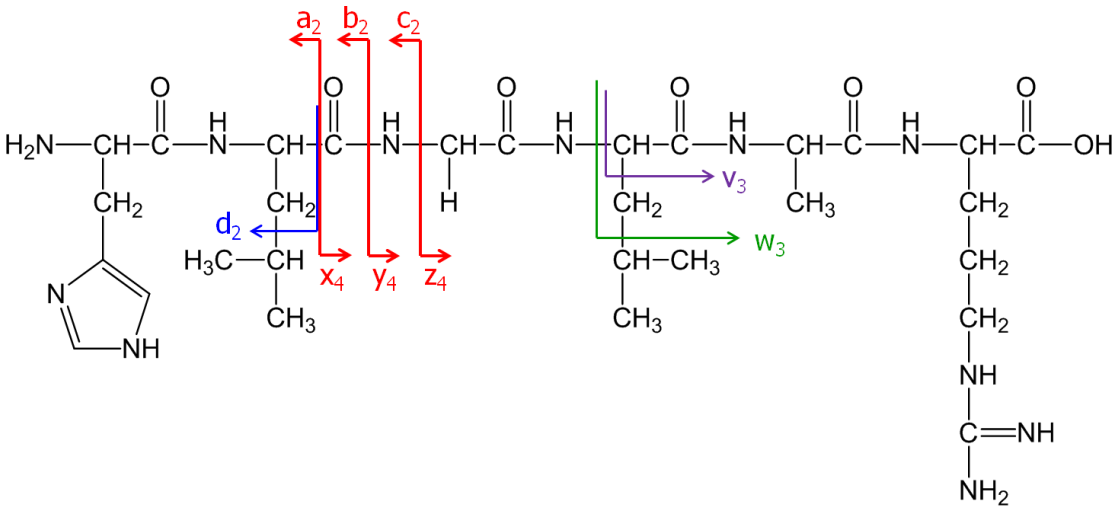

Figure 11: Peptide fragmentation nomenclature as defined by Biemann for the model peptide HLGLAR. The arrow indicates the side of charge retention. Note: no charge is shown in the peptide sketched here for simplicity.

When the charge is retained on the N-terminus, the fragment ion is termed an *a*-, *b*-, or *c*-type ion depending on the site of cleavage, and *x*-, *y*-, and *z*-type ions are formed when the charge is retained on the C-terminus. The other fragmentation sites shown include side-chain cleavages known as *d*-, *v*- and *w*-type ions which involve breaking of the peptide backbone and partial side chain loss. Which fragment ions are observed can vary with respect to the activation method used, but by correctly identifying all fragment ions, the amino acid sequence of the peptide or protein can be determined.

Factors Affecting Peptide Ion Fragmentation

There are a countless number of factors affecting peptide ion fragmentation and the details within every aspect are too numerous to discuss in detail here. Therefore, the focus here will be on the some of the facets influencing fragmentation occurring within MALDI TOF mass spectrometers on peptide ions. It is also worth noting that many of the fragmentation parameters are dependent on one another.

Energy and Timescale

As mentioned previously in the discussions on RRK/RRKM theory, the amount of energy deposited into a system will affect which fragment ions are observed [71]. This feature is further expanded in the Wahrhaftig diagram [2] (Figure 10) where it can be seen that at larger internal energies, certain fragment ions may be favored over others. Theoretically, high ion internal energies will produce more overall fragment ions, but this can be detrimental if the fragment ions created will not provide insights into the ion structure. When relating this idea to RRK theory, E is essentially much larger than many E_0's within the system allowing for more fragment ion pathways to be accessible. The overall distribution of ion internal energies will also have an effect on the fragment ions observed again rationalized by the Wahrhaftig diagram. Narrow ion internal energies will favor formation of a fewer number of fragment ions while broad distributions can favor many pathways.

The fragment ions observed in tandem experiments are also governed by the analysis time after excitation. If the rate of fragmentation is slower than the analysis

time, the fragment ion will not be observed. This point is clarified by noting the horizontal line in Figure 12 which denotes the timescale of the experiment.

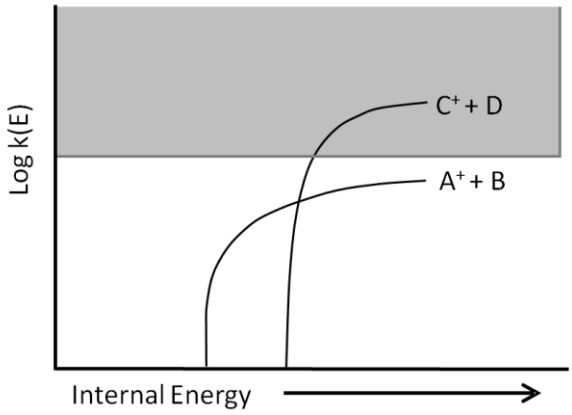

Figure 12: Portion of the Wahrhaftig diagram illustrating the effect of fragmentation timescale. Here the timescale of the instrumentation only examines ions in the shaded area.

The units for the rate, *k(E)*, are inverse seconds, or in other words the amount of times a reaction will occur per second. If the rate of fragmentation is slow (~ 10^3 s^{-1}) compared to our analysis time (~ 10^{-5} s), then the fragment ion will not be observed. This case is illustrated in Figure 12 in which the shaded area represents the analysis time of the instrument. Rates of peptide fragmentation have been reported in ranges from 10^2 s^{-1} to 10^9 s^{-1} [57, 72, 73]. Since a typical tandem TOF experiment occurs on the timescale of tens of microseconds, fragmentation pathways with rates less than 10^5 s^{-1} will not be observed. This feature will be exploited in the experiments described here.

Peptide Fragmentation Models and Amino Acid Influences

The amino acid sequence of the peptide will obviously have a dramatic influence on the fragment ions observed in a tandem mass spectrum, but discussion on some of the fine aspects of this obvious conclusion is warranted. Consider first the location of the ionizing proton in the peptide. If the proton is located toward the N-terminus, then only N-terminal fragment ions will be observed *i.e.* a_i-, b_i-, c_i- and d_i-type fragment ions. Therefore the gas-phase basicity or proton affinity of the individual amino acids will have a large influence on the location of this proton and those values are listed in Table 1.

Table 1: Proton affinities of the 20 common amino acids according to NIST listed in units of kcal/mol [74]. *The amino acid ornithine is not of the 20 common occurring amino acids but it is worth listing here owing to its high proton affinity.

Amino acid	PA (kcal/mol)	Amino acid	PA (kcal/mol)	Amino acid	PA (kcal/mol)
Glycine	211.9	Phenylalanine	220.6	Aspartic Acid	217.2
Alanine	215.5	Tryptophan	226.8	Glutamic Acid	218.2
Valine	217.6	Serine	218.6	Ornithine*	239.3
Leucine	218.6	Threonine	220.5	Histidine	236
Isoleucine	219.3	Asparagine	222	Lysine	238
Methionine	223.6	Glutamine	224.1	Arginine	251.2
Proline	220	Tyrosine	221		

The basic amino acids lysine, histidine, and arginine have large proton affinities and therefore can sequester the ionizing proton. Tryptic peptides, or peptides formed after enzymatic digestion with trypsin, contain a lysine or an arginine at the C-terminus.

The fragmentation of these peptides should reveal more C-terminal fragment ions than N-terminal fragment ions as the proton is most likely located on the basic side chain of arginine or lysine for the case of singly charged analytes.

Other amino acids can also have a large influence on peptide ion fragmentation and a few of those will be discussed here. Wysocki's work examining a large peptide database revealed that certain amino acids show a propensity for fragmentation while others do not [75-77]. The amino acids isoleucine, leucine, and valine, the branched aliphatic amino acids, show enhanced cleavage on the C-terminal side of the residue [75]. In work by Wysocki and others, it has been shown that cleavage at acidic amino acid residues is enhanced [77, 78]. Finally, fragmentation N-terminal to proline is one of the most predictable trends regarding peptide fragmentation likely due to the proline ring structure a feature termed the proline effect [75-77, 79-81]. This feature will be explored in detail in chapter 3.

The influences of secondary structure cannot be overlooked when considering peptide fragmentation [82]. However, these effects may be better understood by coupling fragmentation with ion mobility [83] and theoretical calculations [84] which will not be pursued in this work; however, it must be noted that fragmentation data can provide keen insights into the peptide/protein secondary structure.

In recent years, several research groups have provided insight to try and develop a more general model on how to describe peptide fragmentation in the gas-phase. One theory suggests that the site of fragmentation is located in close proximity to the ionizing charge is referred to as charge-directed fragmentation. This theory was forged upon the

mobile proton model [82, 85, 86]. This model predicts that after ionization, the ionizing proton is located on the most basic site within the molecule, and upon subsequent excitation, the proton can become mobile and shift to other sites within the peptide and generate fragments at that site. This process is shown pictorially in Figure 13.

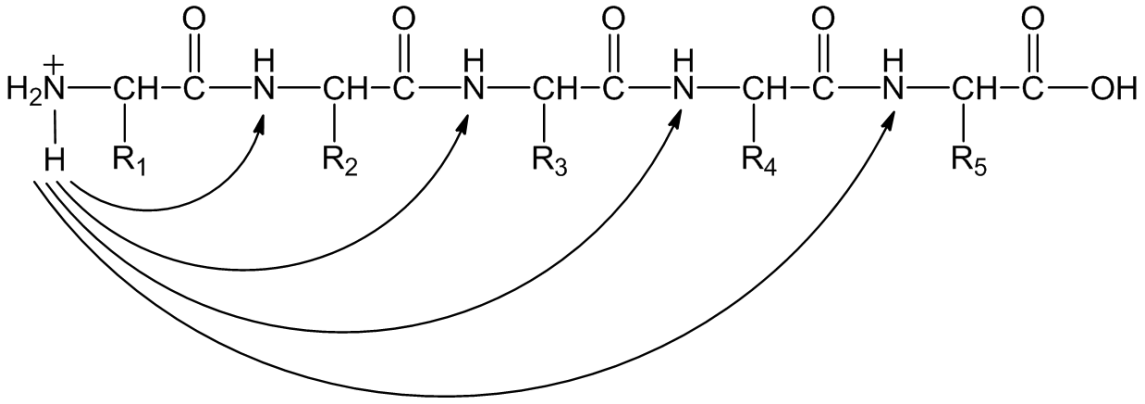

Figure 13: Depiction of mobile-proton model for a model peptide. Initially, the ionizing proton is located on the most basic site, the N-terminus, but after excitation it can migrate to other sites along the peptide backbone as shown.

The ionizing proton would move to the amide backbone nitrogen atoms thereby weakening the adjacent amide bond. Specifically, the location of an extra proton at this site reduces the double bond character of the amide bond which exists as a resonance form of the bond shown in Figure 13. Another possibility of charge-directed fragmentation involves a more structural view; that is, the ionizing proton is not located specifically at one site, but rather is coordinated by multiple ligands. The mobile proton model does not serve to predict all gas-phase peptide ion fragmentation reactions, but it

does provide better knowledge of the factors influencing the fragmentation which will lead to better algorithms to analyze large mass spectrometry data sets.

An alternative to charge-directed fragmentation is charge-remote fragmentation [87, 88]. Here the fragmentation takes place independent of the ionizing proton. Gross has suggested that peptide fragmentation might be more straightforward if the mobile proton was removed, *i.e.* by adding a fixed permanent charge. However, the addition of this permanent charge will affect the secondary structure of the peptide. It can be assumed that the proton remains sequestered on basic side chains, but charge directed effects are still a likely contributor on formation of fragment ions observed in the tandem mass spectrum. However, at high ion internal energies and low experimental timescales, there may not be sufficient time for a proton to be mobilized and any fragmentation observed may favor charge-remote processes. The processes that are more dominant for gas-phase peptide ion fragmentation within MALDI tandem TOF mass spectrometers depends unconditionally on the factors discussed previously: the method of energy deposition, the amount and distribution of energy deposition, and the timescale of the instrument. Since ESI produces multiply charged ions, the number of charges can also have a large influence on fragmentation processes[89]; however, the lack of multiply charged ions resulting from MALDI process averts this discussion.

Influence of the Charge Carrier

Most mass spectrometry studies of peptides and proteins investigate protonated species because of their ease of formation by traditional ionization methods; however, a

significant amount of work has investigated the influence of alternative charge carriers. Initially, Biemann and Zaia investigated several protocols for derivatizing the N-terminus of a peptide to create a quaternary amine with a permanent positive charge [90]. Fragmentation of these derivatized peptides yielded strictly N-terminal fragment ions, specifically *a*- and *d*-type ions. Biemann hypothesized that the use of these procedures will lead to more predictable fragmentation patterns of peptides and proteins increasing the ease of sequencing the peptide.

Alternatively, several groups have explored the use of metal cations to examine their influence on the fragmentation of peptides and proteins. Some groups have focused on the viability of using metal cations to assist in sequencing peptides or proteins while other have utilized tandem mass spectrometry to determine the preferred binding site of specific metal cations. Gross first observed the loss of the C-terminal amino acid from alkali metal cationized peptides and hypothesized that these fragment ions formed as a result of the metal cation being bound to the deprotonated C-terminal carboxylic acid [91]. Teesch and Adams proposed several mechanisms for formation of various other fragment ions (including a_i, b_i, c_i, y_i, and z_i) resulting from the fragmentation of alkali metal cationized peptides [92-94]. Both of these groups showed that by examining the fragmentation pattern of alkali metal cationized peptides one could improve the information content of tandem mass spectra of peptides and proteins.

In addition to the analytical improvements afforded by investigating metalated peptides and proteins, much research has focused on determining the preferred binding sites of metal cations which may provide insights into the binding of metal cations by

proteins in biological systems [95]. Early work by Gross [91] and Teesch and Adams [92-94] hypothesized various locations for the binding sites of alkali metal cations including the C-terminus, the N-terminus, the backbone amide nitrogen, the backbone carbonyl groups, or the side chains of the amino acids. This non-specific binding of alkali metal cations was further confirmed by theoretical calculations performed by Wesdemiotis [96], Dunbar [97], and Ling [98]. Contrary to alkali-metal cations, the binding of copper (I) ions is more specific with preferred binding occurring at basic residues with coordination by other ligands [99, 100]. Improved studies utilizing fragmentation in conjunction with ion mobility are becoming more prevalent for determining the binding sites of metal cations as structural information can be obtained by ion mobility with fragmentation assisting in determining the preferred metal ion binding sites [95].

Excitation Methods

The method of excitation has an outstanding influence on what fragment ions will be observed from peptide fragmentation. Some ions, known as metastable ions, can have excess internal energy from ionization and will fragment after ionization. Since MALDI formed ions are typically just above the threshold for ionization, it would be expected that they would have minimal excess internal energy and therefore only form low energy fragments. Even though investigation of metastable ions can be useful, the majority of ions will need to receive excess internal energy by an activation method in order to fragment.

Numerous methods of peptide ion activation have been developed and successfully employed, *viz.*, collision induced dissociation (CID) [101, 102], electron capture/transfer dissociation (ECD/ETD) [103], surface induced dissociation [104], and photodissociation methods, *e.g*. infrared multiphoton dissociation [105] and ultraviolet (UV) photodissociation [106]. Each method has its own distinct advantages with CID being the most commonly employed technique. Time-of-flight mass analyzers most commonly investigate metastable ions or utilize CID, but the studies here will also explore UV photodissociation.

Excitation Methods: CID

In CID, ions of interest are activated by collisions with a neutral gas and subsequent fragmentation provides structural information [101, 102]. Each collision between the analyte ion and the gas imparts a given amount of vibrational and/or electronic energy into the precursor ion until an energy threshold is reached and the fragmentation occurs. The maximum amount of energy that can be deposited into the ion via a center-of-mass (COM) collision can be determined by equation 8:

$$(8) \qquad E_{com} = \left(\frac{m_{gas}}{m_{gas} + m_{ion}} \right) E_{lab}$$

Where m_{gas} is the mass of the neutral collision gas molecules, m_{ion} is the mass of the ion and E_{lab} is the laboratory energy applied. However, the energy is only valid for COM collisions and what is more probable are "grazing" collisions which impart some fraction of the COM energy [102]. These 'grazing' collisions can result in a wide range

of energies being deposited into the ion of interest. Note also that collisions with larger mass ions will not impart as much energy into the ion.

The amount of energy deposited by each collision also depends on the mass analyzer being used and in some cases multiple collisions are required to generate fragmentation. As such, CID can be more aptly described by division into three subsets as seen in Table 2 adapted from the work by Wells and McLuckey [102]. From this table, it is unfair to group all CID methods into one category, because they have vastly different energy regimes depending on the chosen method of analysis.

Table 2: Typical operating parameters for a variety of CID conditions dependent on the mass analyzer [102]. The shaded area is for tandem TOF instrument which are the focus here. The collision energy values are in terms of E_{lab} and not the actual energy deposited into the system.

	Trapping CID	**"low energy" CID**	**"high energy" CID**
Mass Analyzers	Ion traps, FTICR	Triple quads, QTOF	Sectors, TOF/TOF
Collision energy	1 – 20 eV	1 – 200 eV	2 – 10 keV
Distribution of energy	Few eV	Few eV	Few eV with a tail up to 10 eV
Number of collisions	hundreds	10 – 100	1 – 5
Activation timescale	10 – 100 ms	0.5 – 1 ms	1 – 10 µs
Instrument timescale	10 ms – 1 s	0.1 – 1 ms	10 – 100 µs

Tandem TOF CID can deposit a very wide range of internal energies into the molecule of interest from a few meV to several eV up to the COM energy which is usually on the order of 10s of eV [107]. This can be advantageous for generating as

many fragment ions as possible, but carefully controlled energy deposition experiments are more difficult to perform and still result in a spread of energies [108].

Excitation Methods: UV Photodissociation

While fragmentation via CID is more commonly used in tandem TOF instruments, UV photodissociation is also an effective means of inducing peptide fragmentation [106]. The use of photodissociation to generate peptide fragment ions was first shown by McIver in 1984 on an FTICR [109] and on a TOF instrument by Russell in 1995 [72]. Photodissociation is advantageous over CID as the incorporation of the laser does not interfere with the mass spectrometer as the CID gas molecules can diminish the resolution. In most cases, photodissociation in a TOF mass analyzer involves orthogonally intersecting the ion beam with a focused UV laser. The timing of the laser pulse is critical owing to the high velocity of both the precursor ions ($6.2x10^4$ m/s for a 1000 Dalton ion accelerated at 20kV of energy) and the photons ($3.0x10^8$ m/s) making this experiment extremely difficult.

In UV photodissociation, sufficient energy can be imparted by a single photon to form fragment ions. Two wavelength outputs from excimer lasers commonly used for UV photodissociation of peptides are 193 nm and 157 nm, which correspond to photon energies of 6.4eV and 7.9eV, respectively. These two wavelengths are used because the amide backbone linkages absorb readily at these wavelengths making photon absorption independent of the amino acid side chains [106]. Additionally, these energies are in excess of the carbon-nitrogen (3.61eV) and carbon-carbon (3.16 eV) bonds contained in

the peptide backbone [110]. Other groups have also used the quadrupled output of a neodinium:yttrium aluminum garnet (Nd:YAG) laser to provide photons at 266 nm [111, 112]. However, absorption at this wavelength is dependent on the presence of aromatic amino acid side chains.

Upon absorption of a photon, several dissociation processes can occur which will result in bond dissociation. If the excited molecule exists in the potential energy surface where the dissociation limit is exceeded or if excitation to a dissociative potential energy surface occurs, direct bond dissociation will occur. Direct bond dissociation occurs 'promptly' and can circumvent vibrational redistribution. These processes are typically more common with small rigid, molecules rather than larger molecules *esp.* peptides and proteins as studied herein. Alternatively, indirect bond dissociation occurs when the excited state of a molecule undergoes and intersystem crossing to a dissociative state resulting in bond dissociation as shown in Figure 14**.** This process is likely preferred for large molecules that can more readily redistribute the energy throughout the vibrational modes of the molecule [58].

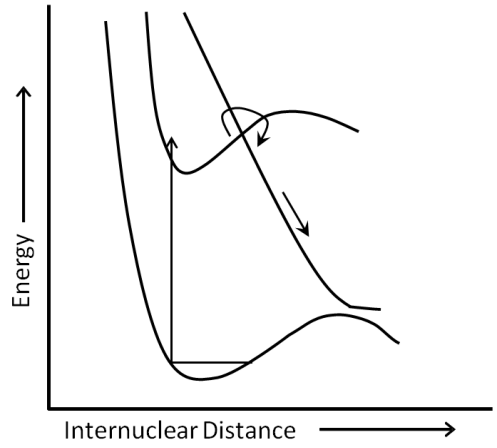

Figure 14: Example of indirect bond dissociation involving an intersystem crossing.

UV photodissociation can also provide an advantage over CID as there is no distribution of energies in UV photodissociation as the energy is defined by the photon and is also not a function of the mass as with CID. A diagram comparing internal energies of excited molecular ions from CID and photodissociation is shown in Figure 15. However, it must be noted that in tandem TOF UV photodissociation all ion internal energies are not the same as there is a distribution of internal energies that originate from the MALDI process.

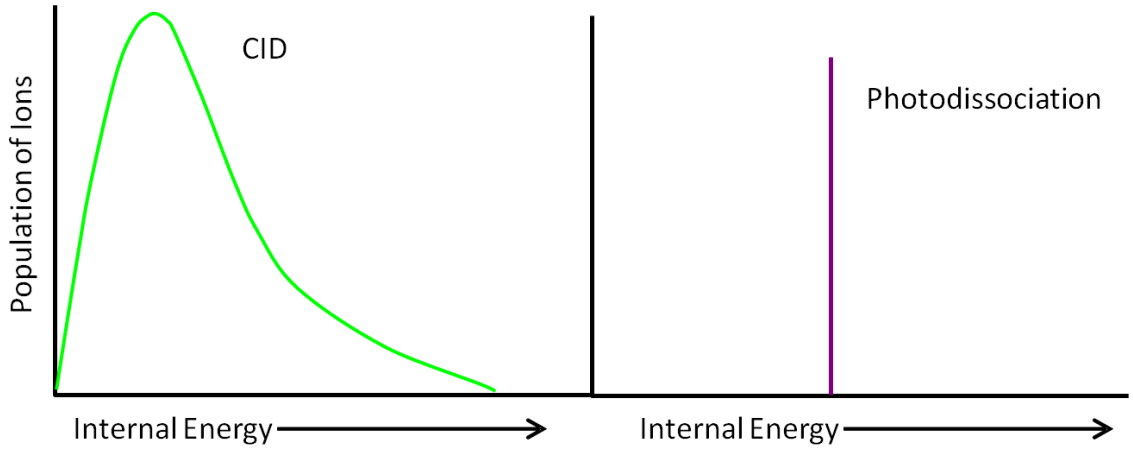

Figure 15: Distribution of ion internal energies resulting from CID and UV photodissociation.

TOF/TOF photodissociation experiments in the Russell research group were originally focused on peptide sequencing [113] but have since evolved into more kinetic based studies [114]. Barbacci's original tandem TOF design incorporating a reflectron [115, 116] applied the "PSD (post source decay) focusing method" to examine fragment ions from 193 nm UV photodissociation. This involved tuning the reflectron voltage to focus different *m/z* fragment ions at the detector. This method sufficed in producing excellent tandem mass spectra, but the instrument duty cycle was not effective as up to 10 individually summed spectra had to be acquired and stitched together to generate the complete mass range of the experiment. Additionally, the contributions from the metastable decay of the ionized peptides contributed to the fragment ion spectrum, a feature that was addressed in the work by Hettick [117].

An additional feature of this instrument is the timescale allotted for decay of photo excited precursor ions. Based on the initial velocity of precursor ions from the

source region, the photo excited ions have approximately 10 μs to dissociate before the ions enter the reflectron. After entrance into the reflectron, the fragment ions cannot be distinguished from the remaining precursor ions. That is, only fragment ions that formed at a rate of $k(e) \geq 1*10^5$ s^{-1} will be detected while those that form with rates $< 1*10^5$ s^{-1} will not be observed.

The instrument modifications made by Morgan involved the incorporation of a biased activation cell to examine fragment ions on shorter timescales, termed "prompt" fragment ions, and to acquire the entire fragment ion spectrum in a single MALDI event [114]. For these experiments, irradiated ions have on average 1 μs to fragment inside the photodissociation cell before reacceleration. Fragment ions that form after exiting the photodissociation cell will not be focused at the detector. Photofragment ion spectra obtained with this design contained abundant *a*- and *x*-type fragment ions. Experiments also identified that "prompt" fragmentation facilitates the identification of post-translational modifications (PTMs) as these modifications are typically lost when examining longer fragmentation timescales [114]. An additional benefit of the photodissociation cell is the ability to acquire the entire mass range at one reflectron voltage, dramatically reducing the analysis time for a given sample.

When comparing mass spectra, differing time scales of fragmentation will reveal different fragment ion distributions. Certain fragment ions may either be observed or not simply based on the allotted time for fragmentation. The investigation of photodissociation on different time scales is known as time-resolved photodissociation and has been explored recently by several groups. Kim and coworkers examined the

splitting of peaks when applying a low voltage to their photodissociation cell design in their TOF/TOF instrument [73]. They attributed this splitting of peaks to fragment ions formed within the activation cell, those formed after reacceleration, and fragment ions formed as a result of consecutive reactions from different fragment ions. They determined that after irradiation peptide ions had on average 65 ns to fragment before exiting the activation cell, while those forming after the cell were on the order of about 10μs. The splitting of peaks creates complex mass spectra where it is difficult to distinguish peak splitting from peak isotopes. Ideally, it would be easier to interpret the data of the experimental timescales if the experiments could be performed separately.

Additionally, Reilly and coworkers recently presented photodissociation data in a linear ion trap instrument where they introduced specific time delays of, 300 ns, 1 μs, 5 μs or 13 μs, after irradiation at 157 nm before analyzing fragment ions with an orthogonal-TOF mass spectrometer [118, 119]. Results from their initial experiments show that a proton is mobilized on shorter time scale with lysine than with arginine and that phosphopeptides lose the phosphate group approximately 1 μs after irradiation. However, the collisions experienced by the irradiated precursor ions could either have a cooling or heating effect resulting in inconclusive results.

Chapters II and III will examine the influences of metal cations on the fragmentation of various peptides ions. Specifically, Chapter II will investigate the influences of alkali metal cations (Li^+, Na^+ and K^+) and copper (I) ions on the collision-induced dissociation of a series of peptides containing various amino acid residues (arginine, lysine, histidine, and aspartic acid) at the N-terminus. Alkali metal

cations reveal a broad range of fragment ions owing to the non-specific binding of the metal cations by various ligands including the N-terminus, C-terminus, backbone amides and carbonyls, and the amino acid side chains. Alternatively, $[M + H]^+$ and $[M + Cu]^+$, reveal abundant N-terminal fragment ions owing to the specific binding by the basic amino acid residues at the N-terminus. Chapter IV examines the appearance of *x*-type fragment ions resulting from collision-induced dissociation of a series of model peptide ions. These fragment ions occur at valine residues but also form C-terminal to an N-terminal arginine residue indicating a large influence by the leaving group.

Additionally, we have developed advanced TOF instrumentation to investigate the fragmentation timescales of UV photodissociation of peptide ions. Chapter IV describes the photodissociation instrument in detail including the first modifications made to improve overall instrument performance. Specifically, these include addition of a series of deceleration lenses for better performance of 'prompt' dissociation studies. Additionally, performance characteristics of the instrumentation are evaluated with 193 nm photodissociation data compared at two different timescales, 1 μs and 10 μs.

Chapter V focuses on a study of the fragmentation characteristics of proline containing peptide ions. Here both CID tandem TOF and 193 nm photodissociation are used to investigate the appearance of *Y*- and *a+1*- type fragment ions which occurring specifically at proline residues. Additionally, the 'prompt' photofragment ion spectra are used to identify any influences by the fragmentation timescale. It should be mentioned that the CID tandem TOF data presented has contributions from both the

metastable ions and from CID fragment ions, while the photodissociation data had very little contribution from the metastable ion spectrum.

Chapters VI and VII will focus on further instrument modifications to help improve the performance of photodissociation tandem TOF. Specifically, a pulsed "second source" after 193 nm photon irradiation will be added to reaccelerate fragment ions and remaining precursor ions to nominally the same kinetic energy. Morgan's prompt photodissociation experiments performed without a pulse produced fragment ions and precursor ions that can still have large differences in their kinetic energies, up to 50%, resulting in ion losses through the reflectron. The incorporation of a pulsed second source also requires improved reflectron focusing which will be tackled by adding a dual-stage reflectron. An additional benefit of the second source is the ability to vary the fragmentation timescale from a 1 microsecond to 10s of microseconds by tuning voltages within the instrument. Evaluation of the instrument performance will be accomplished by examining several model peptides previously well studied. Chapter VIII will provide overall conclusions and suggest possible future directions for this instrumentation.

CHAPTER II

HOW DO METAL ION AFFINITY AND BINDING SITE INFLUENCE THE FRAGMENTATION OF PEPTIDE IONS?

The fragmentation reactions of $[M + H]^+$, $[M + Li]^+$, $[M + Na]^+$, $[M + K]^+$ and $[M + Cu]^+$ ions of RVGVAPG, KVGVAPG, HVGVAPG, and DVGVAPG are examined by using tandem time-of-flight mass spectrometry (TOF-MS) and collision induced dissociation (CID) to probe the effect of charge site on fragmentation reactions. $[M + H]^+$ ions of this series favor formation of N-terminal fragment ions (average N-terminal:C-terminal fragment ion ratio by abundance 3.3, 10.6, 4.1, and 5.4, respectively). $[M + Cu]^+$ ions of RVGVAPG, KVGVAPG, and HVGVAPG strongly favor formation of N-terminal fragment ions (average N/C abundance ratio of 144, 79, and 24, respectively); however, the ratio of N/C-terminal fragment ions (3.0) for $[M + Cu]^+$ ions of DVGVAPG is much lower. The preference for N-terminal fragment ion formation in RVGVAPG is attributed to complexation of the Cu^+ by the guanidine group and the carboxylic acid group and this rationalization is supported by results from theoretical calculations. The fragmentation reactions of alkali metal cationized peptides do not strongly favor N- or C-terminal fragment ions which is attributed to the non-specific binding of these metal ions.

Introduction

The chemistry of gas-phase peptide ions is an active area of mass spectrometry research [75, 120-124]. Much of our understanding of peptide ion chemistry is based on studies of tryptic peptides, those that contain arginine (R) or lysine (K) at the C-terminal position; however, there are many other types of peptides that are important in biological systems, *i.e.*, products of proteolytic digests using proteoases such as chymotrypsin, Asp-N, Glu-C, or Lys-C[125-129], naturally occurring peptides important in endocrinology[130], insect peptides[129], non-ribosomal peptide synthesis[131], and peptide antibiotics[132]. The aims of the studies in this work focus on developing unimolecular dissociation reactions of non-tryptic protonated and metal cationized ions, $[M + H]^+$ and $[M + cat]^+$, where cat represents the metal ion, for determining the amino acid sequence (1^o structure) of peptides, how peptide-Cat^+ binding sites and bond energies of metal ions affect the dissociation reactions, and how intra-molecular interactions, *i.e.*, H-bonds, salt-bridges and/or disulfide bonds, stabilize $2^o/3^o$ structures influence the chemistry.

A number of mechanisms have been proposed to describe peptide ion fragmentation chemistry, including charge-remote[88] and charge-directed[85] fragmentation, which includes the mobile proton model[86]. It is generally assumed that charge-remote fragmentation is important when the charge is localized on the molecule, *i.e.,* a specific site on the molecule such as the N-terminus derivatized with a charged group such as quaternary amine. On the other hand, peptides that contain arginine or lysine, amino acids that have very high proton [74] and metal ion affinities[96, 97, 100,

133], may also promote charge-remote fragmentation. For example, protonation of R and K containing peptides occurs at guanidine or ε-amino group. Although the protonated side chains may H-bond to the peptide backbone, the proton will not freely migrate (delocalize) along the peptide backbone[134]. Likewise, metal cations, especially Cu^+ and possibly Ag^+, which have very high binding energies to N-bases, may act as fixed charge sites similar to quaternary amines.

We previously rationalized the fragmentation reactions of $[M + Cu]^+$ ions of peptide ions containing basic side chains (R and K) using a mechanism originally proposed by Adams [100, 135]. For example, coordination of Cu^+ by the guanidine group of arginine displaces a proton, which then acts as a mobile charge, inducing fragmentation reactions along the peptide backbone [100]. More recent studies on the fragmentation reactions of model peptides have motivated us to revisit this mechanism. Specifically, the fragmentation reactions of cys-kemptide (amino acid sequence CLRRASLG) and the conformations of low internal energy cys-kemptide $[M + Cu]^+$ ions appear to be dictated by coordination of the Cu^+ ions to multiple ligands [136]. Although ion-neutral collision cross sections obtained by using ion mobility spectrometry (IMS) suggest the $[M + Cu]^+$ ions have a compact structure, the product ions of collision-induced dissociation are best rationalized by a more extended structure. That is, it appears that coordination of Cu^+ ions by the thiol group of cysteine results in proton transfer from -SH to the arginine at position four (R^4), and the subsequent fragmentation reactions yield N-terminal, Cu^+ containing fragment ions.

Here, we present a comparison of the fragmentation patterns of a homologous peptide series to which different charge carriers (H^+, Li^+, Na^+, K^+, and Cu^+) are attached. Wesdemiotis, Dunbar, and Ling have performed *ab initio* calculations in an effort to understand the molecular details of metal ion binding to peptides, specifically Na^+ to guanidine ligands [96-98]. Our objectives are to: 1) determine the metal ion binding sites to the peptide, 2) assess differences in the fragmentation chemistry owing to differences in metal ion binding sites, and 3) evaluate the role of charge-remote fragmentation reactions. Our hypothesis is that peptide ion fragmentation is governed by: 1) the location of the charge along the backbone of the peptide, 2) the relative binding energies of the charge carrier to the peptide, and 3) the secondary/tertiary (intramolecular interactions, primarily charge solvation) structures of the ions [137, 138].

The peptide sequence RVGVAPG is used as a scaffold to probe several effects uncomplicated by strongly interacting side chains, specifically, formation of H-bonding, salt-bridges or disulfide bond formation, which can alter tertiary structure. The sequence scaffold (VGVAPG) labeled with an N-terminal fixed charge group (phosphonium acetyl (PhoA)) was used previously by Allison [139] to examine the effects of specific charge carriers on charge-remote fragmentation[100, 135, 140]. For RVGVAPG ions the occurrence of charge-remote fragmentation will depend on where the charge is located and the binding energy of the metal ion or proton located at that site. Although the peptide contains proline, which is known to affect peptide ion fragmentation[76], it is not expected to have a strong influence on metal ion binding

[141] or the fragmentation reactions of the ions. This assumption was confirmed by examining a similar peptide sequence where the proline is replaced by a glycine residue, *viz.* RVGVAGG.

Methods

Materials

Both the syntheses of the model peptides and the cation doping procedures were carried out in scrupulously cleaned glassware or in single-use plastic ware. Water was obtained from a Barnstead Nanopure Model 4741 filtration system (Dubuque, Iowa, USA). All solvents were obtained from EM Science (Gibbstown, New Jersey, USA). HPLC grade dichloromethane, ether and methanol were distilled in glass over appropriate drying agents, and stored over freshly-activated 4 Å molecular sieves. DMF, also HPLC grade, was distilled under reduced pressure, stored over activated 4 Å molecular sieves and was degassed immediately prior to use. α-Cyano-4-hydroxycinnamic acid (Aldrich, Milwaukee, Wisconsin, USA) was recrystallized twice from hot methanol. Other materials were from recognized commercial sources and used as received.

Peptides were prepared using FMOC chemistry on 2-chlorotrityl chloride resin (Novabiochem, San Diego, California, USA) and purified using standard techniques. The identity and purity of each peptide was confirmed by MALDI-TOF-MS before subsequent analyses were performed. Metalation was performed by incubating the peptides at 1 mg mL^{-1} concentration in a 1:1 (v:v) ratio with 20 mM aqueous ($CuSO_4$) or

saturated methanolic (Li_2CO_3, Na_2CO_3, K_2CO_3) solutions for 30 minutes. For copper, this yields a dopant to analyte concentration ratio of roughly 15. Then, the peptide/metal solutions were combined with 30 mg ml^{-1} α-cyano-4-hydroxycinnamic acid in MeOH, mixed thoroughly and spotted onto a MALDI plate for analysis. Each sample was prepared with a matrix-to-analyte ratio of *ca*. 1000, with approximately 150 pmol of analyte deposited per spot. The total sample spot was never consumed in any of the experiments, so the actual amount of analyte detected is unknown.

Matrix-Assisted Laser Desorption/Ionization TOF/TOF Mass Spectrometry

Tandem MS experiments were performed in positive polarity using a 4700 Proteomics Analyzer (Applied Biosystems, Framingham, Massachusetts, USA), which will be referred to as the TOF/TOF. The CID acceleration was 1 kV and the collision gas was air. The fragmentation data obtained in these experiments was first handled using Data Explorer™, histogrammed using Microsoft Excel™, and imported into PSI-Plot™ for clear 3-dimensional visualization. The nomenclature for fragments of the studied peptides follows the scheme established by Roepstorff and Fohlman[69] as modified by Biemann [61, 142], with the addition of "+ metal" to indicate that a particular fragment is metal-bearing, *e.g.* $[b_3 + Na]^+$. It is worth noting that these metal containing fragment ions contain one less proton and have the metal ion adducted, but for simplicity we excluded the "- H" from our labeling scheme.

Theoretical Calculations

The relative stability of peptide-Cu ion structures were theoretically explored using density functional theory, at the B3LYP/LACV3P** level [143-145]. The LACV3P basis set is a triple- ζ contraction of the LACVP basis set [146] developed and tested at Schrödinger, Inc. [147]. In particular, Cu ions were treated using effective core potentials, while all the other atoms were treated with the 6-311G** basis set. No symmetry restriction of any kind was imposed in the process of geometry optimization. All calculations were performed with the Jaguar 7.0 software using the pseudospectral method to minimize the computational time [148].

Results and Discussion

Figure 16a-c contains the TOF-TOF spectra for $[M + H]^+$, $[M + Cu]^+$, and $[M + Na]^+$ ions of RVGVAPG, respectively. Fragmentation of RVGVAPG $[M + H]^+$ ions yields a large number of a_i and b_i ions, and many fewer *y*-ions, *viz.* y_2 and y_3. Clearly, there is a strong preference for charge retention by the N-terminus. The fragmentation chemistry for $[M + Cu]^+$ ion (Figure 16b) is similar to that observed for $[M + H]^+$ ions. Note, however, that compared to $[M + H]^+$, the abundances of the y_i ions for $[M + Cu]^+$ are suppressed, which we attribute to the strong binding of Cu^+ by the N-terminal arginine residue[99]. The similarities in terms of fragmentation channels for $[M + H]^+$ and $[M + Cu]^+$ ions are attributed to the proton and Cu^+ ion affinities by the guanidine side chain (252 kcal/mol for H^+ [74] and ~129 kcal/mol for Cu^+ [99]); however,

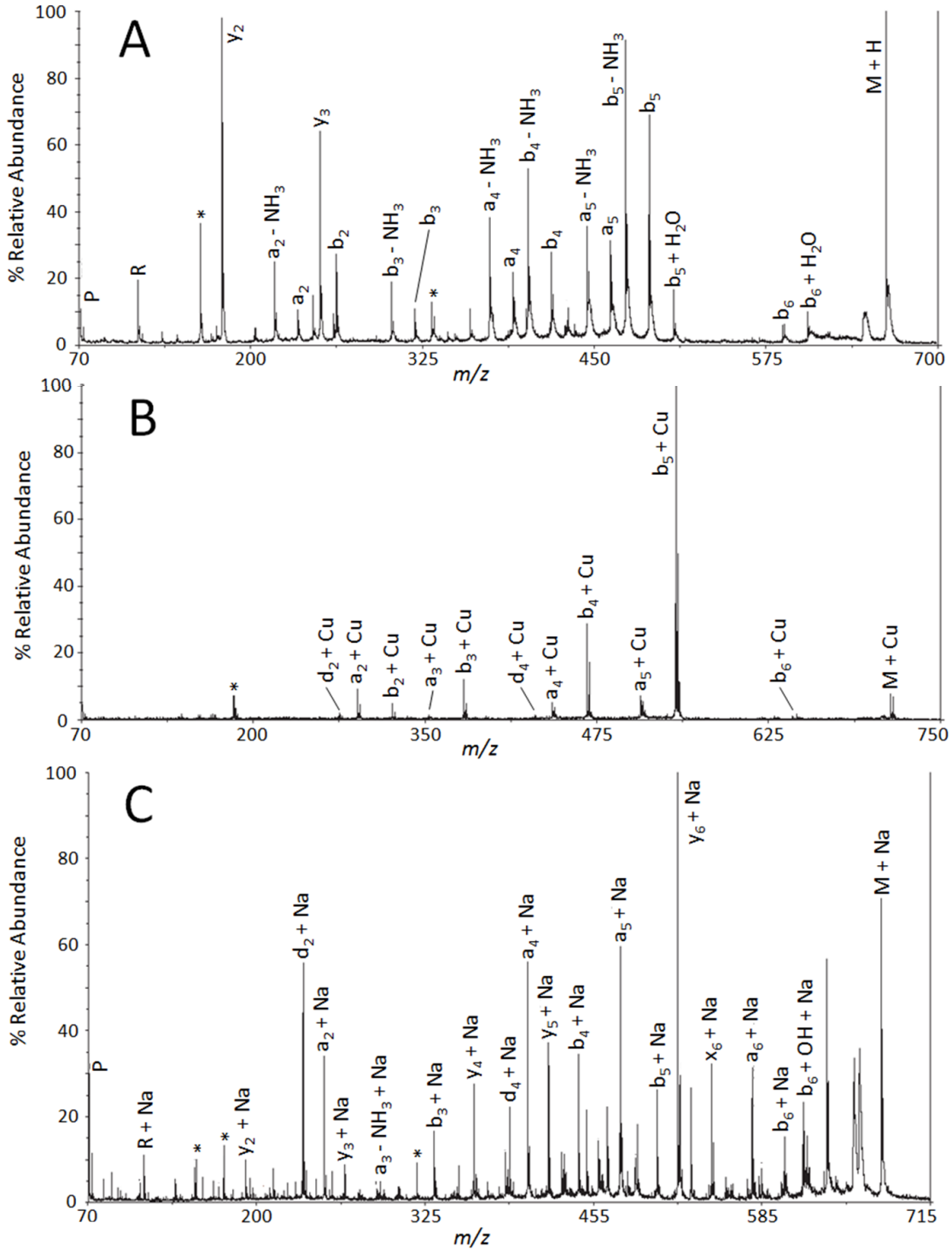

Figure 16: Tandem mass spectra for (**a**) $[RVGVAPG + H]^+$, (**b**) $[RVGVAPG + Cu]^+$ and (**c**) $[RVGVAPG + Na]^+$. Internal fragments have been labeled with an asterisk "*".

the Cu^+ ion is likely coordinated by multiple ligands. This is supported by results from theoretical calculations. For example, structures of $[M + Cu]^+$ ions obtained from B3LYP/LACV3P basis sets for the truncated version of RVGVAPG, namely RG are shown in Figure 17**.** The lowest energy structure **I** has the Cu^+ ion coordinated by the imine group of the guanidine side chain and the C-terminal carboxylic acid group. Structure **II**, which is ~20 kcal mol^{-1} higher in energy relative to structure **I**, has the proton on the guanidine group and the Cu^+ ion is coordinated by the carboxylate anion. We could not find any evidence for salt-bridge type structures involving the guanidinum ion-Cu^+-carboxylate anion as previously suggested.[149, 150] Thus, structure **II** has a more extended confirmation than that of structure **I**. Structure **III** is at an even higher energy level (~24 kcal mol^{-1}) with respect to **I**; Cu^+ ion is coordinated to the N-terminal amine and the first backbone carbonyl. Finally, structure **IV** has Cu^+ ion coordinated to a deprotonated guanidine group and a protonated N-terminus. This structural form is very high energy, ~50 kcal mol^{-1}, suggesting that the mechanism proposed by Adams and Shields is not operative for this system.

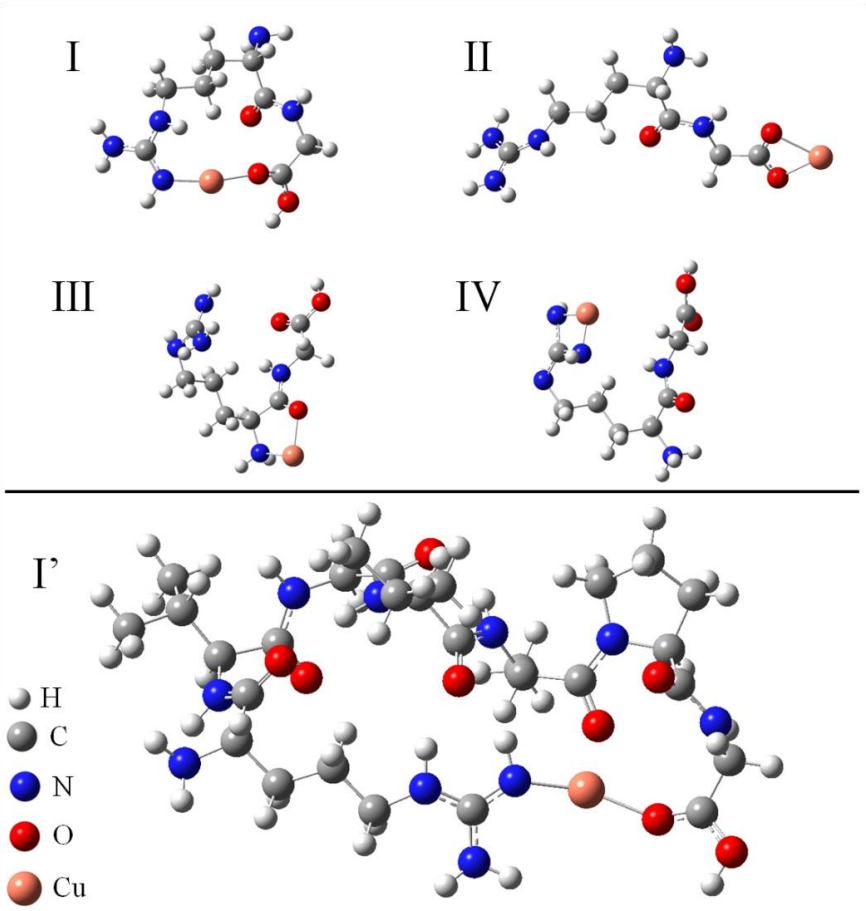

Figure 17: Calculated structures for the di-amino acid, RG with the copper coordinated to I) the guanidine group and the C-terminal carboxylate, II) the deprotonated C-terminus, III) the N-terminus, and IV) to a deprotonated guanidine group. Structure I' shows the complete sequence RVGVAPG with the copper bound to the guanidine group and the C-terminal carboxylate analogous to structure I.

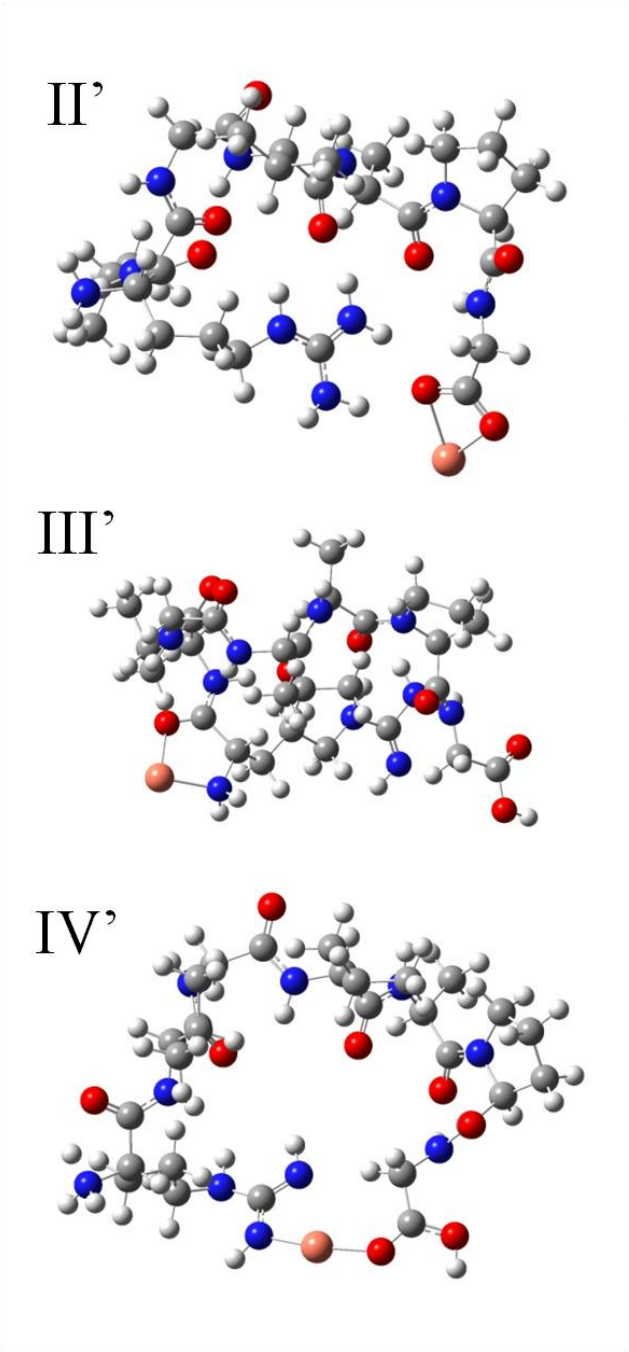

Figure 18: Calculated structures for the peptide RVGVAPG+Cu with the copper coordinated to II’) the deprotonated C-terminus, III’) the deprotonated C-terminus, III) the N-terminus, and IV) to a deprotonated guanidine group and C-terminal carboxylate.

Similar calculations performed on the RVGVAPG $[M + Cu]^+$ ions yielded similar ion conformers. For example, Structure **I'** (see Figure 17) suggests a structure for $[M + Cu]^+$ ions that is very similar to structure **I,** both in terms of Cu^+ ion binding site and overall structure. The other calculated structures of $[M + Cu]^+$ can also be correlated to the structures (**II-IV**) of $[RG + Cu]^+$ (see structures **II'-IV'** in Figure 18). The comparison of $[RG + Cu]^+$ to RVGVAPG $[M + Cu]^+$ appears valid as the relative energies of structures **II'-IV'** occur in the same order. For example, structure **II'** lies ~23 kcal mol^{-1} higher in energy than structure **I'** and structures **III'** and **IV'** are ~50 kcal mol^{-1} and ~58 kcal mol^{-1} higher in energy, respectively. The relative energies of the theoretical structures of $[RG + Cu]^+$ and RVGVAPG $[M + Cu]^+$ are given in Table 3.

Table 3: Calculated energies for the various structures of $[RG + Cu]^+$ and $[\mathbf{1} + Cu]^+$. *ΔE* provided are relative to the lowest energy structure, **I** or **I'** respectively.

Structure	ΔE (kcal mol^{-1})
$[RG + Cu]^+$ **I**	-
$[RG + Cu]^+$ **II**	26
$[RG + Cu]^+$ **III**	26
$[RG + Cu]^+$ **IV**	52
$[RVGVAPG + Cu]^+$ **I'**	-
$[RVGVAPG + Cu]^+$ **II'**	23
$[RVGVAPG + Cu]^+$ **III'**	50
$[RVGVAPG + Cu]^+$ **IV'**	58

The combination of the fragment ion spectrum and the theoretical calculations suggest that interactions between the Cu^+ ions and the C-terminus of RVGVAPG are weak relative to that of the guanidine group. For example, the fragment ion spectrum for the methyl ester of RVGVAPG $[M + H]^+$ and $[M + Cu]^+$ ions do not differ significantly from that for the free-acid form of the peptide, which underscores our arguments that protonation and Cu^+ ion attachment occurs on the N-terminal basic amino acid, and that the appearance of C-terminal fragment ions in the spectrum of $[M + H]^+$ probably arises as a result of charge migration from this site.

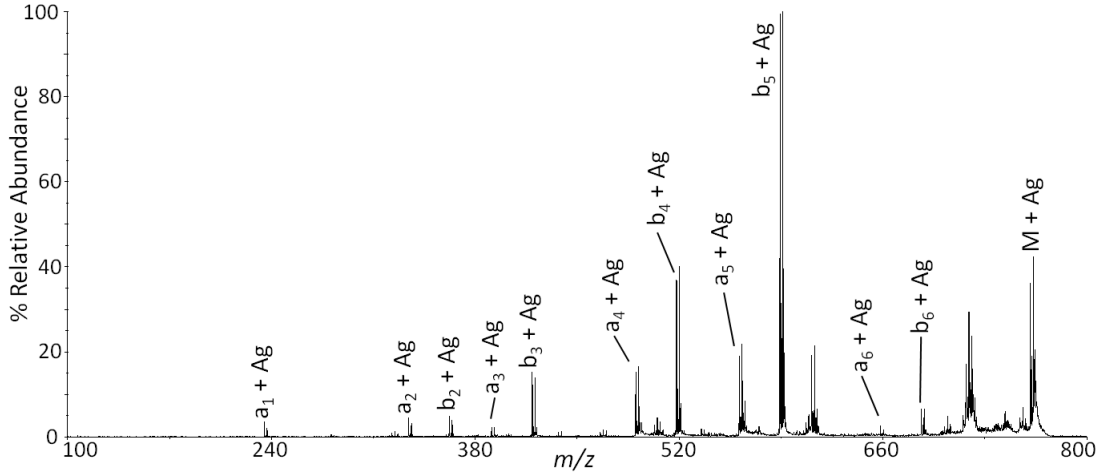

Figure 19: Tandem mass spectra for $[RVGVAPG + Ag]^+$.

It has been previously reported that the fragment ion spectra of $[M + Ag]^+$ peptides is similar to that of $[M + H]^+$ [151] and based on the results obtained here could be comparable to the $[M + Cu]^+$ species. CID of RVGVAPG $[M + Ag]^+$ ions (see Figure 19) yields similar product ions to $[M + Cu]^+$, but the relative abundances of the product

ions are significantly different, which most likely reflect different metal ion binding energies to the guanidine group as well as intramolecular interactions involving the backbone amide groups. It also appears that proline has no significant effect on the fragmentation chemistry. That is, the fragment ion spectrum of the $[M + H]^+$ ion of the peptide RVGVAPG is very similar to that of RVGVAGG (Figure 20). For RVGVAGG $[M + Cu]^+$ ions the b_6 fragment ion is a major product ion, whereas this ion is not observed for $[M + Cu]^+$ ions owing to the presence of proline, which is known to hinder *b*-type ion formation [76].

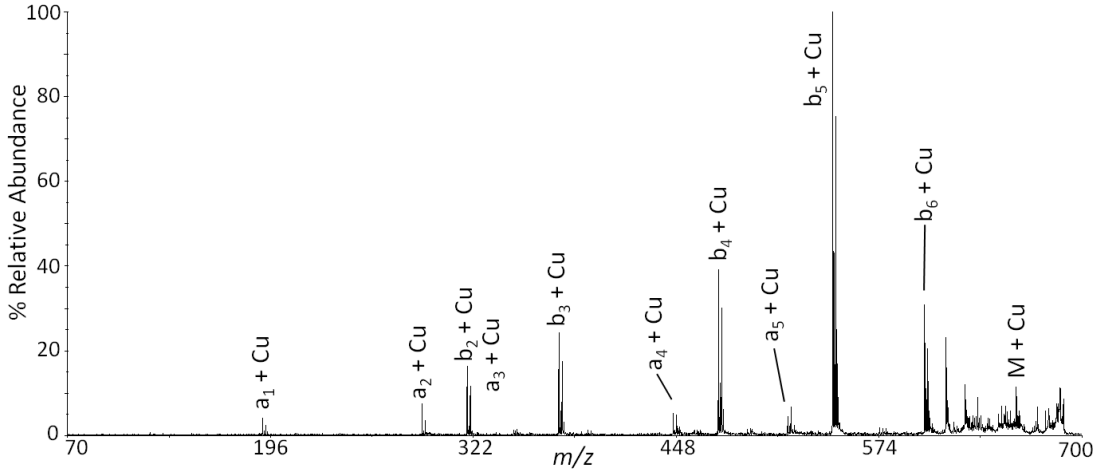

Figure 20: Tandem mass spectra for $[RVGVAGG + Cu]^+$.

It is interesting to compare the fragmentation chemistry of RVGVAPG $[M + H]^+$ and $[M + Cu]^+$ ions to that of $[M + Na]^+$ ions. $[M + Na]^+$ ions (Figure 16c) yield both N- and C-terminal fragment ions, which we interpret as evidence for multiple coordination sites for Na^+ ions. That is, Na^+ ion binding energies by the N-terminus, the

guanidine group, the C-terminus and the amide backbone are comparable, ranging from 38-53 kcal mol^{-1} [96, 141, 152]. Consequently, the ion population is comprised of a number of different conformers that differ in terms of metal ion coordination[141]. TOF-TOF spectra for the $[M + Li]^+$ and $[M + K]^+$ ions are very similar to that for $[M + Na]^+$ for all peptides examined in this study and are not shown. This result is expected as the relative binding energies of these cations to the different functional groups are similar. [96, 99, 133, 141, 152, 153]

We also examined how changing proton and metal ion affinity of the N-terminal amino acid influences the fragmentation chemistry of the peptide, *i.e.,* substituting histidine, lysine or aspartic acid for arginine. We chose to investigate these amino acids because the proton and metal ion affinities for arginine and lysine are similar and differ significantly from that of aspartic acid. On the other hand, proton affinity and metal ion coordination of histidine is considerably less than that of arginine and lysine.[141]

Figure 21a-c contains TOF-TOF spectra for $[M + H]^+$, $[M + Na]^+$, and $[M + Cu]^+$ ions of KVGVAPG, respectively. Again, the observed fragment ions, the ion abundances and N/C terminal fragment ion ratios of $[M + H]^+$ and $[M + Cu]^+$ ions are similar to those observed for RVGVAPG. The fragment ion spectrum of KVGVAPG $[M + Na]^+$ is very similar to that for RVGVAPG, which may be an effect of the flexibility of the Arg and Lys side chains and the peptide backbone to solvate the charge carrier [134]. Alternatively, the similarities could simply be attributed to the metal ion binding affinities of these two amino acids which are similar. Currently, these issues are

being investigated using ion mobility-mass spectrometry and molecular dynamics simulations.

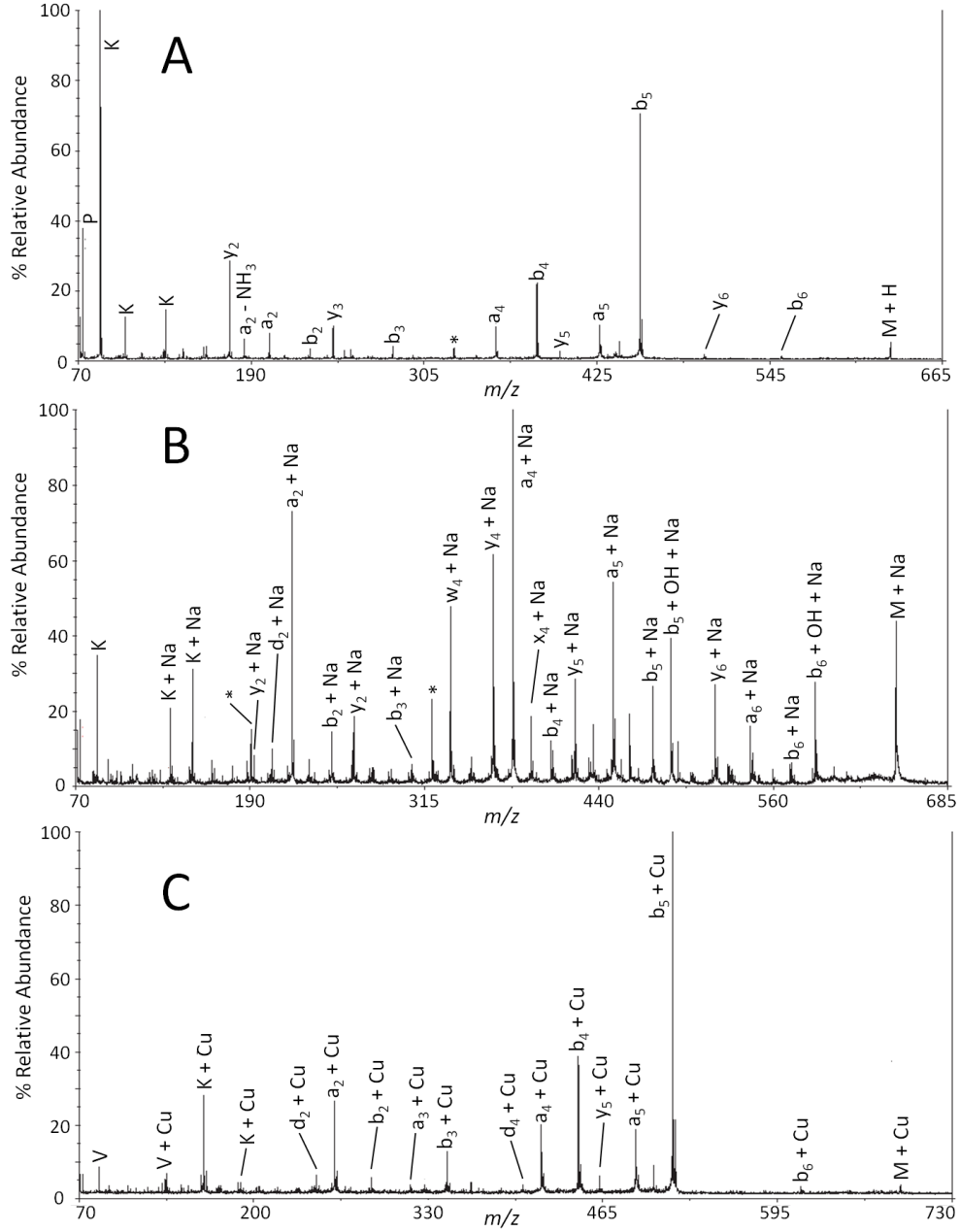

Figure 21: Tandem mass spectra for (**a**) $[HVGVAPG + H]^+$, (**b**) $[HVGVAPG + Na]^+$ and (**c**) $[HVGVAPG + Cu]^+$. Internal fragments have been labeled with an asterisk "*".

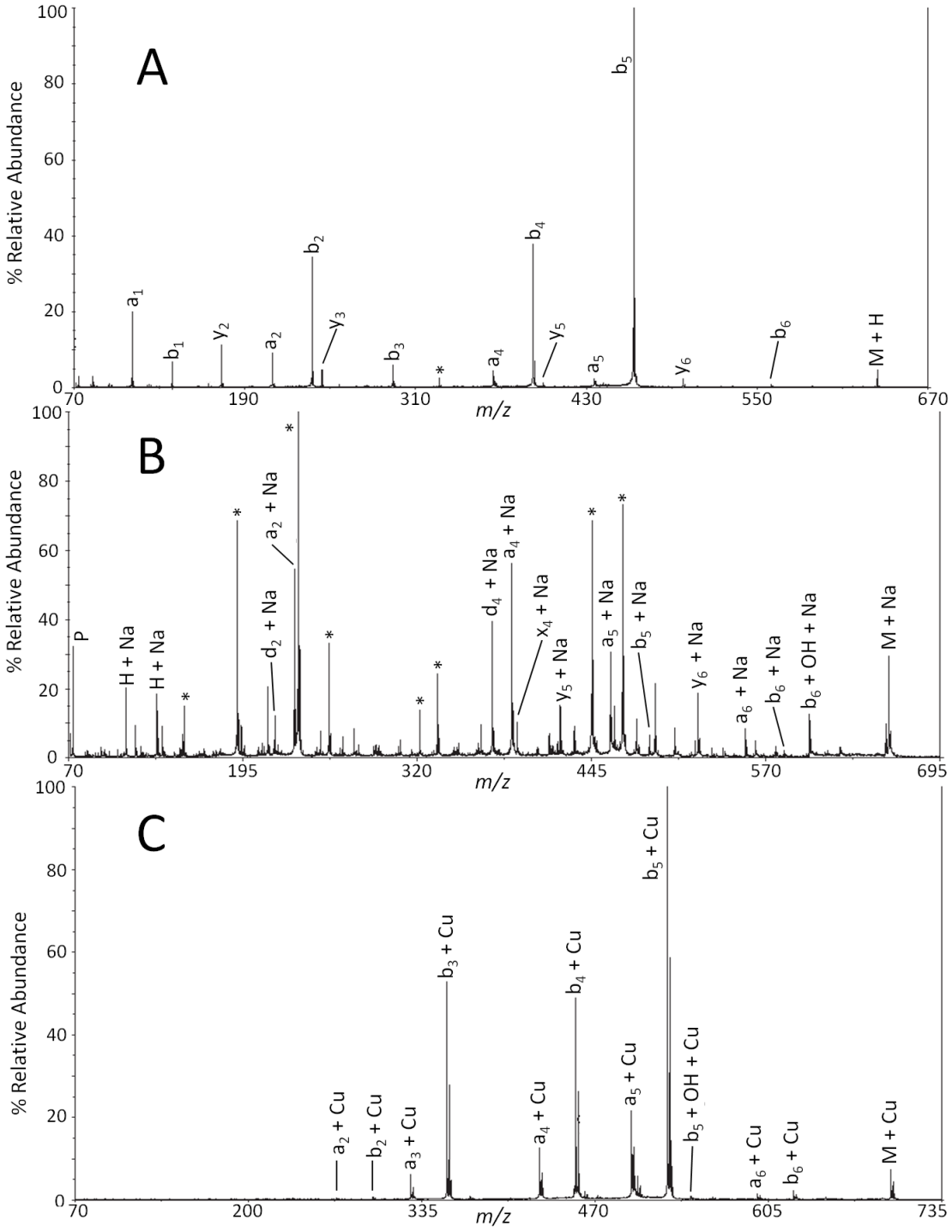

Figure 22: Tandem mass spectra for (**a**) $[KVGVAPG + H]^+$, (**b**) $[KVGVAPG + Na]^+$ and (**c**) $[KVGVAPG + Cu]^+$. Internal fragments have been labeled with an asterisk "*".

Figure 22a-c contains the TOF-TOF spectra for $[M + H]^+$, $[M + Na]^+$, and $[M + Cu]^+$ ions of HVGVAPG, respectively. The fragmentation chemistry of HVGVAPG $[M + Cu]^+$ and $[M + H]^+$ are quite similar to that of peptide RVGVAPG with respect to observed fragment ions and fragment ion abundances; however, the fragment ion spectrum of the $[M + Na]^+$ ion is quite different. Specifically, the spectrum contains abundant a_i ions as well as side-chain cleavage product ions, d_4 and d_2, and y_i ions, y_5 and y_6. In addition, it is also interesting to note the high relative abundance of internal fragment ions such as $(a_n y_m)^+_i$ and $(b_n y_m)^+_i$, which are less important for RVGVAPG $[M + Na]^+$ ions.

On the basis of the results presented here we conclude that for XVGVAPG ions both protonation and metal ion binding is controlled primarily by the N-terminal basic residue, where X = R, H, or K. The conclusions are supported by comparing the fragment ion spectra of peptides containing R, K, and H with that for DVGVAPG (Figure 23a-c). The fragmentation chemistry for DVGVAPG $[M + H]^+$, $[M + Na]^+$, and $[M + Cu]^+$ differ with respect to RVGVAPG, KVGVAPG and HVGVAPG both in terms of observed fragment ions and their abundances. Note that TOF-TOF spectra for DVGVAPG $[M + H]^+$, $[M + Na]^+$, and $[M + Cu]^+$ ions are dominated by C-terminal y_i fragments ions.

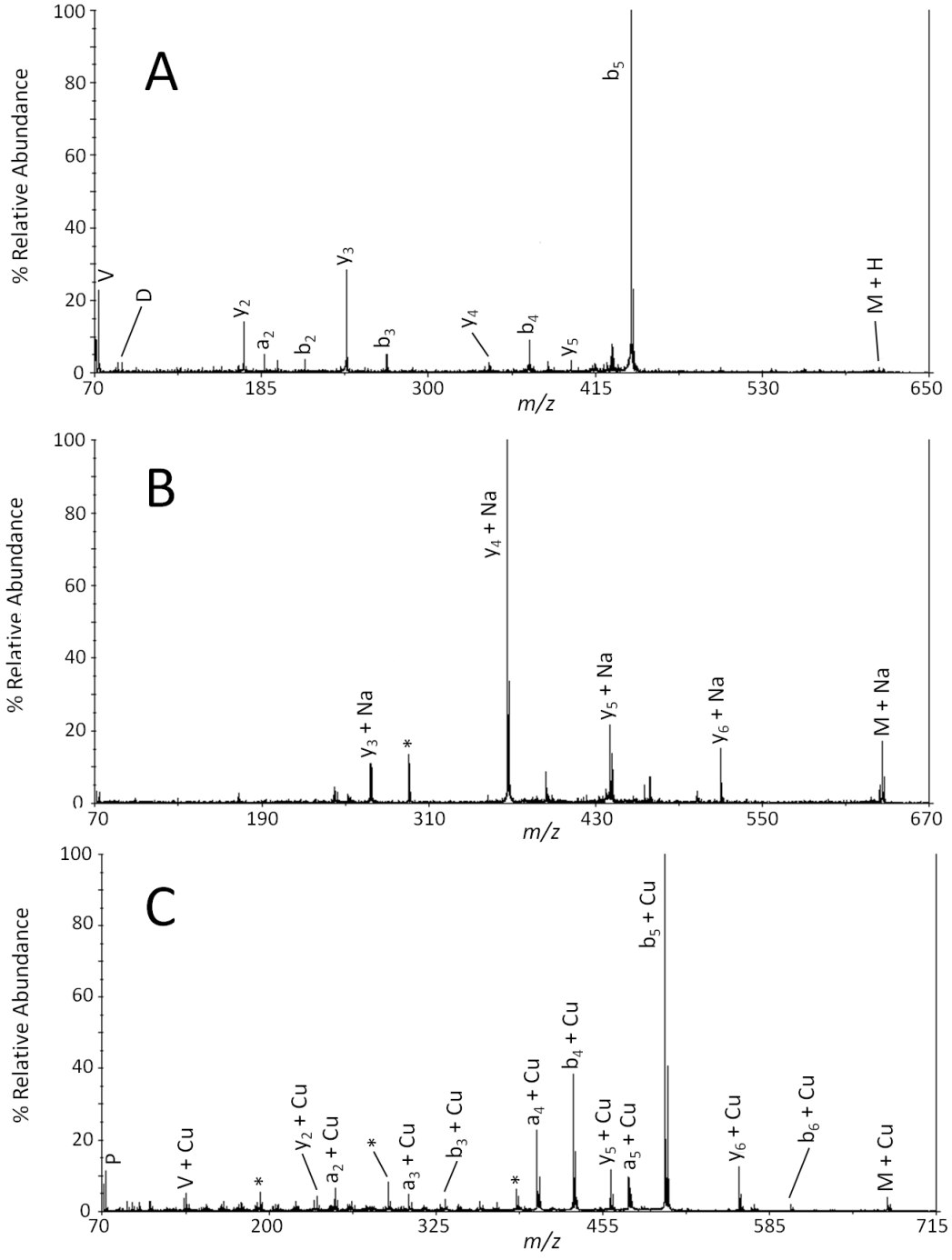

Figure 23: Tandem mass spectra for (**a**) $[DVGVAPG + H]^+$, (**b**) $[DVGVAPG + Na]^+$ and (**c**) $[DVGVAPG + Cu]^+$. Internal fragments have been labeled with an asterisk "*".

Conclusions

The results of the fragmentation study are summarized in Figure 24a-d. Each plot compares the relative abundance of each sequence-informative fragment ion series for the $[M + H]^+$, $[M + Li]^+$, $[M + Na]^+$, $[M + K]^+$, and $[M + Cu]^+$ ions for each peptide described in this paper. For RVGVAPG $[M + Cu]^+$, the preference for N-terminal fragments is clearly visible; note that the ratio of N-terminal to C-terminal charge carrying fragment ions is approximately 140:1, which translates to approximately 75% of the total sequence-informative ions, whereas the total sequence-informative N-terminal ions for the alkali metal species range from 35-55%.

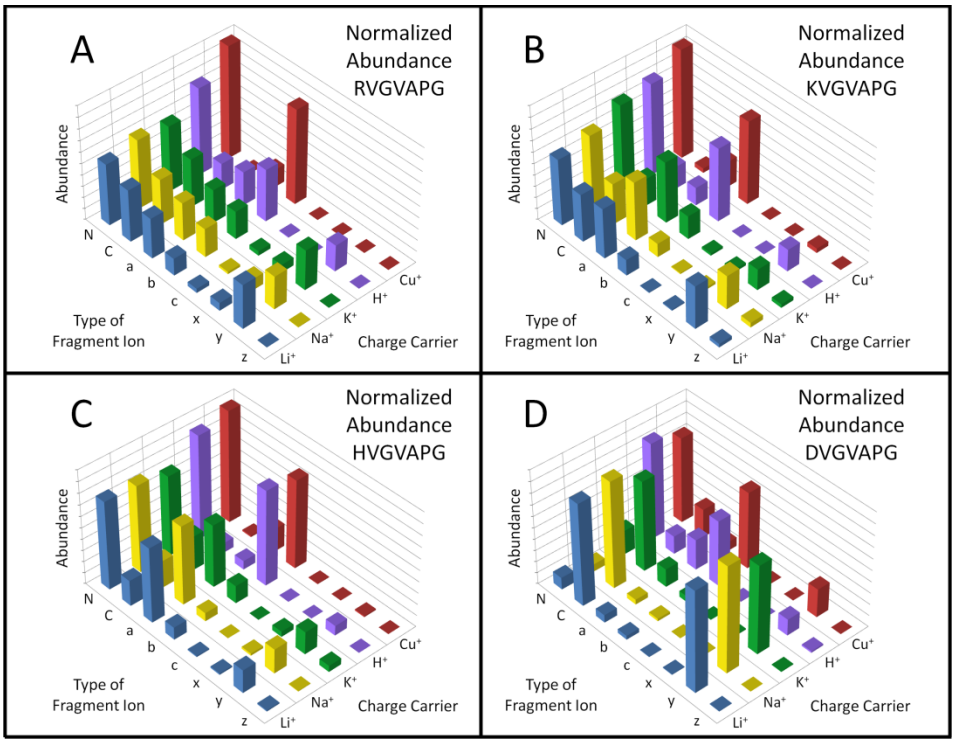

Figure 24: Relative abundances of sequence-informative fragments, with sums of *N*- and *C*-terminal fragments for the $[M + H]^+$, $[M + Li]^+$, $[M + Na]^+$, $[M + K]^+$ and $[M + Cu]^+$ ions of (**a**) RVGVAPG (**b**) HVGVAPG (**c**) KVGVAPG and (**d**) DVGVAPG.

H^+, Li^+, Na^+, K^+, and Cu^+ influence the fragmentation chemistry of peptide ions in different ways, but there are notable similarities (see Figure 24a-d**)**. Particularly noteworthy is the fact that the $[M + H]^+$ and $[M + Cu]^+$ ions are very similar in terms of abundances and types of fragment ions observed. In each case the $[M + H]^+$ and $[M + Cu]^+$ ions show a stronger preference (75% - 99%) for forming N-terminal fragment ions compared to alkali metal cations. For peptides with a basic N-terminal residue, $[M + Cu]^+$ ions show a stronger preference for N-terminal fragment ions than do $[M + H]^+$ ions, which suggest that the Cu^+ ion binding energy for the N-terminal basic residue exceeds that of any other functional group[136]. It is unclear as to whether this is due to the fact that the ionizing proton for $[M + H]^+$ ions can act as a mobile proton and migrate to other sites along the peptide backbone resulting in an increase in C-terminal fragment ions[86] or multi-dentate coordination of Cu^+ ions by the peptide, *i.e.*, coordination of Cu^+ ions by both the guanidine group as well as the N-terminal amine group. These issues are being explored further by theoretical calculations as well as ion mobility spectrometry.

$[M + Li]^+$, $[M + Na]^+$, and $[M + K]^+$ ions can also be grouped together based on similarities in fragment ion type and abundances. Alkali metal cationized peptides with an N-terminal basic residue show a slight preference for forming N-terminal fragment ions (55% - 77%), but this preference is diminished compared to $[M + H]^+$ and $[M + Cu]^+$ (75% - 99%). This observation is likely a result of similar binding energies of the metal ion to specific sites within the peptide, resulting in a broader distribution of fragment ions [96, 133, 141, 152, 153]. Indeed, an increase in c_i, x_i, and z_i fragment ions

is also observed for alkali metal cationized species, which further supports the idea of nonspecific binding for these peptides.

Although the fragment ion spectrum of DVGVAPG $[M + H]^+$ and $[M + Cu]^+$ are similar, both yield abundant b_5 fragment ions, the spectrum of DVGVAPG $[M + H]^+$ and $[M + Cu]^+$ ions differs significantly to that of XVGVAPG (X= R, H, and K). Specifically, both N- and C-terminal fragment ions are observed for the protonated ions of all peptides in this study, whereas spectra of DVGVAPG $[M + Cu]^+$ ions contain higher abundances of N-terminal ions. The N-terminal fragment ion abundance for DVGVAPG $[M + Cu]^+$, shifts from >95% for RVGVAPG, KVGVAPG, and HVGVAPG to about 75%, which suggests that in the absence of a basic side chain, the Cu^+ ion most likely binds to the next most basic site, *i.e.,* the N-terminus. However, the interaction between the N-terminus and the Cu^+ ion is not as strong as the interaction between a basic side chain and a Cu^+ cation resulting in more abundant C-terminal fragment ions. For DVGVAPG, alkali metal cationized peptides show a strong preference for the C-terminus, note that 80% - 90% of the fragment ions correspond to C-terminal fragment ions, specifically *y*-type ions. Although the aspartatic acid side chain should be a good ligand for oxyphilic alkali metal ions, thereby increasing the abundance of N-terminal fragment ions, this does not appear to be the case. The preference for C-terminal ions suggests a strong preference for C-terminal binding of alkali metal ions, which could be an effect of ion structure as noted by Jarrold. [146].

CHAPTER III

FORMATION OF X-TYPE FRAGMENT IONS FROM COLLISION-INDUCED DISSOCATION OF METAL CATIONIZED PEPTIDES

The fragmentation reactions of a series of model alkali metal cationized peptides are investigated by collision induced dissociation tandem time-of-flight mass spectrometry. The major focus is the mechanism for formation of $[x_i - H + Cat]^+$, where Cat is an alkali metal cation. $[x_i - H + Cat]^+$ fragment ions are frequently observed N-terminal to valine residues, which suggest that valine plays a role in *x*-type ion formation, although, $[x_{n-1} - H + Cat]^+$ fragment ions, where *n* is the number of amino acids, are only observed for peptides that contain an N-terminal arginine. N-terminally acetylated or C-terminally methylated peptides do not influence *x*-type fragment ion formation, which suggest that these groups do not affect alkali metal cation binding. A mechanism for formation of *x*-type fragment ions involving alkali metal cation binding to the backbone amide and the carbonyl moieties is proposed.

Introduction

The chemistry of metal-peptide and metal-protein interactions has been an active area of research for many years owing to the important roles these interactions play in biological systems[154, 155]. Many of these studies have been performed in the gas-phase, such as mass spectrometry, to avoid solvent effects which can dramatically alter preferential binding of the metal cation to the peptide or protein. Much of the mass

spectrometry research has focused on determining metal ion binding sites [100, 156-159], binding energies [141], and fragmentation mechanisms, including charge-remote [88, 100, 139] and charge directed mechanisms [85]. While ion mobility spectrometry has been used recently to obtain this information, [160] a more traditional approach is the use of tandem mass spectrometry [*e.g.* collision induced dissociation (CID) mass spectrometry] [161, 162]. Fragmentation studies on metal-peptide complexes can also provide useful information regarding the amino acid sequence of the peptide or protein especially in determining the C-terminal amino acid[156, 162].

Alkali metal cationized peptides and proteins, in particular sodium and potassium, are especially abundant in biological systems and are known to play significant roles in activation of enzymes, cellular metabolism, and stabilization of protein structure[155, 163]. Differences observed in the fragmentation between alkali metal-peptide complexes are attributed to i) differences in the binding energies between the peptide and the metal cation, (ii) the location of the metal cation within the peptide, and (iii) the secondary and tertiary structures of the peptide-cation complex. Possible locations of the metal cation include the N-terminal amide, the C-terminal carboxylate, the side chains of the amino acid residues, or along the peptide backbone coordinated to the carbonyl oxygen and/or the backbone amide.

Studies of alkali metal ion binding sites to peptides have been reported by several groups, and these studies have yielded proposed mechanisms for formation of $[a_i - H + Cat]^+$, $[b_i - H + Cat]^+$, $[c_i - H + Cat]^+$, $[y_i - H + Cat]^+$, $[z_i - H + Cat]^+$, and $[b_{n-1} + OH + Cat]^+$ [156-159]. Gross and coworkers [156] and Renner and Spiteller

[164] proposed that alkali metal ions are coordinated to a deprotonated C-terminal carboxylate where the proton is located elsewhere within the peptide either at the N-terminus, along the peptide backbone, or on the functional side chains of the amino acids. Subsequent nucleophilic attack of the deprotonated C-terminal carboxylate on the amide backbone can promote elimination of the C-terminal amino acid residue or a $[b_{n-1} + OH + Cat]^+$ ion. Other groups proposed similar mechanisms [124, 162]. Teesch and Adams hypothesized that an alkali metal cation could be coordinated to a backbone carbonyl and/or amide groups and they proposed mechanisms for formation of $[a_i - H + Cat]^+$, $[b_i - H + Cat]^+$ $[c_i - H + Cat]^+$, $[y_i - H + Cat]^+$, and $[z_i - H + Cat]^+$, $[b_{n-1} + OH + Cat]^+$, $[b_i - H + Cat]^+$ ions [158, 159]. Additionally, these groups acknowledge that the metal cation could be coordinated to a basic or acidic amino acid side chain which could also influence the fragmentation mechanisms.

The formation of *x*-type fragment ions from protonated peptides is not typically discussed as these ions only appear in high energy vacuum ultraviolet photofragment ion spectra [165-167] and are rarely observed in CID spectra. While *x*-type ions are present in the tandem mass spectra of alkali metal cationized peptides [156, 158, 159], little has been discussed on the formation of these ions and to our knowledge the mechanism for formation of *x*-type fragment ions from alkali metal cationized peptides has not been addressed. Here we propose a mechanism for formation of $[x_i - H + Cat]^+$ from peptides cationized with Li^+, Na^+, and K^+. To probe this mechanism we synthesized a series of peptides which allowed us to examine several factors affecting the fragmentation chemistry, including peptide length, position of valine, acetylation at the N-terminus,

methyl esterification of the C-terminus, and influence of varying amino acid residues at the N-terminus.

Methods

All chemicals used in this study were purchased from Sigma-Aldrich (St. Louis, MO) unless otherwise noted. Peptide synthesis was performed in-house according to standard protocols and those synthesized include: RVGVAPG, VGVAPG, GVAPG, RVGVAP, RVGVA, RVGV, RVGVASG, RVGVAGG, acetyl-RVGVAGG, acetyl-RVGVASG, acetyl-RVGVAPG, RAVGVGG, KVGVAPG, HVGVASG, and DVGVAPG. Each solid peptide was dissolved in water to a final concentration of 1 mg/mL. Peptides were metalated by combining aqueous 5mg/mL LiCl, $NaNO_3$ or KNO_3 in a 1:1 (v:v) ratio with the peptide solution and incubated at room temperature for 30 minutes. Peptide/dopant solutions were combined with 5mg/mL α-cyano-4-hydroxycinnamic acid in MeOH and 0.5μL was spotted onto a MALDI plate for analysis, which corresponds to about 200 pmol of analyte deposited on each spot.

^{18}O exchange was performed by incubating 200 μg of solid peptide in a solution of 25 μL of ^{18}O labeled water and 1 μL of 12M HCl for 72 hours [168]. Both oxygen atoms at the C-terminal carboxylate will exchange shifting all C-terminal fragments by 4 mass units to more confidently identify fragment ions in the spectrum. Methyl esterification was performed on all peptides to determine the influence of the C-terminus on the fragmentation pattern [169]. Briefly, the reagent solution was prepared by the dropwise addition of 800 μL of acetyl chloride to 5 mL of anhydrous methanol while

stirring. After 5 minutes, 30 μL of the reagent solution was combined with 300 μg of dried peptide and allowed to react for two hours. The peptide solution was then dried and combined with H_2O for analysis.

Matrix assisted laser desorption/ionization (MALDI) mass spectrometry was performed using an Applied Biosystems 4800 Proteomics Analyzer operating the collision cell at 1 kV collision energy using air as the collision gas. All fragment ions were labeled according to the scheme established by Roepstorff and Fohlmann [69] as modified by Biemann [61], although there exist subtle issues in the nomenclature regarding metal cationized peptides. Other groups have simply denoted the fragment ions as Biemann proposed but made the broad statement that all fragment ions contain a metal ion adduct. While this is true for most of the fragment ions in a given spectrum, there exists the possibility of observing fragment ions which do not contain the metal cation. The presence of fragment ions without a cation is especially possible if the cation is bound to a deprotonated C-terminal carboxylate. For example, it is generally accepted that a *b*-type fragment ion from a protonated peptide exists as either an acylium ion [61], an oxazolone structure [170, 171] or some other large macro-cyclic structure [172-174]. If we denote a fragment ion as "b_i+Cat" this could imply an acylium ion plus a cation, which results in two overall charges. To avoid this problem we will denote fragment ions according to the Biemann nomenclature but we will also clarify if the fragment ion contains the cation or not.

Results and Discussion

While other research groups have proposed mechanisms for fragment ion formation from alkali metal cationized peptides, no one has addressed the formation of *x*-type fragment ions even though these fragment ions have appeared in tandem mass spectra of alkali metal cationized peptides. By examining CID TOF/TOF mass spectra of several model peptides we were able to test the influence of i) valine residues, ii) the basicity of the N-terminal amino acid, iii) N-terminal amine, and iv) the C-terminal carboxylate on the formation of x-type fragment ions. From the results acquired, we developed a mechanism for *x*-type fragment ion formation which involves cation binding along the peptide backbone with the metal cation coordinated by the amide and carbonyl functional groups. Additionally, we observed a fragment ion 16 mass units less than the x_{n-1} fragment ion which we believe involves oxygen transfer from the x-type fragment ion to the leaving group.

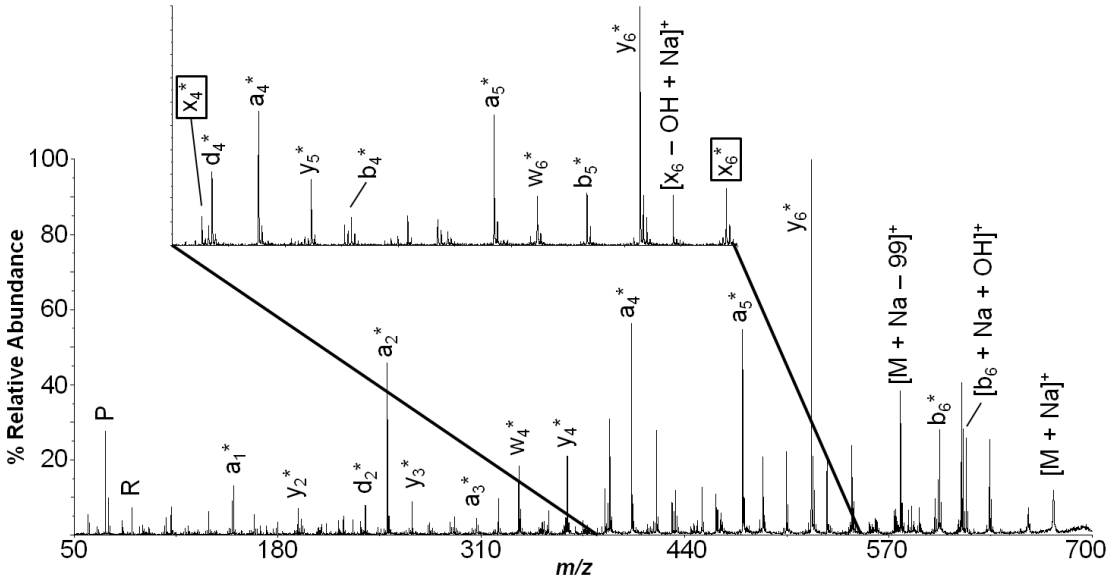

Figure 25: Tandem mass spectrum of $[RVGVAPG + Na]^+$. Fragment ions labeled "*" are less one proton and have the sodium cation adducted *e.*g. $[f_i - H + Na]^+$.

Displayed in Figure 25 is the TOF/TOF mass spectrum of $[RVGVAPG + Na]^+$. Additionally we have investigated the TOF/TOF mass spectra of a) $[RVGVAPG + H]^+$, b) $[RVGVAPG + Li]^+$, c) $[RVGVAPG + Na]^+$, and d) $[RVGVAPG + K]^+$, shown in Figure 26. Abundant *a*-, *b*-, and *y*- type fragment ions are observed for $[RVGVAPG + H]^+$ with a preference for *a*- and *b*-type fragments owing to the presence of the basic arginine residue at the N-terminus. Fragmentation patterns of $[M + Li]^+$ (Figure 26b), $[M + Na]^+$ (Figure 26c), and $[M + K]^+$ (Figure 26d) are similar when comparing the observed fragment ions and fragment ion abundances and therefore we will limit discussion to the $[M + Na]^+$ species.

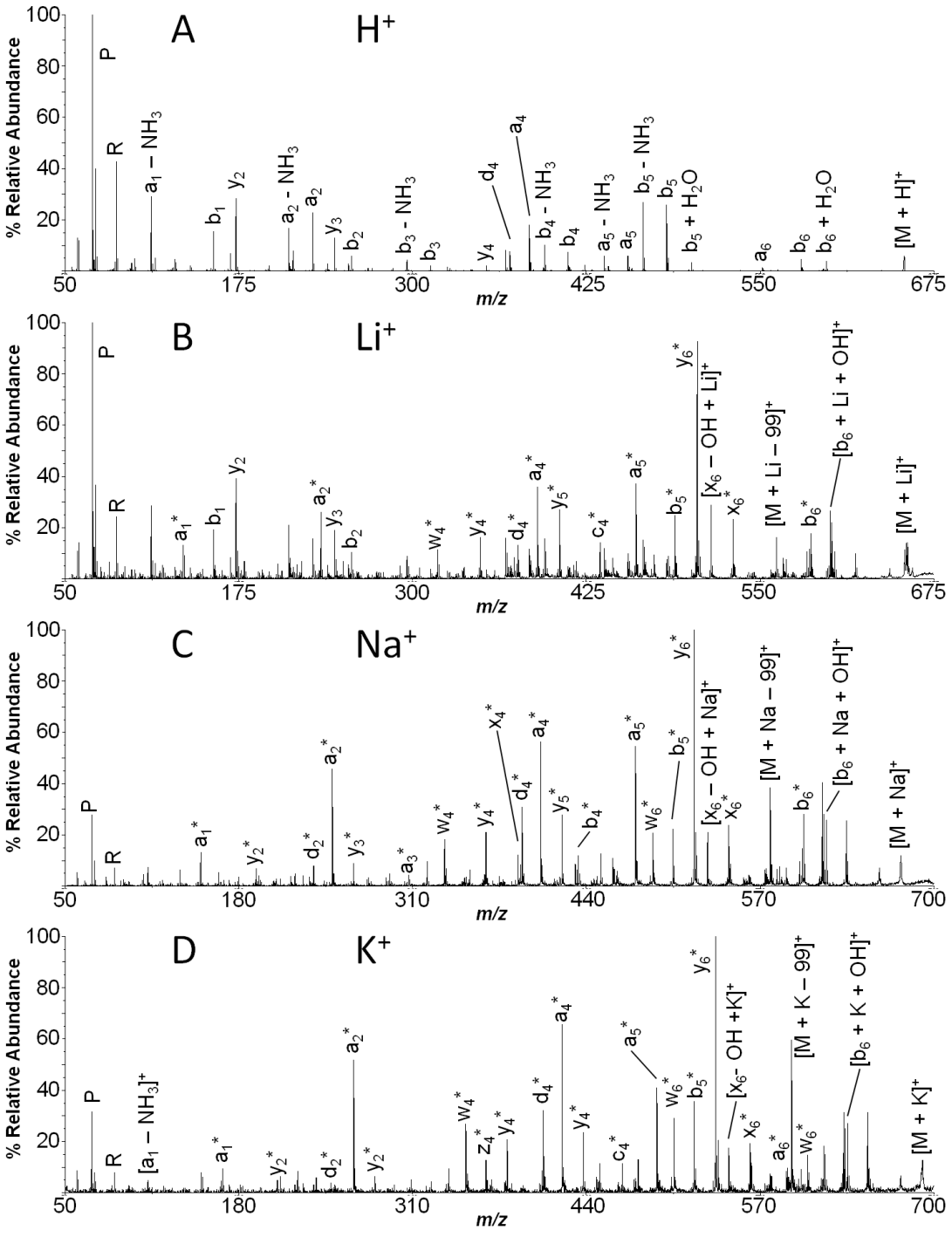

Figure 26: Collision induced dissociation tandem time-of-fight mass spectrometry of a)[RVGVAPG + H]$^+$, b)[RVGVAPG + Li]$^+$, c) [RVGVAPG + Na]$^+$, and d) [RVGVAPG + K]$^+$. Fragment ions labeled with "*" have one less proton and a cation adducted *e*.g. $[f_i - H + Cat]^+$.

The majority of fragment ions in the spectrum of $[RVGVAPG + Na]^+$ (Figure 25) contain one less proton and have a sodium cation adducted and as such are indicated by $[f_i - H + Na]^+$. The spectrum shows an abundance of sequence informative fragment ions including a near complete series of $[a_i - H + Na]^+$, $[b_i - H + Na]^+$, and $[y_i - H + Na]^+$ type fragment ions as well as abundant $[d_i - H + Na]^+$ and $[w_i - H + Na]^+$ fragment ions. The $[b_{n-1} + OH + Na]^+$ fragment ion is also abundant in this spectrum and overall our spectra appear similar to spectra previously obtained by other groups with regards to the fragment ions observed [156, 158, 159].

Mechanisms for the formation of these fragment ions have been hypothesized [156-159] along with mechanisms to form the less commonly observed $[z_i - H + Na]^+$ and $[c_i - H + Na]^+$ fragment ions[157]. Additional to *a*-, *b*-, and *y*-type fragment ions, we also observed several intense peaks corresponding to $[x_i - H + Na]^+$ fragment ions of all peptides investigated in this study. These fragment ions are more clearly observed in the Figure 25 inset. To our knowledge, the formation of *x*-type fragment ions from alkali metal cationized peptides has not been previously addressed.

The *x*-type fragment ions observed are the $[x_4 - H + Na]^+$ and $[x_6 - H + Na]^+$ fragment ions which indicates cleavage N-terminal to the two valine residues within the peptide RVGVAPG, a trend that holds true for most of the peptides analyzed in this study. The peptide RLGLAGG substitutes the two valine residues for two leucine residues to investigate the specificity of valine on the formation of x-type fragment ions and the mass spectrum is seen in Figure 27. Both the $[x_4 - H + Na]^+$ and $[x_6 - H + Na]^+$ fragment ions are observed indicating that presence of valine is not required. Perhaps the

formation of these *x*-ions is affected simply by the presence of a bulky side chain. The fragment ion spectrum of $[RVYIHPF + Na]^+$ (data not shown) reveals the $[x_4 - H + Na]^+$, $[x_5 - H + Na]^+$, and $[x_6 - H + Na]^+$ fragment ions each occurring N-terminal to the side chains of valine, tyrosine, and isoleucine. These x_i-type fragment ions observed were less intense than those shown in Figures 25 and 27 which is likely an effect of the competitive binding between the arginine and histidine and the other side chains which may interact more strongly with the sodium cation.

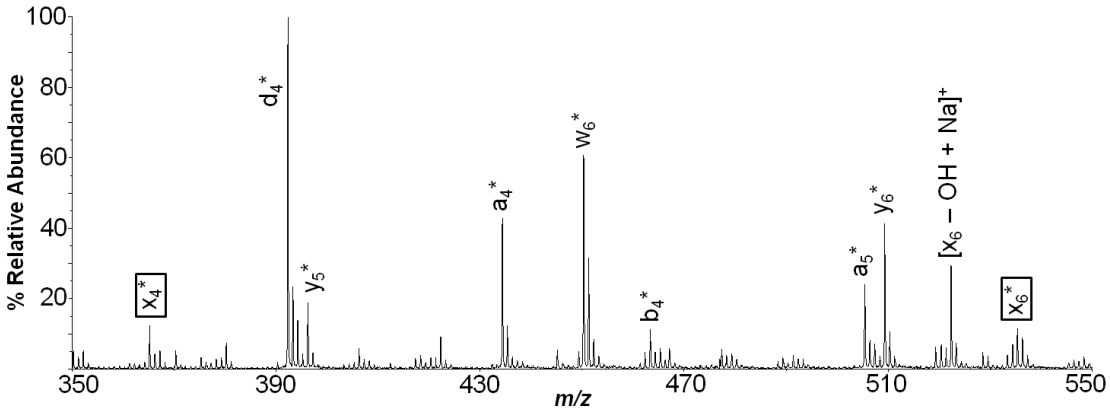

Figure 27: Tandem mass spectra of $[RLGLAGG + Na]^+$. Fragment ions labeled "*" are less one proton and have the sodium cation adducted *e.*g. $[f_i - H + Na]^+$.

The peptide RAVGVGG allows for further examination of the influence of the side chains by shifting position of the two valine residues within the peptide. In the TOF/TOF mass spectrum of RAVGVGG, shown in Figure 28, the $[x_4 - H + Na]^+$ ion is not detected while the $[x_3 - H + Na]^+$ ion appears indicating that the position of valine does impact *x*-ion formation. However, the $[x_6 - H + Na]^+$ ion remains in the spectrum

while the $[x_5 - H + Na]^+$ does not appear implying that valine residues only have partial influence on the formation of *x*-type fragment ions, but that other factors must also play a role. It may be that the valine side chain helps to stabilize the binding site of the metal cation enhancing *x*-type ion formation. Additionally, the results here indicate that the stability of the leaving group may affect the capability of forming the $[x_6 - H + Na]^+$ fragment ion and in the case of $[RVGVAPG + Na]^+$, $[RLGLAGG + Na]^+$, and $[RAVGVGG + Na]^+$ involves the arginine side chain.

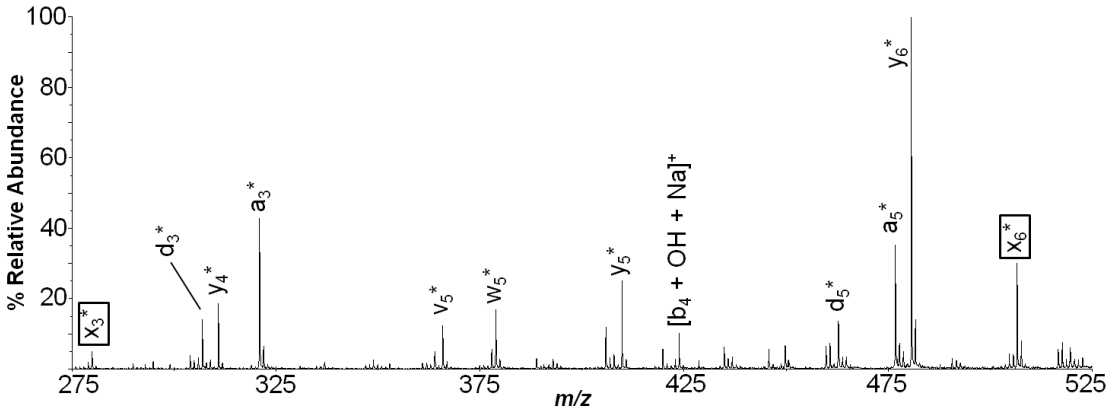

Figure 28: Tandem mass spectra of $[RAVGVGG + Na]^+$. Fragment ions labeled "*" are less one proton and have the sodium cation adducted *e*.g. $[f_i - H + Na]^+$.

To test this hypothesis we examined a series of peptides in which the N-terminal amino acid was varied. Figure 29 contains the fragment ion spectra of **a**) $[KVGVAPG + Na]^+$ and **b**) $[HVGVASG + Na]^+$. When substituting the arginine (RVGVAPG) for lysine (KVGVAPG) or histidine (HVGVASG), the $[x_6 - H + Na]^+$ ion is no longer present, but the $[x_4 - H + Na]^+$ ion remains. Since an *x*-type fragment ion is defined as having one less proton and a sodium ion adducted, the leaving group must

receive a proton from the *x*-type fragment ion. Arginine is the most basic amino acid and perhaps is the only amino acid that has a large enough gas-phase basicity to receive the proton to form the x_{n-1}-type fragment ion in proximity to the basic side chain at the N-terminus. This process may govern the formation of the $[x_6 - H + Na]^+$ fragment ion, but since the $[x_4 - H + Na]^+$ ion is still observed there must be other factors influencing the formation of these x-type ions including the influence of the valine residue. In fact, removal of the N-terminal residue, as investigated with the peptides $[VGVAPG + Na]^+$ and $[GVAPG + Na]^+$, still gives the $[x_4 - H + Na]^+$ fragment ion, but at a very low relative abundance. This low relative abundance agrees with the assessment that the leaving group plays a key role in *x*-type fragment ion formation.

An aspartic acid residue was also substituted for the N-terminal arginine and the fragment ion spectrum of $[DVGVAPG + Na]^+$ is seen in Figure 30. The substitution dramatically changes the fragment ion spectrum and more C-terminal fragment ions are formed. The dominant y_6 fragment ion observed in the spectrum is likely a result of the aspartic acid effect [137]. However, no *x*-type fragment ions are observed. Carboxylate functional groups can interact strongly with alkali metal cations which would lead to N-terminal fragment ions dominating the spectrum if the cation is coordinated to the aspartic acid residue. However, the interaction between the acidic aspartic acid side chain and the basic N-terminal amine could also prevent alkali metal ion binding at this location. Additionally, this interaction could prevent proton transfer thereby hindering *x*-ion formation. The alkali metal cation could also be bound to the carboxylate functional group at the C-terminus or may be coordinated to the carbonyl groups along

the peptide backbone near the C-terminus which will result in preferential C-terminal ions and could be a reason for the lack of *x*-type fragment ions.

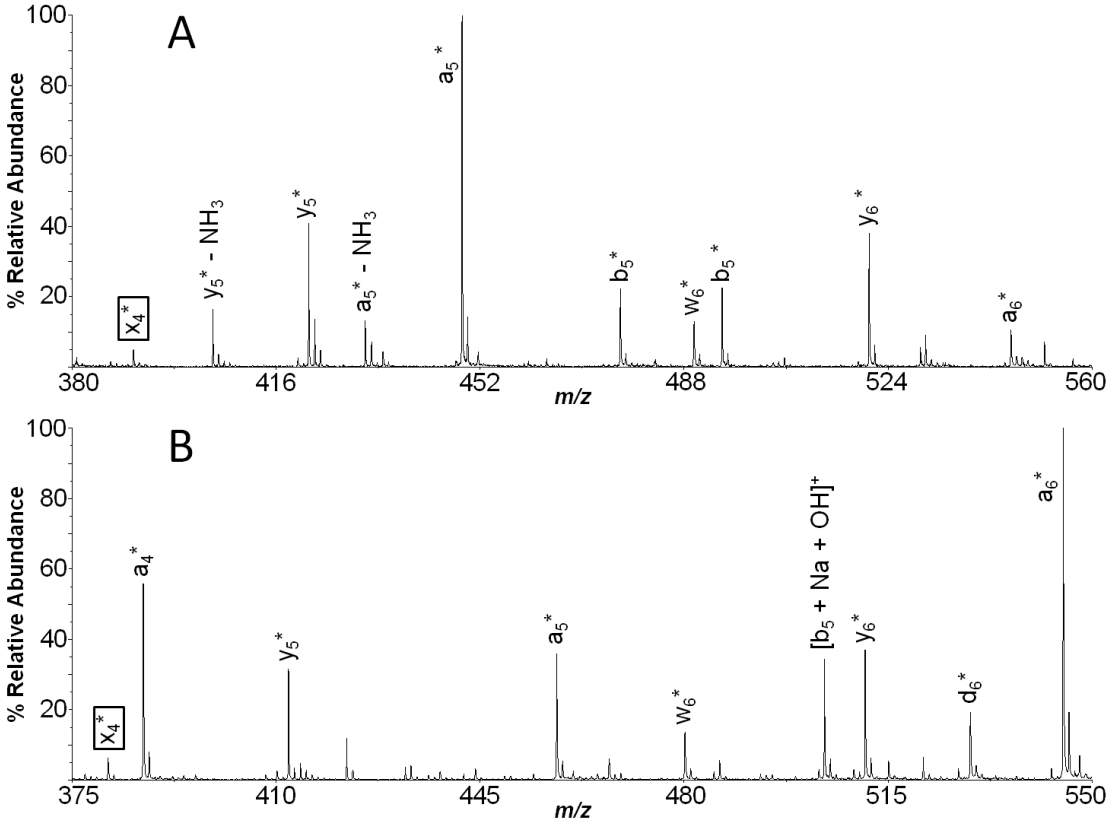

Figure 29: Tandem mass spectra of a) $[KVGVAPG + Na]^+$ and b) $[HVGVAPG + Na]^+$. Fragment ions labeled "*" are less one proton and have the sodium cation adducted *e.*g. $[f_i - H + Na]^+$.

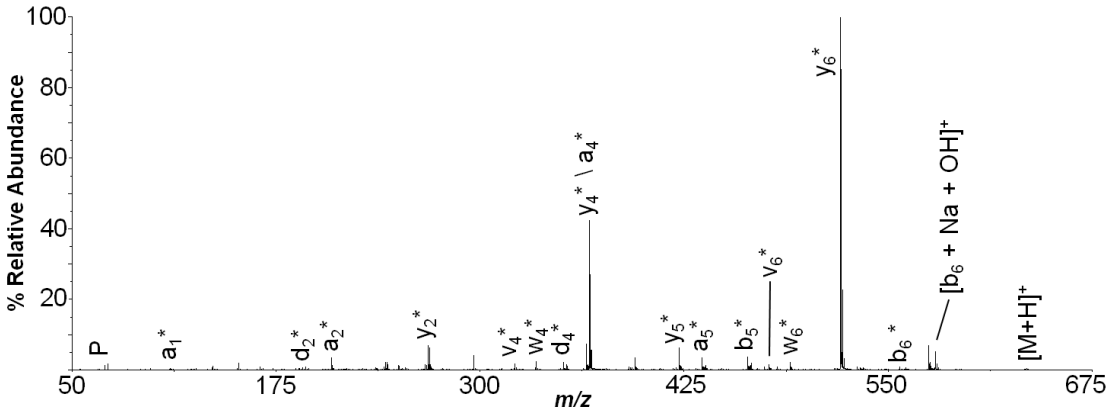

Figure 30: Collision induced dissociation tandem time-of-fight mass spectrometry of $[DVGVAPG + Na]^+$. Fragment ions labeled with "*" have one less proton and a cation adducted *e*.g. $[f_i - H + Cat]^+$.

In order to examine the effect of the N-terminus on *x*-type fragment ion formation, we examined the N-terminal acetylated peptide $[ac\text{-}RVGVAPG + Na]^+$. The $[x_4 - H + Na]^+$ and $[x_6 - H + Na]^+$ fragment ions are again observed, as seen in Figure 31a implying that the N-terminus does not have a significant influence on *x*-type fragment ion formation. In fact, the observed fragments and fragment abundances change very little between the N-terminal amine and the N-terminal acetyl peptide. This observation suggests that the N-terminus is not involved in alkali metal cation binding. As a corollary to the previous experiment, the C-terminus was converted from the carboxylate functional group to a methyl ester and the resulting TOF/TOF fragment ion spectrum is shown in Figure 31b. Once again, the $[x_4 - H + Na]^+$ and $[x_6 - H + Na]^+$ fragment ions are observed in the spectra indicating no major influence of the C-terminus on *x*-type fragment ion formation. One major change is the lack of the $[b_6 + OH + Na]^+$ ion, which is likely due to the inability of the methyl ester to undergo

intramolecular nucleophilic attack causing elimination of the C-terminal amino acid as is the case with the C-terminal carboxylate. This result is in agreement with the mechanism proposed by Gross [156].

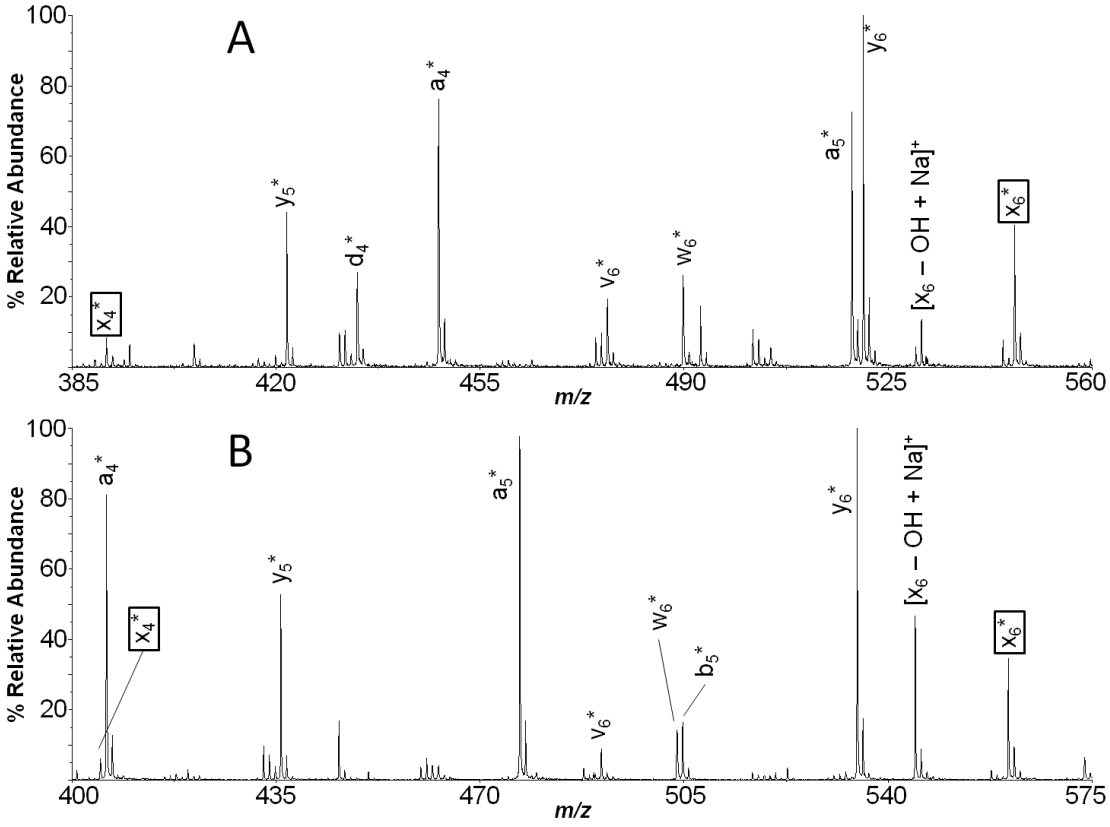

Figure 31: Tandem mass spectra of a) [ac-RVGVAPG + Na]$^+$ and b) [RVGVAPG-OMe + Na]$^+$. Fragment ions labeled "*" are less one proton and have the sodium cation adducted *e*.g. [f_i - H + Na]$^+$.

Table 4: Listing of the peptides in the model series which show $[x_i - H + Na]^+$ fragment ions and the corresponding relative abundance of each x_i-type fragment ion.

	x_3	x_4	x_5	x_6	$x_{n-1} - OH + Cat$
RVGVAPG + H	-	-	-	-	-
RVGVAPG + Li	-	9.60	-	23.36	30.45
RVGVAPG + Na	-	8.88	-	17.32	15.05
RVGVAPG + K	-	10.11	-	20.62	16.92
KVGVAPG + Na	-	4.94	-	-	-
HVGVASG + Na	-	4.82	-	-	-
DVGVAPG + Na	-	-	-	-	-
RVGVASG + Na	-	22.27	-	21.81	18.89
RVGVAGG + Na	-	16.69	-	20.93	19.51
Acetyl-RVGVAPG + Na	-	14.06	-	52.79	14.23
Acetyl-RVGVASG + Na	-	11.46	-	22.30	11.30
Acetyl-RVGVAGG + Na	-	20.86	-	15.56	9.75
RVGVAPG-Methyl + Na	-	6.83	-	35.89	47.29
RVGVASG-Methyl + Na	-	4.07	-	6.46	8.35
RVGVAGG-Methyl + Na	-	8.63	-	34.10	55.04
RAVGVGG + Na	7.20	-	-	25.33	2.61
VGVAPG + Na	-	16.17	-		-
GVAPG + Na	-	2.23			-
RVGVAP + Na	4.40	-	6.57		5.06
RVGVA + Na	-	4.29			2.55
RVGV + Na	1.07				-

Table 4 shows a list of the relative abundance of each *x*-ion observed and the corresponding peptide examined. It is obvious from the table that the valine side chain and neutral leaving group play the most important roles in $[x_i - H + Na]^+$ fragment ion formation. Based on this, a mechanism for the formation of *x*-type fragment ions is

shown in Figure 32. In this mechanism, we hypothesize that the alkali metal cation is coordinated by the carbonyl and amide groups of the peptide backbone. In Figure 32, we show the cation located at the first amide linkage, but we do not propose that the cation is strictly located at this linkage but in fact could be present anywhere along the backbone, where the presence of residues such as leucine, valine, and isoleucine likely enhances alkali metal ion binding at this location. It may be speculated that the presence of such a bulky group forces the carbonyl group of the bulky residue and the carbonyl group N-terminal to that residue to assume a "cis" configuration that allows for the attachment to the metal cation, simultaneously forming a stable intermediate. During the initial step of the mechanism, a proton from the peptide backbone is transferred to the leaving group. For those peptides with an N-terminal arginine, the proton transfer is most likely to occur owing to the basicity of arginine side chain. This will result in more abundant *x*-type fragment ions for peptides with an N-terminal arginine as is observed in the data shown. The H^+ transfer results in protonation of the leaving group and leaves the amide nitrogen with a negative charge which can rearrange to give a negative charge at the backbone oxygen. A heterolytic bond cleavage between the α-carbon and the carbonyl carbon forms the $[x_i - H + Na]^+$ fragment ion. The resulting π systems between the carbon, nitrogen, and oxygen can then form a coordination complex with the alkali metal cation.

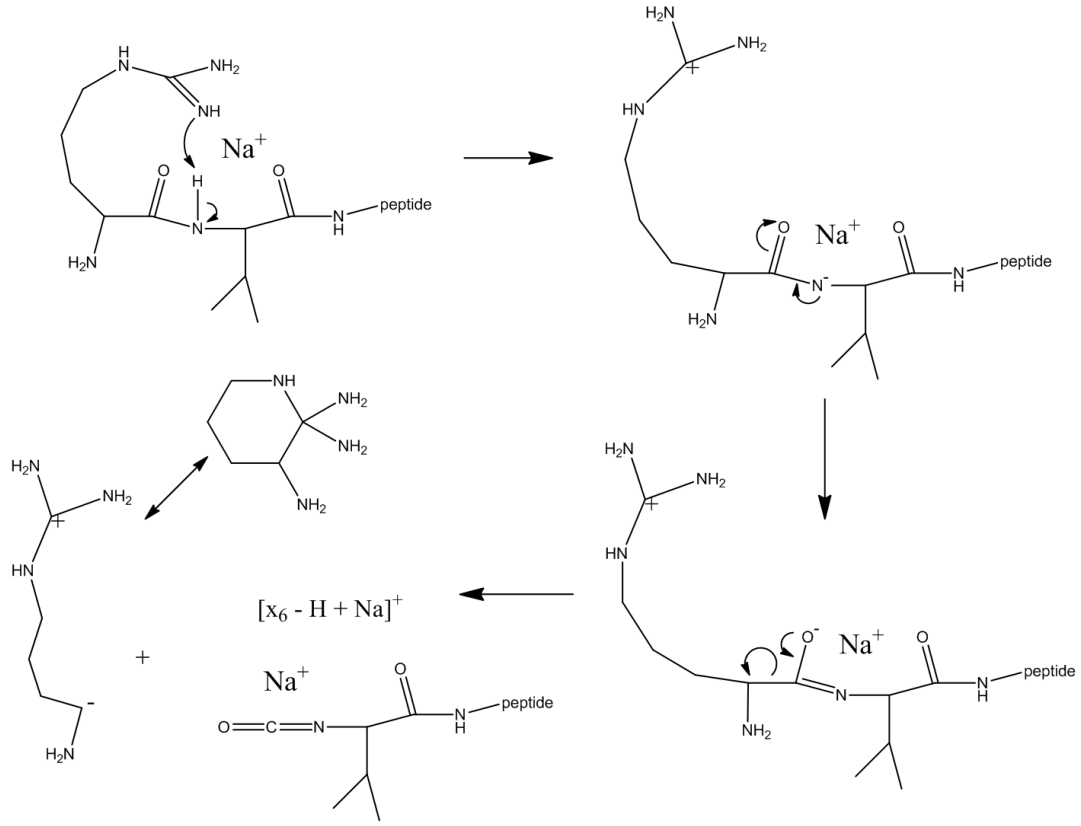

Figure 32: Proposed mechanism for the formation of $[x_i - H + Na]^+$ ions from CID fragmentation of alkali metal cationized peptides.

In addition to the presence of *x*-type fragment ions in all of our spectra, we also observe a peak in nearly all of the mass spectra with a *m/z* 16 mass units less than that of the $[x_{n-1} - H + Na]^+$ fragment ion. We have confirmed through ^{18}O exchange chemistry and examination of the methyl esters of these peptides that this fragment ion is C-terminal. This ion appears in all the mass spectra shown here where an $[x_{n-1} - H + Na]^+$ fragment ion is observed so we believe that the two ions may be formed by a similar mechanism. We hypothesize that this fragment ion is formed by an oxygen transfer from the $[x_{n-1} - H + Na]^+$ to the leaving group. Within the proposed mechanism

for *x*-type fragment ion formation, the carbonyl oxygen can act as a nucleophile and be transferred to the leaving group, providing the corresponding fragment ion 16 mass units less than the corresponding *x*-type fragment ion. While we cannot concretely determine the structure of the $[x_{n-1} - OH + Na]^+$ and the corresponding leaving group, all information gathered in this study does point toward the structures discussed.

Conclusions

Abundant $[x_i - H + Na]^+$ fragment ions are observed in the TOF/TOF mass spectra of peptides $[M + Cat]^+$ where Cat is Li^+, Na^+, and K^+. The proposed mechanism for the formation of these ions requires the location of the metal cation to be along the peptide backbone coordinated to the carbonyl and amide groups. The observation of x-type fragment ions is governed primarily by the presence of an arginine side chain at the N-terminus with some influence from bulky residues such as valine, leucine, and isoleucine, but with no major influence owing to the N-terminal amide or the C-terminal carboxylate. The stability of the leaving group likely has a strong influence on the ability to form these *x*-type fragment ions. We also hypothesized a mechanism for $[x_{n-1} - OH + Na]^+$ fragment ion formation which appear in the majority of our spectra.

CHAPTER IV

INITIAL INSTRUMENT MODIFICATIONS FOR IMPROVED PERFORMANCE OF PHOTODISSOCIATION TANDEM TOF MASS SPECTROMETRY

Introduction

Tandem mass spectrometry (MS) has evolved as a routine peptide sequencing technique since first implemented by Biemann in the 1980s [61]. Collision-induced dissociation (CID) is typically considered the benchmark for efficiently producing fragment ions in a tandem MS experiment and thus preferred to other techniques [101, 102]. However, there are numerous examples where collision-induced dissociation (CID) does not provide the desired information (location of post translation modifications, full sequence coverage, etc.) and other fragmentation methods are implemented including electron (ECD/ETD) [103] and photon based methods [106]. While new dissociation methods continue to be discovered, it is the combination of all dissociation methods that provide the necessary insights regarding peptides fragmentation.

Understanding the mechanisms and kinetics of peptide fragmentation can assist in better predicting the fragment ions that will be observed in a tandem mass spectrum which can in turn lead to improved database searching techniques which are typically implemented in proteomics experiments. CID is traditionally not an ideal method for studying peptide fragmentation kinetics owing to the varying amounts of kinetic energy that can be imparted into the precursor ion; however, the Armentrout group has

developed instrumentation to accurately control the energy imparted through collisional methods using their guided ion beam mass spectrometer [108]. Electron based methods could also be used for such studies, but they typically require ion trap instrumentation and therefore investigate longer fragmentation timescales [103]. Photon based dissociation methods are well suited for kinetics studies as the energy imparted into the ion is defined by the energy of the photon, and the high energy of vacuum UV (193 nm and 157 nm) photons allows for single photon dissociation to occur. Additionally, UV photodissociation is compatible with nearly every type of mass analyzer only requiring a window to introduce the photons.

Gas-phase ion fragmentation can be explained using Rice, Ramsperger, Kassel (RRK) theory [54, 55] or quasi-equilibrium theory (QET) [56] which makes two assumptions: 1) that excess energy flows freely through all degrees-of-freedom with all states being accessible and 2) that intramolecular vibrational redistribution (IVR) occurs faster than the fragmentation rate. The results of these assumptions arrive at the RRK equation:

$$k(E) = \nu\left(\frac{E - E_0}{E}\right)^{S-1}$$

where *k(E)* is the rate constant as a function of internal energy, *v* is the frequency factor, *E* is the internal energy of the molecule, E_0 is the energy required for the dissociation of a specific bond, and *s* is the number of vibrational degrees of freedom in the system. While this equation cannot accurately predict the correct rate, two important conclusions can be made: (1) the rate has a strong inverse dependence on the degrees-of-freedom and

(2) the rate increases rapidly as with excess internal energy. Rice, Ramsperger, Kassel, Marcus (RRKM) theory [60] can more accurately predicts these rates, but QET theory provides a good relative approximation. The relationship between the rate of dissociation, *k(E)*, and the internal energy dependence can be shown with a Wahrhaftig diagram as shown in Figure 33 [2]. From this diagram two important features are noted: 1) as the internal energy increases, different fragment ions will be kinetically favored (log *k(E)* is larger), and 2) at a given rate (*k(E)*), certain fragment ions may not form on the timescale of the experiment . UV and VUV photodissociation is a good probe for determining rates as the value of E is relatively close to the energy of the absorbed photon, 6.42eV for 193 nm and 7.87eV for 157 nm.

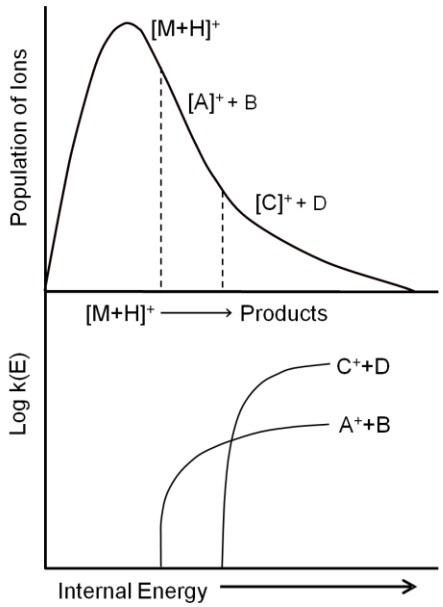

Figure 33: Wahrhaftig diagram comparing the population of ions and the internal energy of the excited molecule and the dissociation rate (*k(E)*) to internal energy of the excited molecule. At a given internal energy, precursor ions will fragment to form fragment ion A and neutral B. If internal energy is higher, fragment ion C and neutral D will be kinetically favored over A and B [2].

We have developed photodissociation TOF/TOF instrumentation for rapid and sensitive generation of photofragment ion spectra. These studies where initially aimed at efficiently producing tandem mass spectra for peptide sequencing [113, 117], but they have since evolved to investigation of dissociation kinetics based studies examining the rates of fragmentation on timescales on the order of microseconds [114]. Examination of 'prompt' forming fragment ions, that is, those that form on fast timescales less than 1 microsecond can also assist in identifying the sites of post translational modifications (PTMs) which can be lost on longer timescales. The loss of PTMs occurs from the vibrational redistribution of energy after initial excitation. While both the proteomics and kinetics pursuits have been successful, instrument performance limitations have hindered the volume of studies that can be undertaken.

While it is relatively straightforward to photodissociate small ions (<1,500 *m/z*), the photodissociation of larger ions is challenging. This is due, in part, to the increased degrees-of-freedom which photon energy partitions into allowing for vibrational relaxation of the input energy (the *s* term in the equation above), but also instrument limitations have hindered our progress. To address this issue, we have improved the instrument setup by developing a biased activation cell with improved ion optics capable of decelerating the ion beam to <50% of its initial kinetic energy with minimal ion losses to investigate 'prompt' forming fragment ions. We describe improvements that have been made to current photodissociation time-of-flight instrumentation in order to improve instrument sensitivity and mass range without comprising the capabilities of the instrumentation to investigate fragment ions forming on distinct timescales.

Methods

SIMION Simulations

SIMION version 8 (SIS; Ringoes, NJ) was used to accurately simulate ion trajectories through the home-built tandem TOF mass spectrometer. During these simulations parameters such as ion position, resolution, and velocities were monitored to determine performance of instrument modifications. Simulations were performed on a 1000 Dalton singly charged particle which most closely resembles the typical samples investigated in the current instrument. Simulated ions have characteristics to mimic those created from a MALDI experiment [175, 176].

Photodissociation TOF/TOF

The photodissociation instrument is a home-built TOF/TOF utilizing an off-axis single stage reflectron as the second stage. Ions are produced by MALDI and energy corrected with delayed extraction. The ions of interest are transmitted *via* a timed ion selector into the photodissociation region where two experiments can be performed with different instrument parameters. In the first experiment, ions of interest exiting the first TOF are selected, and subsequently irradiated with the 193 nm excimer laser. Fragment ions and remaining precursor ions will travel 0.5 meters to a single stage reflectron 1.5° off axis with respect to the ion beam. As fragment ions and remaining precursor ions have a large difference in kinetic energies, the reflectron is tuned to focus a specific range of mass-to-charge ratios and the resulting spectra are stitched together to give the complete mass spectrum, referred to as the "PSD focusing method" [116]. These

experiments examine photofragment ions that form between laser irradiation of the precursor ions and entrance into the reflectron. The time spent in this region is approximately 10 microseconds, but will vary based on the initial velocity of the precursor ions after exiting the source region. The second experiment involves deceleration of the gated ion packet to less than 50% of the ion's initial kinetic energy with a series of radially focusing tube lenses. The decelerated ions enter a field free biased activation cell where irradiation from the 193 nm photons occurs followed by reacceleration to the reflectron which minimizes the kinetic energy difference between fragment ions formed within the biased activation cell and the remaining precursor ions. This allows for all the ions to be imparted onto the detector at a single reflectron voltage so long as the fragment ions form within the biased activation cell; therefore, this experiment will sample fragment ions forming on the timescale of ~1 microsecond, or 'prompt' fragment ions. As is the case with the PSD focusing experiments, the timescale is dependent on the velocity of the precursor ions within the biased activation cell.

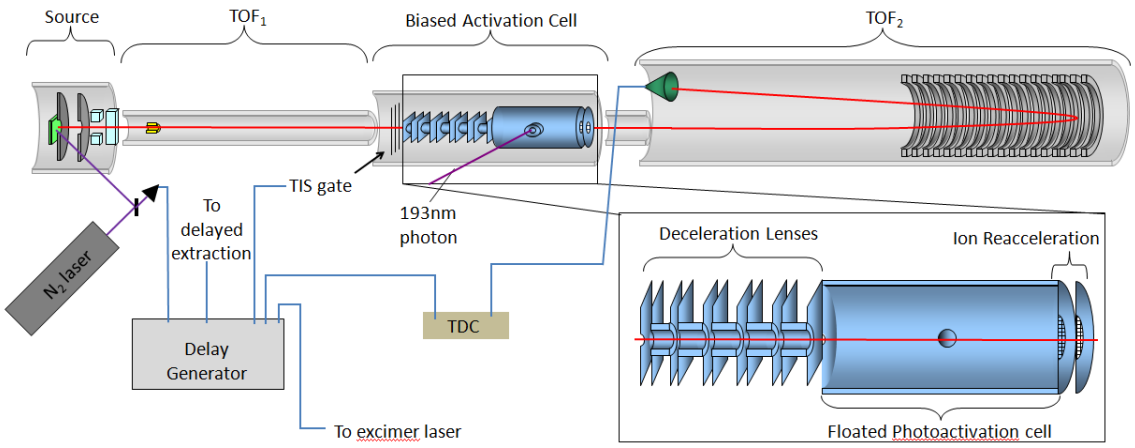

Figure 34: An illustration of the tandem TOF photodissociation instrument with inset highlighting the biased activation cell region. Blue lines indicate cables which carry the pulsing electronics and the ion signal.

The instrument schematic used herein is shown in Figure 34. The source region is a modified version of the Voyager elite originally designed by Vestec Inc., now owned by Applied Biosystems. Ions are formed from the 337 nm output of a nitrogen laser (VSL-337ND, Laser Science, Inc., Franklin, MA). The photon beam is introduced approximately 30 degrees off axis with respect to the source plate. The laser beam intensity is controlled by a neutral density filter and the laser beam starts the TOF clock through utilization of a photodiode which sends the resulting signal to a delay generator (DG 535, Stanford Research Systems Inc., Sunnyvale, CA) which controls all aspects of the timing in this experiment. Specifically, the delayed extraction and timed ion selection (TIS) is performed by two high voltage transistor switches (Behlke HTS 300 and Behlke HTS31, respectively, Behlke Power Electronics, Krunberg, Germany). A start pulse is sent to the time-to-digital converter (TDC) (TDCx4, IonWerks, Houston,

TX). The delay generator also precisely controls the fire time of the excimer laser (LPX-120i, Coherent Lasers Inc., Santa Clara, CA).

As mentioned previously, the source region is a modified form of the Voyager TOF source. The source plate is a 100 well plate designed now incorporated on all MALDI TOF Applied Biosystems instruments (Applied Biosystems, Inc., Foster City, CA). It is viewed by a small camera providing magnification of the sample target. Delayed extraction occurs by an increase in the voltage applied to the MALDI plate. The extraction electrode is located 3.0 mm from the source plate and it contains a grid 70 lines-per-inch nickel (MN17, Precision Eforming LLC, Cortland, NY) stretched across a 4 mm aperture. A gridded ground electrode is located an additional 20.0 mm from the source and it defines the field free region of the first TOF. The instrument is also equipped with *x* and *y* steering lenses and an Einzel lens which are not needed in these experiments.

The timed ion selector (TIS) is located 52.9 cm from the source plate. Approximately 5.0 mm the TIS gate, ions pass through a 6.0 mm aperture and enter the deceleration region. The photodissociation window is located 59.7 cm from the ion source and photons intersect the ion beam at this point. Ions cross the ground grid of the reflectron 0.83 m from the photon irradiation point. The reflectron 0.50 m in length and is positioned 1.5 degrees off axis with respect to the ion beam in order to redirect ions toward the detector. The detector is located 0.5 m from the reflectron ground grid.

Ions are detected with a chevron style microchannel plate detector (Burle 18mm AP-TOF, Lancaster, PA) and the signal is transferred through an amplifier/discriminator

(IonWerks XCD, IonWerks, Houston, TX) to the TDC. The TDC is interfaced to a personal computer via National Instruments PCI card (Fishcamp card, National Instruments Inc., Austin, TX). Spectra are recorded with Chart Recorder Program (IonWerks, Houston, TX) and imported into Microsoft Excel for mass analysis. All photofragment ion spectra shown are obtained by subtracting the 193 nm laser off spectrum, or metastable ion spectrum, from the laser on spectrum in order to eliminate any contribution from metastable fragment ions.

The stainless steel chamber is kept at high vacuum ($1x10^{-7}$ -$1x10^{-8}$ torr) by two air-cooled 250 liter/second turbomolecular pumps (Varian Turbo V-250, Agilent technologies, Santa Clara, CA). The backing pressure for each turbopump is maintained individually by two oil-based mechanical rough pumps (2004A, Alcatel Vacuum Technology, Hingham, MA). Voltages for the source, extraction electrode, Einzel lens, photocell, and reflectron are provided by Bertan 30kV power supplies (2554-2, Spellman High Voltage, Hauppauge, NY). Voltage for the TIS controlled by a 3kV Gamma power supply (RR3-15R, Gamma High Voltage, Ormond Beach, FL). The detector voltage in controlled by a -3kV Bertan power supply (PMT-30C N-1, Spellman High Voltage, Hauppauge, NY). All voltages controls are interfaced to Labview via PCI cards (National Instruments, Austin, TX) via personal computer.

Materials

All chemicals used in this study were purchased from Sigma-Aldrich (St. Louis, MO) unless otherwise noted. Peptides analyzed in this study include Bradykinin 1-8

(RPPGFSPF), Angiotensin III (RVYIHPF), Substance P (RPKPQQFFGLM-NH_2), and ACTH clip 18-39 (RPVKVYPNGAEDESAEAFPLEF). Each solid peptide was dissolved in water to yield a concentration of 1 mg/mL. Matrix solution was prepared by dissolving α-cyano-4-hydroxycinnamic acid in 50:50 acetonitrile:water with the addition of trifluoroacetic acid and ammonium dihydrogen phosphate to generate 0.1% concentrations with respect to the total volume of the matrix solution. Typically 0.5 μL of peptide solution was combined with 20 μL of the matrix solution and 0.5 μL of the mixture was spotted onto the MALDI plate resulting in approximately 12 picomoles of peptide per spot.

Results

SIMION Simulations

In order to clarify focusing terminology, we will define space focusing as focusing in the *xy* plane; that is, when the *z*-direction is defined as the direction of the ion flight path. Temporal focusing will be defined as the focus of ions along a given plane on the *z*-axis. Temporal focusing could also be considered space focusing in the *z* direction, but for clarity we will define the two separately.

Figure 35: SIMION simulation showing precursor ion (m/z = 1000) focusing through A) the previous biased activation cell design with abrupt deceleration and B) the redesigned cell with deceleration lenses. Notice the ion trajectories at the exit of the biased activation cell.

Figure 35A shows the SIMION simulation of ions arriving at the previous biased activation cell design for comparison against the new design (Figure 35B). Note in the previous design that as the ions cross the ground grid into the deceleration region they "scatter" in the *xy* direction. Although not evident in this simulation, recent experimental data has shown that ion signal decreases by more than 60% when 50% of the accelerating voltage is applied to the biased activation cell prior to any photodissociation. This result is interpreted as an effect of the defocusing of ions in the *xy* plane from the abrupt deceleration into the floated photocell. To combat these effects we have designed a new deceleration region with radially focusing ion optics for preventing ion losses from the previous abrupt deceleration design. Additionally, two of

the four total grids in the previous design were replaced with two apertures (3/16" diameter) to diminish ion losses resulting from the use of wire grids (10% ion loss per grid) [177].

SIMION simulations were used to examine the focusing effects of the new biased activation cell design and ion losses from ion deceleration. By extending the deceleration distance and by applying proper voltages on the focusing tube lenses, ions are kept near the center axis and are spatially focused at the point of irradiation. The longer deceleration region allows for a gentler deceleration of ions rather than the abrupt deceleration of the previous design. Also, a series of five tube lenses along this distance keeps ions space focused for efficient overlap with the orthogonal laser beam and assures the ions will traverse the aperture plates. These lenses were modeled after the deceleration lenses designed by Shukla and Futrell [178]. The lenses and the extended deceleration region keep ions on axis for efficient interaction with the 193 nm photons. A sketch of the biased activation cell region and potential energy surface view of the two designs is shown in Figure 36 for comparative purposes.

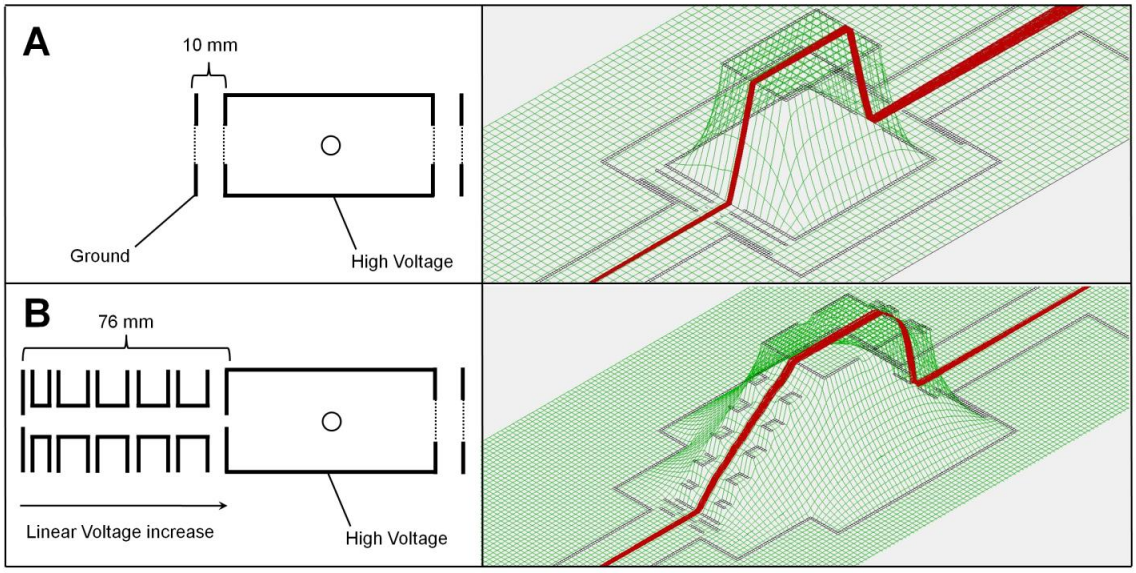

Figure 36: A) Representation the previous biased activation cell design coupled with SIMION potential energy (PE) surface view B) Redesigned biased activation cell region and PE surface view.

If the tube lenses focus the ions more efficiently in *xy* space, then an adverse effect is that the ions should be more defocused in time, or in the *z* dimension. The introduction of apertures rather than grids could also cause undesired temporal defocusing of ions at the irradiation point owing to penetrating fields into the biased activation cell. However, when examining the temporal focusing at laser irradiation in the previous and new design, the arrival time distribution changes only slightly and not significantly enough that the dimensions of the laser beam cannot overcome.

During the 'prompt' photodissociation experiment, the reacceleration of fast forming fragment ions and remaining precursor ions after exit from the biased activation cell allows for sampling of only these 'prompt' dissociating precursor ions. This result can be seen in the SIMION simulation in Figure 37. Note in the figure that only

fragment ions which form prior to reacceleration toward the reflectron TOF will be focused at the detector, while those that form subsequent to reacceleration will not arrive at the detector. When examining longer timescale fragmentation, fragment ions must form in the time between precursor ion irradiation and when the ion enters the reflectron as the reflectron voltage is tuned to direct fragment ions within a given mass range toward the detector.

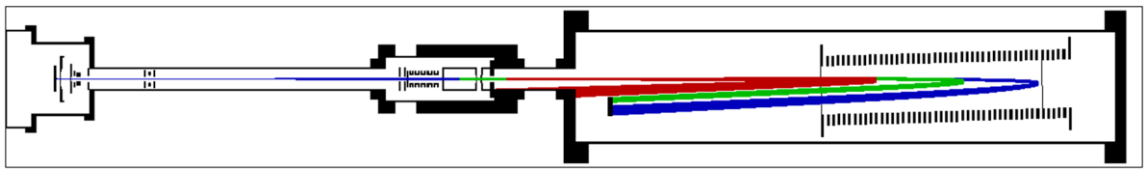

Figure 37: SIMION simulation showing focusing of precursor ions (blue), fragment ions formed within the biased activation cell (green) and a fragment ion formed after exiting the biased activation cell (red).

Instrument Modifications and Improvement in Instrument Sensitivity

After accurate modeling of the instrument alterations via SIMION, each modification was implemented into the current instrumentation. The radially focusing deceleration lenses were constructed based on the design by Shukla and Futrell [52, 178] and consist of 5 lenses with inner diameter of 0.625" with 1 lens having a length of 0.25" and the remaining 4 lenses with a length of 0.4375". Each lens is designed to press-fit into an eV part plate with and inner diameter of 0.75". Ceramic rods are then used to mechanically connect each lens while keeping each lens electrically isolated. The ceramic rods mount onto a PEEK (polyether ether ketone) support piece which slides on

4 stainless steel rods for adjustment of the position of the biased activation cell to properly align with the beam from the excimer laser. The lenses are electrically connected by a series of 25MΩ resistors in order to generate an approximate linear deceleration field.

Wire mesh grids are beneficial for defining electric fields but can decrease overall ion transmission; therefore, removal of two grids from the previous design should improve instrument sensitivity. Other work has shown the ion transmission is comparable to optical transmission [52, 177], which is 90 percent per grid in the case of the 70 lines-per-inch nickel grid used here. Therefore, our design should increase overall ion transmission by ~125% improving the sensitivity of the instrument. With the new biased activation cell, Bradykinin 1-8 was detected (signal-to-noise ratio of 10:1) at a 500 femtomoles per spot whereas the previous design required 1-5 picomoles per spot.

For efficient production of photofragment ion spectra, an adequate amount of precursor ion signal is required in order to form detectable amounts of photofragment ions. Previous studies in our research group have routinely required tens of picomoles of peptide for generation of photofragment ion spectra [113]. The modified biased activation cell requires only 1-2 picomoles of peptide per spot for generation of photofragment ion spectra. The improvement in sensitivity results from the improvement in ion deceleration and the reduction of 4 grids to 2 grids design thereby expanding the experimental capabilities of the current instrumentation by allowing for photodissociation of smaller concentrations necessary for proteomics experiments.

An improvement in sensitivity could also prove beneficial for photodissociation of larger *m/z* ions. This is typically more difficult since ions of larger mass can fragment though a larger number of pathways compared to smaller mass ions all pathways being equal. However, we have encountered difficulties as a result to instrument limitations. Experiments with the previous biased activation cell revealed that the ion signal from ACTH clip (18-29) (m/z =2465.20) does not achieve a reasonable S/N ratio of at least 3. TOF/TOF experiments with the new design show a much larger ion signal for ACTH (18-39) approaching the levels where photodissociation experiments are possible (Figure 38).

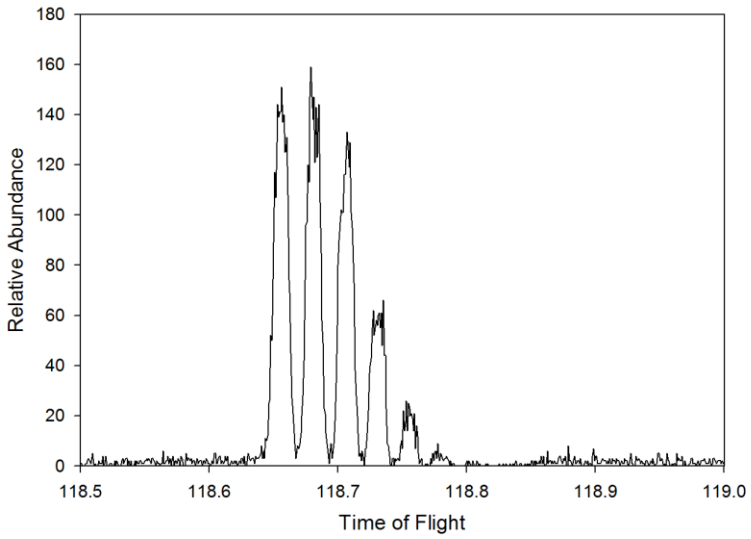

Figure 38: Mass selected TOF detection of ACTH 18-39 (RPVKVYPNGAEDESAEAFPLEF). Note the discrepancy in the peak shape is a result of improper bin within the spectrum recording software.

Photodissociation

Figure 39a shows the 'prompt' photofragment ion spectrum of Angiotensin III. A near complete series of *a*-type fragment ions is observed along with several *d*-type fragment ions as well as abundant immonium ions. Figure 39b is the photofragment ion spectrum of slow (< 10 microseconds) dissociating ions. All ions observed in the 'prompt' photofragment ion spectrum are also observed in this spectrum; however, more total fragment ions are detected. Specifically, *b*- fragment ions along with ammonia loss fragment ions appear in the mass spectrum here which do not appear in the 'prompt' photofragment ion spectrum. It is also obvious that the relative abundance of immonium ions is decreased in the slow dissociating fragment ion spectrum.

The 'prompt' photofragment ion spectrum of Substance P (Figure 40a) results in a mass spectrum showing only *a*- and *d*-type fragment ions. While a reduction in fragment ion variety can serve to simplify the mass spectrum, fewer fragment ions is usually not desired in traditional proteomics experiments. In comparison, the photofragment ion spectrum of slow dissociating precursor ions (Figure 40b) shows an abundance of fragment ions including the *a*- and *d*-ions observed in the 'prompt' spectrum, but with the addition of several *b*-type ions, ammonia loss fragment ions, and a few others including *y*-type fragment ions and b_i+H_2O fragment ions.

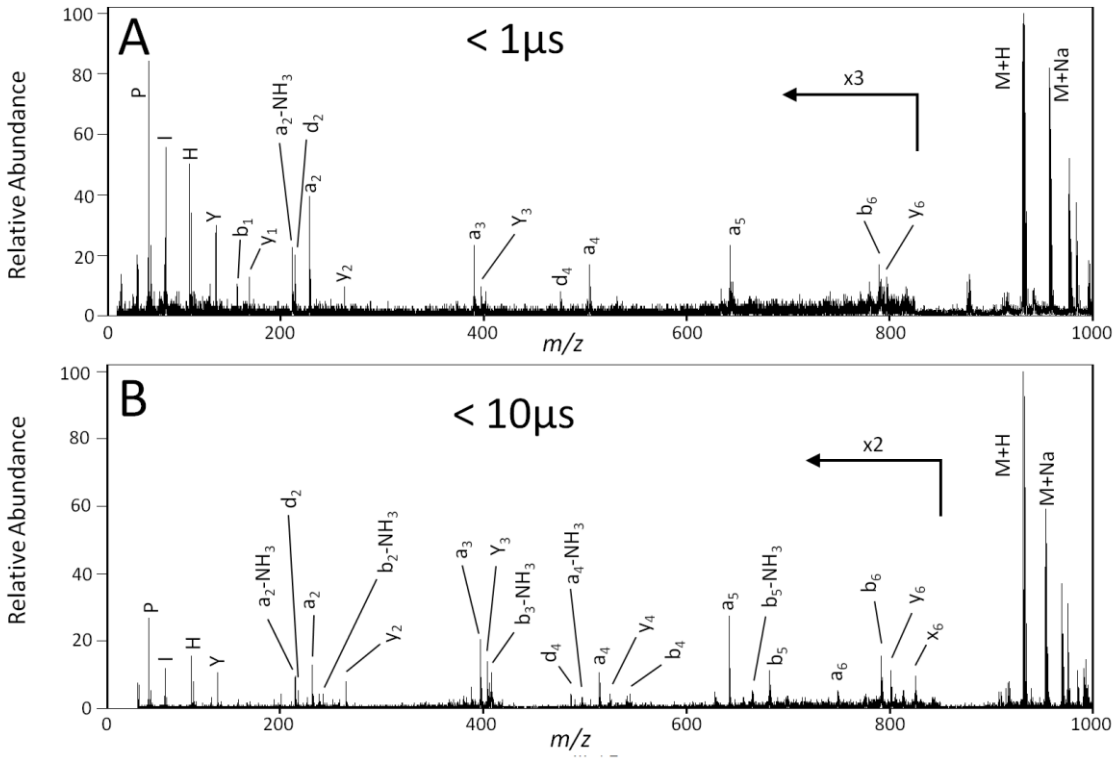

Figure 39: A) 'Prompt' photofragment ion spectrum of Angiotensin III (RVYIHPF) B) photofragment ion spectrum of slow dissociating ions.

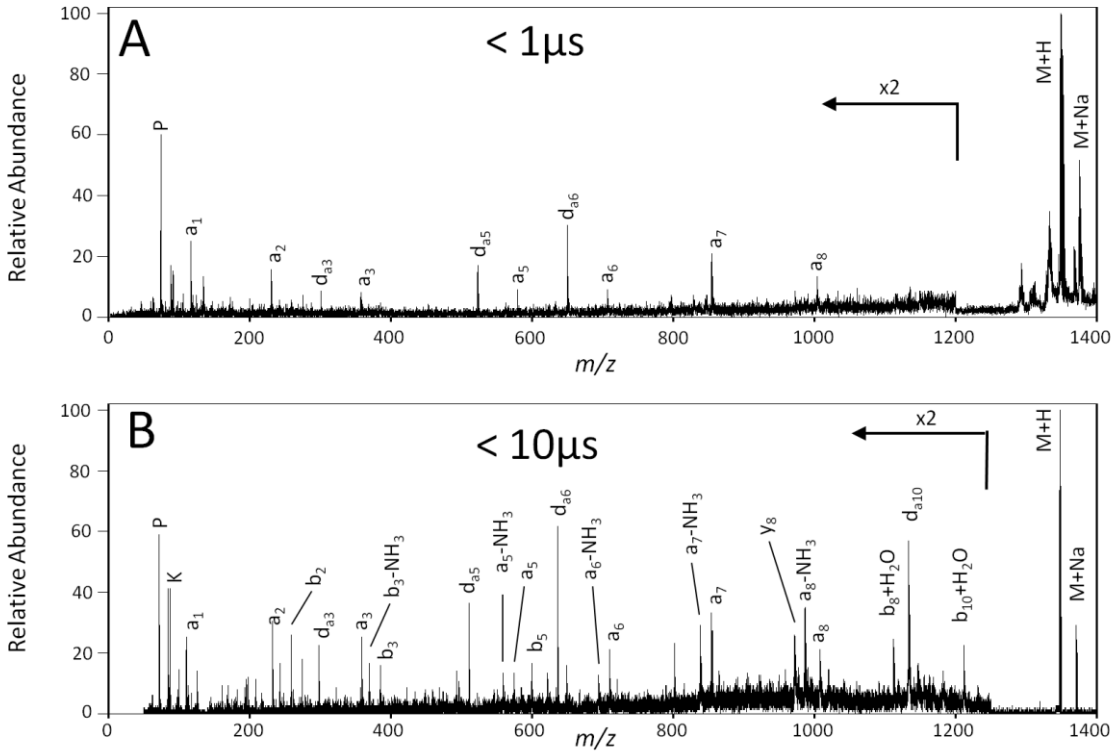

Figure 40: A) 'Prompt' photofragment ion spectrum of Substance P (RPKPQQFFGLM-NH_2) B) photofragment ion spectrum of slow dissociating ions.

The 'prompt' photofragment ion spectrum of Substance P (Figure 40a) results in a mass spectrum showing only *a*- and *d*-type fragment ions. While a reduction in fragment ion variety can serve to simplify the mass spectrum, fewer fragment ions is usually not desired in traditional proteomics experiments. In comparison, the photofragment ion spectrum of slow dissociating precursor ions (Figure 40b) shows an abundance of fragment ions including the *a*- and *d*-ions observed in the 'prompt' spectrum, but with the addition of several *b*-type ions, ammonia loss fragment ions, and a few others including *y*-type fragment ions and b_i+H_2O fragment ions.

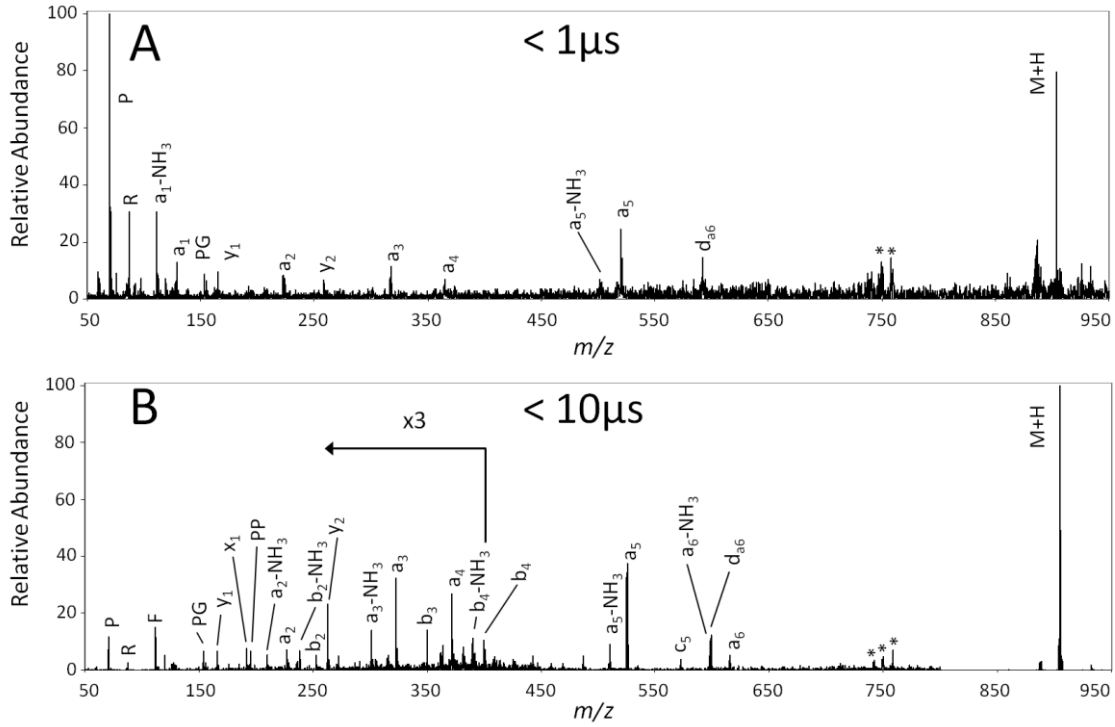

Figure 41: A) 'Prompt' photofragment ion spectrum of Bradykinin 1-8 (RPPGFSPF) B) photofragment ion spectrum of slow dissociating ions.

Lastly, in Figure 41a the 'prompt' photofragment ion spectrum of Bradykinin 1-8 is shown, and again a series of *a*-ions are observed along with *d*-ions and a few *y*-type fragment ions. This spectrum is similar to the others observed except in the case of the y-type fragment ions which are more readily observed on the longer timescale experiments. However, the y_1 fragment ion observed here is very low mass whose formation could be similar to formation of immonium ion. The y_2 fragment ion occurs at a proline residue which is known to enhance *y*-type ion formation. The slow dissociating photofragment ion spectrum (Figure 41b) exhibits many more total

fragment ions but specifically *b*-type and ammonia loss fragment ions are detected in contrast to the 'prompt' spectrum.

Overall, the comparisons in this study between slow and 'prompt' dissociating ions of different peptides show similar results. The spectra of slow dissociating ions contain many more total fragment ions than in the 'prompt' experiments, a result desired in most tandem mass spectra. However, upon closer examination of each data set there exist obvious trends. In all of the 'prompt' spectra, mostly *a*- and *d*-type fragment ions are observed which indicates these ions form in the time between irradiation and reacceleration in the biased activation cell, approximately 1 microsecond. The time spent in this region corresponds to a rate of fragment ion formation of $\geq 1 \times 10^{6} s^{-1}$; that is, all fragment ions that form with rates equal to or faster than $1 \times 10^{6} s^{-1}$ will be observed in the 'prompt' fragment ion spectrum. In contrast, the slow dissociating photofragment ion spectra show many more overall fragment ions which is to be expected considering the longer timeframe allowed for fragmentation. Fragment ions observed in these spectra include the same fragment ions observed in the corresponding 'prompt' spectrum, but with the addition of several other fragment ions especially, *b*-type and ammonia loss fragment ions. These fragment ions must form on a timescale of approximately 10 microseconds or have a rate of formation $\geq 1 \times 10^{5} s^{-1}$.

As discussed previously, the Wahrhaftig Diagram [2] (Figure 33**)** shows that at specific internal ion energy, various fragment ions are favored over others. However, if we assume that the internal energy is high, as is the case in a precursor ion which has just absorbed a 193-nm photon, sampling of specific rates is possible by controlling the

timeframe of the experiment. In the photodissociation experiments performed here, *a*-type and *d*-type fragment ions form faster than 1 micro second since they appear in the 'prompt' photofragment ion spectrum of the peptides examined here. That is, the rates of formation of the *a*-type and *d*-type fragment ions observed in the 'prompt' spectrum are greater than or equal to $1x10^6s^{-1}$. While the rates of formation of *b*-type fragment ions and ammonia loss fragment ions must be between $1x10^5s^{-1}$ and $1x10^6s^{-1}$ as these ions only appear in the slow dissociation ion spectrum.

Conclusions

SIMION simulations reveal an enhancement in ion focusing with the modified biased activation cell equipped with a deceleration lens system for gentler deceleration of precursor ions. Improved ion focusing through this region results in improved sensitivity for time-of-flight experiments and improved S/N ratios for photodissociation experiments. Additionally, removal of two grids from the deceleration system improves the overall ion counts detected at high *m/z*. Comparison of 'prompt' photofragment ion spectra and longer timescale photofragment ion spectra assists in determining the relative rates of fragmentation of specific fragment ions. Most *a*-type and *d*-type fragment ions have a rate of formation greater than or equal to $1x10^6s^{-1}$ while *b*-type and ammonia loss fragment ions must have a rate of formation between $1x10^5s^{-1}$ and $1x10^6s^{-1}$. Other groups have also examined the role of fragmentation timescale on the appearance of specific fragment ions [73, 118, 119], but few have made conclusions regarding the rates of fragment ion formation especially concerning rates of this order.

CHAPTER V

FRAGMENTATION OF PROLINE CONTAINING PEPTIDES VIA COLLISION-INDUCED DISSOCIATION AND 193-NM PHOTOFRAGMENTATION TANDEM TOF MASS SPECTROMETRY

Introduction

Determination of the chemistry affecting gas-phase peptide and protein fragmentation has been a focus of mass spectrometry research for many years owing to the importance of peptide sequencing for proteomics studies [61, 179]. While current technologies and methodologies have sufficed thus far, the specific links between the methodology and fragmentation products are not well understood. More accurate prediction of product ions resulting from specific fragmentation methods *e.g.* collision induced dissociation (CID) [102, 150, 180], electron capture dissociation (ECD) [181], and photodissociation [106, 167], allow for more confident identification of peptides and proteins. Furthermore, theories regarding peptide fragmentation such as the mobile proton model [85] and charge remote fragmentation [88, 139] are also essential in describing fragmentation mechanisms and predicting fragment ion spectra. Additionally, observation of specific fragment ions in tandem mass spectrometry can provide insights regarding the gas-phase structure of the peptide or protein that are helpful in determining the overall 3-dimensional structure in the absence of solvent effects.

The chemistry of proline containing peptides and proteins has frequently appeared in the literature as the pyrrolidine ring structure can have a large influence on the gas-phase structure of the protein [182-185]. It is initially obvious when looking at the structure of proline in Figure 42 that the proline has limited degrees of freedom owing to the rigid ring structure of the amino acid. Lack of an amide hydrogen at the proline residue also prevents intramolecular hydrogen bonding, a major influence on secondary and tertiary protein structure [186, 187]. This may lead to other electron delocalization interactions such as $n \rightarrow \pi^*$ interactions recently reported by Raines and Woolfson [188]. These interactions involve a lone pair of electrons on a oxygen atom delocalizing to the antibonding orbital of a subsequent carbonyl bond and are especially prevalent in polyproline helices[188]. Additionally, the *cis* and *trans* forms of proline will largely alter the structure of the peptide or protein [154] and these two forms have been separated by ion mobility mass spectrometry studies on series of proline containing tryptic peptides [189]. Additionally, polyproline peptides can form two distinct helix structures, one characterized by all *cis* bonds and the other characterized by all *trans* bonds [190] whose size difference can also be separated by ion mobility.

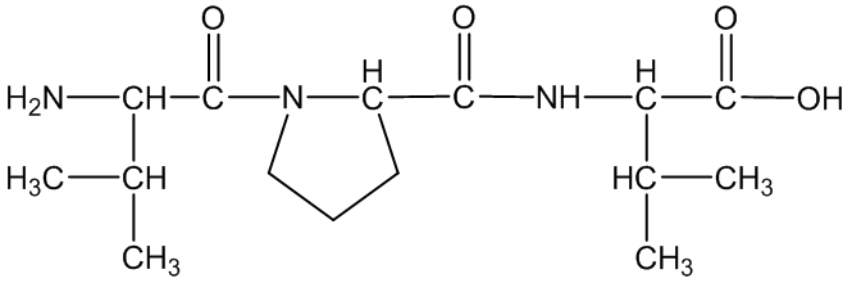

Figure 42: Sketch of the peptide sequence VPV. Notice that the pyrrolidine ring would be expected to have far less flexibility than the comparative valine residues.

Proline also has a large effect on gas-phase fragmentation reactions. The ring structure and lack of amide hydrogen may lead to specific fragment ions to be formed preferentially or biased against. Wysocki and coworkers first determined proline enhances cleavage N-terminal to the proline residue, *y*-type fragment ions, while hindering fragment ion formation C-terminal to the residue, *b*-type fragment ions [76]. Others have also examined the effect of proline on the fragmentation patterns including the effect of proline on fragmentation of deprotonated peptides[80], fragmentation patterns resulting from ETD of proline containing peptides[81], and proline's effect on the fragmentation of several model peptides with a varying proline position[79]. Reilly and Clemmer have examined the fragmentation of proline containing peptides by 157 nm photodissociation and attributed the formation of *a*- and *b*-type fragment ions to the *cis* and *trans* isomers of proline [184]. Additionally, they hypothesized that *Y* and *x* ion formation could also be promoted by these two isomers when the charge is retained C-terminal to the proline residue.

Herein we have examined the fragmentation patterns of several proline containing peptides by high-energy CID and photodissociation TOF/TOF mass spectrometry. We have investigated peptides with the containing a N- or C-terminal arginine which should sequester the ionizing proton. The fragmentation data acquired lead us to propose a mechanism for formation of Y_i, a_i, and $a_i + 1$ fragment ions which occur consistently at proline residues. Our mechanism slightly disagrees with that of Reilly, as we observe similar fragmentation spectra resulting from both high-energy CID and photofragmentation indicating that initial bond cleavage may not be occurring between the α– and carbonyl carbon.

Methods

CID TOF/TOF MS

Tandem TOF CID experiments were performed on an Applied Biosystems 4800 Proteomics Analyzer operating at a collision energy of 2 kV with the collision gas as air. All fragment ions are labeled according to the scheme established by Roepstorff and Fohlmann [69] as modified by Biemann [61].

Photodissociation TOF/TOF MS

Photofragment ion spectra were acquired on a home-built TOF/TOF MS equipped with a matrix assisted laser desorption ionization (MALDI) source which utilizes a nitrogen laser (λ = 337 nm). MALDI formed ions are separated after delayed extraction in the first TOF. For 'prompt' timescale experiments [167], ions of interest

are selected and decelerated over a length of 3 inches by a series of radially focusing tube lenses to roughly one half of their initial kinetic energy where the ions then enter a biased activation cell. Precursor ions are then irradiated with a precisely-timed pulse from 193 nm excimer laser increasing the internal energy of ions that absorb a photon by 6.42 eV. After irradiation, resulting fragment ions and remaining precursor ions are reaccelerated into the second TOF, a linear field reflectron 1.5° off axis from the ion beam. Ions are detected with a microchannel plate and the signal is acquired with a time-to-digital converter (TDC) and imported into Microsoft Excel for mass analysis. For longer timescale experiments, ions of interest exiting the first TOF are selected, and subsequently irradiated with the excimer laser. As fragment ions and remaining precursor ions have a large difference in kinetic energies the reflectron is tuned to focus a specific range of mass-to-charge ratios and the resulting spectra are stitched together to give the complete mass spectrum [117]. All photofragment ion spectra shown are obtained by subtracting the 193 nm laser off spectrum, or metastable ion spectrum from the laser on spectrum in order to eliminate any contribution from metastable fragment ions.

Materials

All chemicals used in this study were purchased from Sigma-Aldrich (St. Louis, MO) unless otherwise noted. Peptides analyzed in this study include $P_{14}R$ (PPPPPPPPPPPPPR), RP_{13} (RPPPPPPPPPPPP), GPPGPPR, GPPRPPG all purchased from GenScript and des-Arg_1-bradykinin (PPGFSPFR) and des-Arg_9-bradykinin

(RPPGFSPF) both purchased from Sigma. Each solid peptide was dissolved in water to yield a concentration of 1 mg/mL. Matrix solution was prepared by dissolving α-cyano-4-hydroxycinnamic acid in 50:50 acetonitrile:water with the addition of trifluoroacetic acid and ammonium dihydrogen phosphate to generate 0.1% concentrations with respect to the total volume of the matrix solution. 1 μL of peptide solution was combined with 20 μL of the matrix solution and 1 μL of the mixture was spotted onto the MALDI plate resulting in approximately 50 pmol of peptide per spot.

We also examined the N-terminally acetylated and C-terminally methylated forms of $P_{14}R$ to determine the influence of the N- and C-terminus. Briefly, N-terminal acetylation was carried out by combining the peptide solution consisting of 1nmol of solid peptide dissolved in 20 μL 50mM ammonium bicarbonate with the reagent solution, composed of 20 μL of acetic acid and 80 μL of methanol. The solutions were allowed to react for one hour then lyophilized to dryness. C-terminal methylation was performed according that described by Reid [169]. The reaction mixture was made by the dropwise addition of 80 μL of acetyl chloride to 0.5 mL of methanol while stirring. After 5 min, a 100 μL aliquot of this mixture was added to 1 mg of dry peptide, allowed to react for 2 hours at room temperature and then dried.

Results and Discussion

Figure 43 shows the TOF/TOF CID tandem mass spectra of the peptide PPPPPPPPPPPPPR ($P_{14}R$). A complete series of *y*-type fragment ions and a near complete series of *w*-type fragment ions are observed along with several abundant

a-type, *b*-type, and ammonia loss fragment ions. The dominant y_{13} fragment ion is consistent with loss of two proline units from the intact peptide which appears to arise from a different competing fragmentation pathway and will be discussed later. It is important to note that for this peptide, b_i-type fragment ions are isobaric with P_i internal fragment ions, and the loss of 28 mass units, or CO, from internal P_i fragment ions is isobaric with a_i-type fragment ions. In the spectra of $P_{14}R$ we will label these ions as a_i and b_i respectively to avoid confusion. The high abundance of *w*-type fragment ions in this spectrum is also interesting since the formation of these fragment ions requires that the pyrrolidine ring is cleaved.

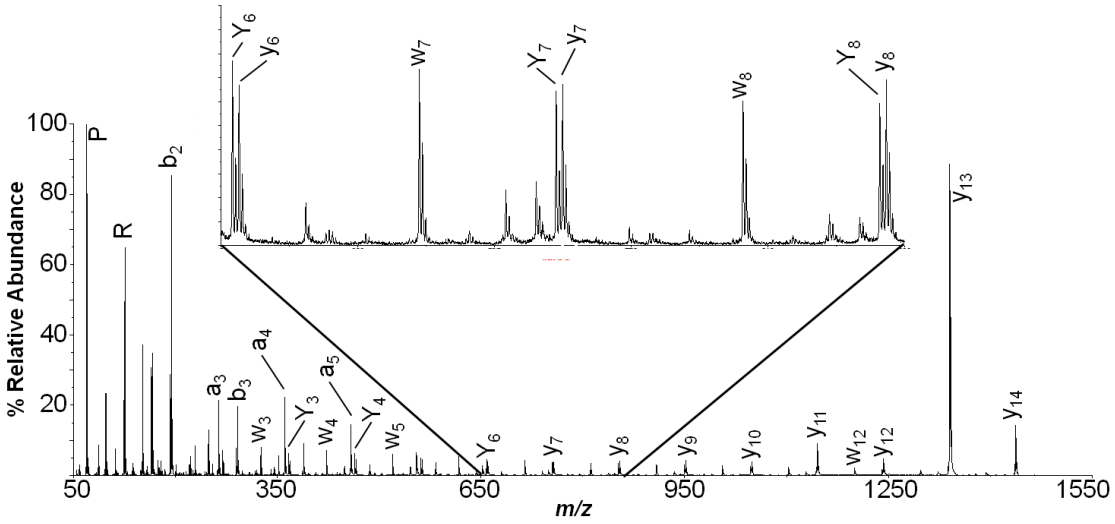

Figure 43: Collision induced dissociation tandem mass spectrum of PPPPPPPPPPPPPR ($P_{14}R$). Here the more dominant of the y_i or Y_i fragment ion is labeled but both ions are present in the spectrum.

Upon closer examination, a peak appears 2 mass units less than each *y*-type fragment ion which corresponds to a *Y*-type fragment ion as clearly seen in the inset of Figure 43. During the formation of a *y*-type fragment ion, an H must be transferred from the leaving group to the forming *y*-ion. On the other hand, an H transfer to the leaving group from the fragment ion or simple loss of H from the fragment ion will result in a *Y*-type fragment ion. We have referred to "H" transfer since this could denote either transfer of a proton or a hydrogen atom. The two differing structures can be seen in Figure 44.

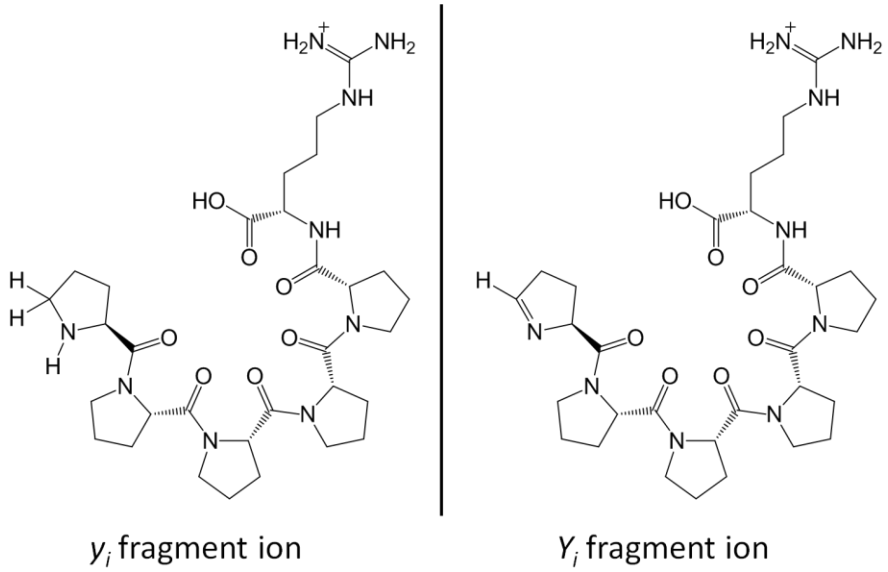

Figure 44: y_5 and Y_5 fragment ions showing the structural differences between *Y*- and *y*-type fragment ions.

One might assume that the formation of the *Y*-ion would not be favorable at proline residues owing to the cyclic nature of the proline side chain resulting in no labile hydrogen attached to the amide nitrogen to lose or transfer to the leaving group. However, the stability of the proline ring containing a double bond may cause H transfer from the α-carbon giving the *Y*-ion structure as seen in Figure 44. It is also possible that the H could be transferred from one of the two hydrogen atoms bound to the δ-carbon resulting in the *Y*-ion proposed by Reilly [184]. Another interesting feature of the CID data is that the *Y*-type fragment ions appear to decrease in relative abundance with increasing fragment ion size, when comparing each *Y*-ion with the corresponding *y*-type fragment ion. This could either be an effect of the stability of the *Y*-ion or may be influenced by the ability of the leaving group to accept the hydrogen. Low-energy CID experiments, such as those within trapping type instruments, do not provide w_i- or Y_i-ions, but are strictly limited to y_i-ions for the case of $P_{14}R$ as seen in Figure 45.

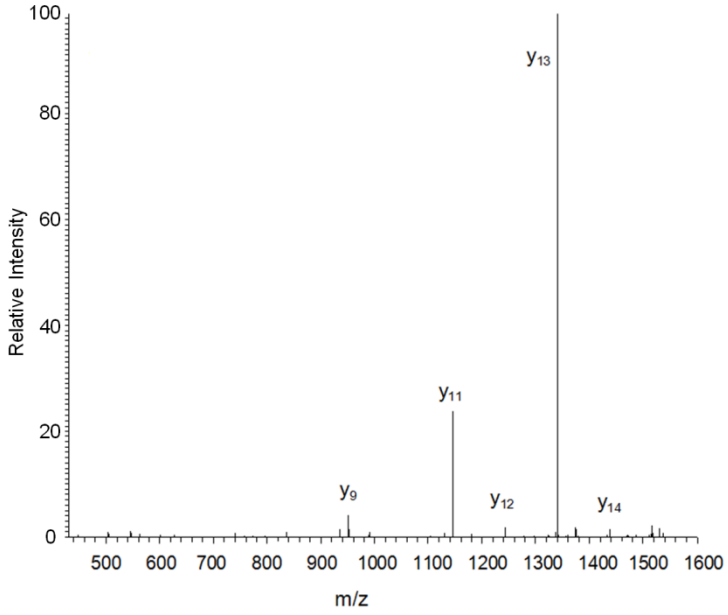

Figure 45: MS/MS spectrum of protonated $P_{14}R$ in an LCQ ion trap at a collision energy of 30 eV. [191]

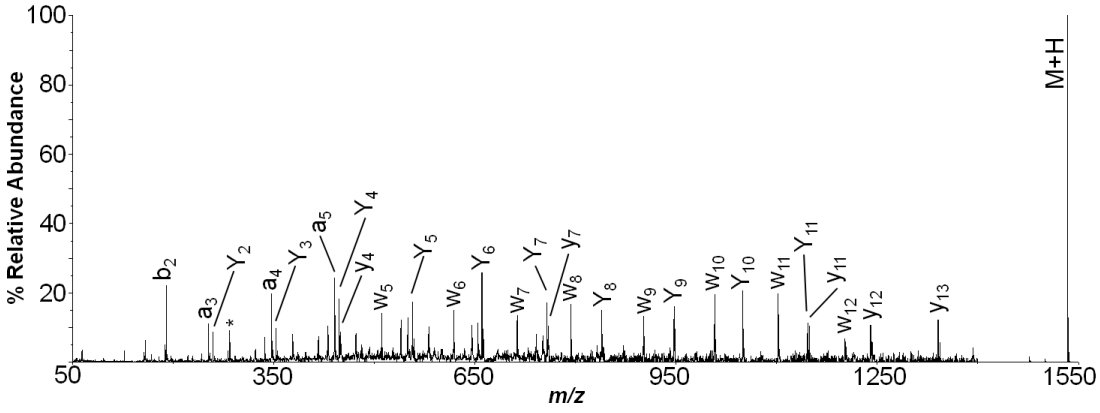

Figure 46: Photofragment ion spectrum of $P_{14}R$. Internal fragments are labeled with "*".

The photofragment ion spectrum of $P_{14}R$ (Figure 46) shows a distinct series of *Y*- and *w*-type fragment ions. Additionally, *a*- and *b*-type fragment ions along with ammonia loss fragment ions are observed similar to the CID studies. While there are a few instances of *y*-ions in the spectrum, there is a strong preference for *Y*-type ions in contrast to ions observed in the CID spectrum which shows a slight preference for *y*-ions. The lack of *y*-ions may be an effect of the subtraction of the metastable ion spectrum from the photofragment ion spectrum if the *y*-ions are metastable fragment ions which may also be the case in the CID spectrum. The *Y*-ions are dominant throughout the spectrum and do not appear to change in relative abundance with increasing fragment ion size as with CID. The *w*-type fragment ions in the photofragment ion spectrum have a higher relative abundance than those observed in the CID spectrum with respect to the *Y*-type fragment ions. While the y_{13} ion is observed in this spectrum, it is in much lower relative abundance and is likely not a photofragment ion, but in fact is a metastable ion which was not eliminated by subtracting the metastable ion spectrum. Overall, except for the absence of a dominant y_{13} ion, the photofragment ion spectrum does not show any major differences to the CID tandem mass spectrum.

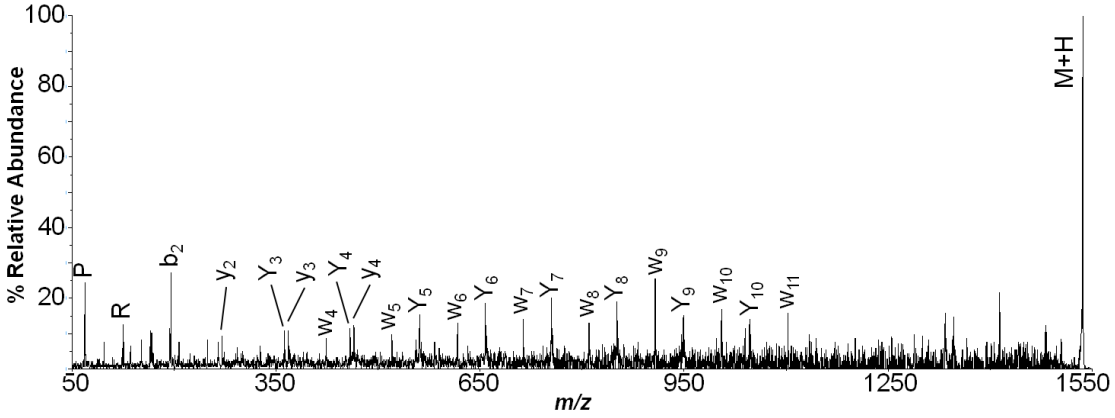

Figure 47: 'Prompt' photofragment ion spectrum of $P_{14}R$ where only fragment ions that form on a timescale of 1 us are observed. Internal fragments are labeled with "*".

To obtain further information regarding the fragmentation of proline containing peptides, the 'prompt' photofragment ion spectrum of $P_{14}R$ was acquired and is seen in Figure 47. Overall, the photofragment ion spectra examining both timescales are similar in terms of fragment ions observed and relative abundances of those fragment ions. Peaks absent from the 'prompt' photofragment ion spectrum are mostly *y*-ions and ammonia loss fragment ions. We typically do not observe any *b*-type fragment ions in our 'prompt' photofragment ion spectra and the lack of a b_3 fragment ion agrees with this assessment. However, the observation of the b_2 fragment ion may be attributed to some stability of the PP unit which allows this fragment ion to form on a 'prompt' timescale, in comparison to typical *b*-type fragment ions and this result has been investigated by others [191]. As with the longer timescale photofragment ion spectrum, the y_{13} fragment ion has a large contribution from the metastable ion spectrum as is likely not a photofragment ion. Overall, the 'prompt' photofragment ion spectrum does

not show major differences from the photofragment ion spectrum and therefore the timescale variations on the order of microseconds do not appear to have a strong effect on the fragmentation occurring at proline residues with these peptides.

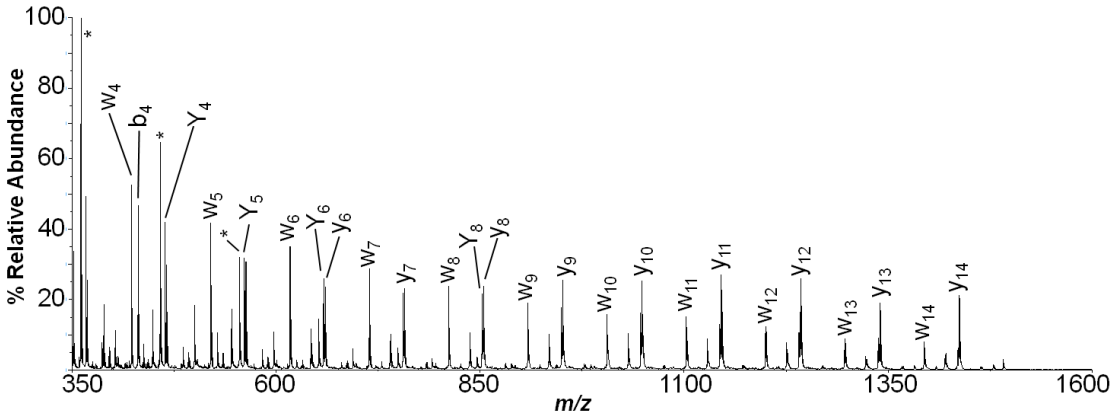

Figure 48: CID tandem mass spectrum of Ac-$P_{14}R$. Here the more dominant of the y_i or Y_i fragment ion is labeled but both ions are present in the spectrum. Internal fragments are labeled with "*".

In order to examine the influence of the N-terminus on the fragmentation of $P_{14}R$, the CID mass spectra of the N-terminally acetylated peptide is shown in Figure 48. The primary spectral feature in the acetylated form of the peptide is the dramatic decrease in the relative abundance of the y_{13} fragment ion compared to unmodified $P_{14}R$. This implies that by blocking the N-terminal amine, the loss of two proline units is no longer preferentially formed. This observation is in agreement with a separate preferential fragmentation pathway for the formation of a dominant y_{13} ion that involves the N-terminus of the peptide [191]. Acetylation at the N-terminus not only increases the steric hindrance at the N-terminus but also decreases the basicity of the N-terminal

amine, decreasing the probability of a nucleophilic attack of this amine on the second carbonyl group. Therefore, the mechanism that generates the dominant y_{13} ion in the case of the unmodified $P_{14}R$ may be attributed to a fragmentation pathway that involves nucleophilic attack of the N-terminal amine on the second carbonyl carbon, resulting in a stable diketopiperazine product as reported previously[123, 192]. Dominant *y*-, *Y*-, and *w*-type fragment ions are consistent in this spectrum indicating that the N-terminal modification has no other major effect on proline fragmentation. However, it is interesting to note that *a*- and *b*-type fragment ions are no longer isobaric with the corresponding internal fragment ion owing to the N-terminal acetyl group. However, both the b_i fragment ions and the corresponding P_i internal cleavage fragment ion are present in the spectrum along with a_i fragment ions and their corresponding P_i-28 internal cleavage fragment ions implying that both species are present in the spectrum of the unmodified form of $P_{14}R$.

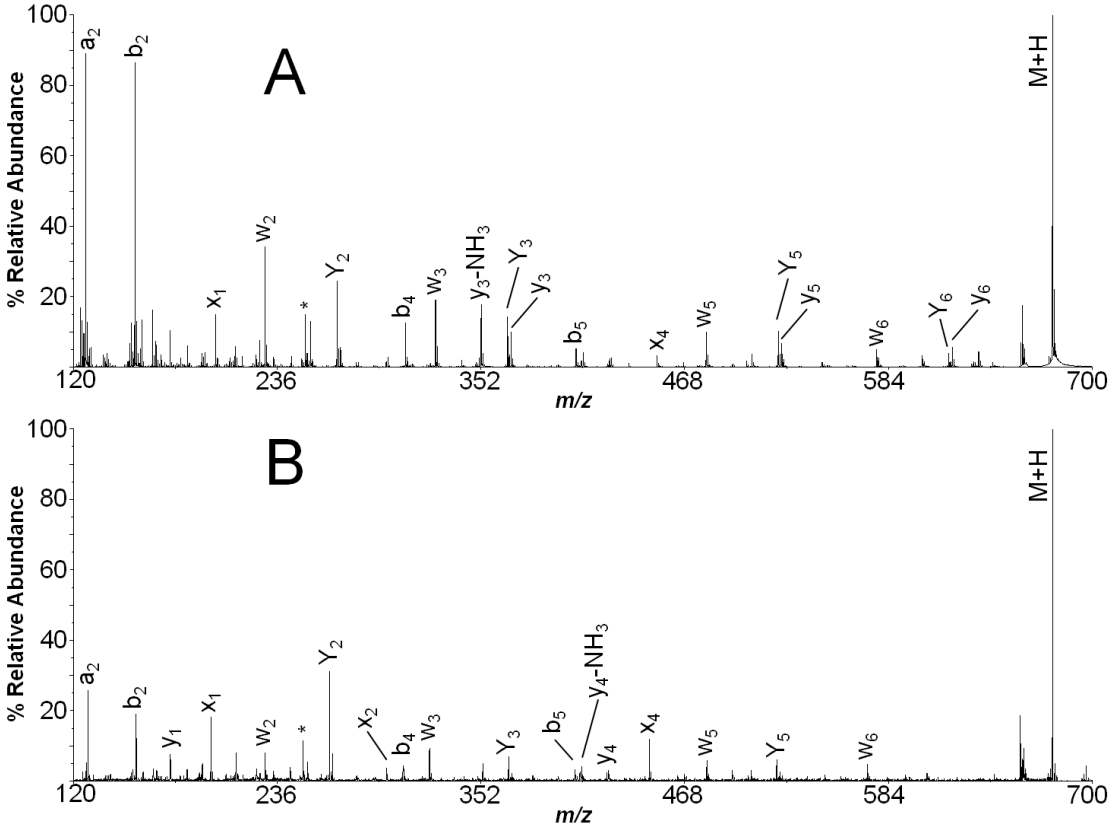

Figure 49: Tandem mass spectra of GPPGPPR a) CID and b) photodissociation as the dissociation methods, respectively. Internal fragments are labeled with "*".

The poly-proline peptides investigated thus far may limit the amount of fragmentation observable as the majority of the residues are proline. However, the peptides GPPGPPR and des-Arg_1-bradykinin (PPGFSPFR) are proline containing peptides that more closely resemble tryptic peptides originated from proteins that may be encountered within a proteomics experiment. The CID tandem mass spectrum of GPPGPPR shown in Figure 49a reveals dominant *Y*- and *w*-type fragment ions observed at each proline residue, consistent with the results from the poly-proline peptides. The Y_2, Y_3, and Y_5 fragment ions are observed with high relative abundance while the Y_6

fragment ion is less intense with respect to each corresponding *y*-type fragment ion. The decreasing relative abundance of the higher mass *Y*-type fragment ions is also observed in the $P_{14}R$ tandem mass spectrum. This result may indicate that *Y*-type fragment ions require a higher amount of energy to form and when the mass of the potential *Y*-type fragment ion becomes large, the energy can be redistributed through a greater number of vibrational degrees of freedom thereby favoring *y*-type fragment ion formation. Another interesting feature in Figure 49a is the presence of the x_4 fragment ion occurring near the proline residues. Reilly and coworkers proposed that the relative abundance of x_i fragment ions would be enhanced at the amino acid residue C-terminal to the proline residue and the presence of this fragment ion agrees with that assessment [184]. However, the photofragment ion spectrum of GPPGPPR (Figure 49b) shows a greater enhancement of this effect than the CID tandem mass spectrum.

The CID tandem mass spectrum of des-Arg_1-bradykinin (PPGFSPFR) also agrees with the previous observations regarding proline fragmentation (Figure 50a). Abundant *Y*- and *w*-type fragment ions are observed at each proline residue with a decreased relative abundance for the larger Y_7 fragment ion. In Figure 50a, an abundant x_2 fragment ion is observed for proline in position 3, but there is no x_6 fragment ion present from proline position 7 indicating that *x*-ion formation may not be preferentially formed from the presence of proline. However, when examining the photofragment ion spectrum (Figure 50b) abundant *x*-type fragment ions are observed throughout the spectrum indicating that perhaps *x*-ions are preferentially formed by UV photofragmentation methods. Analysis of these peptides reveals that fragmentation at

proline residues for a C-terminal charge carrier is predictable for both synthetic proline containing peptides and naturally occurring peptides.

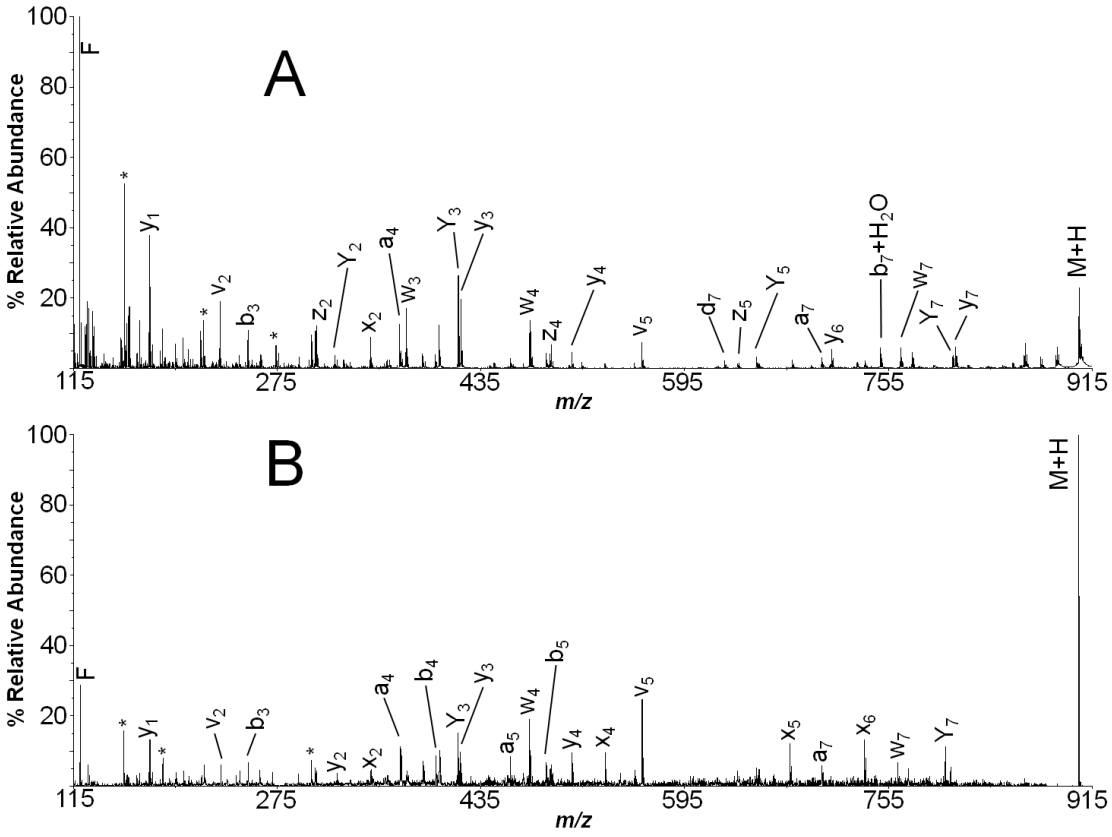

Figure 50: Tandem mass spectra of PPGFSPFR a) CID and b) photodissociation as the dissociation methods, respectively. Internal fragments are labeled with "*".

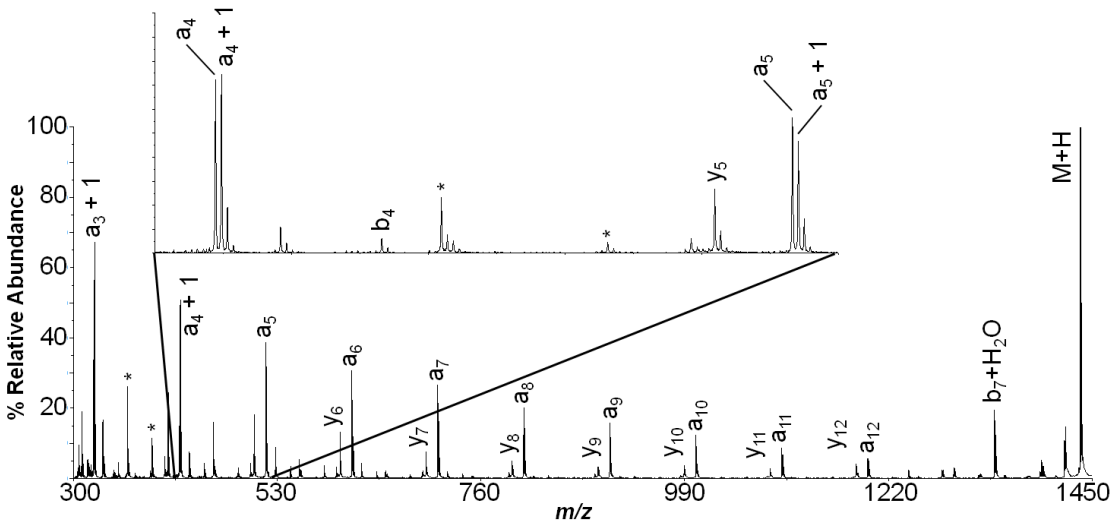

Figure 51: CID tandem mass spectrum of RPPPPPPPPPPPPP (RP_{13}). Here the more dominant of the a_i or a_i + 1 fragment ion is labeled but both ions are present in the spectrum. Internal fragments are labeled with "*".

Further examination on the fragmentation of proline containing peptides involves investigation of N-terminal charge carrying peptides. The CID tandem mass spectrum of RP_{13} (RPPPPPPPPPPPPP) is found in Figure 51. Abundant *a*-type fragment ions are observed at each proline residue along with the less abundant *y*-type fragment ions. These *y*-type fragment ions are likely formed by a low energy pathway and are present when examining the metastable ion tandem mass spectrum. Upon closer examination of the observed *a*-ions, a peak is present one mass unit larger that each *a*-type ion, which upon initial examination could be attributed to the ^{13}C peak. While it is not easy to select the ^{12}C peak from a given analyte within a TOF/TOF instrument, by fitting the theoretical ^{13}C intensity relative to the ^{12}C peak we determine that the peak one mass unit above each *a*-ion must be attributed to an a_i + 1 ion. This fragment ion must be a

radical as it is an odd electron ion formed by the homolytic cleavage of a backbone bond. These $a_i + 1$ fragment ions are more abundant in the lower mass region of Figure 51, but they are consistent for each *a*-type fragment ion in the spectrum. The photofragment ion spectrum of this peptide is similar with regards to the presence of a_i and $a_i + 1$ fragment ions and is thus not shown here.

The structure of the *a*-type fragment ions requires a brief explanation in order to define the difference between the a_i and $a_i + 1$ fragment ions. Originally Biemann proposed that an *a*-ion consisted of a double bond between the nitrogen and the α-carbon on the backbone, and therefore a charge on the amide nitrogen [61], implying that the charge is located in proximity to the site of fragmentation. However, if the charge is located remote from the site of fragmentation, the amide nitrogen could lose the hydrogen attached so that no charge is at this location. On the other hand, a double bond could be formed between the α– and β–carbon implying loss of a hydrogen from the β-carbon resulting in the *a*-type fragment ion, a structure investigated by Reilly [193]. In the case of proline, no amide hydrogen exists therefore the *a*-type fragment ion must consist of a double bond between the α- and β-carbon if the charge is located remote from the site of fragmentation. The $a_i + 1$ fragment ions are attributed to bond cleavage between the α- and carbonyl carbon with an electron remaining on the α-carbon and the charge lying remote from the site of fragmentation.

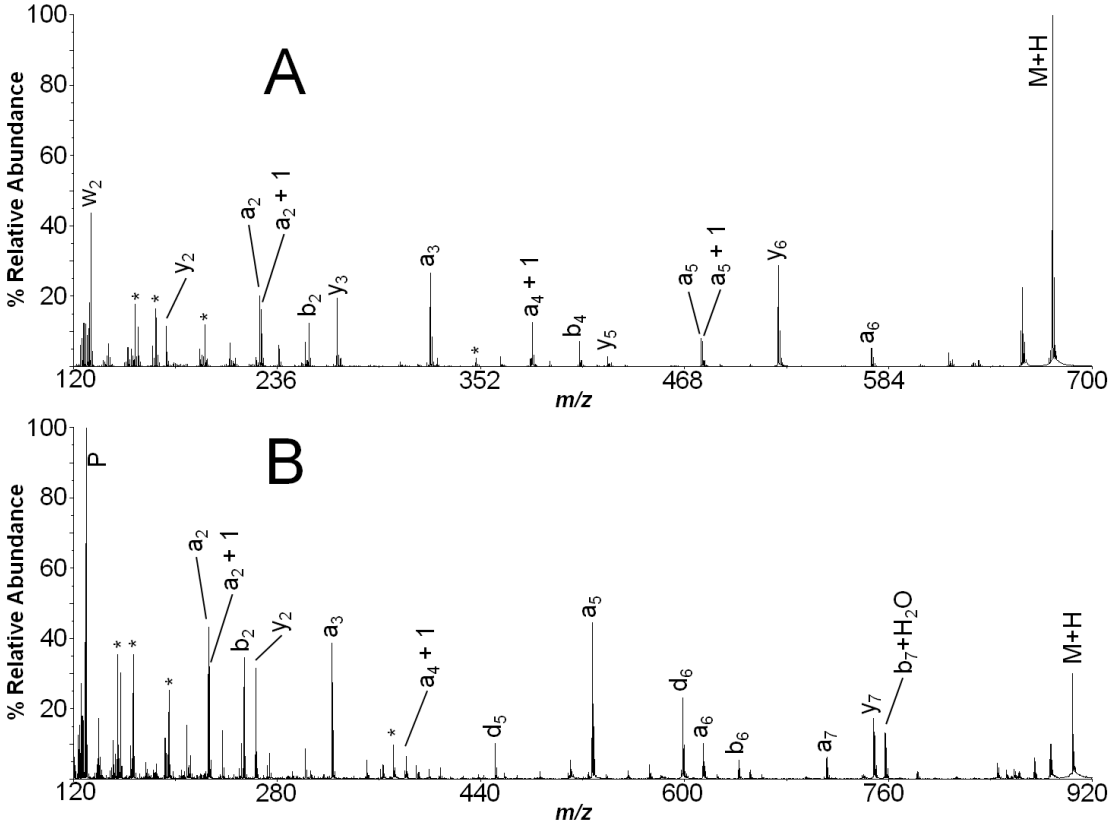

Figure 52: CID tandem mass spectra of a) RPPGPPG and b) des-Arg$_9$-bradykinin (RPPGFSPF). Internal fragments are labeled with "*".

To further explore the appearance of a_i and a_i + 1 fragment ions at proline residues, we investigated the peptides RPPGPPG and des-Arg$_9$-bradykinin (RPPGFSPF) by tandem TOF mass spectrometry. The CID tandem mass spectrum of RPPGPPG is shown in Figure 52. Abundant a_i ions are observed at all proline residues with a_i + 1 fragment ions appearing at only two of the four possible proline sites (a_2 + 1 and a_5 + 1), specifically when the adjacent amino acid is proline. Perhaps the presence of glycine, or simply an amino acid other than proline, enhances the probability for hydrogen transfer to the leaving group or hydrogen atom loss in order to preferentially form a_i fragment

ions whereas an adjacent proline hinders the formation of a_i ions resulting in increased abundance of a_i + 1. The presence of a dominant a_4 + 1 fragment ion at the glycine residue agrees with this assessment; however, the presence of this ion is also influenced by the fact that a double bond cannot be formed between the α– and β–carbon to form an a_i since glycine has no β–carbon. The *a*-type ion formed here must contain a double bond between the α-carbon and amide nitrogen with loss of the amide hydrogen.

The CID tandem mass spectrum of des-Arg_9-bradykinin (RPPGFSPF) shown in Figure 52 also shows abundant a_i fragment ions at proline residues, but with only a single a_2 + 1 fragment ion at the proline in position 2. Here the adjacent amino acid is proline which is in agreement with the previous assessment; however, the presence of a_4 + 1 in which the adjacent amino acid is not proline indicates that proline is not the only contributing factor. The lack of an α–β carbon-carbon bond must be the primary influence on the lack of an a_4 fragment ion in this instance thereby enhancing formation the a_4 + 1 fragment ion. However, the a_i + 1 can also be formed when proline is the adjacent amino acid residue as evidenced by the slight presence of a_6 + 1. Here the a_i + 1 ion is of low relative abundance after subtraction of the ^{13}C peak, but as observed in the fragmentation of RP_{13}, there is a decreasing relative abundance of a_i + 1 ions with increasing ion size.

From the data acquired herein we propose mechanisms for formation of Y_i-, a_i-, and a_i + 1-type fragment ions as seen in Figure 53. In this scheme, we have not shown the location of the charge but will simply state that the charge is remote from the site of fragmentation and the labeled structures are only valid if a proton is included. Initially,

the high energy collision or 193 nm photon generates a homolytic bond cleavage of the amide bond at the proline residue. The presence of the radical site on the nitrogen atom leads to facile loss of a hydrogen atom to form the *Y*-type fragment ion if the charge is C-terminal to the site of fragmentation. Tureček and workers found that loss of a hydrogen atom from a nitrogen radical is an exothermic process and a favorable route of dissociation [81]. It is also quite plausible that this reaction occurs similarly but with transfer of a hydrogen atom toward the fragment ion resulting in the corresponding *y*-type fragment ion (not shown).

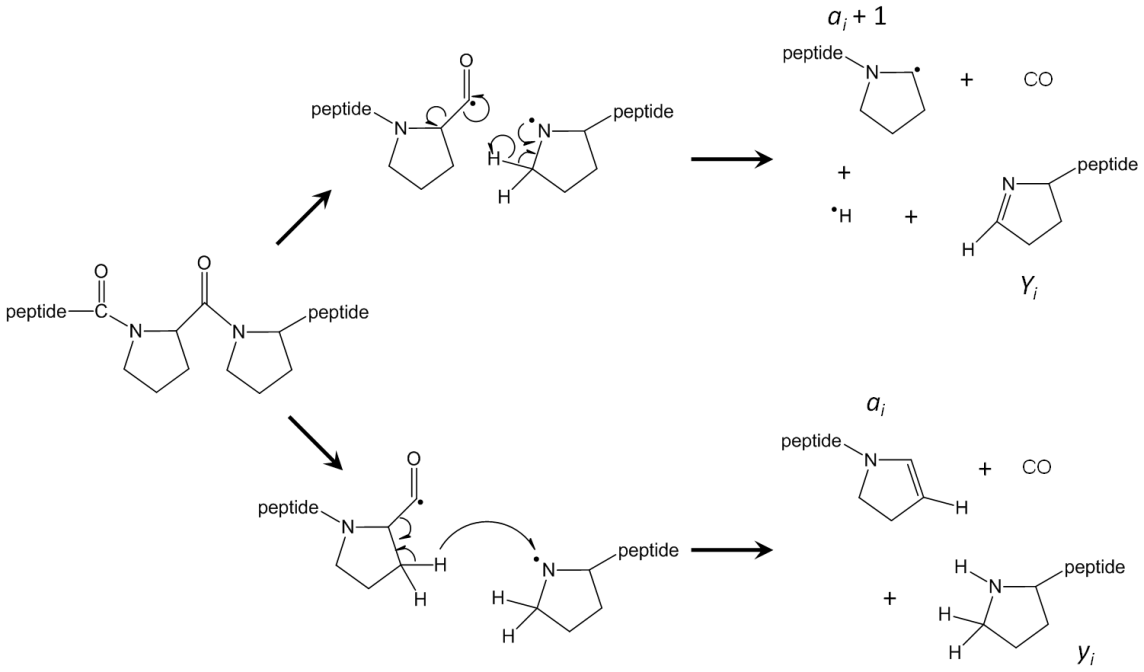

Figure 53: Proposed mechanism for the formation of Y_i, a_i, and $a_i + 1$ fragment ions occurring at proline residues. Note that no charge is shown and that the fragment ions labeled are only correct if there is a charge contained in the 'peptide' portion of the structure.

If the charge resides N-terminal to the site of fragmentation, an a_i or a_i + 1 fragment ion would result and each is indicated in Figure 53. The a_i + 1 fragment ion simply involves decarbonylation after in the initial cleavage of the amide bond resulting in a radical site on the α-carbon. Similar to the formation of the Y_i-type fragment ion, the a_i type fragment ion involves electron rearrangement and loss of a hydrogen atom. The contrast between our mechanism and Reilly's mechanism [184] in the formation of a_i and a_i + 1 type fragment ions is simply whether the initial fragmentation occurs at the amide bond or between the α- and carbonyl carbons. Also, our mechanism does not account for the *cis* and *trans* forms of proline.

In all of the data acquired here when the charge is C-terminal to the site of fragmentation, a *w*-type fragment ion consistently appears with each *Y*-type fragment ion indicating the two may form by a similar mechanism. While we cannot conclusively recommend a mechanism for formation of these ions, we believe that partial side chain loss must be occurring after the initial homolytic cleavage of the amide bond. The leaving neutral side chain would also contain a radical site in order to provide the *w*-type fragment ion.

Conclusions

Collision induced dissociation and 193 nm photodissociation of proline containing peptides result in a predictable series of fragment ions at proline residues depending on the location of the basic amino acid. For peptides with an arginine at the C-terminus, dominant Y_i- and w_i-type ions are observed. Prevailing a_i and a_i + 1

fragment ions are observed when an arginine is located at the N-terminus. Based on these results we have suggested that these ions form by initial homolytic bond cleavage of the amide bond adjacent to the proline residue followed by electron rearrangement and possible hydrogen atom loss. This mechanism slightly contrasts that proposed by Reilly as their mechanism proposes initial cleavage of the α- and carbonyl carbons while ours proposes initial cleavage of the amide bond. We suggest this difference since we observed similar fragmentation in collision induced dissociation which preferentially fragments amide backbone bonds.

CHAPTER VI

DEVELOPMENT OF A SECOND SOURCE AND A DUAL-STAGE REFLECTRON FOR IMPROVED INSTRUMENT PERFORMANCE

Previous photodissociation TOF/TOF results in our research group have been adequate; however, there is always a desire to improve the overall performance of the instrumentation. An earlier iteration of the photodissociation TOF/TOF instrument involved tuning the reflectron voltage to focus a narrow mass-to-charge window at the detector and subsequently stitching the individual spectra together to produce the entire mass spectrum [116]. While this method produced excellent mass spectra, the duty cycle was incredibly low since as many as 10 summed spectra at various reflectron voltages had to be acquired to generate the data for a single sample. Morgan improved this design by adding a biased activation cell which allowed the entire mass spectrum to be focused at the detector at a single reflectron voltage [114]; however, this experiment only examined fragment ions that formed on a very short timescale (< 1μs). The 'prompt' forming fragment ions investigated resulted in fewer total fragment ions that could reach the detector. In an effort to improve the existing instrumentation, several modifications have been implemented into the current instrument. A detailed discussion of reflectron focusing will first be addressed as one of the modifications is the addition of dual stage reflectron.

Reflectron Time-of-Flight Focusing

The focusing effects of the reflectron mass analyzer have been previously discussed in this work; however, an in-depth examination of the focusing parameters of reflectrons is warranted. While Mamyrin's original design was a dual-stage reflectron [48], for simplicity, the discussion here will begin with a single-stage reflectron, or an ion mirror [49, 50], as seen in Figure 54.

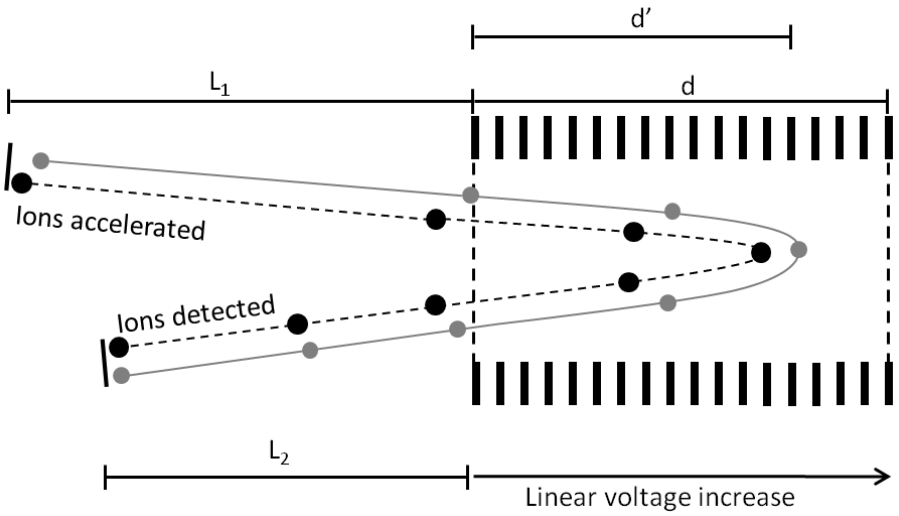

Figure 54: Diagram of a single-stage reflectron mass analyzer examining two ions of the same *m/z*. Note the grey ion penetrates deeper into the reflectron owing to its higher kinetic energy than the black ion. Ideally, the grey ion will catch up to the black ion precisely at the detector as shown.

Single-Stage Reflectron

In Figure 54, two ions are shown with differing kinetic energies separated in the reflectron region and then refocused at the detector. To determine the optimum distance for *d* and *d'*, the spread of ion kinetic energies must be considered, but we will begin by

considering a single ion. The ion spends the majority of its flight time in the field-free regions, L, ($L = L_1 + L_2$) and the time spent in this region is related to equation 9, where d the distance can be modified to L, m is the mass of the ion, e is the charge of an electron, and E_v is the accelerating voltage applied in the source.

$$(9) \qquad t_{drift} = L\left(\frac{m}{2eE_V}\right)^{1/2}$$

The time spent in the reflectron is related to the electric field within the reflectron and the initial kinetic energy of ions entering the reflectron according to equation 7:

$$(10) \qquad t_{ref} = 4d'\left(\frac{m}{2eE_v}\right)^{1/2}$$

where d' is the distance at which the ions turn around within the reflectron and E_v is the voltage applied to the reflectron and in this case is equal to the accelerating voltage. The total flight time is therefore:

$$(11) \qquad t = t_{drift} + t_{ref} = L\left(\frac{m}{2eE_V}\right)^{1/2} + 4d'\left(\frac{m}{2eE_v}\right)^{1/2}$$

The focusing effects of the reflectron device result from the fact that penetration depth varies with initial ion kinetic energy. A nominally higher kinetic energy will result in shorter time spent in the drift region but a longer time spent in the reflectron owing to the deeper penetration depth. Maximum resolution can be achieved when the time spent in the drift region and in the reflectron are equal:

$$(12) \qquad L\left(\frac{m}{2eE_V}\right)^{1/2} = 4d'\left(\frac{m}{2eE_v}\right)^{1/2}$$

Equation 12 can be reduced to obtain the optimum turn around distance in the reflectron $L = 4d'$, or approximately the optimum length of a single-stage reflectron, $L = 4d$. A single-stage reflectron is sufficient for many purposes, except when size constraints are an issue. Additionally, the single-stage reflectron only focuses ions to the first-order whereas a dual-stage reflectron can focus ions to the second order thereby increasing the maximum achievable resolution.

Dual-Stage Reflectron

The dual-stage reflectron that was originally introduced by Mamyrin [48] has several advantages over the single-stage reflectron, but it is slightly more complex. A schematic of a typical dual stage reflectron is shown in Figure 55.

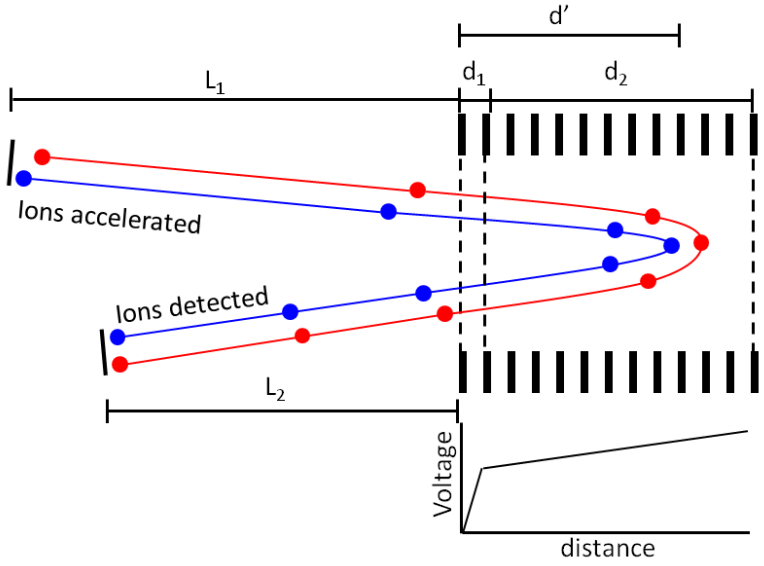

Figure 55: Model of a dual-stage reflectron similar to the one originally used by Mamyrin [48]. Notice according to the lower right portion of the diagram that there is a larger voltage drop across d_1 than d_2.

Here two differing deceleration stages are observed consisting of a short retarding region and a longer reflecting region. A larger portion of the ion kinetic energy is dropped across the first retarding stage, usually 2/3 of the total initial ion kinetic energy. This results in shorter total reflectron lengths such that $L > 4d$ as is the optimum case for a single stage. Therefore, dual-stage reflectrons can be much shorter in length than their dual-stage counterparts.

Additionally, the dual stage reflectron can focus ions with a broader range of kinetic energies because they correct ion arrival times to the second-order. A detailed derivation of first order focusing and second order focusing reflectron mass spectrometers can be found in the work by Wang and coworkers [51]. While the detailed derivations undertaken in their work will not be reprinted here, there are several parameters that are worth discussion when designing a dual stage reflectron. In the work by Wang, they discuss the parameter C which is the ratio of the electric field in the first region to the electric field in the second region of the reflectron:

$$C = \frac{E_{vref1} / d_1}{\left(E_{vref2} - E_{vref1}\right) / d_2} \tag{13}$$

Here E_{vref1} is the potential applied to the first region, E_{vref2} is the potential applied to the back of reflectron, and d_1 and d_2 are the distances of the two regions of the reflectron. To achieve the maximum possible resolution, this ratio should be sufficiently large which consequently results in a short d_1. A short d_1 can create ion losses because of the sharp increase in field and because of the close proximity of two wire mesh grids which

can also be detrimental to ion transmission. Additionally, electric discharging can be a problem if machining imperfections exit between the two electrodes that define d_1.

Wang further elaborates on the C value be describing its relationship between the parameters d_1, d_2, L, E_{vref1}, and E_{vref2} which can be valuable when designing a reflectron to be input into an existing mass spectrometer [51]. Alternatively, the work by Le Beyec and coworkers describes an alternate method of determining the optimum dimension of L for an existing dual-stage reflectron [194]. Le Beyec also discusses the influences of the accelerating and reflectron voltages on the maximum resolution obtainable resolution for a given dual-stage reflectron. These two papers along with Mamyrin's original work allow one to develop an ideal dual-stage reflectron and achieve excellent mass resolution.

Addition of Source 2

Ion collection efficiencies in reflectron tandem TOF mass spectrometry can be inefficient owing to the difference in kinetic energies between fragment ions and remaining precursor ions according to the equation 14:

$$KE_{fragment} = \left(\frac{m_f}{m_p}\right) KE_{precursor} \qquad (14)$$

Our group has addressed this feature in our photodissociation tandem TOF experiments by tuning the reflectron voltage to focus varying *m/z* ratios (or kinetic energies) at the detector [116]. Recall also that Morgan developed a biased activation cell which reaccelerated 'prompt' forming fragment ions in order to obtain the entire mass spectrum

at a single reflectron voltage [114]. However, this produced only a limited number of fragment ions owing to the short timescale of the experiment. Additionally, the range of kinetic energies between the precursor ions and fragment ions still resulted in ion losses which could not be overcome with the current design. Modification of the existing biased activation cell may allow for improved mass spectral features enabling the instrument to perform more advanced experiments.

The difference in kinetic energies between fragment ions and precursor ions cannot be eliminated but can be minimized if the ions had nominally the same kinetic energies before entering the reflectron. After excitation and subsequent fragmentation, all ions could be reaccelerated to a kinetic energy much larger than the difference in kinetic energy between fragment ions and precursor ions. This method is used on the tandem TOF instrument design by Vestal marketed as the Applied Biosystems 4700 which incorporates high energy CID [38]. In this work, precursor ions are decelerated to a defined laboratory frame collision energy before entering the collision cell. After collisional excitation and subsequent fragmentation, all ions are then reaccelerated toward TOF2 with a short voltage pulse.

Ideally, the same experiments could be performed on the photodissociation tandem TOF instrument in our lab requiring on slight modification of the biased activation cell. Figure 56 shows the SIMION rendering of the differences in the two constructions of the biased activation region.

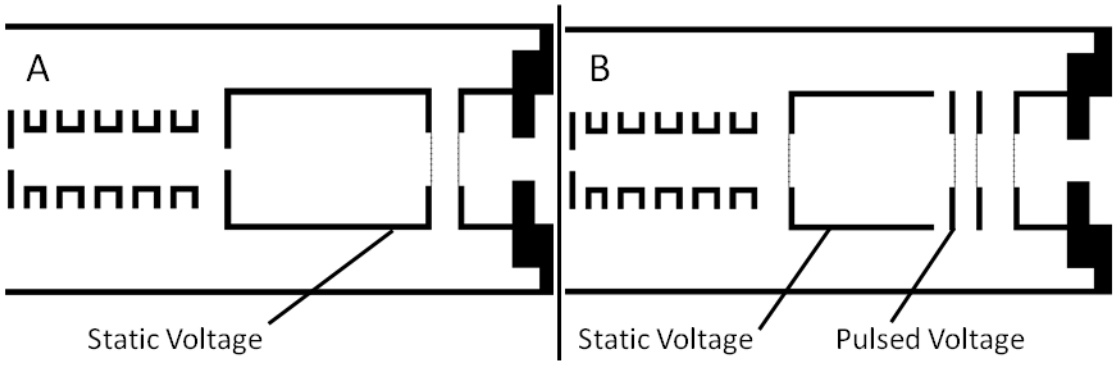

Figure 56: SIMION rendering of A) the biased activation cell with no pulse, and B) the biased activation cell with a pulsed source 2.

Initially, the pulsed electrode is held constant at the same potential as the biased activation cell. Precursor ions are first decelerated by the series of lenses to a much lower voltage than their initial kinetic energy. Precursor ions will drift across the field free activation region where they are irradiated with 193 nm photons. Remaining precursor ions and fragment ions will travel cross the grid held at the same potential as the field-free activation region at the same velocity but differing kinetic energies. After ions cross this region, a voltage pulse is applied accelerating all ions to nominally the same kinetic energy. The fragment ions and remaining precursor ions should penetrate to nominally the same position within the reflectron so long as the difference in kinetic energies between precursor and fragment ions is small relative to the pulsed accelerating potential of Source 2.

Precursor ion trajectories (1000 *m/z*; +1 charge) obtained via SIMION simulations of the modified biased activation cell with addition of Source 2 are shown in Figure 57.

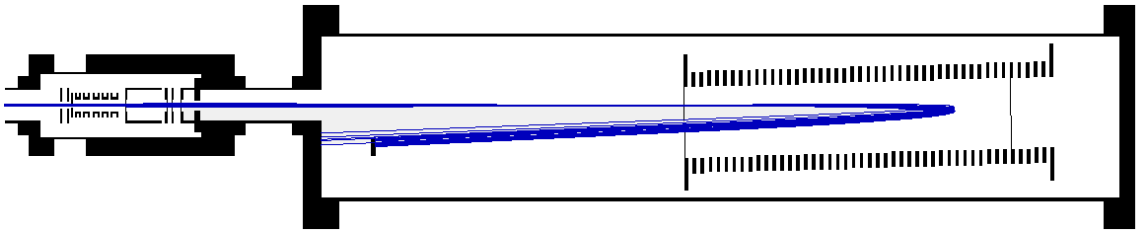

Figure 57: SIMION simulation showing precursor ion trajectories in a pulsed cell design. This utilizes the single stage reflectron originally constructed by Barbacci [116].

Of first notice it the fact that not all ions are collected at the detector which is not is not uncommon in some simulations; however, ion collection efficiencies remain high (>80%). What is not shown in the simulation here is the poor resolution (<500) of ions arriving at the detector which is caused by the large range of kinetic energies the ions receive based on their position once the Source 2 pulsed starts. This spread is easily seen in Figure 58.

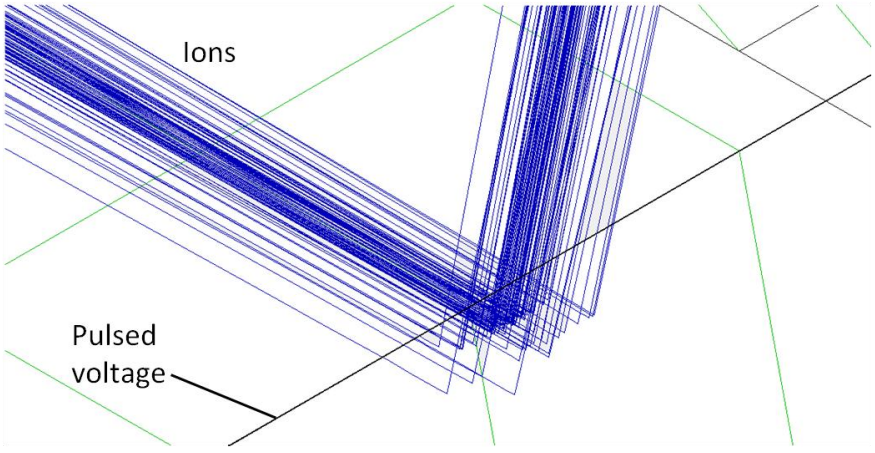

Figure 58: SIMION simulation showing the spatial spread of ions once the Source 2 voltage is applied. The pulse accelerates ions toward TOF 2 but a large spread in ion kinetic energies results owing to the ions positions when the pulse is applied.

The resolution observed at the detector can be improved by tuning the voltage on the reflectron to the optimum setting which increases the resolution to ~4000; however, the ions only traverse 50% of the total reflectron length making half of the reflectron essentially obsolete. Additionally, this turn around position does not allow for proper spatial focusing onto the detector, which can be alleviated by adjusting the reflectron angle. However, the voltages needed to create the reasonable resolutions are exceedingly high requiring potentials upwards of 25 kV which can be dangerous and require power supplies that are expensive and not readily available. Essentially, the current single-stage reflectron is too long to effectively focus ions properly.

Addition of Source 2 and a Dual-Stage Reflectron

Utilization of a dual-stage reflectron in the tandem photodissociation TOF instrument will improve resolution when using the pulsed source 2 within the biased activation region. As discussed earlier, the dual-stage reflectron also effectively focuses a broader range of kinetic energies over a shorter physical dimension. After thoroughly investigating the work and derivations completed by Wang *et al.* [51], we selected a design to investigate via SIMION simulations which meets the requirements discussed in their work.

A cross section of the SIMION rendering of the dual stage reflectron design is shown in Figure 59. The SIMION design consists of 13 electrodes with a thickness and spacing of 6 mm. The first stage of the reflectron, d_1, is defined by two wire mesh grids placed on the front face of the first electrode and the back face of the second electrode, a

distance of 18 mm. The second-stage consists of 9 electrodes and is also defined by two grids and the remaining electrodes provide a voltage drop to ground for the voltage applied to the second stage. The total length is 172 mm and the dimensions of the dual-stage reflectron satisfy the requirement of an ideal design according to the C-value defined by Wang [51].

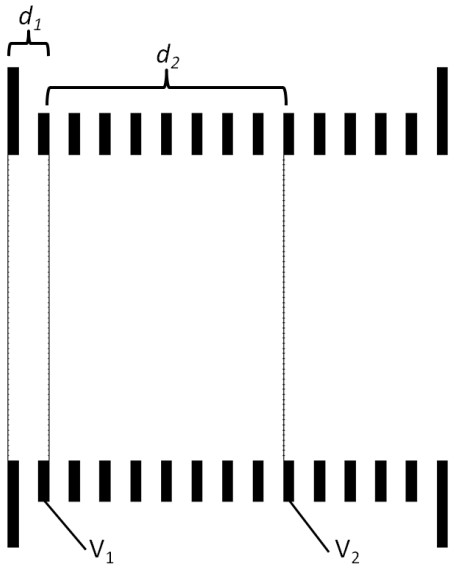

Figure 59: Cross section of a SIMION rendering of the dual-stage reflectron. V_1 and V_2 correspond to the voltages applied and first and second stages, respectively. Note that the large electrodes in the front and back are at ground potential.

The design here is of sharp contrast to the previous single-stage reflectron most notably in terms of length, 172 mm compared to 558 mm. The dual-stage reflectron has been implemented into the current TOF design to match the distances of L_1 and L_2. This should alleviate issues with changing the position ion beam image after reflection, which is critical to examining various ion timescales.

Initial ion trajectory simulations calculated via SIMION of the dual-stage reflectron are shown in Figure 60 with no voltage in the biased activation region.

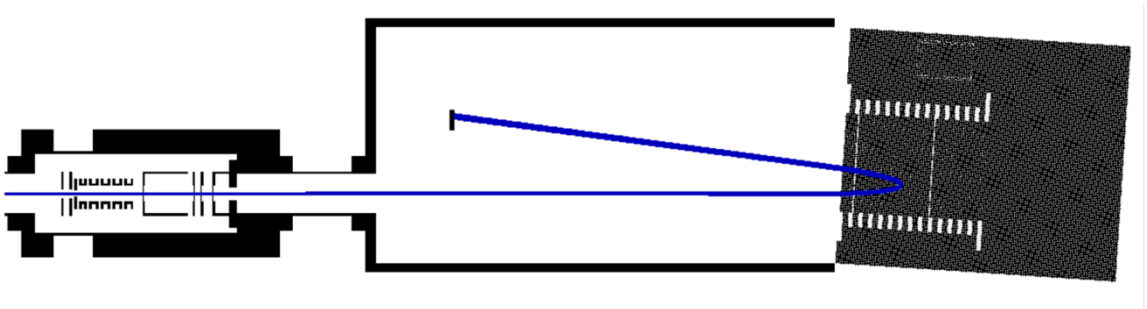

Figure 60: SIMION simulation showing the ion trajectories on the photodissociation TOF instrument with no voltage on the biased activation cell. Note that the dual-stage reflectron is distorted here owing to the angle of the reflectron in the simulation.

In order to accurately impart the beam onto the detector surface, the reflectron must be at a steeper angle (4 degrees) than the single-stage counterpart (1.5 degrees) as an effect of the lower penetration depth in the dual-stage design. This can create a decrease in the measurable resolution at the detector since the detector angle does not match the reflectron angle. To counter this, another simulation has been completed which partially corrects this angle discrepancy, but will not be shown here. Simulations from the design shown in Figure 60 provide a resolution of ~15000, comparable to similar experiments on the single stage reflectron. Additionally, the dual-stage reflectron is amenable to the PSD focusing experiments which require reflectron voltage tuning.

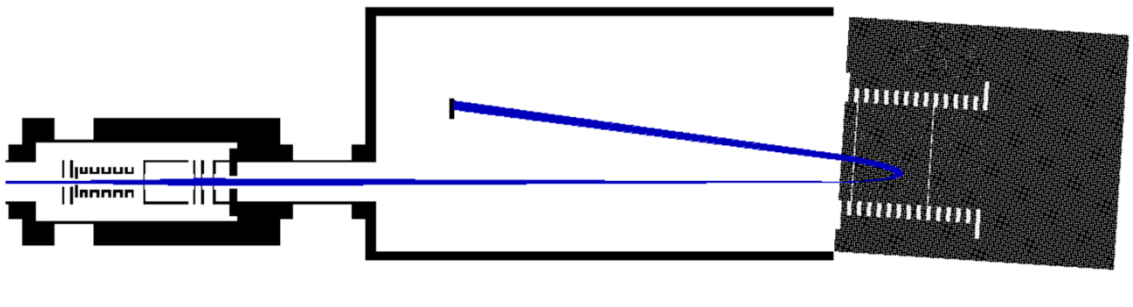

Figure 61: SIMION simulation showing the ion trajectories on the photodissociation TOF instrument with pulsed source 2 in the biased activation cell. Note that the dual-stage reflectron is distorted here owing to the angle of the reflectron in the simulation.

The SIMION simulations shown in Figure 61 utilize the pulse within Source 2 to reaccelerate ions toward the dual-stage reflectron. Initially the two simulations seem identical; however, the difference can be seen in the beam expanding in the biased activation cell region owing to the deceleration of ions from the source. The mass resolution approaches ~10,000 for routine simulations much higher than the previously reported value of ~3,000 for the single stage reflectron. This improvement is purely based on the improved resolving power of the dual-stage reflectron. The resolution of 10,000 can be further improved to values of 30,000 by accurately tuning the first stage of the reflectron by a few volts.

The reflectron also performs adequately for fragment ions formed within the biased activation cell. The SIMION simulations of these fragment ions formed within the biased activation cell and subsequently accelerated by source 2 visually appear quite similar to the precursor ion trajectories. Several fragment ions from the peptide

Bradykinin 1-8 (RPPGFSPF) were examined via SIMION and the performance results on these simulations are shown in Table 5.

Table 5: Results from SIMION simulations of several fragment ions of the peptide Bradykinin 1-8 (RPPGFSPF).

Species	m/z	TOF (μs)	Resolution (Δm/m)
$[M + H]^+$	904.47	63.371	28980
$b_7 - H_2O$	757.40	60.810	33460
y_7	748.37	60.645	26500
a_7	711.39	59.958	21870
d_6	598.35	57.740	29560
a_5	527.31	56.236	31480
a_3	323.22	51.229	20040
y_2	263.14	49.463	20220
b_2	254.16	49.183	21010
a_2	226.17	48.274	19150
$a_1 - NH_3$	112.09	43.796	16130
R	87.09	42.533	11350
P	70.07	41.564	10400

Notice the slight decrease in resolution when moving toward smaller *m/z* ratios which is an effect of the difference in kinetic energy between the precursor ion and the low m/z fragment ion. On previous experiments with no Source 2 pulse examining 'prompt' forming fragment ions, this kinetic energy difference resulted in fragment ion losses while here near 100% ion collection is attained.

In addition to the improved performance of the photodissociation tandem TOF instrumentation by the addition of Source 2 and a dual-stage reflectron, investigations of

varying fragmentation timescales are still possible. The PSD focusing experiments originally explored by Barbacci will still investigate fragmentation timescales of ~10-15 microseconds depending on the kinetic energy of ions received in the source. The experiments described above will investigate fragmentation timescales of ~3 μs, which is slightly longer than the previous experiments investigating 'prompt' forming fragment ions (~1 μs). The value of 3 μs can be reduced by increasing the velocity of ions through the biased activation cell while still utilizing Source 2. However, this will inevitably result in larger kinetic energy differences between precursor ions and fragment ions. As discussed previously the dual-stage reflectron will correct for a portion of this discrepancy; however, if the difference is large, low *m/z* fragment ions may be reflected in the first stage of the reflectron and therefore not be collected at the detector. To what extent this timescale can be investigated is not clear from simulations and will be explored in the initial experiments on this instrument.

CHAPTER VII

PERFORMANCE OF PHOTODISSOCIATION TIME-OF-FLIGHT INSTRUMENT & TIME-RESOLVED PHOTODISSOCIATION MASS SPECTROMETRY

Modification of tandem time-of-flight mass spectrometry instrumentation is often desirable when the goal is improved instrument performance with regards to several factors including sensitivity, resolution, fragment ion yields, and ion collection efficiencies. The implementation of a second source and dual-stage reflectron within our photodissociation tandem TOF instrument should provide improved sensitivity, resolution, and fragment ion collection efficiency while reducing the time necessary to perform a given experiment. Additionally, the modifications utilizing a second source will allow for investigation of various fragmentation timescales on the order of 1 - 10 microseconds. These experiments are similar to those performed previously in our research group examining 'prompt' dissociation fragment ions [114] and PSD focused photofragment ions [116, 195]. Herein, a comparison between the data obtained on the modified instrument and the previous data acquired before modifications will be undertaken. Furthermore, fragment ion spectra of varying fragmentation timescales will be investigated for a synthetic series of peptides to determine the effect of changing the basic residue. Firstly, the fragment ion calibration equations utilized by Barbacci and Morgan will be modified to account for the instrument modifications implemented.

Methods

Mass Spectrometry

The modified photodissociation instrument is a home-built MALDI TOF/TOF utilizing an off-axis dual-stage reflectron as the second stage. In order to sample various fragmentation timescales, various instrument parameters are altered to control the velocity of ions after photon absorption. In the first experiment which samples longer timescales (~10 microseconds), ions are accelerated with 15keV of energy in the source region; ions are transmitted via time ion selector, irradiated by 193-nm photons then continue to the dual-stage reflectron. The reflectron voltage is then turned to focus specific regions of the mass range onto the detector, because of the large difference in kinetic energy between precursor ions and fragment ions formed before entering the reflectron. The individual spectra are then stitched to generate a complete mass spectrum; a procedure that is similar to that originally performed by Barbacci utilizing a single-stage reflectron [116].

The 1 and 3 microsecond experiments are performed in a far different manner but have the capabilities of generating a complete mass spectrum from a single analysis. The 3 microsecond experiment accelerates ions to 8.5 keV within the source region. After transmission through the timed ion selector, precursor ions are decelerated by a series of tube lenses to approximately 1 keV of energy. After irradiation by 193 nm photons, remaining precursor ions and newly formed fragment ions drift across a gridded electrode (source 2) where a high voltage pulse of 15 keV accelerates these ions toward the detector. After this acceleration pulse, fragment ions and precursor ions have small

differences in kinetic energy and can therefore be collected at the detector using a single voltage in the dual-stage reflectron. The 1 microsecond experiment is nearly identical except that a larger initial acceleration pulse of 13keV and deceleration to 6 keV allows the ions to retain a larger amount of their initial kinetic energy, or velocity, and thus the time between irradiation by 193-nm photons and the reacceleration by Source 2 is decreased.

Peptides

All chemicals used in this study were purchased from Sigma-Aldrich (St. Louis, MO) unless otherwise noted. Peptides analyzed in this study include Angiotensin III, (RVYIHPF), Substance P (RPKPQQFFGLM-NH_2), Bradykinin clip 1-8 (RPPGFSPF), Fibrinopeptide A (ADSGEGDFLAEGGGVR), Glu-Fibrinopeptide B (EGVNDNEEGFFSAR), and Indolicidin (ILPWKWPWWPWRR-NH_2) (American Peptide, Sunnyvale, CA). Additionally, several synthetic peptides are used in this study including, GPPRGGP (GenScript, Piscataway, NJ), RVGVASG, KVGVASG, and HVGVASG previously synthesized in house. Each solid peptide was dissolved in water to yield a concentration of 1 mg/mL. Matrix solution was prepared by dissolving α-cyano-4-hydroxycinnamic acid in 50:50 acetonitrile:water to a concentration of 10 mg/mL with the addition of trifluoroacetic acid to generate 0.1% concentration with respect to the total volume of the matrix solution. Typically 1.0 μL of peptide solution was combined with 25 μL of the matrix solution and 1.0 μL of the mixture was spotted

onto the MALDI plate resulting in approximately 30 picomoles of peptide per spot and a matrix-to-analyte ratio of ~1000:1.

Derivation of Fragment Ion Calibration Equation (PSD focusing)

Barbacci originally developed the fragment ion calibration equation for the post source decay focusing method in order to covert the TOF of fragment ions to *m/z* for a given set of instrument parameters [116]. Recall that the PSD focusing method requires the reflectron voltage to be tuned in order to focus various mass to charge ratios at the detector. The calibration equation Barbacci developed is only valid for a single-stage reflectron thus an alternate equation will need to be derived. The TOF of any ion in the mass spectrometer is the sum of the time the ion spends in each region:

$$(15) \qquad TOF = t_{1stTOF} + t_{2ndTOF} + t_{reflectron} + t_{\mathrm{detector}}$$

For ions analyzed by the PSD method, the time spent in the first and second TOF is constant for precursor and fragment ions which will be termed *K1*.

The TOF of a fragment ion and a precursor ion differ in both the reflectron and detector regions. However, the time spent in the detector region has a root relationship with the ion mass and for simplicity will be ignored for the studies here. Equation 15 can then be reduced to equation 16:

$$(16) \qquad TOF = K1 + t_{reflectron}$$

For a single stage reflectron, $t_{reflectron}$ is simply twice the stopping time *i.e.* $t_{reflectron} = 2*v_{drift}/a_{reflectron}$. However, this equation is not valid for a dual stage reflectron as the acceleration applied by the reflectron is not constant.

The time the precursor ion spends in the reflectron is twice the sum of the time in the first stage and the turnaround time in the second stage:

$$(17) \qquad tp_{reflectron} = tp_{reflectron-1ststage} + tp_{reflectron-2ndstage}$$

The time the ion spends in the first stage is a function of the *m/z* of the precursor ion, the distance of the first stage (d_1), and the kinetic energy of the ion through this region. This kinetic energy varies depending on the electric field applied in the first stage. We will define the kinetic energy of the ion after the first stage of the reflectron as KE_{ion1}:

$$(18) \qquad KE_{ion1} = KE_{acceleration} - KE_{reflectron-1ststage}$$

As KE_{ion1} is the kinetic energy of the ion after the first stage, the average kinetic energy within the first stage is $0.5*KE_{ion1}$. The time spent in this region can then be determined by rearranging the kinetic energy equation:

$$(19) \qquad tp_{reflectron-1ststage} = \sqrt{\frac{m_{parent} \times d_1^{\,2}}{KE_{ion1}}}$$

The time the ion spends in the second stage more closely resembles the time in the reflectron of a single stage as defined by Barbacci: $t_{reflectron} = 2*v_{drift}/a_{reflectron}$. In the case here, the v_{drift} will actually be the velocity of the ion exiting the first stage of the reflectron, v_{ion1}.

$$(20) \qquad v_{ion1} = \sqrt{\frac{2 \times KE_{ion1}}{m_p}}$$

The acceleration of the second stage is defined by the *m/z* of the precursor ion, the distance of the second stage (d_2), and the kinetic energy difference between the first and second stage ($KE_{stage2} = KE_{ref2} - KE_{ref1}$).

$$(21) \qquad a_{ref-2ndstage} = \frac{KE_{stage2}}{m_p \times d_2}$$

As previously discussed, the time in the second stage of the reflectron is the twice the velocity of the ion entering the second stage divided by the acceleration of the second stage.

$$(22) \qquad tp_{reflectron-2ndstage} = 2 \times \frac{v_{ion1}}{a_{reflectron-2ndstage}} = \frac{m_p \times d_2}{KE_{stage2}} \sqrt{\frac{2 \times KE_{ion1}}{m_p}}$$

From equation 16 the total time in the reflectron can now be determined:

$$(23) \qquad tp_{reflectron} = tp_{ref-1ststage} + tp_{ref-2ndstage} = 2\left(\sqrt{\frac{m_p \times d_1^{\,2}}{KE_{ion1}}}\right) + 2\left(\frac{m_p \times d_2}{KE_{stage2}} \sqrt{\frac{2 \times KE_{ion1}}{m_p}}\right)$$

When applying the PSD focusing method to focus ions of varying *m/z* at the detector at differing reflectron potentials, $t_{reflectron}$ scales with the ratio of the mass of the fragment to the mass of the precursor and the PSD ratio. The PSD ratio is defined as the ratio of the lower reflectron potential to the higher reflectron potential:

$$(24) \qquad tf_{reflectron} = \frac{m_f}{m_p} \times \frac{1}{PSD} \times tp_{reflectron}$$

This equation can be substituted into equation 16 and solved to give the *m/z* of the fragment ion.

$$(25) \qquad TOF = K1 + \frac{m_f}{m_p} \times \frac{1}{PSD} \times tp_{reflectron}$$

$$(26) \qquad m_f = \frac{TOF - K1}{tp_{ref}} \times m_p \times PSD$$

Equation 25 can only be used if the parameters *K1* and $tp_{reflectron}$ can be determined either experimentally or empirically. Both *K1* and $tp_{reflectron}$ are functions of the total *TOF*. That is, both *K1* and $t_{reflectron}$ can be calculated by simply taking a fraction of the total TOF or *TOF = (aTOF) + (bTOF)* where $a + b = 1$. $t_{reflectron}$ can be calculated according to equation 23 which then can be used to determine *K1*. Practically, equation 25 is used to calibrate mass spectra for all PSD focusing experiments in this work. For a dual-stage reflectron, it can be estimated that the time spent outside the reflectron is roughly 2/3 the total flight time; therefore, to a first approximation, *K1* is 0.666 and $t_{reflectron}$ is 0.333.

Derivation of Fragment Ion Calibration Equation (Pulsed Cell)

The calibration equation used by Morgan [114] in his work investigating 'prompt' forming fragment ions is much more straightforward than the equation used by Barbacci. Since only a single reflectron potential is used, no calibration adjustments are necessary to account for the varying reflectron potentials. The calibration equation used by Morgan is also valid for the dual stage reflectron, however a detailed discussion of the equation is beneficial.

Precursor and photofragment ions formed within the biased activation cell have identical velocities and therefore have varying kinetic energies based on the fragment ion masses. This difference in kinetic energy can be expressed by equation 26:

$$(26) \qquad KE_{fragment} = e \times (V_0 - V_1) \times \frac{m_f}{m_p}$$

where e is the charge of an electron, V_1 is the potential applied to the source plate (accelerating voltage), V_2 is the potential applied to the biased activation cell, m_f is the mass of the fragment ion, and m_p is the mass of the precursor ion. After these ions exit the biased activation cell they are reaccelerated by the pulsed voltage, V_2, and have kinetic energies according to the equation 27.

$$KE_{fragment} = e \times (V_0 - V_1) \times \frac{m_f}{m_p} + eV_2 \qquad (27)$$

This equation can be arranged and solved for t after inputting the equation for kinetic energy, $KE = (1/2)mv^2$.

$$t = \frac{d}{\sqrt{2}} \sqrt{\frac{m_f}{e \times (V_0 - V_1)\left(\frac{m_f}{m_p}\right) + eV_2}} \qquad (28)$$

In more general terms the equation can be simplified to incorporate several variables as instrument constants and rearranged to solve for m_f.

$$t = a\sqrt{\frac{m_f}{bm_f + c}} + t_0 \qquad (29)$$

$$m_f = a \frac{\left(\frac{t - t_0}{a}\right)^2 \times c}{1 - \left(\frac{t - t_0}{a}\right)^2 \times b} \qquad (30)$$

The constants a and c are constant for a given set of instrument conditions while the constants b and t_0 are functions of the m/z of the precursor ion. Regression analysis

using SigmaPlot on known fragment ions can be used to determine the parameters *a*, *b*, *c* and t_0.

Improvement in Mass Range

Initial experiments utilizing Source 2 and the dual-stage reflectron examine the ability to generate quality mass spectra for a wide range of mass-to-charge ratios in a swift manner. 5 standard peptides (Angiotensin III, Substance P, Fibrinopeptide A, Glu-Fibrinopeptide B, and Indolicidin) ranging in mass from 900 to 1900 were studied. Previously the largest *m/z* ratio examined on this instrument was 1536.6 corresponding to Fibrinopeptide A, a spectrum that was obtained after an exceedingly large number of individual spectra were summed (~5000-10000).

Figure 62 contains the photofragment ion spectrum of Angiotensin III which shows an abundance of fragment ions with high signal-to-noise ratios and good resolution. A complete series of *a*-type fragment ions allow for the sequence to be easily confirmed. Previous results were capable of completely sequencing this peptide as well, but required the reflectron to be tuned to various voltages and stitching of the mass spectra to generate a complete spectrum. This procedure took a significantly longer amount of time (~60-90 minutes) compared to the data shown in Figure 62 which was acquired in 10 minutes.

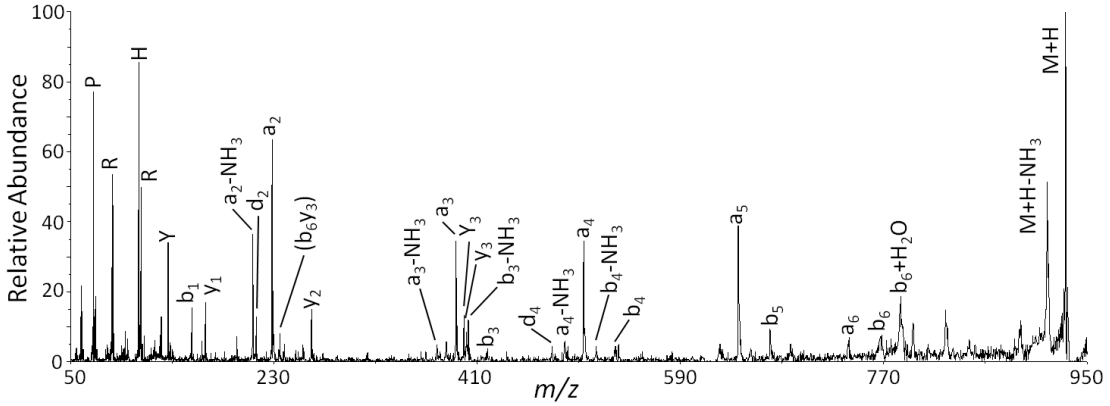

Figure 62: Photofragment ion spectrum of Angiotensin III (RVYIHPF).

A large number of *a*- and *d*-type fragment ions are generated in the photofragmentation of Substance P (Figure 63). Again the spectrum consists of a large number of high signal-to-noise peaks attributed to the excellent ion collection efficiency owing to the modifications of the instrument. While these two peptides do not extend the mass range originally achieved by the photodissociation tandem TOF instrument, they do serve as excellent models for comparison studies.

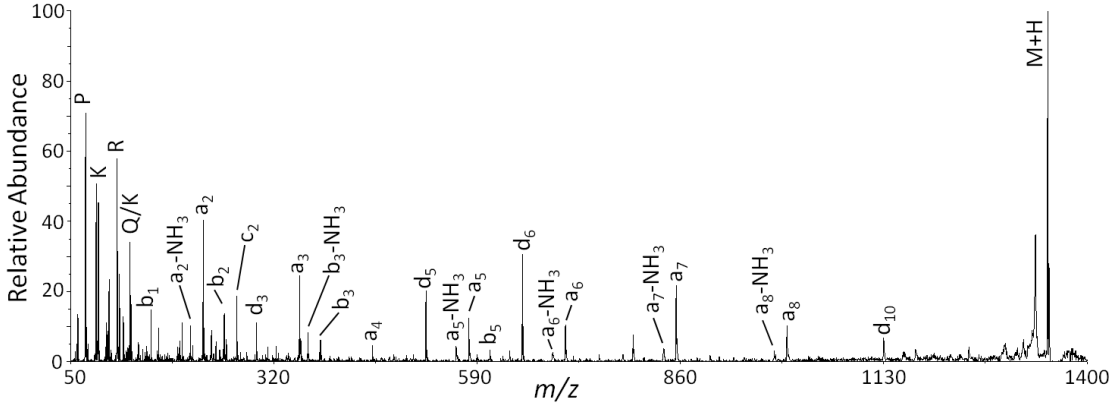

Figure 63: Photofragment ion spectrum of Substance P (RPKPQQFFGLM-NH_2).

Figure 64 shows a spectrum for Fibrinopeptide A, the largest peptide investigated before instrument modification. The photofragment ion spectrum of Fibrinopeptide A shows a large number of *x*- and *y*-type fragment ions along with several side chain cleavage fragment ions (*w*- and *v*-ions). This data is superior to previously generated data on this instrument as much lower noise levels are observed allowing for a higher confidence in peak assignment. The figure inset shows the large number of fragment ions that are generated and identified. The *x*-type fragment ions observed here are expected as these are typically generated in UV photodissociation experiments when there is a basic residue on the C-terminus. These ions are less common when using collisional methods where typically *y*-type fragment ions dominate.

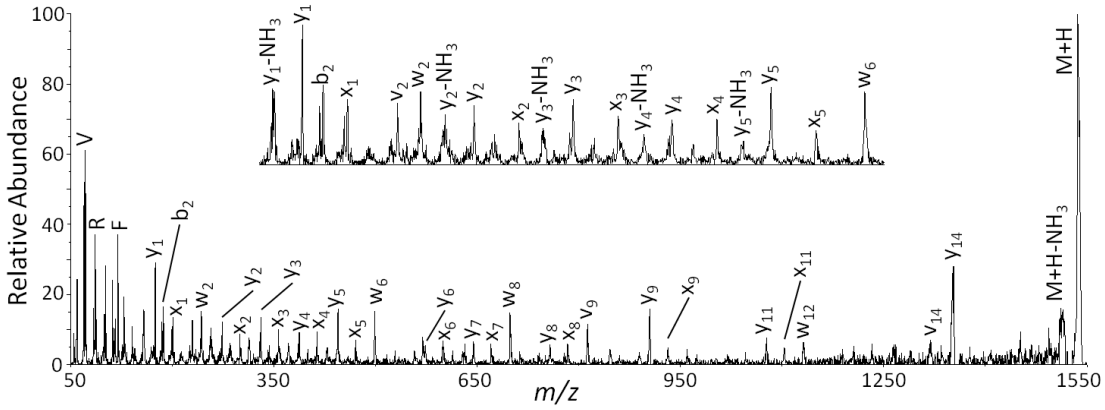

Figure 64: Photofragment ion spectrum of Fibrinopeptide A (ADSGEGDFLAEGGGVR).

The photofragment ion spectrum of Glu-Fibrinopeptide B (Figure 65) is quite similar to Fibrinopeptide A as the two peptides are both tryptic with similar mass-to-charge ratios. Again the majority of fragment ions are *x*- and *y*-type ions with additional *w*- and *v*-type side chain cleavage fragment ions as well. The inset highlighting the large number of identified fragment ions.

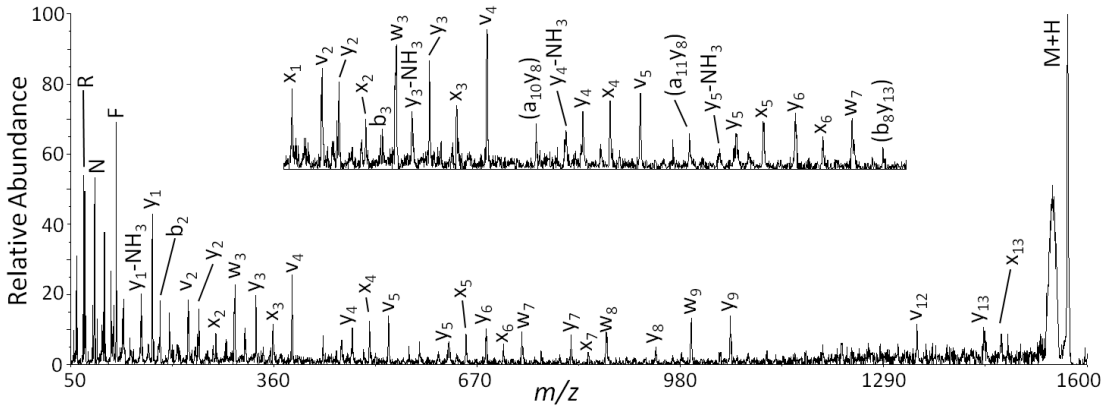

Figure 65: Photofragment ion spectrum of Glu-Fibrinopeptide B (EGVNDNEEGFFSAR).

Finally, the photofragment ion spectrum of Indolicidin, a peptide which is unique as it is composed primarily of tryptophan and proline residues is shown in Figure 66. A wide variety of fragment ions are observed in this spectrum including all possible types of C-terminal fragment ions (x_i, y_i, z_i, w_i, and v_i) and several internal fragment ions. This peptide extends the *m/z* range (1906.3) of this instrument and the data generated required only 10 minutes of data summation which is not excessive compared to other data acquired on this instrument before modification. The results indicate that the addition of

a second source and incorporation of a dual-stage reflectron have dramatically improved overall instrument performance with regards to signal-to-noise, mass range, and ion collection efficiency.

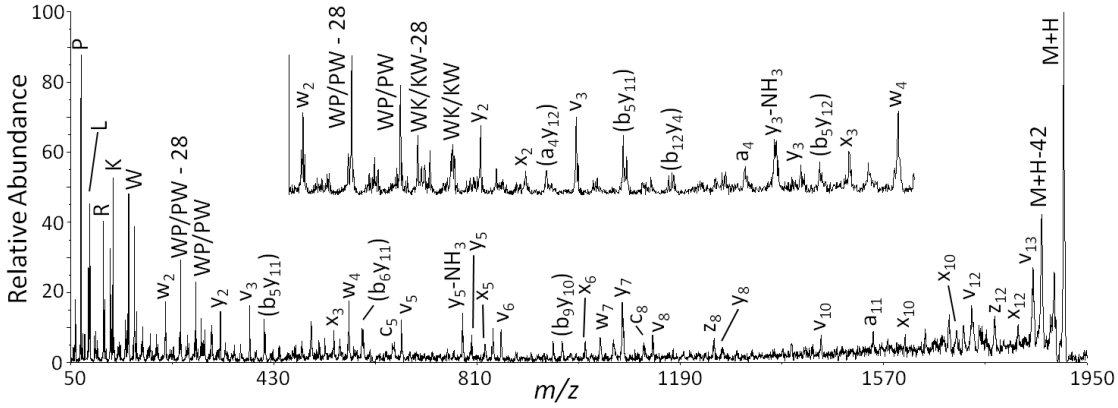

Figure 66: Photofragment ion spectrum of Indolicidin (ILPWKWPWWPWRR-NH_2).

Time-Resolved Photodissociation: Comparison

As mentioned in the previous chapter, the utilization of a second source after initial ion separation allows for various fragmentation timescales to be investigated. These timescales, or rates (*k(E)*) of fragment ion formation, are defined by the velocity of ions as they traverse the biased activation cell. In these studies, we utilized source 2 to examine fragmentation timescales of 1 microsecond ($k(E) \geq 1E10^6$) and 3 microseconds ($k(E) \geq 3.3E10^5$) and coupled these studies to the PSD focusing studies which examine timescales up to ~10 microseconds ($k(E) \geq 1E10^5$). The reacceleration of fast forming fragment ions and remaining precursor ions will provide a smaller

difference in kinetic energy between the two resulting in better ion collection through the reflectron at the detector.

Figure 67 shows the photofragment ion spectra at 3 different timescales: a) ~1 microsecond, b) ~3 microseconds, and c) ~10 microseconds of the peptide Angiotensin III. The data shown in panels A and C are quite similar to that shown in Chapter 2 for Angiotensin III with respect to the identities of the fragment ions observed; however, lower noise levels are observed in these spectra while additional fragment ions are detected as well. These two results are likely an effect of the improved fragment ion collection efficiencies owing to the addition of the second source and dual-stage reflectron. The fragmentation timescale of 3 microseconds shown in panel B has similarities to both other timescales, a result that is expected. Since 1 microsecond samples 'prompt' forming fragment ions and 10 microseconds samples longer decaying precursor ions, one would expect that a timescale of 3 microseconds would bridge the differences observed in the 1 and 10 microsecond timescales. The appearance of fragment ions not observed in Figure 67A occurs in Figure 67B with a further increase in relative abundance occurring in 67C. It should be noted, the ammonia loss fragment ions are not observed in panel 67A but are detected in 67B with a further increase in relative abundance in 67C. It can be hypothesized that the ammonia loss fragment ions are occurring from a series of consecutive reactions. If initial loss of ammonia by the excited precursor ion does not remove a significant amount of the precursor ion's internal energy, an additional fragmentation may occur resulting in ammonia loss

fragment ions. Examination of other peptides should confirm or contradict this hypothesis.

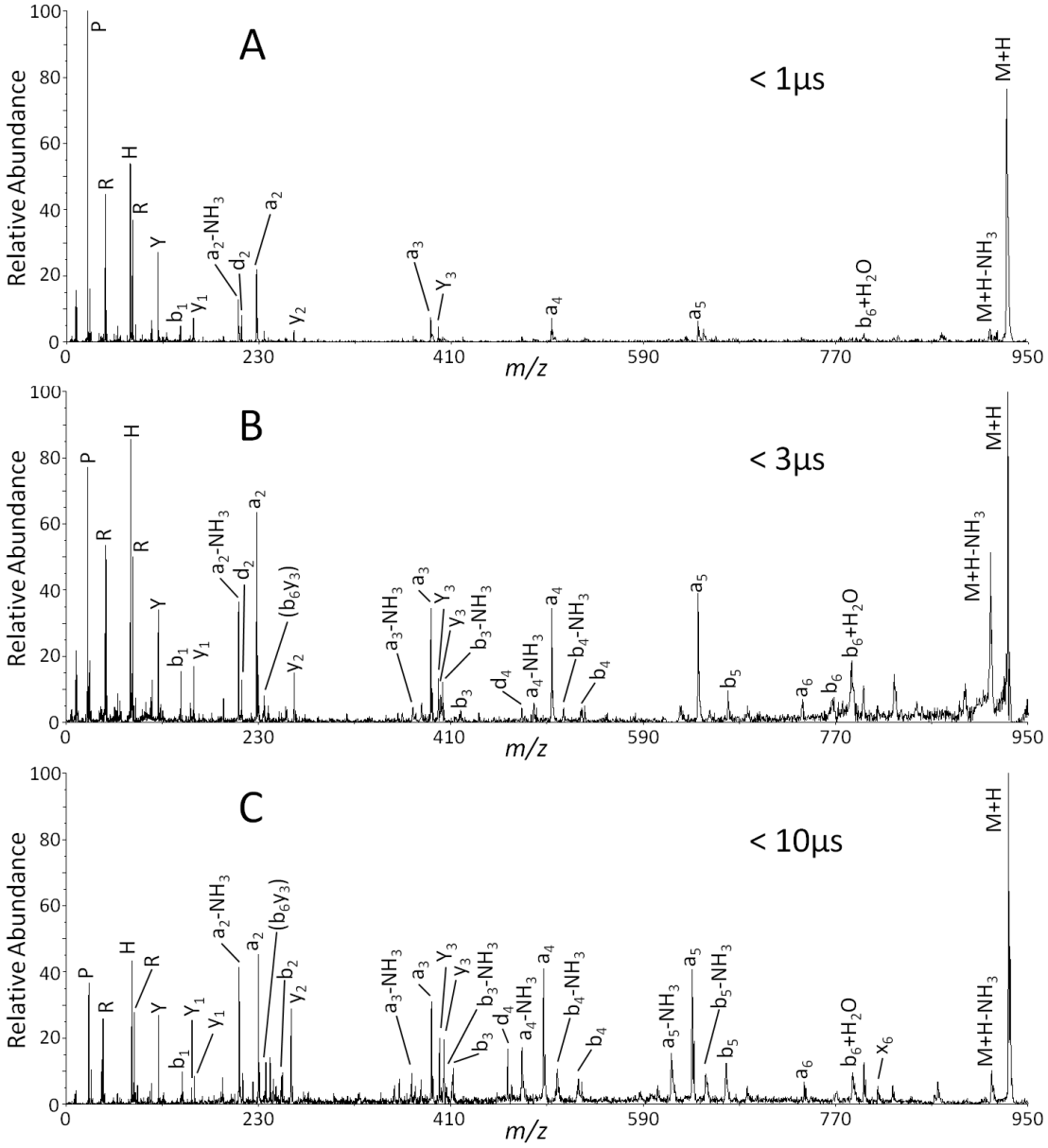

Figure 67: Photofragment ion spectrum of Angiotensin III (RVYIHPF) examining the timescales of A) 1 µs, B) 3 µs, and C) 10 µs.

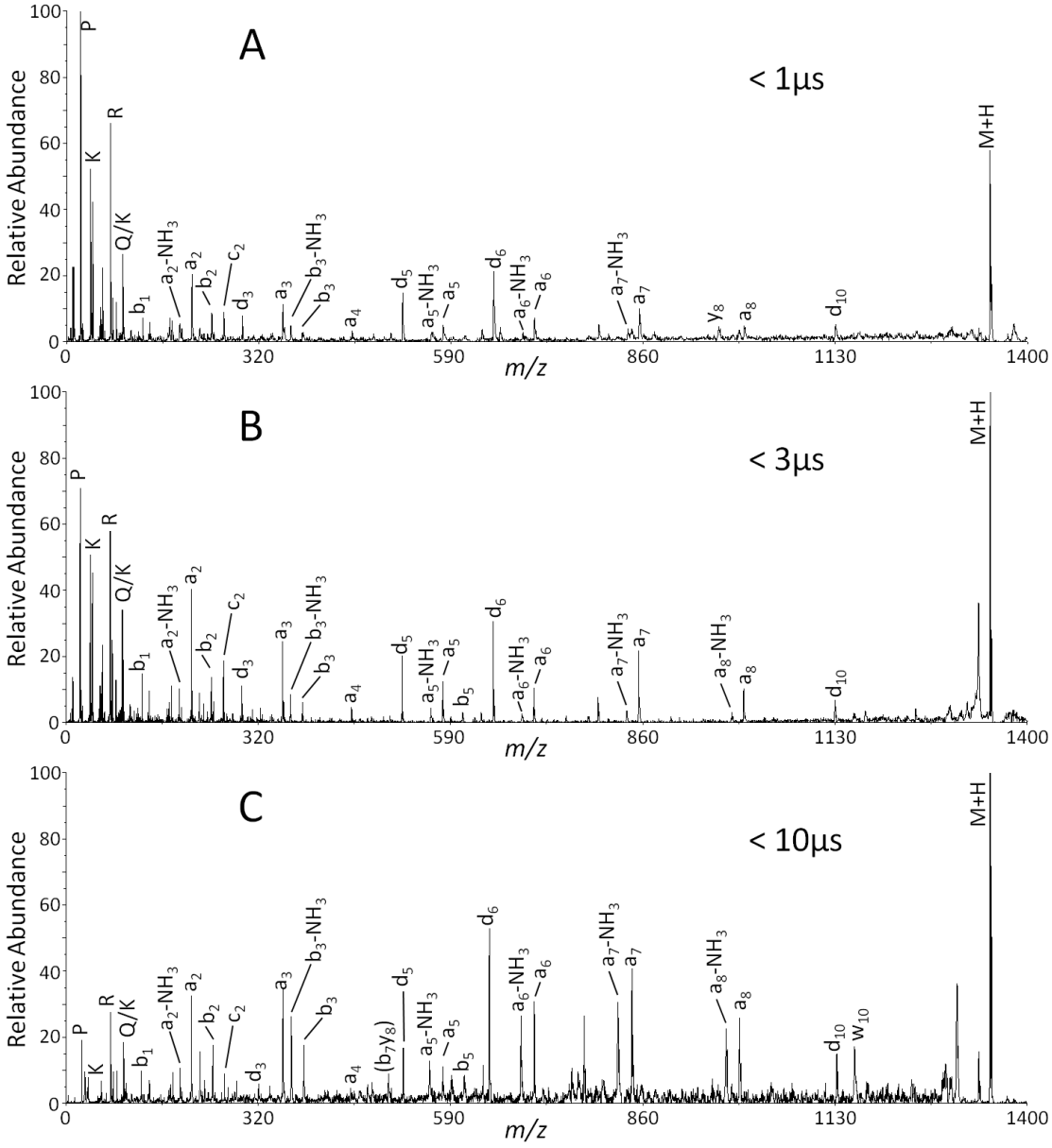

Figure 68: Photofragment ion spectrum of Substance P (RPKPQQFFGLM-NH_2) examining the timescales of A) 1 μs, B) 3 μs, and C) 10 μs.

The fragment ion spectra of Substance P (Figure 68) also show dramatic improvement in signal-to-noise ratio and total number of fragment ions observed compared to previously obtained data (Chapter 2). Primarily *a*- and *d*-type fragment

ions are observed in Figure 68A with a few ammonia loss fragment ions and *b*-type fragment ions. When transitioning to longer timescales, most of the fragment ions increase in relative abundance owing to the longer time allotted for formation. However, the appearance of several *b*-type fragment ions and internal fragment ions occurs at 3 microseconds (Figure 68B) with continued increases in relative abundance at 10 microseconds (Figure 68C). A particular fragment ion to note is the w_{10} fragment which only appears in Figure 68C. One would not expect a *w*-type fragment ion to occur at a proline residue as it requires internal cleavage of the pyrrolidine ring; however, this type of cleavage has been observed by others, [196] If this cleavage were to be observed, one would expect this fragment ion to only be observed at longer timescales based on the requirement for two cleavages. Additionally, ammonia loss fragment ions show increased relative abundance when transitioning to longer timescales indicating that these ions may form by consecutive reactions in agreement with results from Angiotensin III.

Figure 69 shows fragment ion spectra of Bradykinin clip 1-8 at various timescales and again the data here show vast improvement over previous results with regards to signal-to-noise ratio and total number of fragment ions observed. Again, an increased number of internal fragments are observed when examining longer timescales. The observation of a high number of internal fragments could be attributed to the presence of proline residues within the peptide sequence. As previously discussed in Chapter 3, peptides are known to have a propensity to fragment at proline residues [75].

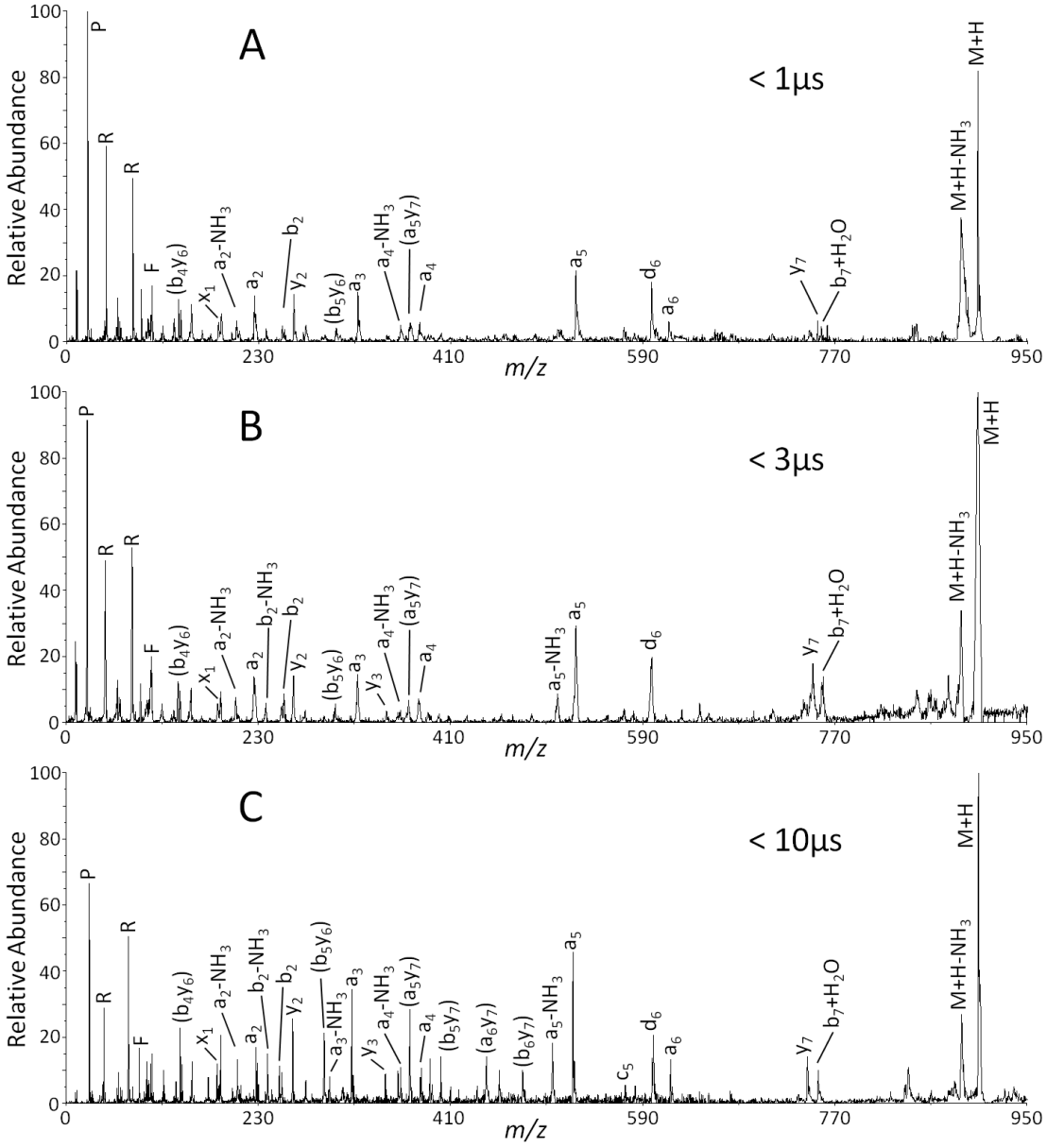

Figure 69: Photofragment ion spectrum of Bradykinin clip 1-8 (RPPGFSPF) examining the timescales of A) 1 µs, B) 3 µs, and C) 10 µs.

If an initial fragmentation pathway of Bradykinin clip 1-8 does not release enough of the precursor ion's internal energy, there may be sufficient energy remaining to induce a second fragmentation which may be directed by the proline residue. The

data in Figure 69C agrees with this assessment as all of the internal fragments observed occur at y_6 or y_7, both at proline residues. Additionally, the presence of these fragment ions in higher relative abundance within the 10 microsecond timescales further argues these are occurring through a series of consecutive reactions.

The fragment ion spectra of the peptides Angiotensin III, Substance P, and Bradykinin clip 1-8 all show significant reduction in noise level, improvement if signal-to-noise ratio, and fragment ion collection efficiency. Furthermore the incorporation of the 3 microsecond timescale experiment allows more time for fragment ions to form while still collecting the entire mass spectrum at a single reflectron voltage.

Time-Resolved Photodissociation

The ability to investigate various fragmentation timescales provides a method to study the fragmentation rates of various molecules, specifically peptides and proteins. Although determination of exact rates of fragment ion formation is quite difficult, relative comparisons between various experiments which sample specific fragmentation rates can help to identify consecutive reactions occurring the gas phase or mobilization of a proton from a basic residue. These possibilities will be investigated utilizing the instrumentation to sample specific fragmentation timescales.

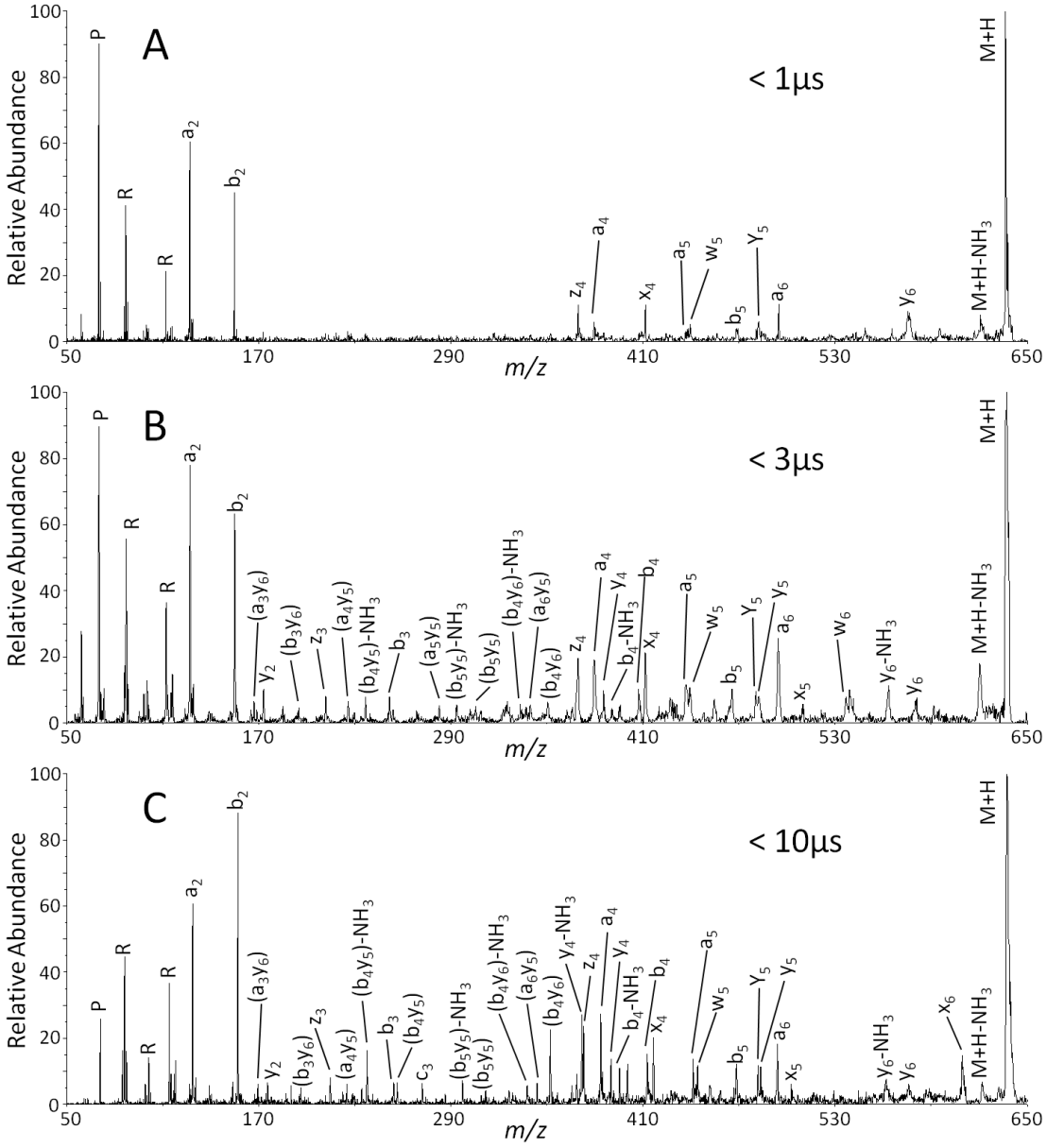

Figure 70: Photofragment ion spectrum of GPPRGGP examining the timescales of A) 1 µs, B) 3 µs, and C) 10 µs.

Figure 70 shows the photofragment ion spectrum of the peptide GPPRGGP at varying fragmentation timescales. In the spectrum examining the 1 microsecond fragmentation timescale (Figure 70A), a large portion of the spectrum (b_2 to z_4) consists of no fragment ions. One might notice that the majority all fragment ions detected that are larger contain the arginine residue beginning with the z_4 fragment ion. If the ionizing proton is located on the basic side chain of the arginine, it would seem logical to observe only fragment ions which contain said arginine. The fragments which appear that do not contain the arginine residue consist of immonium ions, and the a_2 and b_2 fragment ions which occur between two proline residues. The propensity to fragment at proline residues may cause the peptide to fragment at this site. Interestingly, the fragment ion spectra of this peptide at longer timescales reveal a large number of identified peaks ions in the previously bare section of the spectrum (Figure 70B and 70C). A total of 13 (B) and 14 (C) identified fragment ions are observed in this portion of spectrum. A number of the identified peaks ions are internal cleavages ions which contain the basic arginine residue. Since these fragment ions involve two backbone cleavages, they likely form at a much slower rate than traditional backbone fragments. Several backbone fragment ions are also observed in this region which could result from mobilization of the ionizing proton from the arginine side chain inducing fragmentation at these sites as hypothesized by the mobile proton model [82, 85, 86].

A series of peptides that could provide insight into the mobilization of the ionizing proton from a basic residue include the sequence XVGVASG where X is either H, K, or R. Although each amino acid is basic, the arginine has a significantly higher

proton affinity (251 kcal/mol) than the histidine (236 kcal/mol) or lysine (238 kcal/mol) [74] which could generate significant differences in the fragment ion spectra.

Figure 71 shows the photofragment ion spectrum of KVGVASG at various fragmentation timescales. Each timescale examined shows abundant *a*- and *b*-type fragment ions as expected owing to the presence of the basic lysine side chain at the N-terminus. Figure 71A is by far the simplest of the three spectra containing almost exclusively a_i and b_i fragment ions. When shifting to the longer timescales examined in Figures 71B & 71C, an increase in the total number of peaks is observed with the majority of these peaks being internal and ammonia loss fragment ions. Interestingly, the y_2, y_3, and y_6 fragment ions increase in relative abundance with each timescale increase demonstrating that these ions are favored when examining slow rates of fragment ion formation. This indicates that at longer timescales the ionizing proton may no longer be located on the basic lysine side chain, but instead has migrated to other sites within the peptide.

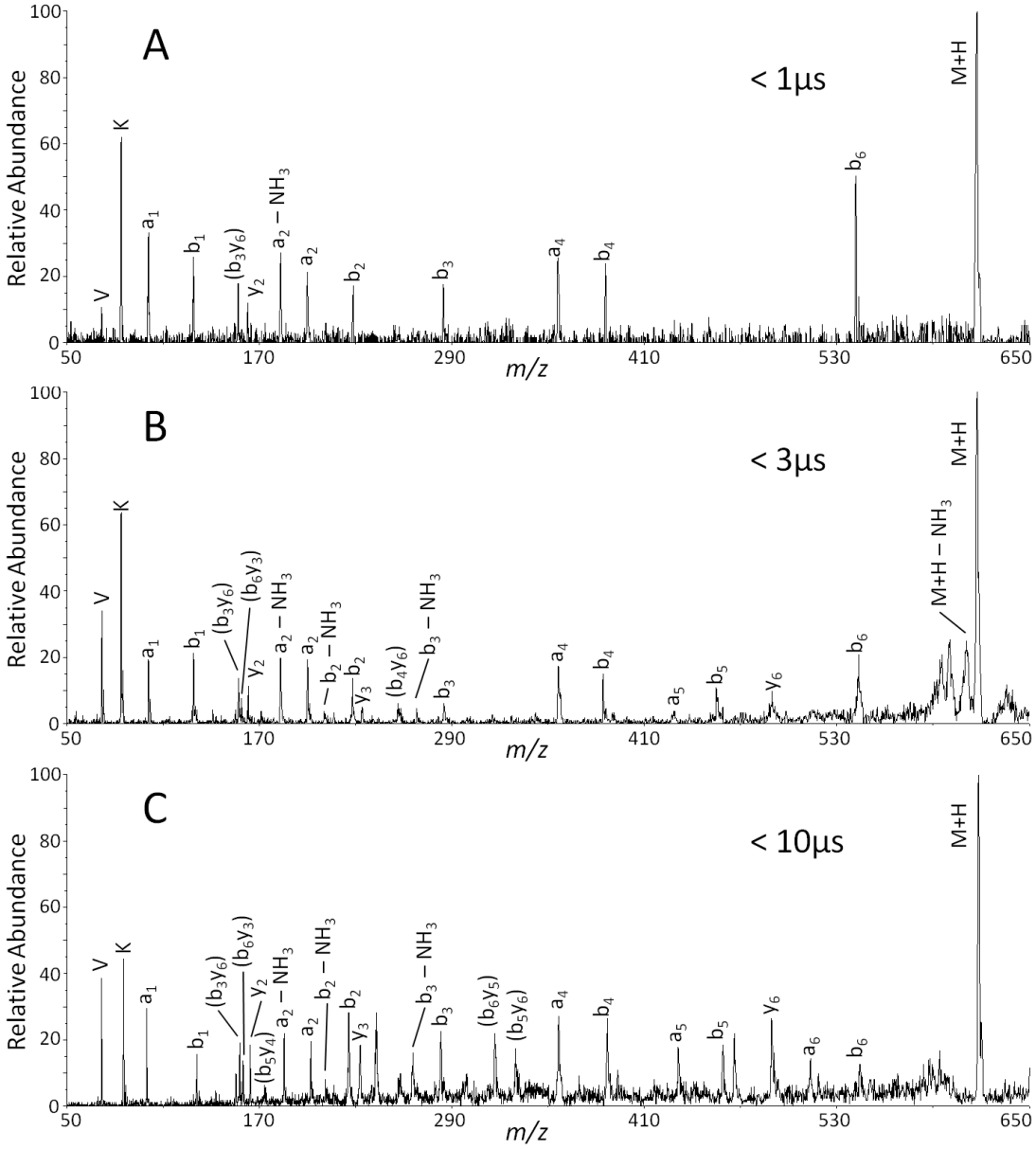

Figure 71: Photofragment ion spectrum of KVGVASG examining the timescales of A) 1 µs, B) 3 µs, and C) 10 µs.

It is important to mention that for these spectra, high intensity fragment ion peaks are observed when examining only the metastable fragment ions. Abundant *b*-type fragment ions are observed in these experiments and cannot be eliminated from the mass

spectrum by altering the MALDI parameters (matrix-to-analyte ratio, laser fluence, etc.). However, when examining the photofragment ion spectrum, these peaks increase in relative abundance indicating these fragments form both as metastable ions and as photofragment ions.

The photofragment ion spectra of HVGVASG (Figure 72) are similar in several aspects to that of KVGVASG. Abundant *a*- and *b*-type fragment ions dominate the spectra on all timescales, with the one microsecond timescale (Figure 72A), again being the simplest containing almost exclusively *a*- and *b*-type fragment ions. Internal and a few *y*-type fragment ions appear in the spectra examining the longer timescales (Figure 72B & 72C); however, no ammonia loss fragment ions are observed for this peptide as ammonia loss is more commonly observed from lysine and arginine containing peptides but to a lesser extent with histidine. The lack of ammonia loss fragment ions is truly the only major difference in the spectra of KVGVASG and HVGVASG. Even though the side chains of lysine and histidine have differing structures, they have similar proton affinities indicating that the fragmentation patterns here are governed more so by the proton affinities rather than structural differences. Since the two peptides have identical sequences other than the N-terminal residue, any amino acid influences on the fragmentation pattern should be negligible. Similar to the lysine containing peptides, there is a large contribution to the fragment ion intensities from metastable ions for HVGVASG; however, photofragment ion intensities are slightly larger resulting in a positive ion intensity for these spectra.

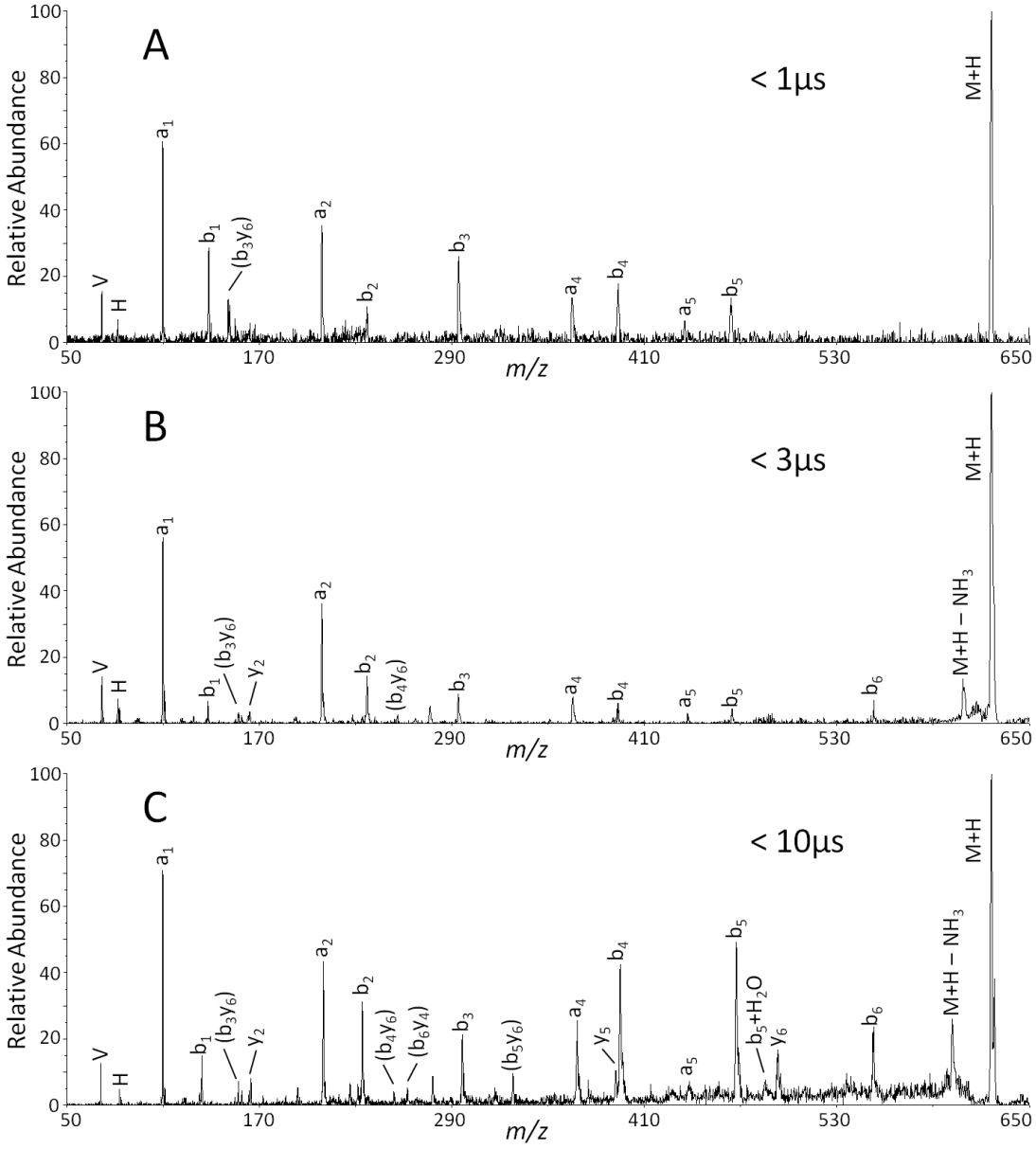

Figure 72: Photofragment ion spectrum of HVGVASG examining the timescales of A) 1 µs, B) 3 µs, and C) 10 µs.

The spectra of RVGVASG at various timescales show several distinct differences from the preceding spectra containing lysine or histidine (Figure 73). In the 1 microsecond spectrum shown in Figure 73A, no *b*-type fragment ions are observed

while *a*-type fragment ions remain abundant. Additionally, three *d*-type fragment ions are observed that were not detected in the fragmentation of KVGVASG or HVGVASG. These side chain cleavage ions are typically observed in higher energy fragmentation processes, but since the dissociation process for all the peptides investigated here are the same, the arginine must be playing a role in *d*-type ion formation. Furthermore, a few internal fragment ions are observed in Figure 73A in greater relative abundance than those observed for the lysine and histidine containing peptides.

The changes in fragment ion spectra shown in Figures 73B and 73C of RVGVASG when transitioning from the short 1 microsecond timescales are similar to the changes that are observed with the lysine and histidine; more total fragment ions are observed specifically internal and ammonia loss fragment ions. Interestingly, only low intensity *b*-type fragment ions appear in the spectra examining longer timescales. It appears as though *a*-type fragment ions are the preferred fragmentation channel for the arginine containing peptide. It is likely that *b*-type fragment ions form through an oxazolone pathway which involves a mobile proton[123]. The high proton affinity of the guanidine group may sequester the proton inhibiting fragmentation by this pathway. The lysine and histidine side chains do not sequester the proton as strongly as the arginine resulting in proton migration from those sites favoring *b*-type ion formation along the peptide backbone for these peptides.

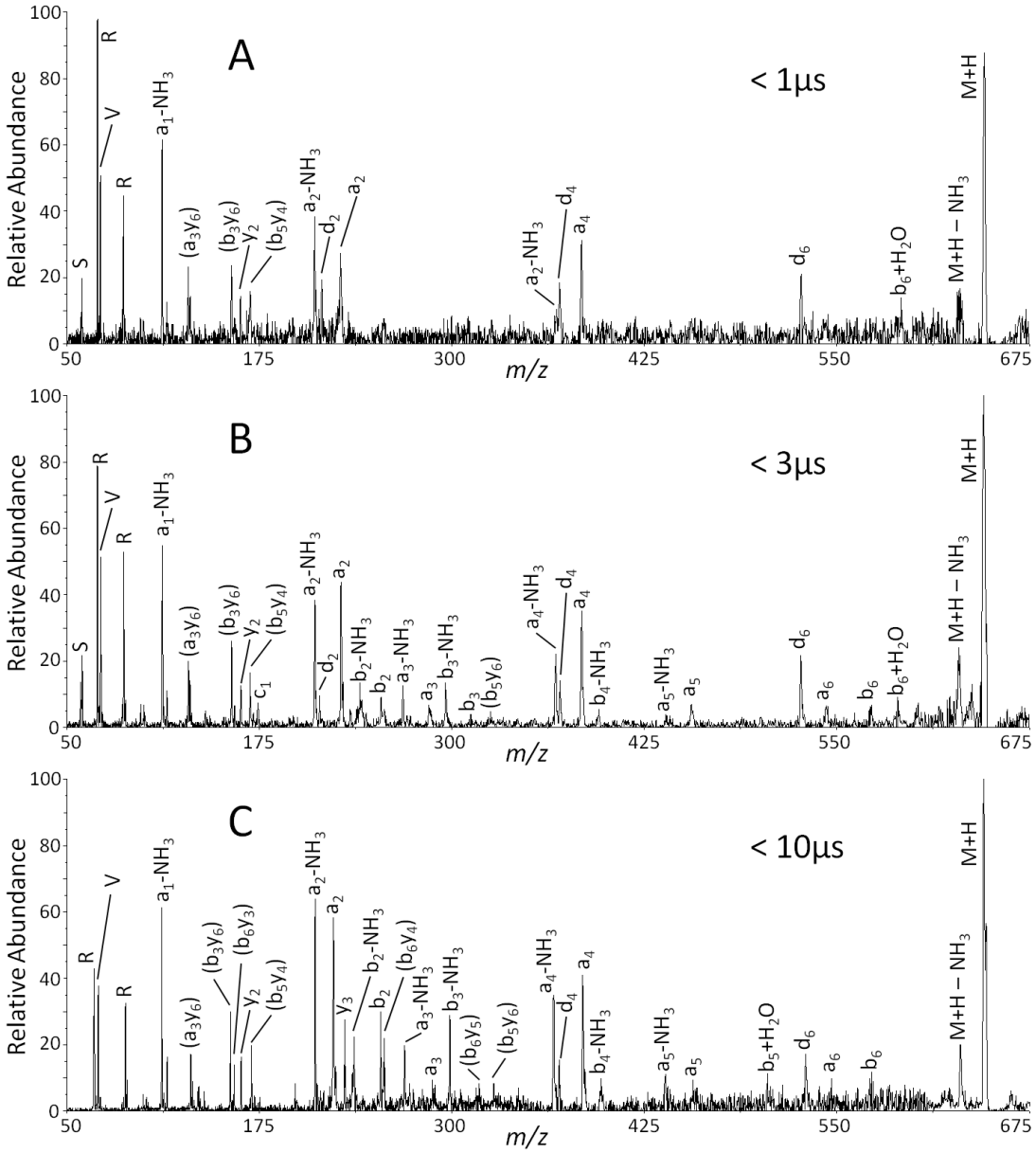

Figure 73: Photofragment ion spectrum of RVGVASG examining the timescales of A) 1 µs, B) 3 µs, and C) 10 µs.

Conclusions

High-quality photofragment ion spectra can quickly and accurately be obtained with the current instrumentation design. The instrument modifications performed here allow for increased fragment ion collection efficiencies and improved mass range. Additionally, the ability to investigate various fragmentation timescales provides insights into the factors affecting peptide fragmentation. The studies here reveal that arginine containing peptides can sequester a proton and favor formation of *a*-type fragment ions when the arginine is located at the N-terminus. Alternatively, lysine and histidine containing peptides favor formation of *b*-type fragment ions which may result from the proton migrating away from the basic side chain inducing *b*-type ion formation along the backbone. Longer fragmentation timescales can produce a larger total number of fragment ions which can be desirable for achieving complete sequence coverage; however, an excessive amount of peaks in the spectrum may complicate data interpretation.

CHAPTER VIII

CONCLUSIONS AND FUTURE DIRECTIONS

Exploring all the factors affecting peptide fragmentation is impractical to pursue; however, an extensive study on the effects of metal cationization and fragmentation timescale has yielded interesting results. Collision induced dissociation tandem time-of-flight mass spectrometry of $[M + H]^+$ and $[M + Cu]^+$ ions yield abundant N-terminal fragment ions owing to the strong binding affinity by an N-terminal basic residue. While the proton prefers the most basic site *i*.e. a basic side chain or the N-terminus, the copper cation is likely coordinated by multiple ligands with the basic amino acid side chain having the strongest interaction with the cation. The results regarding $[M + Cu]^+$ ions are further supported by theoretical calculations which reveal a shared coordination by the guanidine group of the arginine side chain and C-terminal carboxylic acid further stabilized by hydrogen bonding along the backbone. The fragmentation patterns of alkali metal cationized peptides show distinct differences from the copper and proton adducted counterparts. No preference for N- or C-terminal fragment ions is observed, likely an effect of the non-specific binding of these metal ions.

Further investigation of the collision induced dissociation of alkali metal cationized peptides revealed abundant *x*-type fragment ions. Although these ions have consistently appeared in the literature investigating fragmentation of alkali metal cationized peptides, a mechanism for the formation of these ions has not been proposed.

In the studies here, *x*-ions dominate at valine residues and are also abundant C-terminal to peptides containing an N-terminal arginine. It is likely that these ions are preferentially formed owing to the non-specific binding of alkali metal cations by the backbone carbonyls, amide nitrogens and the side chains of the amino acids.

Alternative dissociation methods to the traditional collision induced dissociation can provide insights into the fragmentation of peptides. Vacuum ultraviolet 193-nm photofragmentation affords the ability to define the amount of energy input into the precursor ion as well as allowing for the determination of the exact time at which energy excitation occurs. Knowledge of this photon absorption provides the opportunity to investigate varying fragmentation timescales based on the instrument design. Initial results indicated that for peptides containing an N-terminal arginine, *a*- and *d*-type fragment ions are prompt forming with rates of formation greater than or equal to $1*10^6$ s^{-1} while ammonia loss and *b*-type fragment ions have rates of formation between $1*10^5$ s^{-1} and $1*10^6$ s^{-1}.

Investigation of proline containing peptides by collision induced dissociation and 193-nm photodissociation yield *Y*- and *w*-type fragment ions if a basic residue is located on the C-terminus whereas a_i and $a_i + 1$ fragment ions form when a basic residue is located on the N-terminus. The presence of the $a_i + 1$ ions indicates that these fragment ions form through homolytic cleavage of the backbone amide bond followed by electron rearrangement. It is probable that the formation of the *Y*- and *w*-type fragment ions occur by a similar process involving homolytic cleavage of the backbone amide bond. Typically CID and 193-nm photodissociation show several differences in the fragment

ion spectra; however, the propensity of peptides to fragment at or near proline residues precludes this feature resulting in nearly identical fragment ion spectra here. Furthermore, the presence of proline also appears to hinder any differences that may appear in the fragment ion spectra when investigating varying fragmentation timescales.

The modifications of the existing instrumentation, including the addition of a second source and a dual-stage reflectron, provide improved performance of the 193-nm photodissociation tandem TOF instrument with regards to fragment ion collection efficiency and mass range. The addition of a second source for reacceleration of fragment ions and precursor ions to nominally the same kinetic energy allows for faster acquisition of mass spectra. High quality mass spectra are obtained over a range of mass-to-charge ratios from 617.2 (KVGVASG) to 1906.1 (Indolicidin). The modifications implemented also allow the ability to investigate a series of fragmentation timescales extending the previous capabilities of the instrumentation.

Possible future directions for this project could include the investigation of various fragmentation timescales of metal cationized peptides. An ionizing proton can be sequestered on a basic side chain or could be located at countless other sites within a peptide whereas metal cations are more likely to be coordinated by multiple ligands as a result of the non-specific binding by a single site. Determining the preferred binding sites may provide insights into the coordination of metal cations occurring in biological processes. Absorption of a 193-nm photon provides a fast deposition of energy and by sampling the prompt fragmentation channels (1 and 3 microseconds) it could be possible to avoid rearrangement of the coordinated metal cation. Utilizing collisional methods to

investigate sodium binding sites may lead to rearranged coordination of the sodium ion through the slow ion heating by multiple collisions. Similar experiments could have utility for determining site-specific H/D exchange products. CID has limitations for such studies owing to H/D scrambling prior to dissociation, while ECD/ETD transfer large amounts of energy and favor rapid dissociation. That is, the ion lifetimes are short relative to the rate of scrambling. UV photodissociation experiments sampling short ion lifetimes may also circumvent the possibility of scrambling.

Further instrumentation modifications could also seek to improve the experimental capabilities. While the current setup provides excellent resolution (~2500) and sensitivity, it is possible that the dual-stage reflectron and detector are not perfectly aligned. The best way to optimize the two would be to incorporate a multi-anode detector. By properly placing the anodes parallel to one another, the current at each anode can be measured to determine if the ion cloud is being efficiently imparted onto the detector. This will help to optimize the current instrumentation, while switching to a "pie-shaped" multi anode detector will increase the signal-to-noise ratio by summing the individual anodes to generate improved ion spectra.

REFERENCES

[1] F.W. McLafferty, Advances in Mass Spectrometry, John Wiley & Sons Ltd., New York, 1985.

[2] F.W. McLafferty, F. Turacek, Interpretation of Mass Spectra, 4th ed., University Science Books, Sausalito, CA, 1993.

[3] T.D. Märk, Electron Impact Ionization, Springer-Verlag, Vienna, 1985.

[4] M.S.B. Munson, F.H. Field, Chemical Ionization Mass Spectrometry I. General Introduction, Journal of the American Chemical Society, 88; 1966; 2621-2630.

[5] J.A. Syage, M.D. Evans, Photoionization Mass Spectrometry - A Powerful New Tool for Drug Discovery, Spectroscopy, 16; 2001; 14-18.

[6] H.R. Morris, M. Panico, M. Barber, R.S. Bordoli, R.D. Sedgwick, A. Tyler, Fast Atom Bombardment - A New Mass-Spectrometric Method for Peptide Sequence Analysis, Biochemical and Biophysical Research Communications, 101; 1981; 623-631.

[7] J.B. Fenn, M. Mann, C.K. Meng, S.F. Wong, C.M. Whitehouse, Electrospray Ionization for Mass Spectrometry of Large Biomolecules, Science, 246; 1989; 64-71.

[8] M. Karas, F. Hillenkamp, Laser Desorption Ionization of Proteins with Molecular Masses Exceeding 10000 Daltons, Analytical Chemistry, 60; 1988; 2299-2301.

[9] J. Zeleny, The Electrical Discharge from Liquid Points, and a Hydrostatic Method of Measuring the Electric Intensity at Their Surfaces, Physical Review, 3; 1914; 69-91.

[10] S. Chapman, Carrier Mobility Spectra of Spray Electrified Liquids, Physical Review, 52; 1937; 0184-0190.

[11] M. Dole, L.L. Mack, R.L. Hines, Molecular Beams of Macroions, Journal of Chemical Physics, 49; 1968; 2240-2249.

[12] N.B. Cech, C.G. Enke, Practical Implications of Some Recent Studies in Electrospray Ionization Fundamentals, Mass Spectrometry Reviews, 20; 2001; 362-387.

[13] K.L. Busch, R.G. Cooks, Mass Spectrometry of Large, Fragile, and Involatile Molecules, Science, 218; 1982; 247-254.

[14] K.W. Tanaka, Hiroaki; Ido, Yutaka; Akita, Saroshi; Yoshida, Yoshikazu; Yoshida, Tamio, Protein and Polymer Analyses up to m/z 100000 by Laser Ionization Time-of-Flight Mass Spectrometry, Rapid Communications in Mass Spectrometry, 2; 1988; 151-153.

[15] R. Knochenmuss, Ion Formation Mechanisms in UV-MALDI, Analyst, 131; 2006; 966-986.

[16] B.H. Wang, K. Dreisewerd, U. Bahr, M. Karas, F. Hillenkamp, Gas-Phase Cationization and Protonation of Neutrals Generated by Matrix-Assisted Laser Desorption Ionization, Journal of the American Society for Mass Spectrometry, 4; 1993; 393-398.

[17] A.J. Dempster, Further Experiments on the Mass Analysis of the Chemical Elements, Proceedings of the American Philosophical Society, 75; 1935; 755.

[18] A.O. Nier, T.R. Roberts, The Determination of Atomic Mass Doublets by Means of a Mass Spectrometer, Physical Review, 81; 1951; 507-510.

[19] J.J. Thomson, Rays of Positive Electricity, Proceedings of the Royal Society of London Series a-Containing Papers of a Mathematical and Physical Character, 89; 1913; 1-20.

[20] W.E. Stephens, A Pulsed Mass Spectrometer with Time Dispersion, Physical Review, 69; 1946; 691-691.

[21] W.R. Paul, H.P.; von Zahn,U., Ein neues Massenspektrometer ohne Magnetfeld, Naturforsch, 8; 1953; 448.

[22] R.E. March, An Introduction to Quadrupole Ion Trap Mass Spectrometry, Journal of Mass Spectrometry, 32; 1997; 351-369.

[23] A.G. Marshall, C.L. Hendrickson, G.S. Jackson, Fourier Transform Ion Cyclotron Resonance Mass Spectrometry: A Primer, Mass Spectrometry Reviews, 17; 1998; 1-35.

[24] T. Matsuo, High-Performance Sector Mass Spectrometers - Past and Present, Mass Spectrometry Reviews, 8; 1989; 203-236.

[25] R.E.T. March, John F. J., Quadrupole Ion Trap Mass Spectrometry, John Wiley and Sons, Inc., New York, 2005.

[26] J.D. Morrison, Personal Reminiscences of 40 years in Mass Spectrometry in Australia, Organic Mass Spectrometry, 26; 1991; 183-194.

[27] R.A. Yost, C.G. Enke, Selected Ion Fragmentation with a Tandem Quadrupole Mass Spectrometer, Journal of the American Chemical Society, 100; 1978; 2274-2275.

[28] I.V. Chernushevich, A.V. Loboda, B.A. Thomson, An Introduction to Quadrupole-Time-of-Flight Mass Spectrometry, Journal of Mass Spectrometry, 36; 2001; 849-865.

[29] J.A. Hipple, H. Sommer, H.A. Thomas, A Precise Method of Determining the Faraday by Magnetic Resonance, Physical Review, 76; 1949; 1877-1878.

[30] C.S. Hsu, C.L. Hendrickson, R.P. Rodgers, A.M. McKenna, A.G. Marshall, Petroleomics: Advanced Molecular Probe for Petroleum Heavy Ends, Journal of Mass Spectrometry, 46; 2011; 337-343.

[31] B. Bogdanov, R.D. Smith, Proteomics by FTICR Mass Spectrometry: Top Down and Bottom Up, Mass Spectrometry Reviews, 24; 2005; 168-200.

[32] D.A. Church, Storage-Ring Ion Trap from Linear Quadrupole Radio-Frequency Mass Filter, Journal of Applied Physics, 40; 1969; 3127-3134.

[33] D.J. Douglas, A.J. Frank, D.M. Mao, Linear Ion Traps in Mass Spectrometry, Mass Spectrometry Reviews, 24; 2005; 1-29.

[34] Q.Z. Hu, R.J. Noll, H.Y. Li, A. Makarov, M. Hardman, R.G. Cooks, The Orbitrap: A New Mass Spectrometer, Journal of Mass Spectrometry, 40; 2005; 430-443.

[35] A. Makarov, Electrostatic Axially Harmonic Orbital Trapping: A High-Performance Technique of Mass Analysis, Analytical Chemistry, 72; 2000; 1156-1162.

[36] M. Guilhaus, Principles and Instrumentation in Time-of-Flight Mass Spectrometry - Physical and Instrumental Concepts, Journal of Mass Spectrometry, 30; 1995; 1519-1532.

[37] A.E. Cameron, D.F. Eggers, An Ion Velocitron, Review of Scientific Instruments, 19; 1948; 605-607.

[38] K.F. Medzihradszky, J.M. Campbell, M.A. Baldwin, A.M. Falick, P. Juhasz, M.L. Vestal, A.L. Burlingame, The Characteristics of Peptide Collision-Induced Dissociation Using a High-Performance MALDI-TOF/TOF Tandem Mass Spectrometer, Analytical Chemistry, 72; 2000; 552-558.

[39] M. Vestal, P. Juhasz, Resolution and Mass Accuracy in Matrix-Assisted Laser Desorption Ionization Time-of-Flight, Journal of the American Society for Mass Spectrometry, 9; 1998; 892-911.

[40] M.L. Vestal, Modern MALDI Time-of-Flight Mass Spectrometry, Journal of Mass Spectrometry, 44; 2009; 303-317.

[41] C. Weickhardt, F. Moritz, J. Grotemeyer, Time-of-Flight Mass Spectrometry: State-of-the-Art in Chemical Analysis and Molecular Science, Mass Spectrometry Reviews, 15; 1996; 139-162.

[42] R.J. Cotter, Time-of-Flight Mass Spectrometry, American Chemical Society, Washington, DC, 1994.

[43] W.C. Wiley, I.H. McLaren, Time-of-Flight Mass Spectrometer with Improved Resolution, Review of Scientific Instruments, 26; 1955; 1150-1157.

[44] U. Bahr, J. StahlZeng, E. Gleitsmann, M. Karas, Delayed Extraction Time-of-Flight MALDI Mass Spectrometry of Proteins Above 25,000 Da, Journal of Mass Spectrometry, 32; 1997; 1111-1116.

[45] R.S. Brown, J.J. Lennon, Mass Resolution Improvement by Incorporation of Pulsed Ion Extraction Source in a Matrix Assisted Laser Desorption/Ionization Time-of-Flight Mass Spectrometer, Analytical Chemistry, 67; 1995; 1998-2003.

[46] D.C. Barbacci, R.D. Edmondson, D.H. Russell, Evaluation of the Variables That Affect Resolution in Delayed Extraction MALDI-TOF, International Journal of Mass Spectrometry, 165; 1997; 221-235.

[47] M.L. Vestal, P. Juhasz, S.A. Martin, Delayed Extraction Matrix-Assisted Laser Desorption Time-of-Flight Mass Spectrometry, Rapid Communications in Mass Spectrometry, 9; 1995; 1044-1050.

[48] B.A. Mamyrin, V.I. Karataev, D.V. Shmikk, V.A. Zagulin, Mass-Reflectron: A New Non-Magnetic Time-of-Flight High-Resolution Mass Spectrometer, Zhurnal Eksperimentalnoi Teor. Fiz., 64; 1973; 82-89.

[49] K.G. Standing, R. Beavis, G. Bolbach, W. Ens, F. Lafortune, D. Main, B. Schueler, X. Tang, J.B. Westmore, Secondary Ion Time-of-Flight Mass Spectrometers and Data Systems, Analytical Instrumentation, 16; 1987; 173-189.

[50] X. Tang, R. Beavis, W. Ens, F. Lafortune, B. Schueler, K.G. Standing, A Secondary Ion Time-of-Flight Mass Spectrometer with an Ion Mirror, International Journal of Mass Spectrometry and Ion Processes, 85; 1988; 43-67.

[51] T.I. Wang, C.W. Chu, H.M. Hung, G.S. Kuo, C.C. Han, Design Parameters of Dual-Stage Reflectrons, Review of Scientific Instruments, 65; 1994; 1585-1589.

[52] M. Lewin, M. Guilhaus, J. Wildgoose, J. Hoyes, B. Bateman, Ion Dispersion Near Parallel Wire Grids in Orthogonal Acceleration Time-of-Flight Mass Spectrometry: Predicting the Effect of the Approach Angle on Resolution, Rapid Communications in Mass Spectrometry, 16; 2002; 609-615.

[53] J.L. Wiza, Microchannel Plate Detectors, Nuclear Instruments & Methods, 162; 1979; 587-601.

[54] L.S. Kassel, Studies in Homogeneous Gas Reactions II Introduction of Quantum Theory, Journal of Physical Chemistry, 32; 1928; 1065-1079.

[55] O.K. Rice, H.C. Ramsperger, Theories of Unimolecular Gas Reactions at Low Pressures II, Journal of the American Chemical Society, 50; 1928; 617-620.

[56] H.M. Rosenstock, M.B. Wallenstein, A.L. Wahrhaftig, H. Eyring, Absolute Rate Theory for Isolated Systems and the Mass Spectra of Polyatomic Molecules, Proceedings of the National Academy of Sciences of the United States of America, 38; 1952; 667-678.

[57] Y.J. Hu, B. Hadas, M. Davidovitz, B. Balta, C. Lifshitz, Does IVR Take Place Prior to Peptide Ion Dissociation?, Journal of Physical Chemistry A, 107; 2003; 6507-6514.

[58] L.L. Griffin, D.J. McAdoo, The Effect of Ion Size on Rate of Dissociation - RRKM Calculations on Model Large Polypeptide Ions, Journal of the American Society for Mass Spectrometry, 4; 1993; 11-15.

[59] R.A. Marcus, Lifetimes of Active Molecules 1, Journal of Chemical Physics, 20; 1952; 352-354.

[60] J.I. Steinfeld, J.S.H. Francisco, William L., Chemical Kinetics and Dynamics, Prentice Hall, Upple Saddle River, NJ, 1999.

[61] K. Biemann, S.A. Martin, Mass Spectrometric Determination of the Amino Acid Sequence of Peptides and Proteins, Mass Spectrometry Reviews, 6; 1987; 1-75.

[62] R. Aebersold, M. Mann, Mass Spectrometry-Based Proteomics, Nature, 422; 2003; 198-207.

[63] I.C. Guerrera, O. Kleiner, Application of Mass Spectrometry in Proteomics, Biosci. Rep., 25; 2005; 71-93.

[64] N.L. Anderson, N.G. Anderson, Proteome and Proteomics: New Technologies, New Concepts, and New Words, Electrophoresis, 19; 1998; 1853-1861.

[65] T. Wehr, Top-Down Versus Bottom-Up Approaches in Proteomics, Liquid Chromatography/ Gas Chromatography North America, 24; 2006; 1004-1010.

[66] N.L. Kelleher, Top-Down Proteomics, Analytical Chemistry, 76; 2004; 196A-203A.

[67] R. Aebersold, D.R. Goodlett, Mass Spectrometry in Proteomics, Chemical Reviews, 101; 2001; 269-295.

[68] G.E. Reid, S.A. McLuckey, 'Top Down' Protein Characterization via Tandem Mass Spectrometry, Journal of Mass Spectrometry, 37; 2002; 663-675.

[69] P. Roepstorff, J. Fohlman, Proposal for a Common Nomenclature for Sequence Ions in Mass Spectra of Peptides, Biomedical Mass Spectrometry, 11; 1984; 601-601.

[70] R.S. Johnson, S.A. Martin, K. Biemann, J.T. Stults, J.T. Watson, Novel Fragmenatation Process of Peptides by Collision-Induced Decomposition in a Tandem Mass Spectrometer - Differentiation of Leucine and Isoleucine, Analytical Chemistry, 59; 1987; 2621-2625.

[71] K. Vekey, Internal Energy Effects in Mass Spectrometry, Journal of Mass Spectrometry, 31; 1996; 445-463.

[72] M.E. Gimon-Kinsel, G.R. Kinsel, R.D. Edmondson, D.H. Russell, Photodissociation of High-Molecular Weight Peptides and Proteins in a 2-Stage Linear Time-of-Flight Mass Spectrometer, Journal of the American Society for Mass Spectrometry, 6; 1995; 578-587.

[73] S.H. Yoon, M.S. Kim, Development of a Time-Resolved-Method for Photodissociation Mechanistic Study of Protonated Peptides: Use of a Voltage-Floated Cell in a Tandem Time-of-Flight Mass Spectrometer, Journal of the American Society for Mass Spectrometry, 18; 2007; 1729-1739.

[74] E.P.L. Hunter, S.G. Lias, Evaluated Gas Phase Basicities and Proton Affinities of Molecules: An Update, Journal of Physical and Chemical Reference Data, 27; 1998; 413-656.

[75] L.A. Breci, D.L. Tabb, J.R. Yates, V.H. Wysocki, Cleavage N-terminal to Proline: Analysis of a Database of Peptide Tandem Mass Spectra, Analytical Chemistry, 75; 2003; 1963-1971.

[76] Y.Y. Huang, J.M. Triscari, L. Pasa-Tolic, G.A. Anderson, M.S. Lipton, R.D. Smith, V.H. Wysocki, Dissociation Behavior of Doubly-Charged Tryptic Peptides: Correlation of Gas-Phase Cleavage Abundance with Ramachandran Plots, Journal of the American Chemical Society, 126; 2004; 3034-3035.

[77] Y.Y. Huang, J.M. Triscari, G.C. Tseng, L. Pasa-Tolic, M.S. Lipton, R.D. Smith, V.H. Wysocki, Statistical Characterization of the Charge State and Residue Dependence of Low-Energy CID Peptide Dissociation Patterns, Analytical Chemistry, 77; 2005; 5800-5813.

[78] I.A. Papayannopoulos, The Interpretation of Collision-Induced Dissociation Tandem Mass Spectra of Peptides, Mass Spectrometry Reviews, 14; 1995; 49-73.

[79] C. Bleiholder, S. Suhai, A.G. Harrison, B. Paizs, Towards Understanding the Tandem Mass Spectra of Protonated Oligopeptides. 2: The Proline Effect in Collision-Induced Dissociation of Protonated Ala-Ala-Xxx-Pro-Ala (Xxx = Ala, Ser, Leu, Val, Phe, and Trp), Journal of the American Society for Mass Spectrometry, 22; 2011; 1032-1039.

[80] A.G. Harrison, A.B. Young, Fragmentation Reactions of Deprotonated Peptides Containing Proline. The Proline Effect, Journal of Mass Spectrometry, 40; 2005; 1173-1186.

[81] S. Hayakawa, M. Hashimoto, H. Matsubara, F. Turecek, Dissecting the Proline Effect: Dissociations of Proline Radicals Formed by Electron Transfer to Protonated pro-gly and gly-pro Dipeptides in the Gas Phase, Journal of the American Chemical Society, 129; 2007; 7936-7949.

[82] G. Tsaprailis, H. Nair, A. Somogyi, V.H. Wysocki, W.Q. Zhong, J.H. Futrell, S.G. Summerfield, S.J. Gaskell, Influence of Secondary Structure on the Fragmentation of Protonated Peptides, Journal of the American Chemical Society, 121; 1999; 5142-5154.

[83] S.M.L. Zucker, Sunyoung; Webber, Nathaniel; Valentine, Stephen J.; Reilly, James P.; Clemmer, David E., An Ion Mobility/Ion Trap/Photodissociation Instrument for Characterization of Ion Structure, Journal of the American Society for Mass Spectrometry, 22; 2011; 1477-1485.

[84] L.X. Chen, Q. Shao, Y.Q. Gao, D.H. Russell, Molecular Dynamics and Ion Mobility Spectrometry Study of Model beta-Hairpin Peptide, Trpzip1, Journal of Physical Chemistry A, 115; 2011; 4427-4435.

[85] V.H. Wysocki, G. Tsaprailis, L.L. Smith, L.A. Breci, Special Feature: Commentary - Mobile and Localized Protons: a Framework for Understanding Peptide Dissociation, Journal of Mass Spectrometry, 35; 2000; 1399-1406.

[86] A.R. Dongre, J.L. Jones, A. Somogyi, V.H. Wysocki, Influence of Peptide Composition, Gas-Phase Basicity, and Chemical Modification on Fragmentation Efficiency: Evidence for the Mobile Proton Model, Journal of the American Chemical Society, 118; 1996; 8365-8374.

[87] C.F. Cheng, E. Pittenauer, M.L. Gross, Charge-Remote Fragmentations are Energy-Dependent Processes, Journal of the American Society for Mass Spectrometry, 9; 1998; 840-844.

[88] C.F. Cheng, M.L. Gross, Applications and Mechanisms of Charge-Remote Fragmentation, Mass Spectrometry Reviews, 19; 2000; 398-420.

[89] J.M. Wells, J.L. Stephenson, S.A. McLuckey, Charge Dependence of Protonated Insulin Decompositions, International Journal of Mass Spectrometry, 203; 2000; A1-A9.

[90] J. Zaia, K. Biemann, Comparison of Charged Derivatives for High-Energy Collision-Induced Dissociation Tandem Mass Spectrometry, Journal of the American Society for Mass Spectrometry, 6; 1995; 428-436.

[91] R.P. Grese, R.L. Cerny, M.L. Gross, Metal-Ion Peptide Interactions in the Gas-Phase - A Tandem Mass-Spectrometry Study of Alkali-Metal Cationized Peptides, Journal of the American Chemical Society, 111; 1989; 2835-2842.

[92] L.M. Teesch, J. Adams, Intrinsic Interactions Between Alkaline-Earth Metal Ions and Peptides - A Gas-Phase Study, Journal of the American Chemical Society, 112; 1990; 4110-4120.

[93] L.M. Teesch, J. Adams, Fragmentations of Gas-Phase Complexes Between Alkali-Metal Ions and Peptides - Metal-Ion Binding to Carbonyl Oxygens and Other Neutral Functional Groups, Journal of the American Chemical Society, 113; 1991; 812-820.

[94] L.M. Teesch, R.C. Orlando, J. Adams, Location of Alkali-Metal Ion in Gas-Phase Peptide Complexes, Journal of the American Chemical Society, 113; 1991; 3668-3675.

[95] L.X. Chen, Y.Q. Gao, D.H. Russell, How Alkali Metal Ion Binding Alters the Conformation Preferences of Gramicidin A: A Molecular Dynamics and Ion Mobility Study, Journal of Physical Chemistry A, 116; 2012; 689-696.

[96] P. Wang, G. Ohanessian, C. Wesdemiotis, The Sodium Ion Affinities of Asparagine, Glutamine, Histidine and Arginine, International Journal of Mass Spectrometry, 269; 2008; 34-45.

[97] A. Gapeev, R.C. Dunbar, Na+ Affinities of Gas-Phase Amino Acids by Ligand Exchange Equilibrium, International Journal of Mass Spectrometry, 228; 2003; 825-839.

[98] S.L. Ling, W.B. Yu, Z.J. Huang, Z.J. Lin, M. Haranczyk, M. Gutowski, Gaseous Arginine Conformers and Their Unique Intramolecular Interactions, Journal of Physical Chemistry A, 110; 2006; 12282-12291.

[99] B.K. Bluhm, S.J. Shields, C.A. Bayse, M.B. Hall, D.H. Russell, Determination of Copper Binding Sites in Peptides Containing Basic Residues: a Combined Experimental and Theoretical Study, International Journal of Mass Spectrometry, 204; 2001; 31-46.

[100] S.J. Shields, B.K. Bluhm, D.H. Russell, Fragmentation Chemistry of M+Cu (+) Peptide Ions Containing an N-Terminal Arginine, Journal of the American Society for Mass Spectrometry, 11; 2000; 626-638.

[101] A.K. Shukla, J.H. Futrell, Collisional Activation and Dissociation of Polyatomic Ions, Mass Spectrometry Reviews, 12; 1993; 211-255.

[102] J.M. Wells, S.A. McLuckey, Collision-Induced Dissociation (CID) of Peptides and Proteins, in, 2005, pp. 148-185.

[103] R.A. Zubarev, Reactions of Polypeptide Ions with Electrons in the Gas Phase, Mass Spectrometry Reviews, 22; 2003; 57-77.

[104] M.D.A. Mabud, M.J. Dekrey, R.G. Cooks, Surface Induced Dissociation of Molecular Ions, International Journal of Mass Spectrometry and Ion Processes, 67; 1985; 285-294.

[105] D.P. Little, J.P. Speir, M.W. Senko, P.B. Oconnor, F.W. McLafferty, Infrared Multiphoton Dissociation of Large Multiply-Charged Ions for Biomolecule Sequencing, Analytical Chemistry, 66; 1994; 2809-2815.

[106] J.P. Reilly, Ultraviolet Photofragmentation of Biomolecular Ions, Mass Spectrometry Reviews, 28; 2009; 425-447.

[107] J. Laskin, J.H. Futrell, Collisional Activation of Peptide Ions in FT-ICR Mass Spectrometry, Mass Spectrometry Reviews, 22; 2003; 158-181.

[108] P.B. Armentrout, Mass Spectrometry - Not Just a Structural Tool: The Use of Guided Ion Beam Tandem Mass Spectrometry to Determine Thermochemistry, Journal of the American Society for Mass Spectrometry, 13; 2002; 419-434.

[109] W.D. Bowers, S.S. Delbert, R.L. Hunter, R.T. McIver, Fragmentation of Oligopeptide Ions Using Ultraviolet-Laser Radiation and Fourier-Transform Mass Spectrometry, Journal of the American Chemical Society, 106; 1984; 7288-7289.

[110] A.H. Streitweieser, C.H., Introduction to Organic Chemistry, 3rd ed., Macmillan Publishing Company, New York, 1985.

[111] W. Gabryelski, L. Li, Photo-Induced Dissociation of Electrospray Generated Ions in an Ion Trap/Time-of-Flight Mass Spectrometer, Review of Scientific Instruments, 70; 1999; 4192-4199.

[112] L. Joly, R. Antoine, M. Broyer, P. Dugourd, J. Lemoine, Specific UV Photodissociation of Tyrosyl-Containing Peptides in Multistage Mass Spectrometry, Journal of Mass Spectrometry, 42; 2007; 818-824.

[113] J.W. Morgan, J.M. Hettick, D.H. Russell, Peptide Sequencing by MALDI 193-nm Photodissociation Time-of-Flight Mass Spectrometry, 2005, pp. 186-209.

[114] J.W. Morgan, Development of Tandem Time-of-Flight Instrumentation for the Examination of Prompt Photodissociation of Peptides Using 193-nm Radiation, Texas A&M University, College Station, 2005.

[115] D.C. Barbacci, D.H. Russell, Sequence and Side-Chain Specific Photofragment (193 nm) Ions from Protonated Substance P by Matrix-Assisted Laser Desorption Ionization Time-of-Tlight Mass Spectrometry, Journal of the American Society for Mass Spectrometry, 10; 1999; 1038-1040.

[116] D.C. Barbacci, Photodissociation of Peptide Ions in a Matrix-Assisted Laser Desorption Ionization Reflectron Time-of-Flight Mass Spectrometer, Texas A&M University, College Station, 2000.

[117] J.M. Hettick, D.L. McCurdy, D.C. Barbacci, D.H. Russell, Optimization of Sample Preparation for Peptide Sequencing by MALDI-TOF Photofragment Mass Spectrometry, Analytical Chemistry, 73; 2001; 5378-5386.

[118] T.Y. Kim, J.P. Reilly, Time-Resolved Observation of Product Ions Generated by 157 nm Photodissociation of Singly Protonated Phosphopeptides, Journal of the American Society for Mass Spectrometry, 20; 2009; 2334-2341.

[119] T.Y. Kim, J.C. Schwartz, J.P. Reilly, Development of a Linear Ion Trap/Orthogonal-Time-of-Flight Mass Spectrometer for Time-Dependent Observation of

Product Ions by Ultraviolet Photodissociation of Peptide Ions, Analytical Chemistry, 81; 2009; 8809-8817.

[120] W.J. Griffiths, A.P. Jonsson, Gas-Phase Conformation Can Have an Influence on Peptide Fragmentation, European Journal of Mass Spectrometry, 7; 2001; 89-99.

[121] J.A.A. Demmers, D.T.S. Rijkers, J. Haverkamp, J.A. Killian, A.J.R. Heck, Factors Affecting Gas-Phase Deuterium Scrambling in Peptide Ions and Their Implications for Protein Structure Determination, Journal of the American Chemical Society, 124; 2002; 11191-11198.

[122] A.G. Harrison, To b or not to b: The Ongoing Saga of Peptide b Ions, Mass Spectrometry Reviews, 28; 2009; 640-654.

[123] B. Paizs, S. Suhai, Fragmentation Pathways of Protonated Peptides, Mass Spectrometry Reviews, 24; 2005; 508-548.

[124] W.Y. Feng, C. Gronert, K.A. Fletcher, A. Warres, C.B. Lebrilla, The Mechanism of C-Terminal Ffragmentations in Alkali Metal Ion Complexes of Peptides, International Journal of Mass Spectrometry, 222; 2003; 117-134.

[125] Mendez, II, Y.M. She, W. Ens, K.M. Coombs, Digestion Pattern of Reovirus Outer Capsid Protein Sigma 3 Determined by Mass Spectrometry, Virology, 311; 2003; 289-304.

[126] K.E. Williams, T.A. Carver, J.J.L. Miranda, A. Kautiainen, J.S. Vogel, K. Dingley, M.A. Baldwin, K.W. Turteltaub, A.L. Burlingame, Attomole Detection of in vivo Protein Targets of Benzene in Mice - Evidence for a Highly Reactive Metabolite, Molecular & Cellular Proteomics, 1; 2002; 885-895.

[127] S.M.R. Stanley, A. Poljak, Matrix-Assisted Laser-Desorption Time-of-Flight Ionisation and High-Performance Liquid Chromatography-Electrospray Ionisation Mass Spectral Analyses of two Glycosylated Recombinant Proteins, Journal of Chromatography B-Analytical Technologies in the Biomedical and Life Sciences, 785; 2003; 205-218.

[128] G. Choudhary, S.L. Wu, P. Shieh, W.S. Hancock, Multiple Enzymatic Digestion for Enhanced Sequence Coverage of Proteins in Complex Proteomic Mixtures Using Capillary LC with Ion Trap MS/MS, Journal of Proteome Research, 2; 2003; 59-67.

[129] R.J. Nachman, W.K. Russell, G.M. Coast, D.H. Russell, R. Predel, Mass Spectrometric Assignment of Leu/Ile in Neuropeptides from Single Neurohemal Organ Preparations of Insects, Peptides, 26; 2005; 2151-2156.

[130] M. Ramstrom, C. Hagman, Y.O. Tsybin, K.E. Markides, P. Hakansson, A. Salehi, I. Lundquist, R. Hakanson, J. Bergquist, A Novel Mass Spectrometric Approach to the Analysis of Hormonal Peptides in Extracts of Mouse Pancreatic Islets, European Journal of Biochemistry, 270; 2003; 3146-3152.

[131] U. Keller, F. Schauwecker, Combinatorial Biosynthesis of Non-Ribosomal Peptides, Combinatorial Chemistry & High Throughput Screening, 6; 2003; 527-540.

[132] C. Liepke, H.D. Zucht, W.G. Forssmann, L. Standker, Purification of Novel Peptide Antibiotics from Human Milk, Journal of Chromatography B-Analytical Technologies in the Biomedical and Life Sciences, 752; 2001; 369-377.

[133] W.Y. Feng, S. Gronert, C. Lebrilla, The Lithium Cation Binding Energies of Gaseous Amino Acids, Journal of Physical Chemistry A, 107; 2003; 405-410.

[134] H.A. Sawyer, J.T. Marini, E.G. Stone, B.T. Ruotolo, K.J. Gillig, D.H. Russell, The Structure of Gas-Phase Bradykinin Fragment 1-5 (RPPGF) Ions: An Ion Mobility Spectrometry and H/D Exchange Ion-Molecule Reaction Chemistry Study, Journal of the American Society for Mass Spectrometry, 16; 2005; 893-905.

[135] S.J. Shields, B.K. Bluhm, D.H. Russell, Novel Method for M+Cu (+) Ion Formation by Matrix-Assisted Laser Desorption Ionization, International Journal of Mass Spectrometry, 182; 1999; 185-195.

[136] Z.X. Wu, F.A. Fernandez-Lima, D.H. Russell, Amino Acid Influence on Copper Binding to Peptides: Cysteine Versus Arginine, Journal of the American Society for Mass Spectrometry, 21; 2010; 522-533.

[137] S.W. Lee, H.S. Kim, J.L. Beauchamp, Salt Bridge Chemistry Applied to Gas-Phase Peptide Sequencing: Selective Fragmentation of Sodiated Gas-Phase Peptide Ions Adjacent to Aspartic Acid Residues, Journal of the American Chemical Society, 120; 1998; 3188-3195.

[138] E.F. Strittmatter, E.R. Williams, Structures of Protonated Arginine Dimer and Bradykinin Investigated by Density Functional Theory: Further Support for Stable Gas-Phase Salt Bridges, Journal of Physical Chemistry A, 104; 2000; 6069-6076.

[139] P.C. Liao, Z.H. Huang, J. Allison, Charge Remote Fragmentation of Peptides Following Attachment of a Fixed Positive Charge: A Matrix-Assisted Laser Desorption/Ionization Postsource Decay Study, Journal of the American Society for Mass Spectrometry, 8; 1997; 501-509.

[140] P.C. Liao, J. Allison, Enhanced Detection of Peptides in Matrix-Assisted Laser-Desorption Ionization Mass-Spectrometry Through the Use of Charge Localized Derivatives, Journal of Mass Spectrometry, 30; 1995; 511-512.

[141] M.M. Kish, G. Ohanessian, C. Wesdemiotis, The Na+ Affinities of Alpha-Amino Acids: Side-Chain Substituent Effects, International Journal of Mass Spectrometry, 227; 2003; 509-524.

[142] R.S. Johnson, S.A. Martin, K. Biemann, Collision-Induced Fragmentation of [M+H]+ Ions of Peptides - Side-Chain Specific Sequence Ions, International Journal of Mass Spectrometry and Ion Processes, 86; 1988; 137-154.

[143] C.T. Lee, W.T. Yang, R.G. Parr, Development of the Colle-Salvetti Correlation-Energy Formula into a Functional of the Electron-Density, Physical Review B, 37; 1988; 785-789.

[144] A.D. Becke, Density-Functional Thermochemistry .3. The Role of Exact Exchange, Journal of Chemical Physics, 98; 1993; 5648-5652.

[145] P.J. Stephens, F.J. Devlin, C.F. Chabalowski, M.J. Frisch, Ab-Initio Calculation of Vibrational Absorption and Circular-Dichroism Spectra Using Density-Functional Force-Fields, Journal of Physical Chemistry, 98; 1994; 11623-11627.

[146] M. Kohtani, B.S. Kinnear, M.F. Jarrold, Metal-Ion Enhanced Helicity in the Gas Phase, Journal of the American Chemical Society, 122; 2000; 12377-12378.

[147] M.J. Tomlinson, J.R. Scott, C.L. Wilkins, J.B. Wright, W.E. White, Fragmentation of an Alkali Metal-Attached Peptide Probed by Collision-Induced Dissociation Fourier Transform Mass Spectrometry and Computational Methodology, Journal of Mass Spectrometry, 34; 1999; 958-968.

[148] Jaguar 6.0 Manual, Portland, OR, 2004.

[149] R.E. Gimon-Kinsel, D.C. Barbacci, D.H. Russell, Conformations of Protonated Gas-Phase Bradykinin Ions: Evidence for Intramolecular Hydrogen Bonding, Journal of Mass Spectrometry, 34; 1999; 124-136.

[150] R.W. Vachet, M.R. Asam, G.L. Glish, Secondary Interactions Affecting the Dissociation Patterns of Arginine-Containing Peptide Ions, Journal of the American Chemical Society, 118; 1996; 6252-6256.

[151] H.B. Li, K.W.M. Siu, R. Guevremont, J.C.Y. LeBlanc, Complexes of Silver(I) with Peptides and Proteins as Produced in Electrospray Mass Spectrometry, Journal of the American Society for Mass Spectrometry, 8; 1997; 781-792.

[152] V. Ryzhov, R.C. Dunbar, B. Cerda, C. Wesdemiotis, Cation-pi Effects in the Complexation of Na+ and K+ with Phe, Tyr, and Trp in the Gas Phase, Journal of the American Society for Mass Spectrometry, 11; 2000; 1037-1046.

[153] A.L. Heaton, P.B. Armentrout, Experimental and Theoretical Studies of Potassium Cation Interactions with the Acidic Amino Acids and Their Amide Derivatives, Journal of Physical Chemistry B, 112; 2008; 12056-12065.

[154] L. Stryer, Biochemistry, W.H. Freeman, New York, 1988.

[155] M.J. Page, E. Di Cera, Role of Na+ and K+ in Enzyme Function, Physiological Reviews, 86; 2006; 1049-1092.

[156] R.P. Grese, R.L. Cerny, M.L. Gross, Metal-Ion Peptide Interactions in the Gas-Phase - A Tandem Mass Spectrometry Study of Alkali-Metal Cationized Peptides, Journal of the American Chemical Society, 111; 1989; 2835-2842.

[157] L.M. Teesch, J. Adams, Intrinsic Interactions Between Alkaline-Earth Metal Ions and Peptides: A Gas-Phase Study, Journal of the American Chemical Society, 112; 1990; 4110-4120.

[158] L.M. Teesch, J. Adams, Fragmentations of Gas-Phase Complexes between Alkalie Metal Ions and Peptides: Metal Ion Binding to Carbonyl Oxygens and Other Neutral Functional Groups, Journal of the American Chemical Society, 113; 1991; 812-820.

[159] L.M. Teesch, R.C. Orlando, J. Adams, Location of the Alkali Metal Ion in Gas-Phase Peptide Complexes, Journal of the American Chemical Society, 113; 1991; 3668-3675.

[160] B.T. Ruotolo, D.H. Russell, Gas-phase Conformations of Proteolytically Derived Protein Fragments: Influence of Solvent on Peptide Conformation, Journal of Physical Chemistry B, 108; 2004; 15321-15331.

[161] L.M. Mallis, D.H. Russell, Fast Atom Bombardment-Tandem Mass-Spectrometry Studies of Organo-Alkali Metal Ions of Small Peptides, Analytical Chemistry, 58; 1986; 1076-1080.

[162] T. Lin, G.L. Glish, C-terminal Peptide Sequencing Via Multistage Mass Spectrometry, Analytical Chemistry, 70; 1998; 5162-5165.

[163] M.J. Page, R.T.A. MacGillivray, E. Di Cera, Determinants of Specificity in Coagulation Proteases, Journal of Thrombosis and Haemostasis, 3; 2005; 2401-2408.

[164] D. Renner, G. Spiteller, Linked Scan Investigation of Peptide Degradation Initiaed by Liquid Secondary Ion Mass-Spectrometry, Biomedical and Environmental Mass Spectrometry, 15; 1988; 75-77.

[165] M.S. Thompson, W.D. Cui, J.P. Reilly, Fragmentation of Singly Charged Peptide Ions by Photodissociation at Lambda=157 nm, Angewandte Chemie-International Edition, 43; 2004; 4791-4794.

[166] J.P. Reilly, Ultraviolet Photofragmentation of Biomolecules, Mass Spectrometry Reviews, 28; 2009; 425-447.

[167] J.W. Morgan, D.H. Russell, Comparative Studies of 193-nm Photodissociation and TOF-TOFMS Analysis of Bradykinin Analogues: The Effects of Charge Site(s) and Fragmentation Timescales, Journal of the American Society for Mass Spectrometry, 17; 2006; 721-729.

[168] K.D. Ballard, S.J. Gaskell, Intramolecular O^{18} Isotopic Exchange in the Gas-Phase Observed During the Tandem Mass-Spectrometric Analysis of Peptides, Journal of the American Chemical Society, 114; 1992; 64-71.

[169] G.E. Reid, R.J. Simpson, R.A.J. O'Hair, A Mass Spectrometric and *ab initio* Study of the Pathways for Dehydration of Simple Glycine and Cysteine-Containing Peptide M+H (+) Ions, Journal of the American Society for Mass Spectrometry, 9; 1998; 945-956.

[170] T. Yalcin, I.G. Csizmadia, M.R. Peterson, A.G. Harrison, The Structure and Fragmentation of B-n (n>=3) Ions in Peptide Spectra, Journal of the American Society for Mass Spectrometry, 7; 1996; 233-242.

[171] T. Yalcin, C. Khouw, I.G. Csizmadia, M.R. Peterson, A.G. Harrison, Why are b Ions Stable Species in Peptide Spectra?, Journal of the American Society for Mass Spectrometry, 6; 1995; 1165-1174.

[172] A.G. Harrison, A.B. Young, C. Bleiholder, S. Suhai, B. Paizs, Scrambling of Sequence Information in Collision-Induced Dissociation of Peptides, Journal of the American Chemical Society, 128; 2006; 10364-10365.

[173] I. Riba-Garcia, K. Giles, R.H. Bateman, S.J. Gaskell, Evidence for Structural Variants of a- and b-Type Peptide Fragment Ions Using Combined Ion Mobility/Mass Spectrometry, Journal of the American Society for Mass Spectrometry, 19; 2008; 609-613.

[174] C.X. Jia, W. Qi, Z.M. He, Cyclization Reaction of Peptide Fragment Ions During Multistage Collisionally Activated Decomposition: An Inducement to Lose Internal Amino-Acid Residues, Journal of the American Society for Mass Spectrometry, 18; 2007; 663-678.

[175] R.C. Beavis, B.T. Chait, Velocity Distributions of Intact High Mass Polypeptide Molecule Ions Produced by Matrix Assisted Laser Desorption, Chemical Physics Letters, 181; 1991; 479-484.

[176] F. Aksouh, P. Chaurand, C. Deprun, S. Dellanegra, J. Hoyes, Y. Lebeyec, R.R. Pinho, Influence of the Laser-Beam Direction on the Molecular Ion Ejection Angle In Matrix Assited Laser Desorption Ionization, Rapid Communications in Mass Spectrometry, 9; 1995; 515-518.

[177] A. Bhowmick, W.C.J. Carvalho, A.V. Korgaonkar, J.V. Yakhmi, V.C. Sahni, A New Gridless Ion Optics for High Resolution Time-of-Flight Mass Spectrometer, International Journal of Modern Physics B, 19; 2005; 2621-2626.

[178] A.K. Shukla, J.H. Futrell, A Beam Scattering Instrument for the Dynamics Studies of Surface-Induced Dissociation Processes, Review of Scientific Instruments, 74; 2003; 168-175.

[179] M.A. Baldwin, Mass Spectrometers for the Analysis of Biomolecules, in, 2005, pp. 3-48.

[180] K. Biemann, I.A. Papayannopoulos, Amino-Acid Sequencing of Proteins, Accounts of Chemical Research, 27; 1994; 370-378.

[181] R.A. Zubarev, N.L. Kelleher, F.W. McLafferty, Electron Capture Dissociation of Multiply Charged Protein Cations. A Nonergodic Process, Journal of the American Chemical Society, 120; 1998; 3265-3266.

[182] G. Vanhoof, F. Goossens, I. Demeester, D. Hendriks, S. Scharpe, Proline Motifs in Peptides and Their Biological Processing, FASEB Journal, 9; 1995; 736-744.

[183] D. Pal, P. Chakrabarti, Cis Peptide Bonds in Proteins: Residues Involved, Their Conformations, Interactions and Locations, Journal of Molecular Biology, 294; 1999; 271-288.

[184] T.Y. Kim, S.J. Valentine, D.E. Clemmer, J.P. Reilly, Gas-Phase Conformation-Specific Photofragmentation of Proline-Containing Peptide Ions, Journal of the American Society for Mass Spectrometry, 21; 2010; 1455-1465.

[185] M.W. Macarthur, J.M. Thornton, Influence of Proline Residues on Protein Conformation, Journal of Molecular Biology, 218; 1991; 397-412.

[186] A.E. Mirsky, L. Pauling, On the Structure of Native, Denatured, and Coagulated Proteins, Proceedings of the National Academy of Sciences of the United States of America, 22; 1936; 439-447.

[187] F. Weinhold, Resonance Character of Hydrogen-Bonding Interactions in Water and Other H-Bonded Species, in, 2006, pp. 121-156.

[188] G.J. Bartlett, A. Choudhary, R.T. Raines, D.N. Woolfson, n ->pi* Interactions in Proteins, Nature Chemical Biology, 6; 2010; 615-620.

[189] A.E. Counterman, D.E. Clemmer, Cis-trans Signatures of Proline-Containing Tryptic Peptides in the Gas Phase, Analytical Chemistry, 74; 2002; 1946-1951.

[190] A.E. Counterman, D.E. Clemmer, Anhydrous Polyproline Helices and Globules, Journal of Physical Chemistry B, 108; 2004; 4885-4898.

[191] C.M. Gamage, L.M. Perez, C.K. Barlow, P.J. Pai, K.L. Kmiec, D.H. Russell, The Preferential Decay of Two N-Terminal Proline Units in Gas-Phase Peptide Fragmenatation when No Mobile Protons are Present, 2012; In Preparation.

[192] L.L. Smith, K.A. Herrmann, V.H. Wysocki, Investigation of Gas Phase Ion Structure for Proline-Containing b(2) Ion, Journal of the American Society for Mass Spectrometry, 17; 2006; 20-28.

[193] L.Y. Zhang, W.D. Cui, M.S. Thompson, J.P. Reilly, Structures of Alpha-Type Ions Formed in the 157 nm Photodissociation of Singly-Charged Peptide Ions, Journal of the American Society for Mass Spectrometry, 17; 2006; 1315-1321.

[194] A. Brunelle, S. Dellanegra, J. Depauw, H. Joret, Y. Lebeyec, Time-of-Flight Mass Spectrometry with a Compact 2-Stage Electrostatic Mirror - Metastable Ion Studies with High Mass Resolution and Ion Emission from Thick Insulators, Rapid Communications in Mass Spectrometry, 5; 1991; 40-43.

[195] J.M. Hettick, Optimization and Utilization of MALDI 193-nm Photofragment Time-of-Flight Mass Spectrometry for Peptide Sequencing, Texas A&M University, College Station, 2003.

[196] S.L. Cook, O.L. Collin, G.P. Jackson, Metastable Atom-Activated Dissociation Mass Spectrometry: Leucine/Isoleucine Differentiation and Ring Cleavage of Proline Residues, Journal of Mass Spectrometry, 44; 2009; 1211-1223.

APPENDIX A

AUTOCAD DRAWINGS OF PARTS CONSTRUCTED FOR PHOTODISSOCIATION TANDEM TIME-OF-FLIGHT INSTRUMENT

AUTOCAD RENDERING OF FULL INSTRUMENT

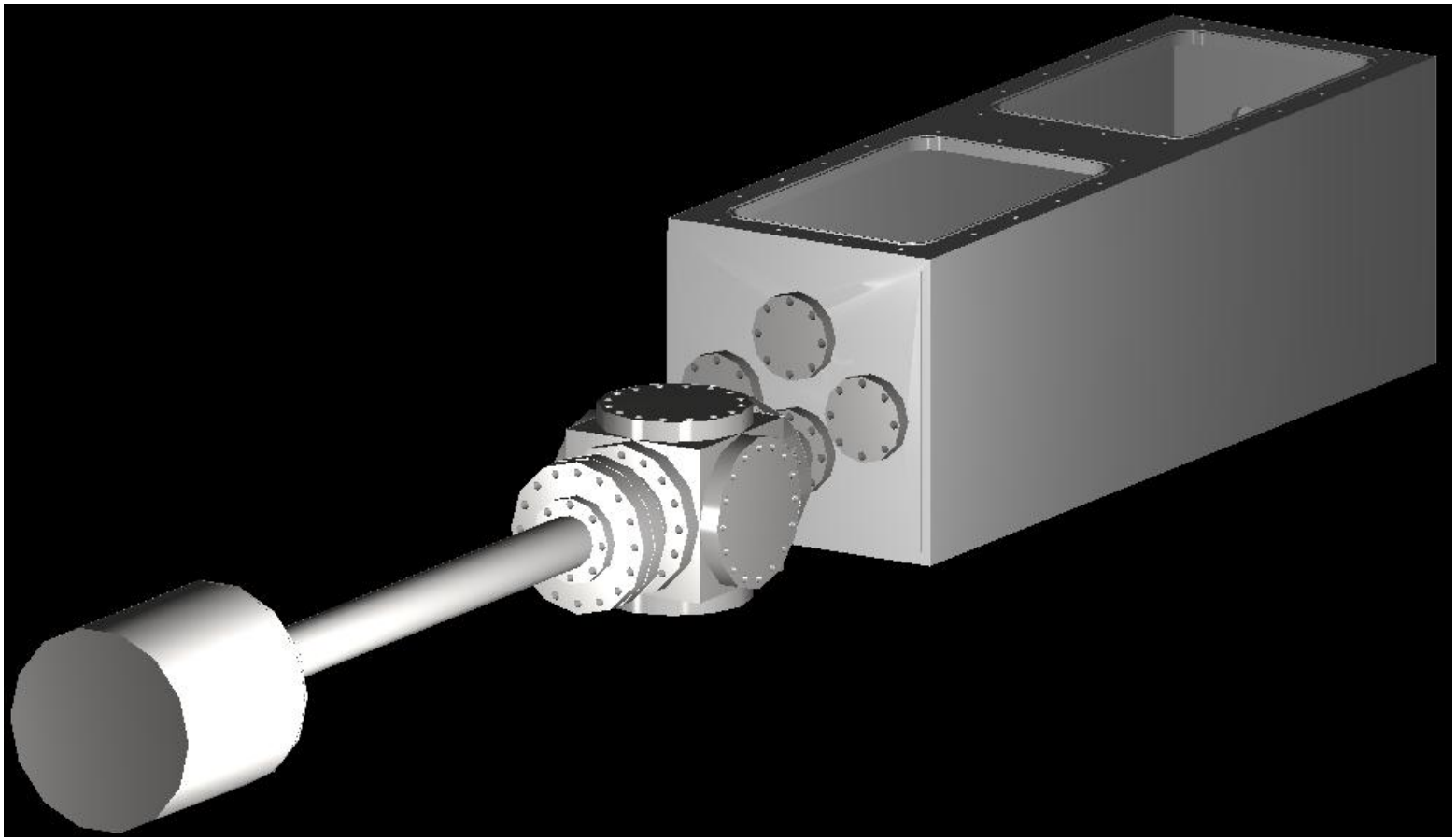

AUTOCAD RENDERING OF PHOTOCELL INCLUDING SOURCE 2 REGION

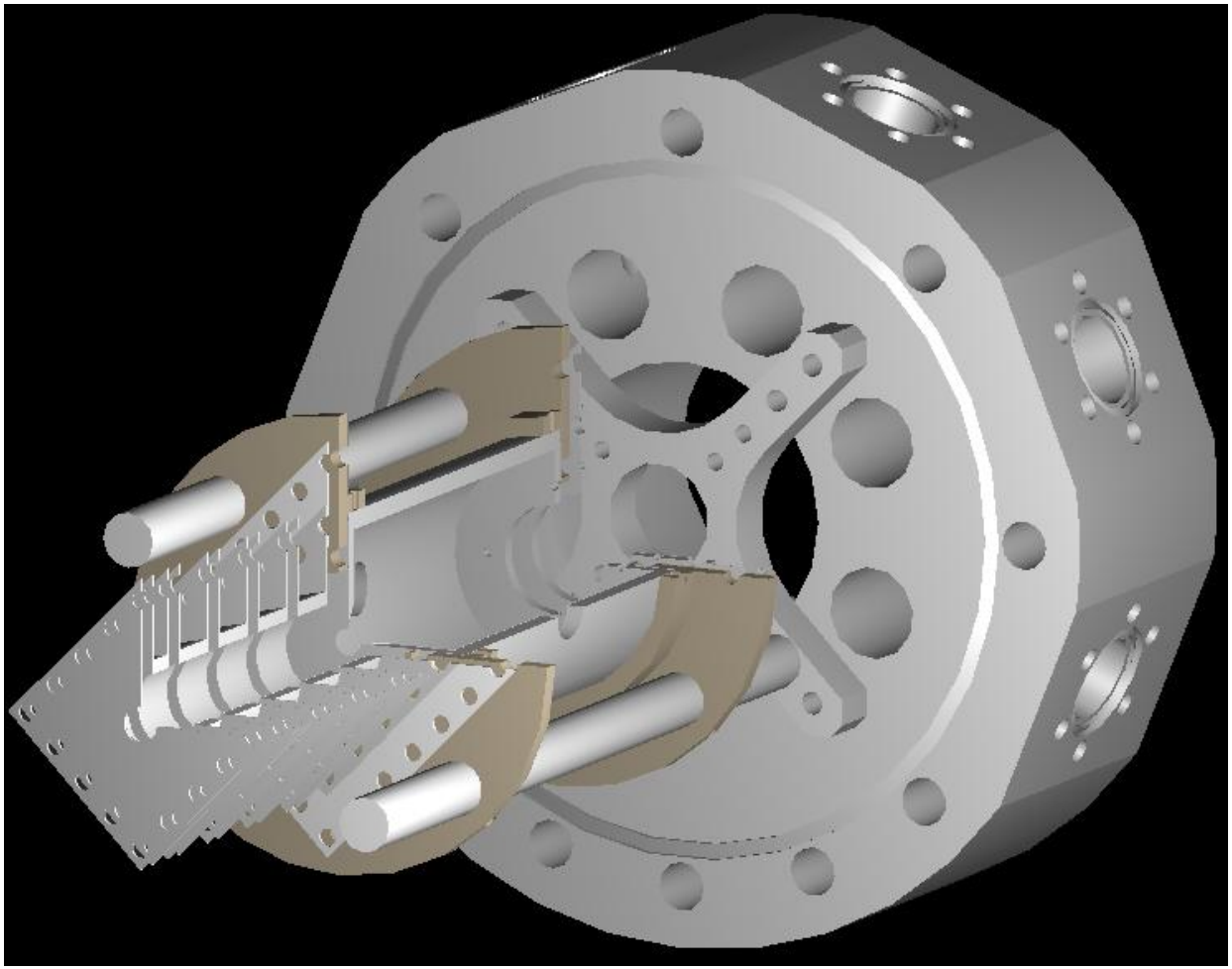

DECELERATION LENS FOR PHOTO-TOF – SHORT BARREL

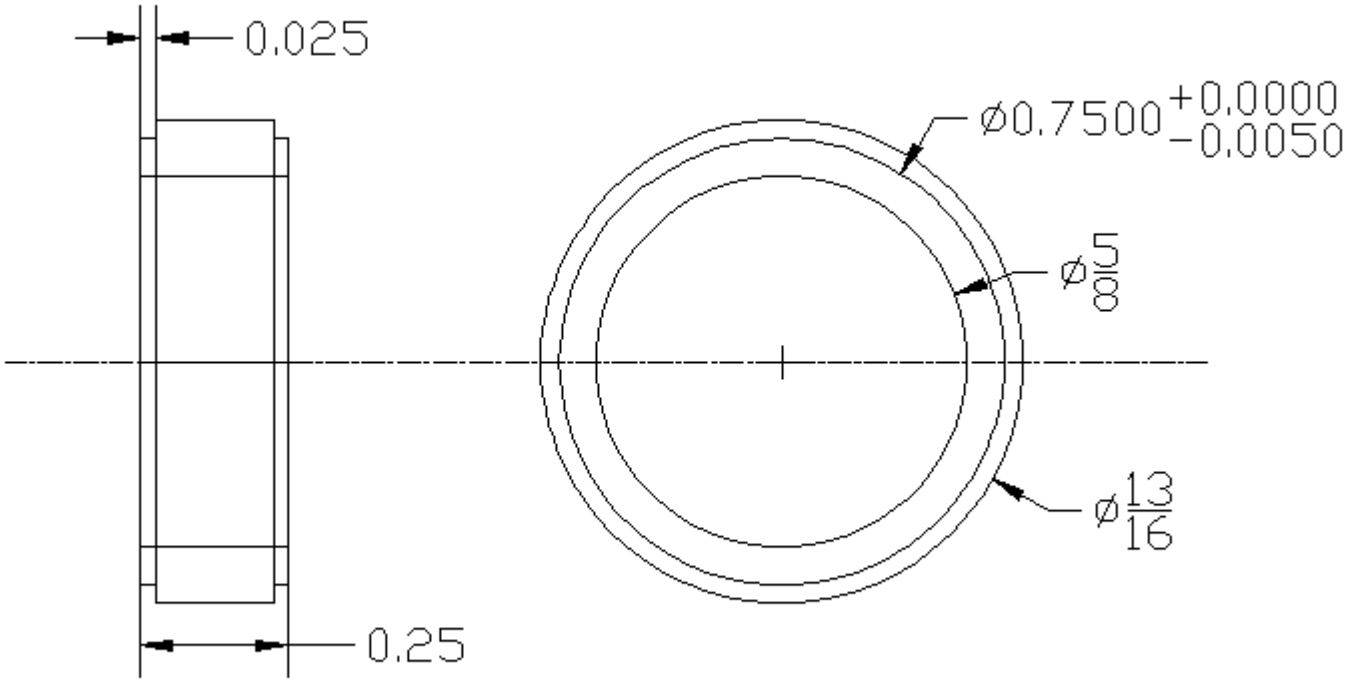

DECELERATION LENS FOR PHOTO-TOF – LONG BARREL

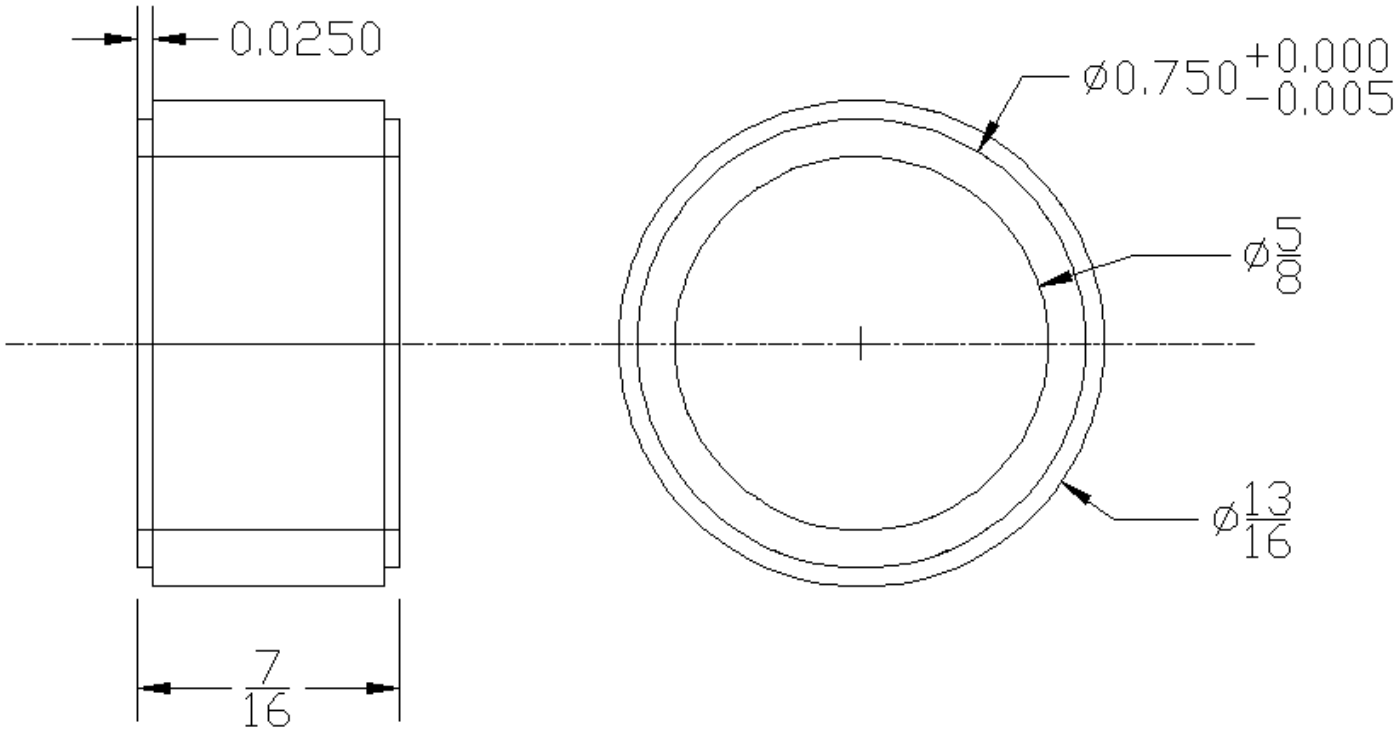

PHOTOCELL CUP TO ATTACH TO BRACING RODS – SECOND ITERATION

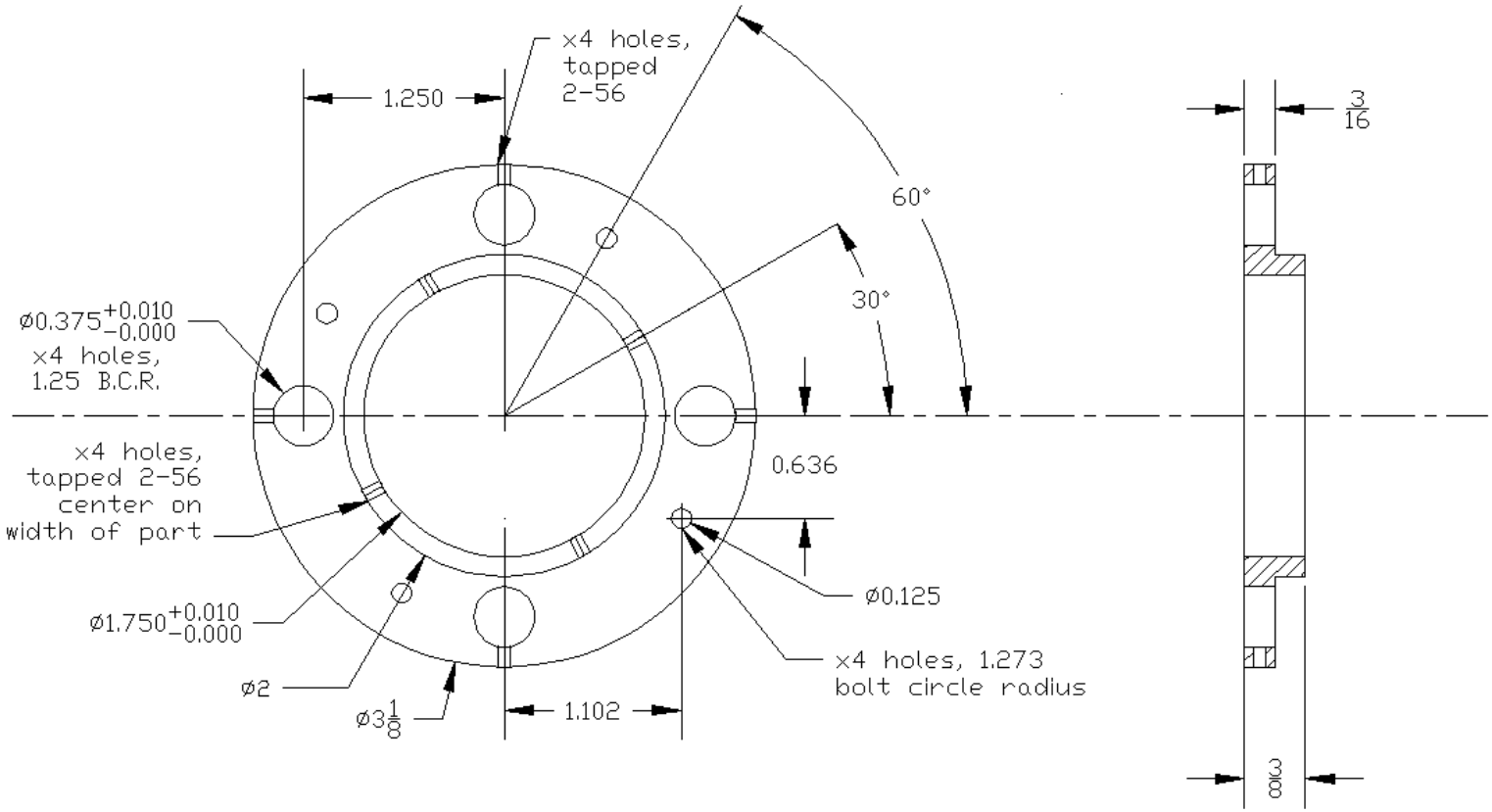

PHOTOCELL CUP TO ATTACH TO BRACING RODS – FOR DECELERATION LENSES

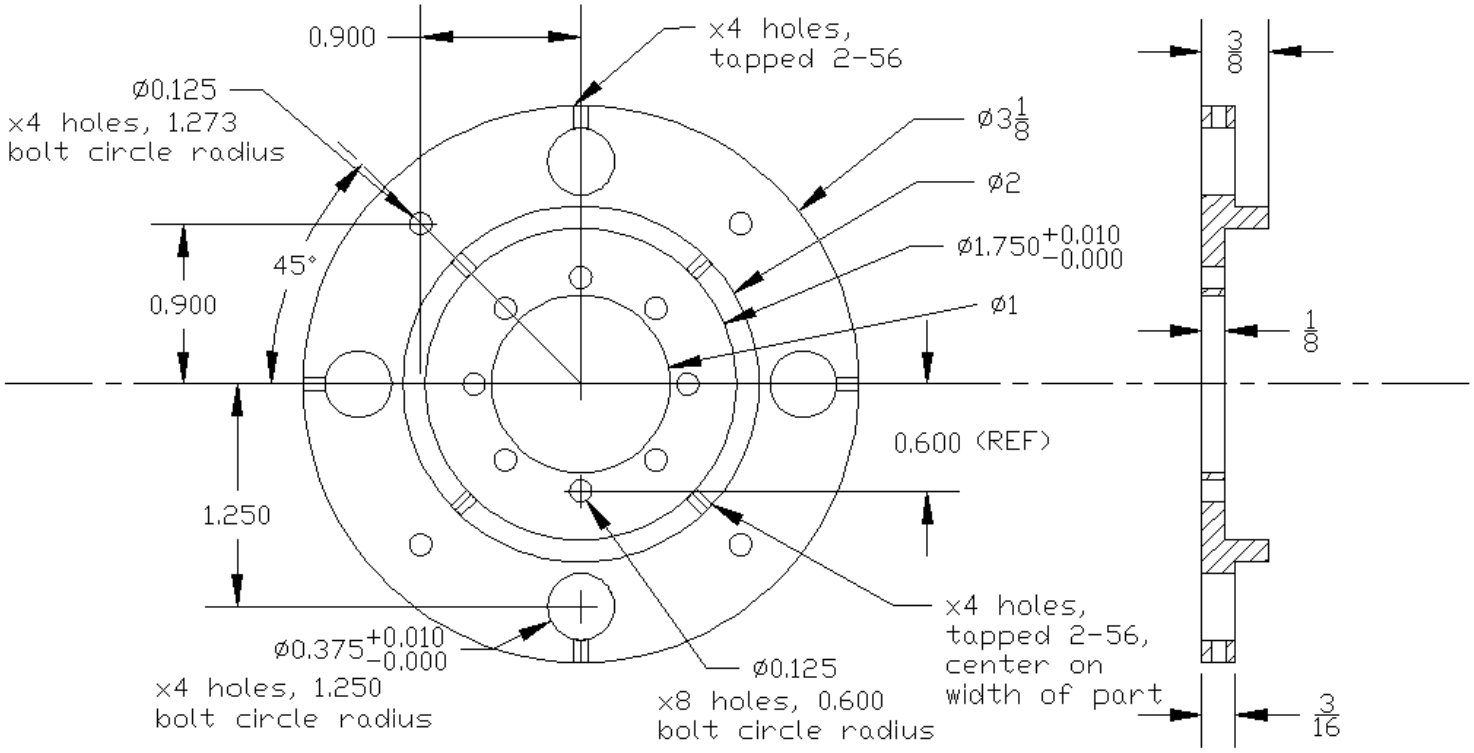

MOUNTING FLANGE FOR PHOTOCELL OPTICS

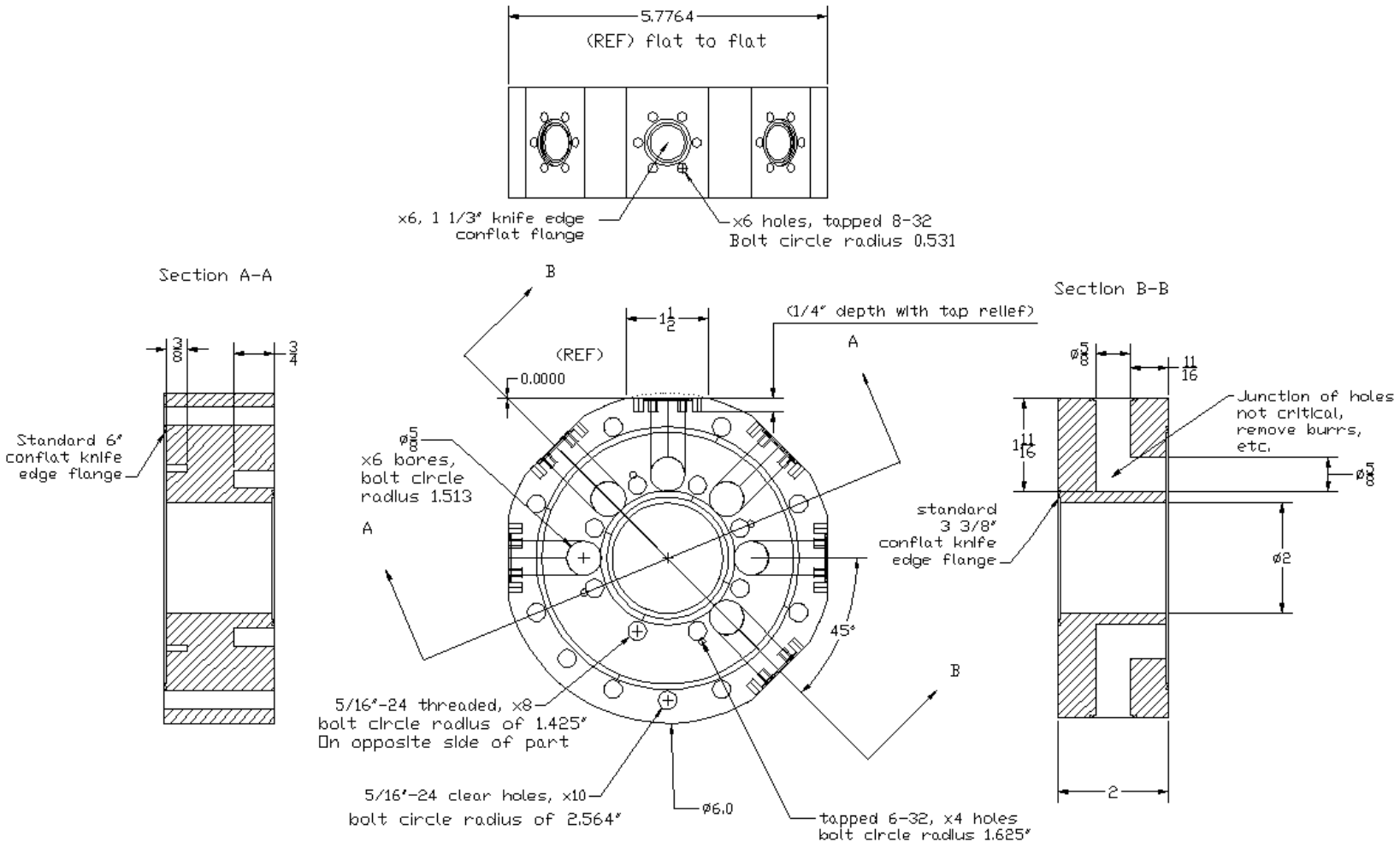

ADAPTER FLANGE FOR MOUNTING PHOTOCELL OPTICS

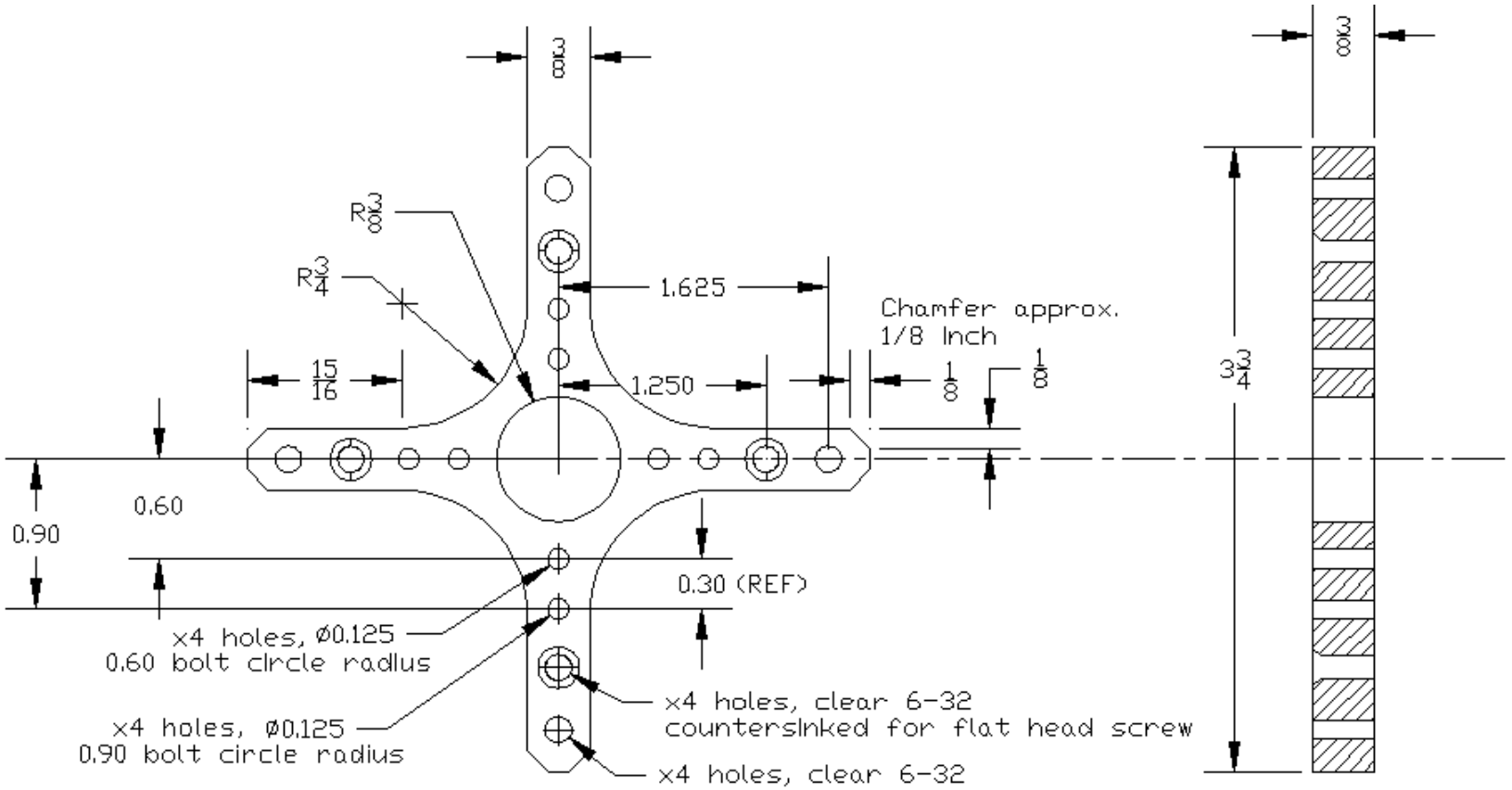

GRIDLESS ENCAPS FOR PHOTOCELL

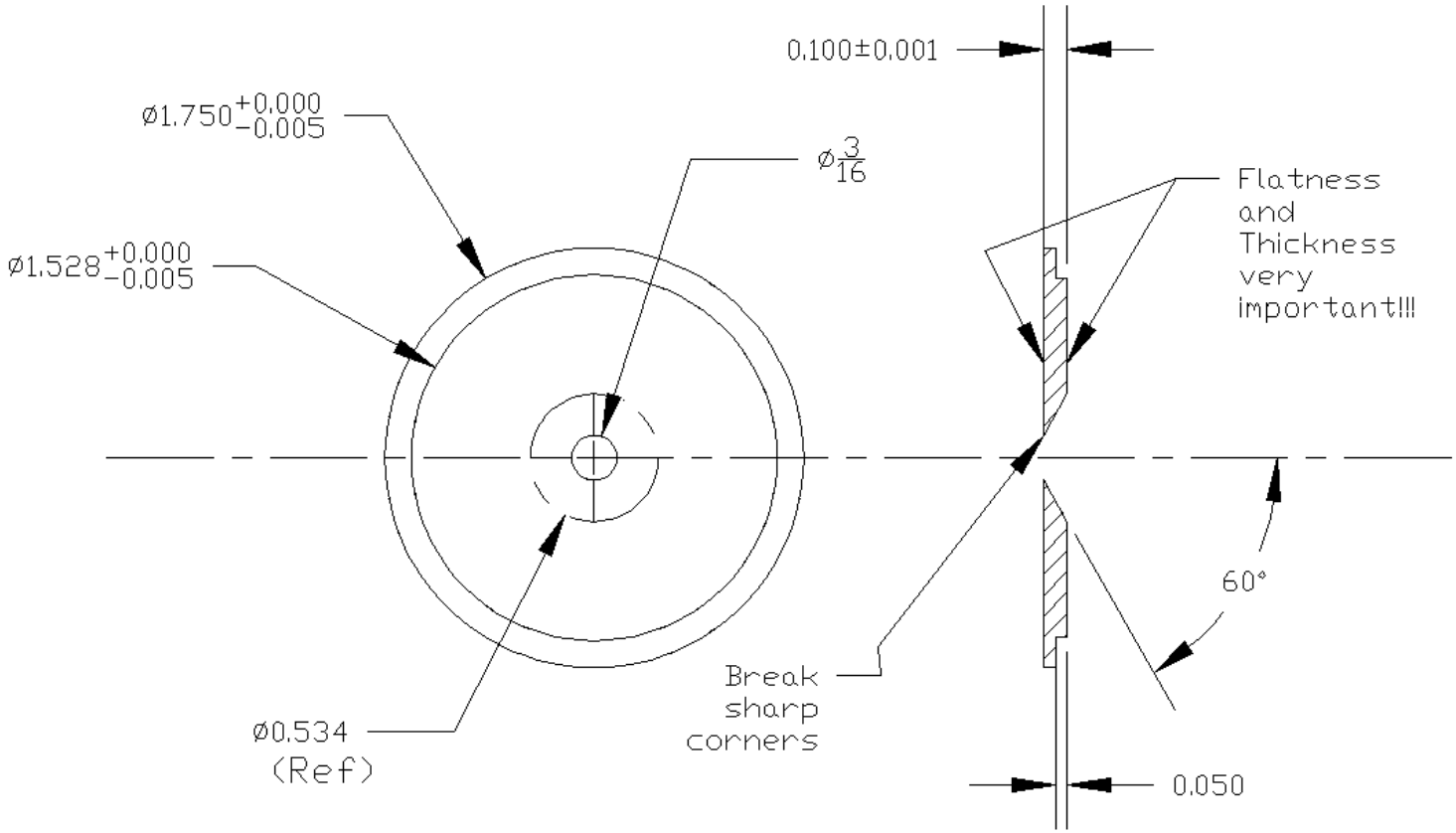

PHOTOCELL ENCAPS FOR GRID

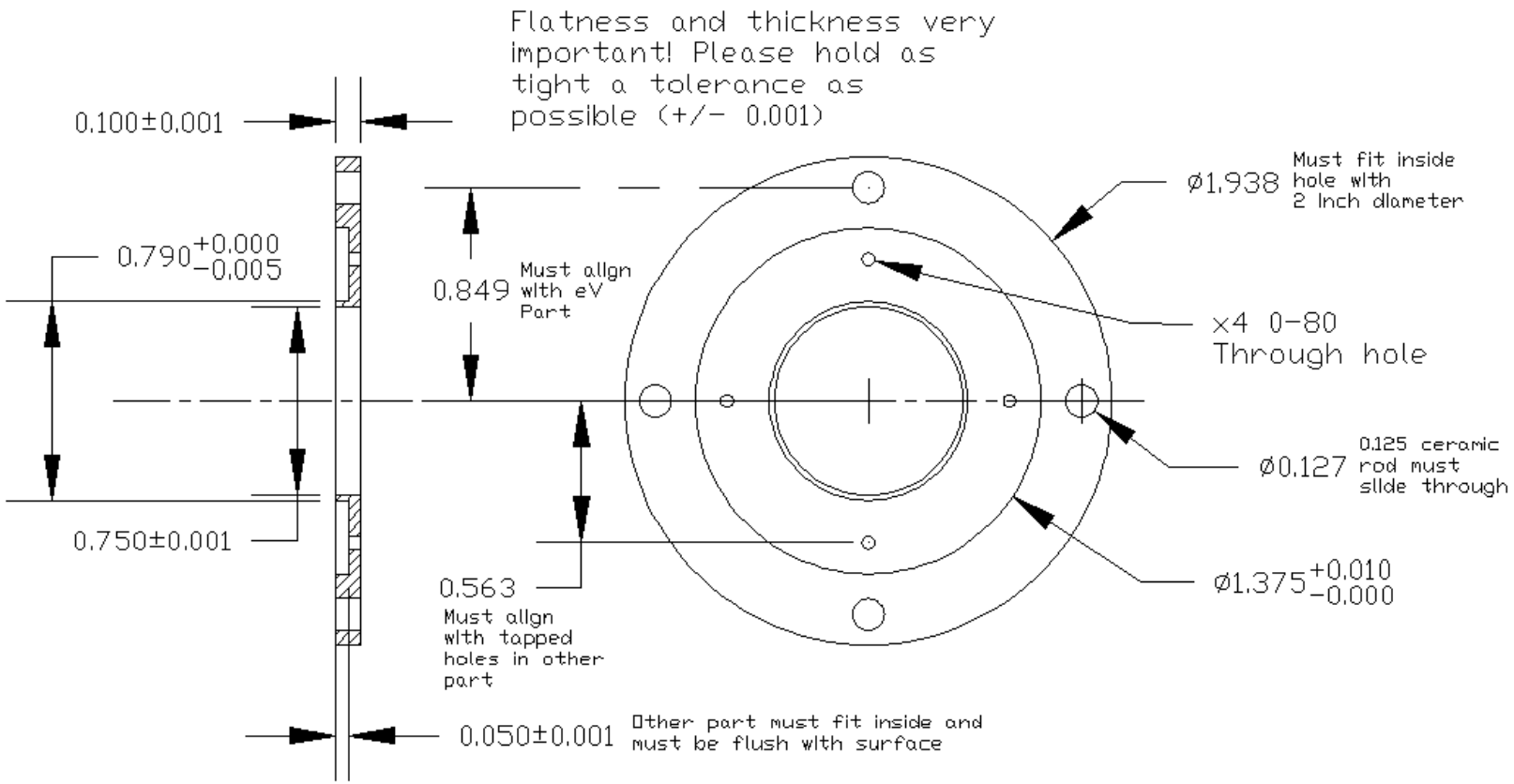

GRIDDED CROSS PIECE FOR PHOTOCELL – PART 1

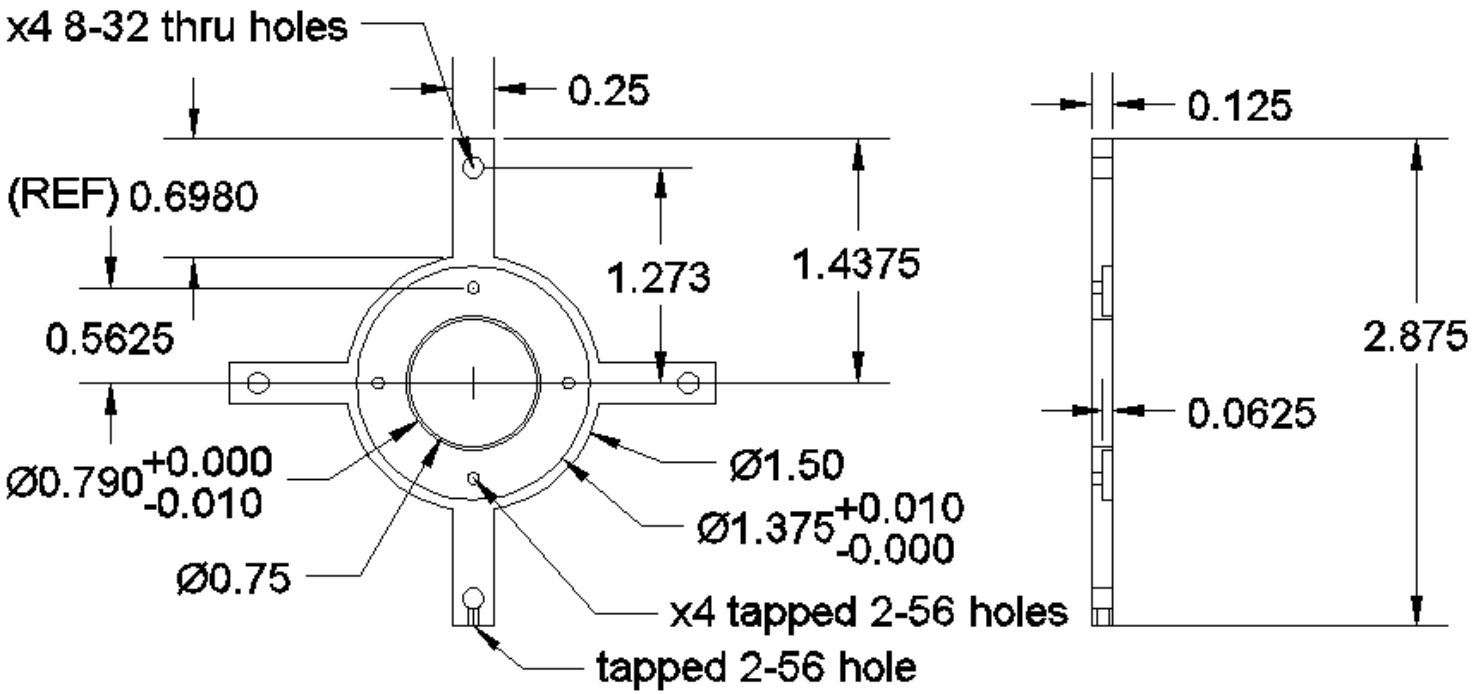

GRIDDED CROSS PIECE FOR PHOTOCELL – PART 2

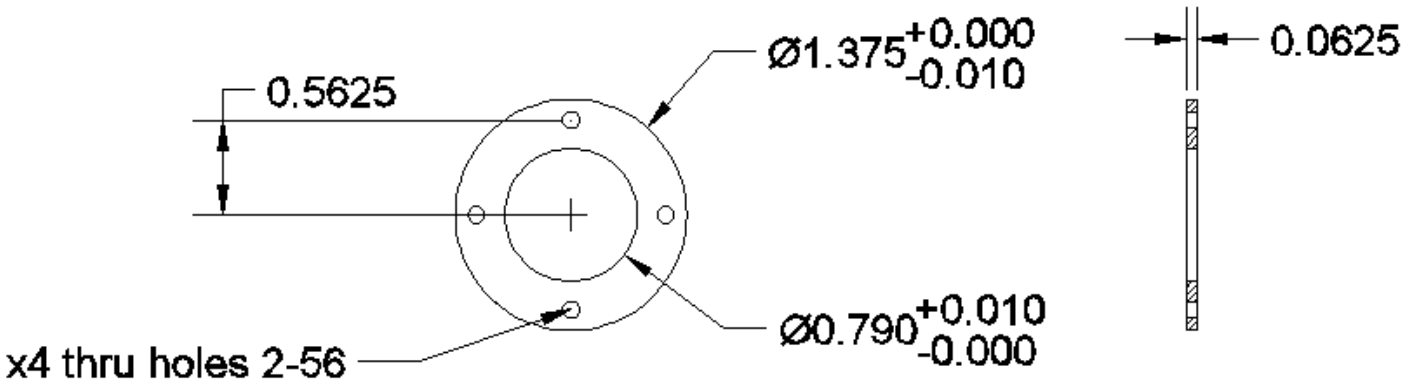

SUPPORT PIECE FOR SOURCE REGION – PART 1

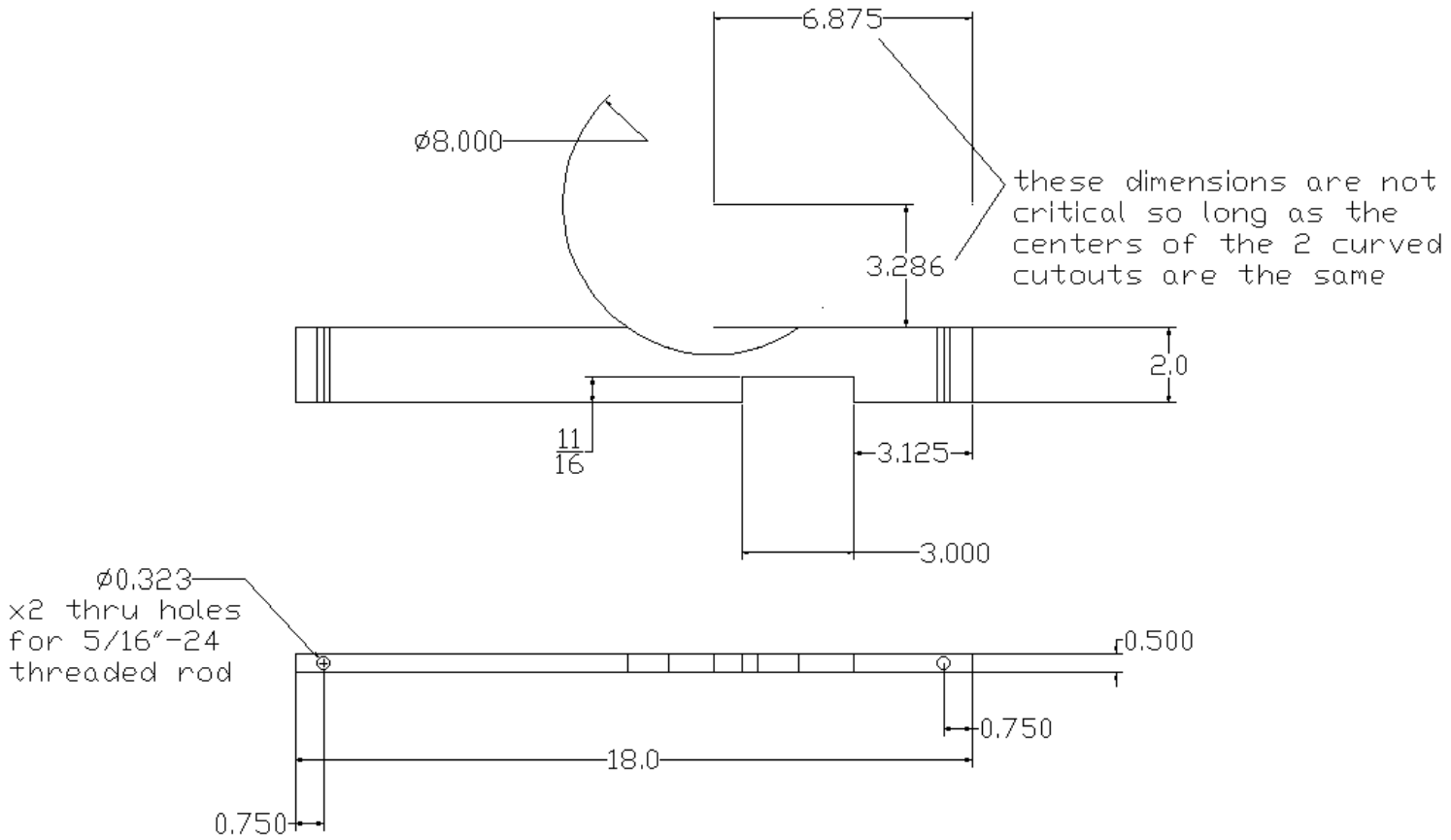

SUPPORT PIECE FOR SOURCE REGION – PART 2

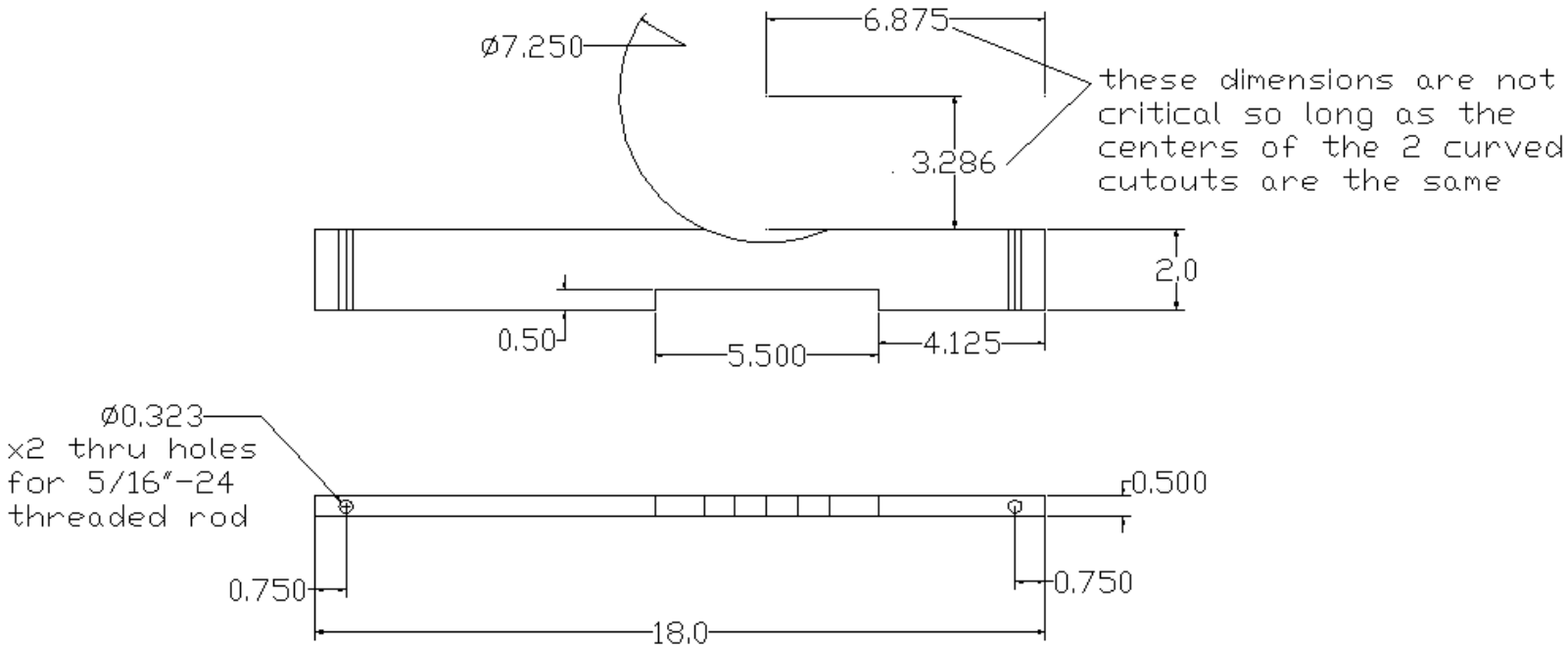

FULL ASSEMBLY OF REFLECTRON CAN

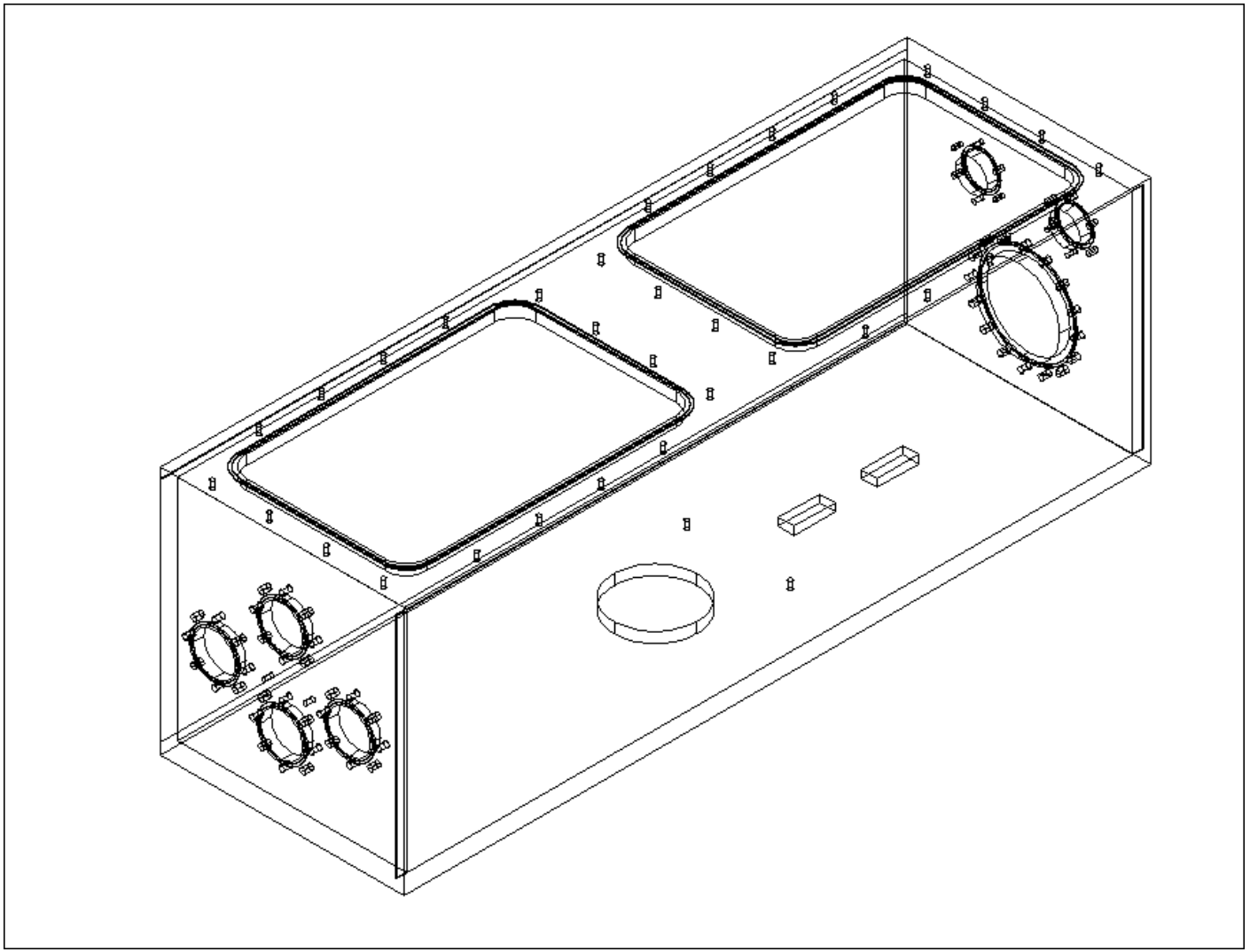

REFLECTRON CAN – BOTTOM PIECE

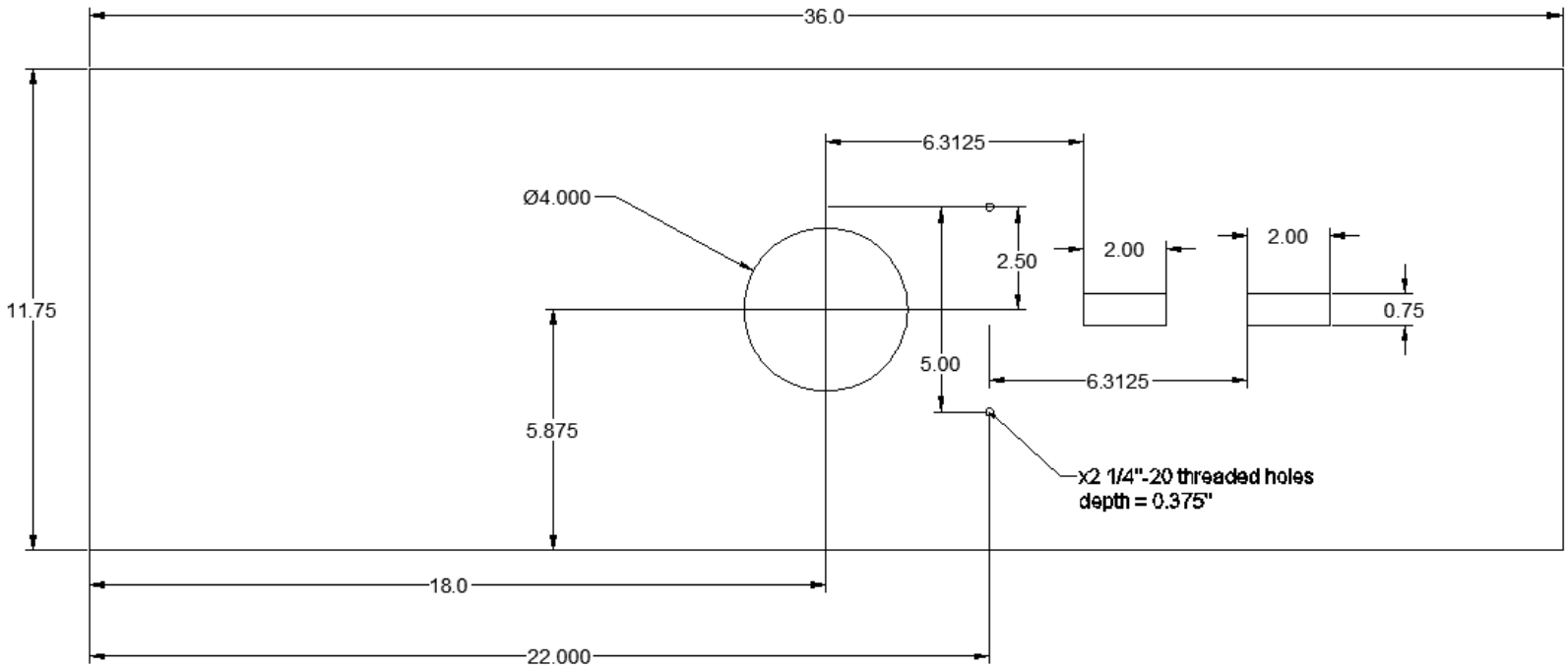

REFLECTRON CAN – TOP PIECE

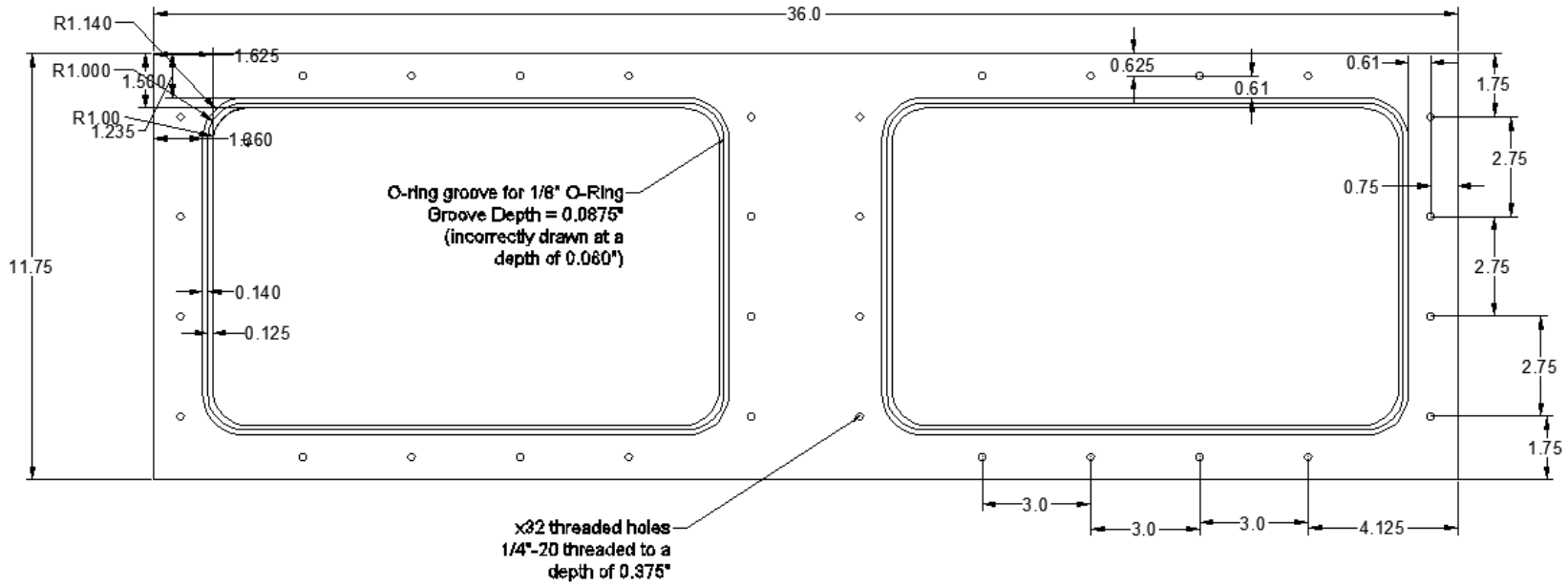

REFLECTRON CAN – FRONT PIECE

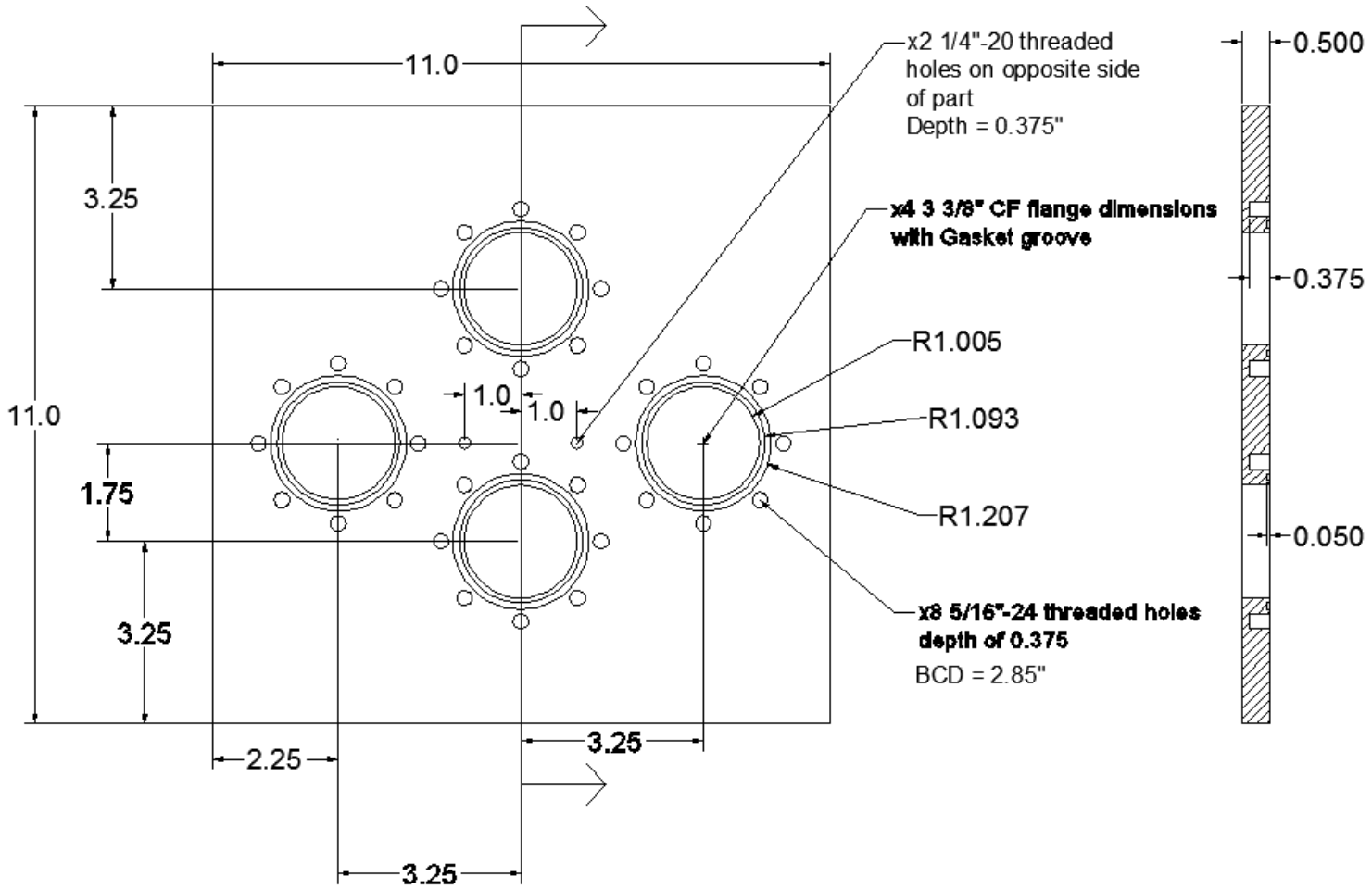

REFLECTRON CAN – BACK PIECE

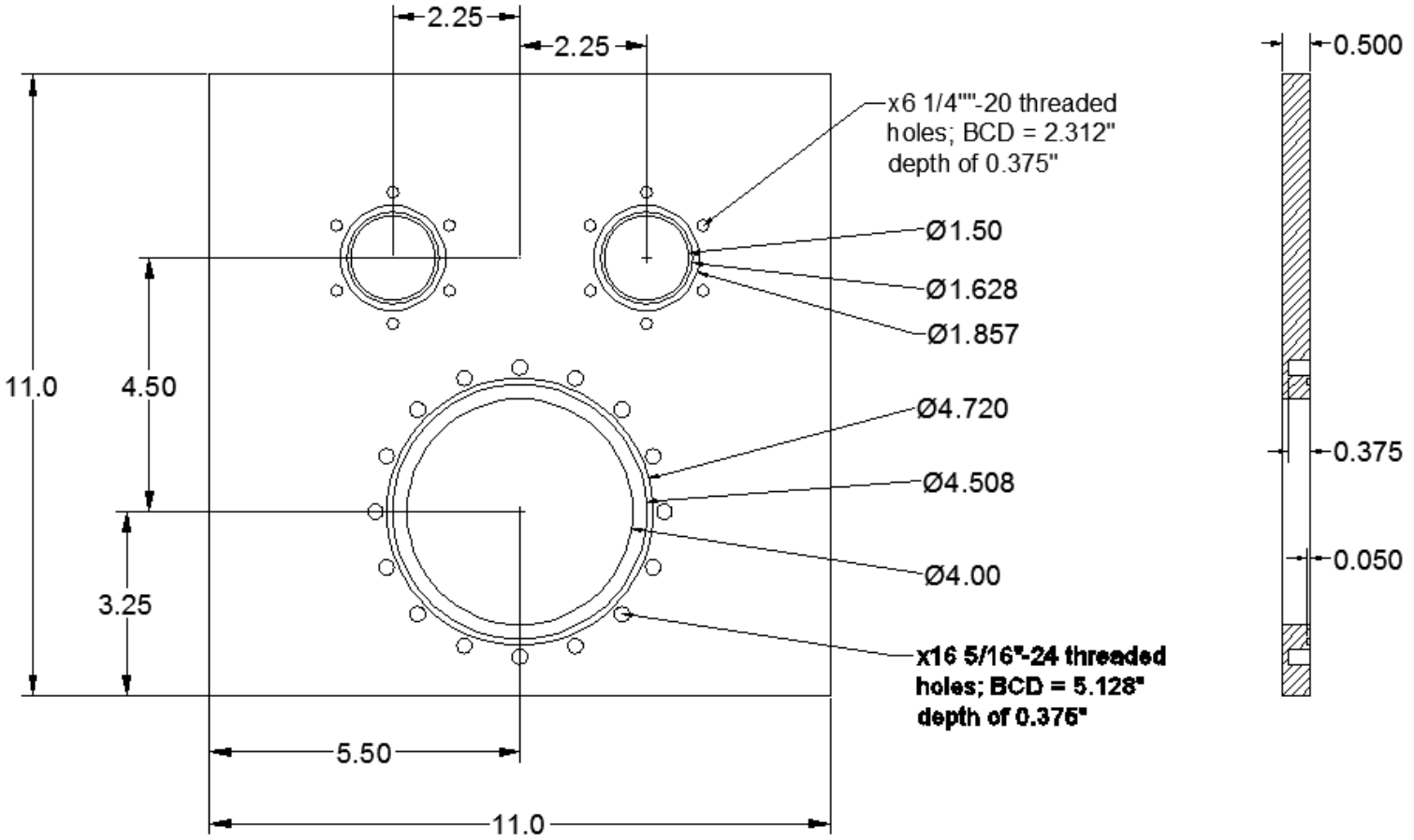

REFLECTRON CAN – SIDE PIECES

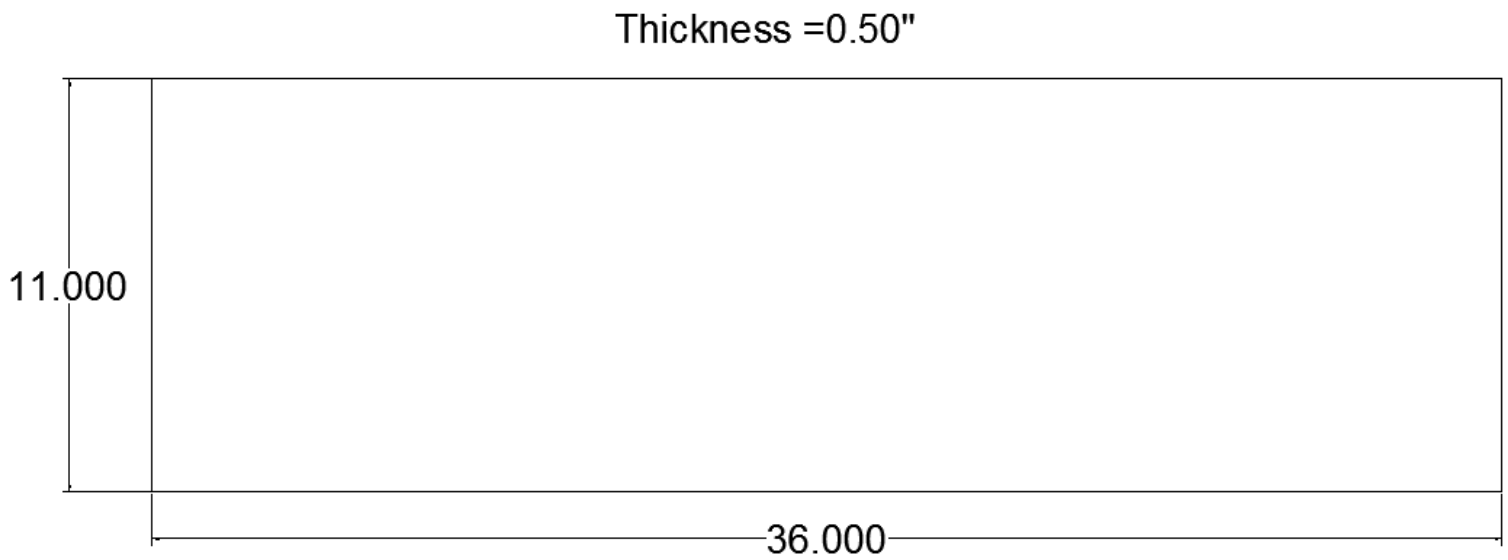

REFLECTRON CAN – GLASS PIECES

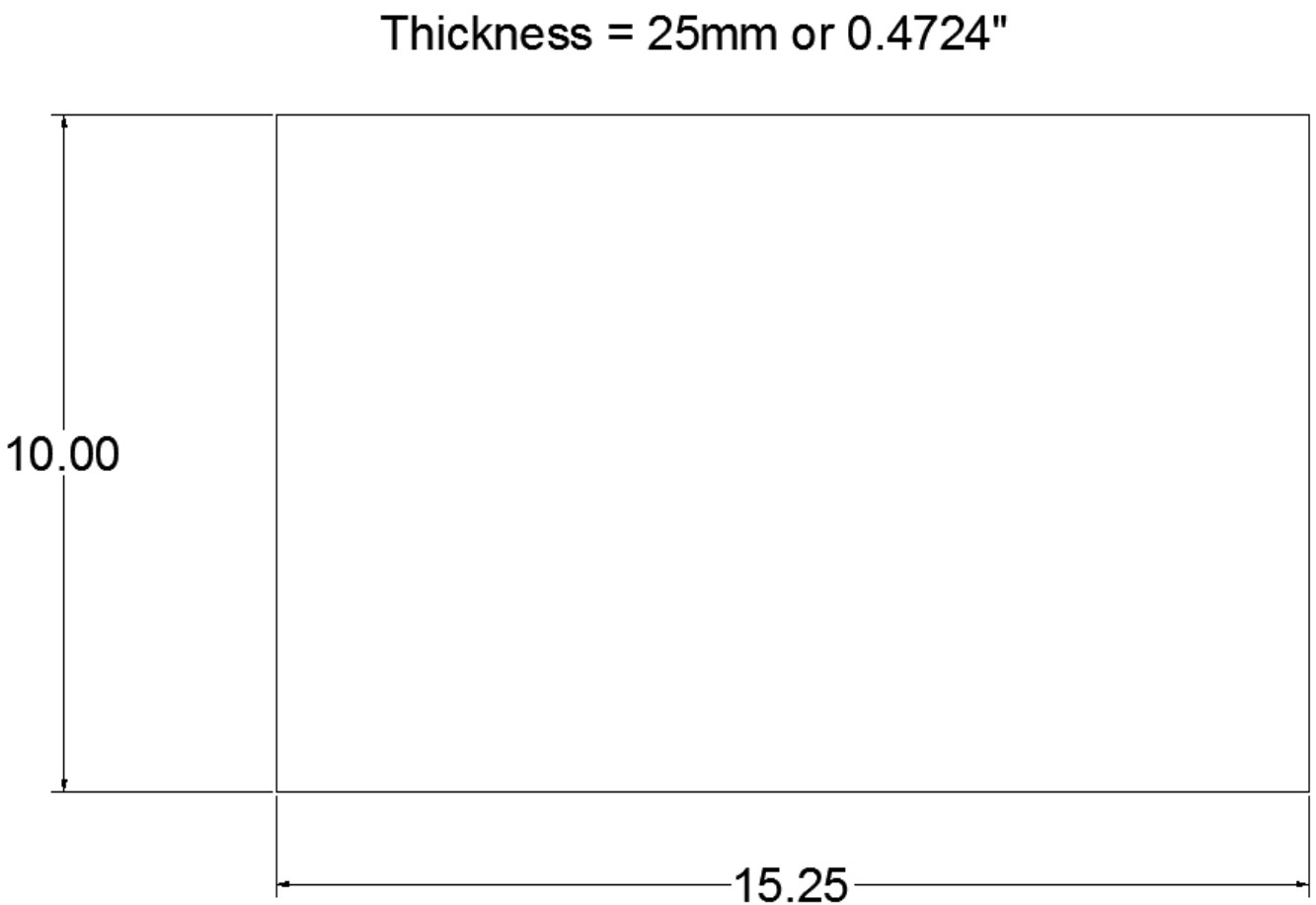

6 INCH CONFLAT FLANGE WITH GASKET GROOVE

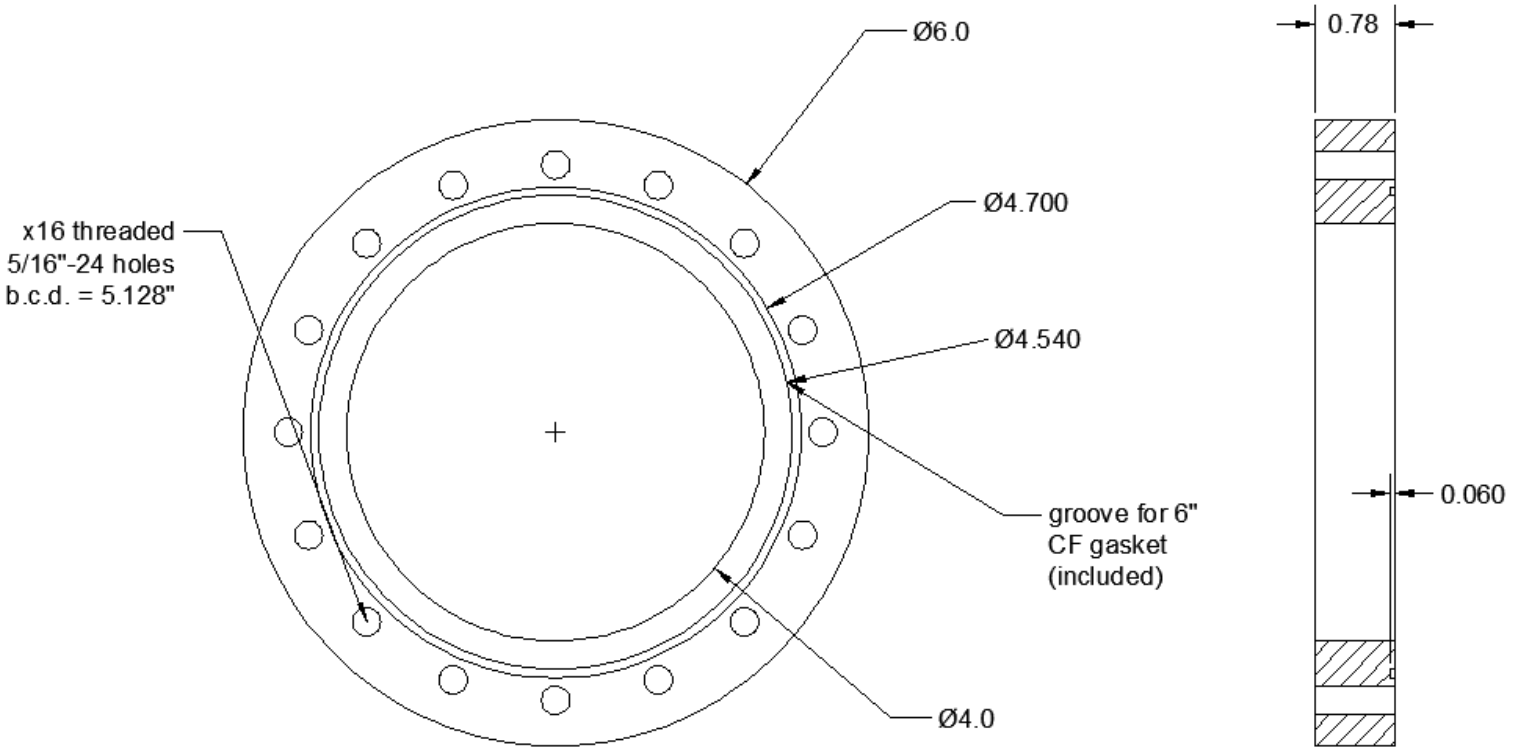

Weld end opposite of groove to 2.5" length of aluminum tube (4" I.D.) and weld to 4 " hole on "Reflectron can - bottom flange"

REFLECTRON BRACE – PART 1

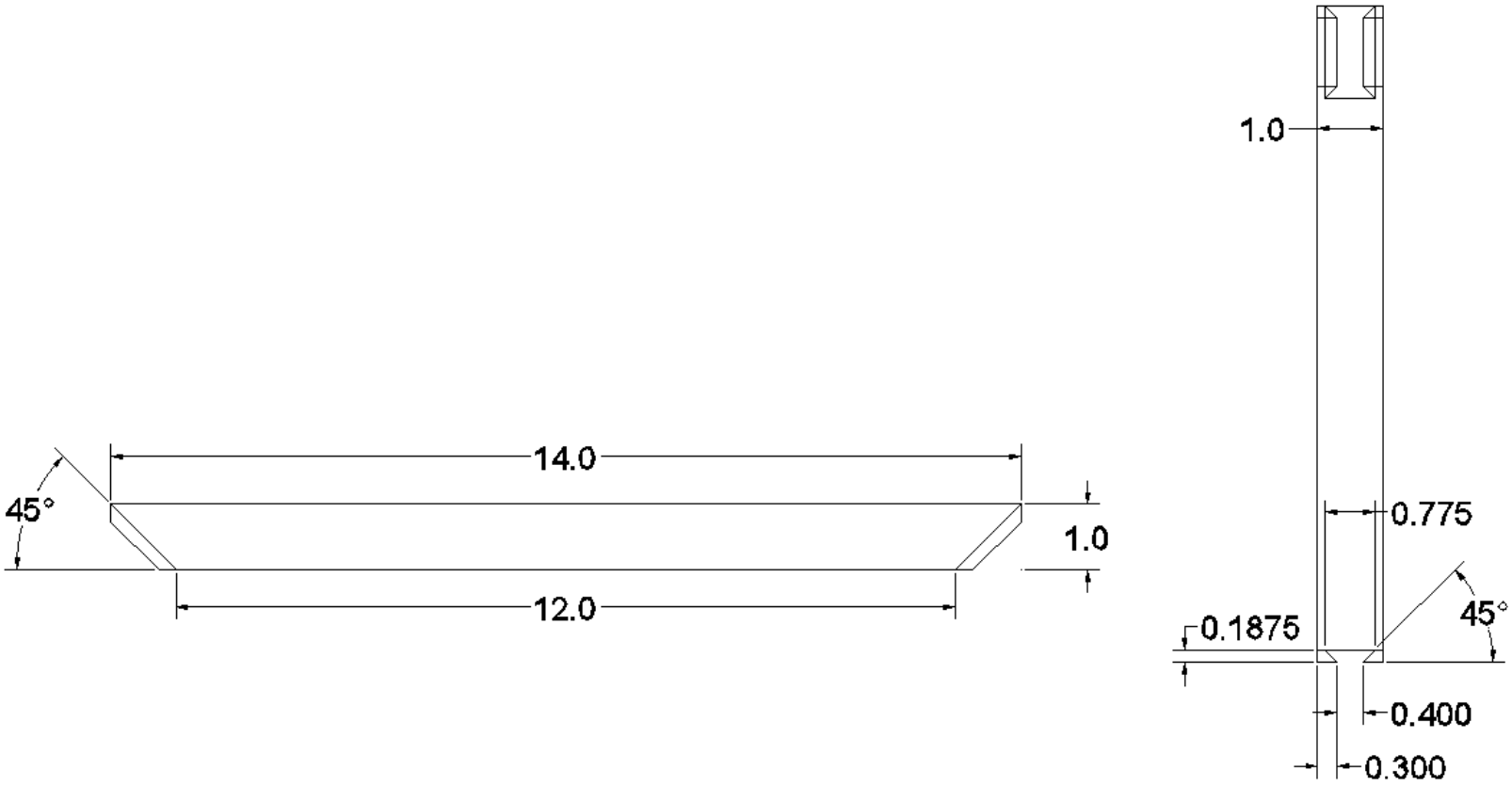

REFLECTRON BRACE – PART 2

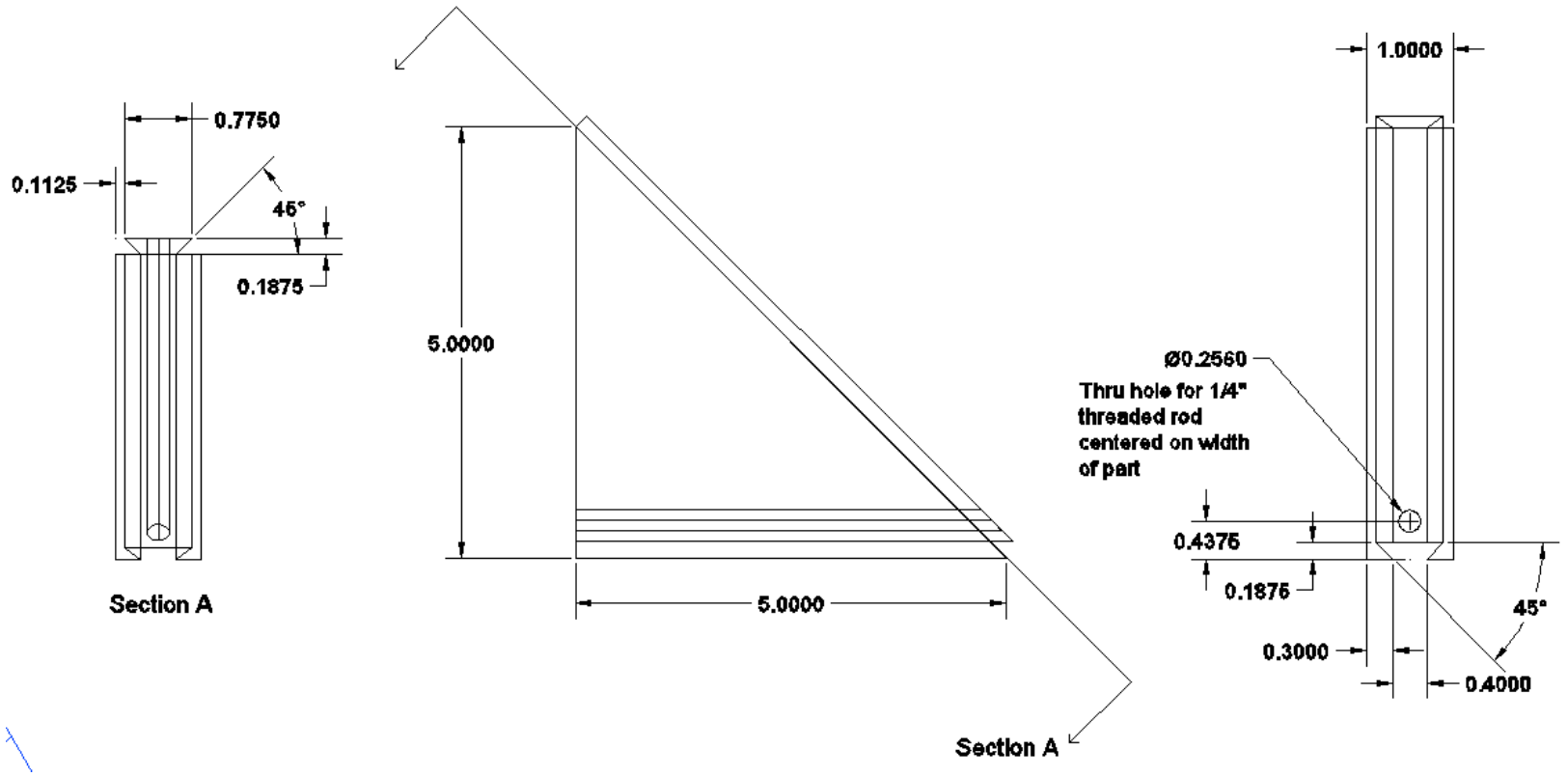

REFLECTRON BRACE – PART 3

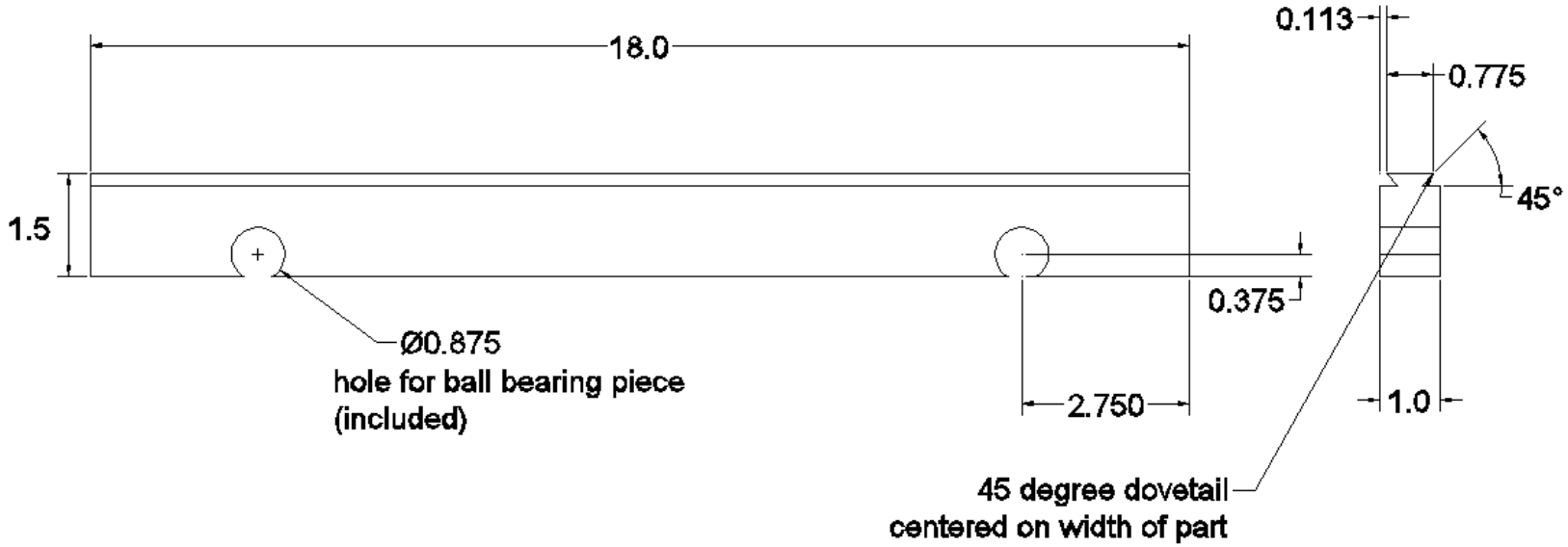

REFLECTRON SIDE-TO-SIDE ADJUSTMENT – RAIL PIECE

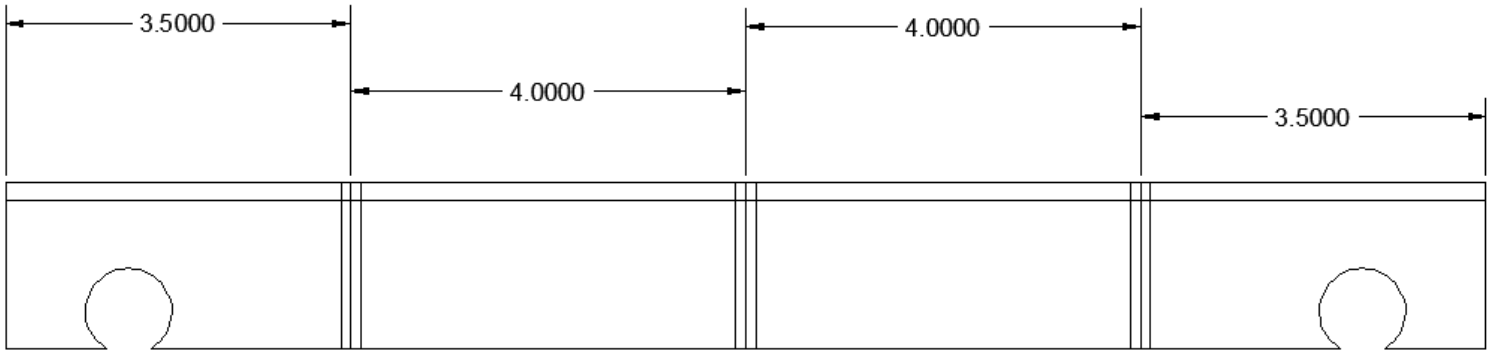

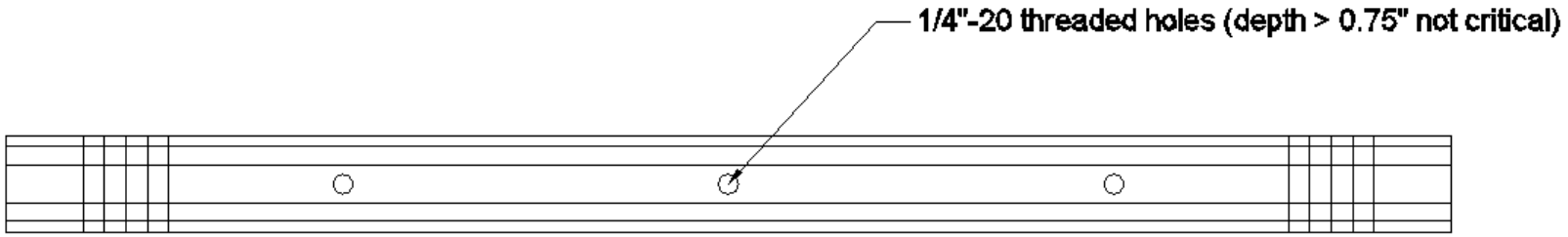

REFLECTRON SIDE-TO-SIDE ADJUSTMENT – U PIECE 1

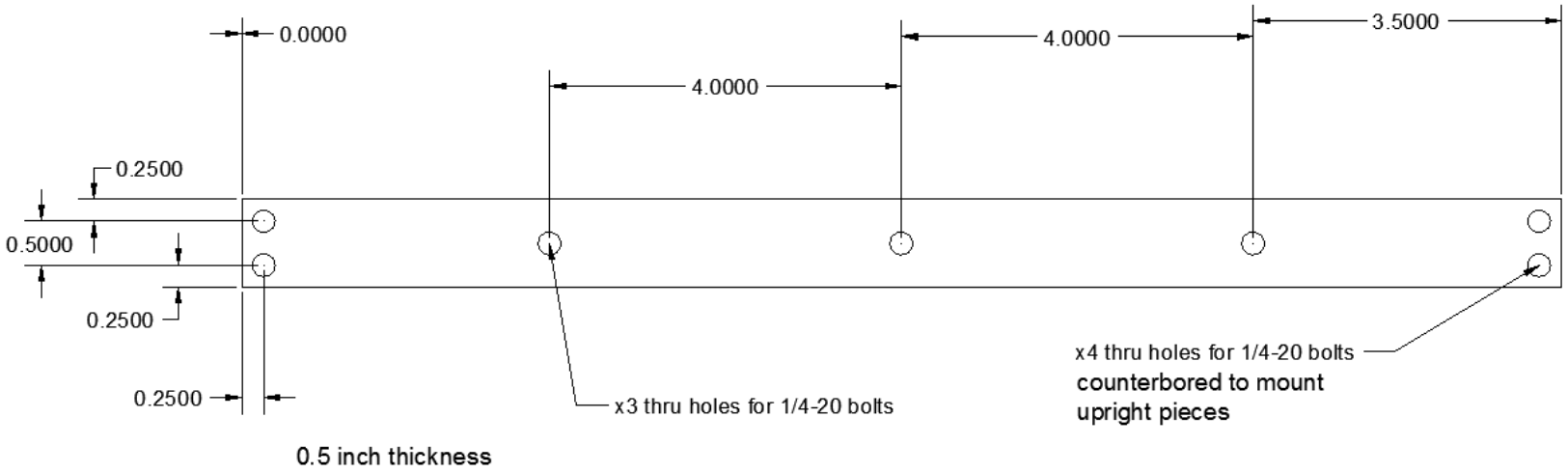

REFLECTRON SIDE-TO-SIDE ADJUSTMENT – U PIECE 2

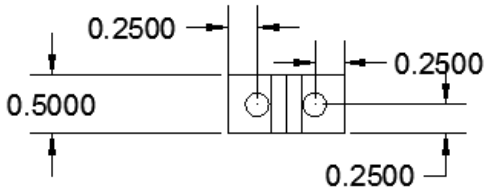

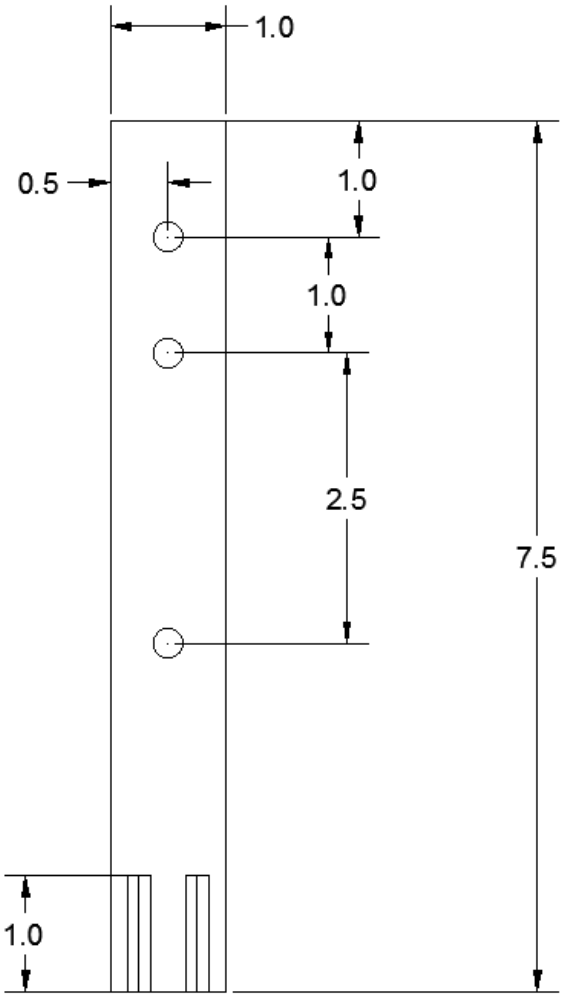

REFLECTRON GRID COMPRESSION PIECE – LARGE ELECTRODE

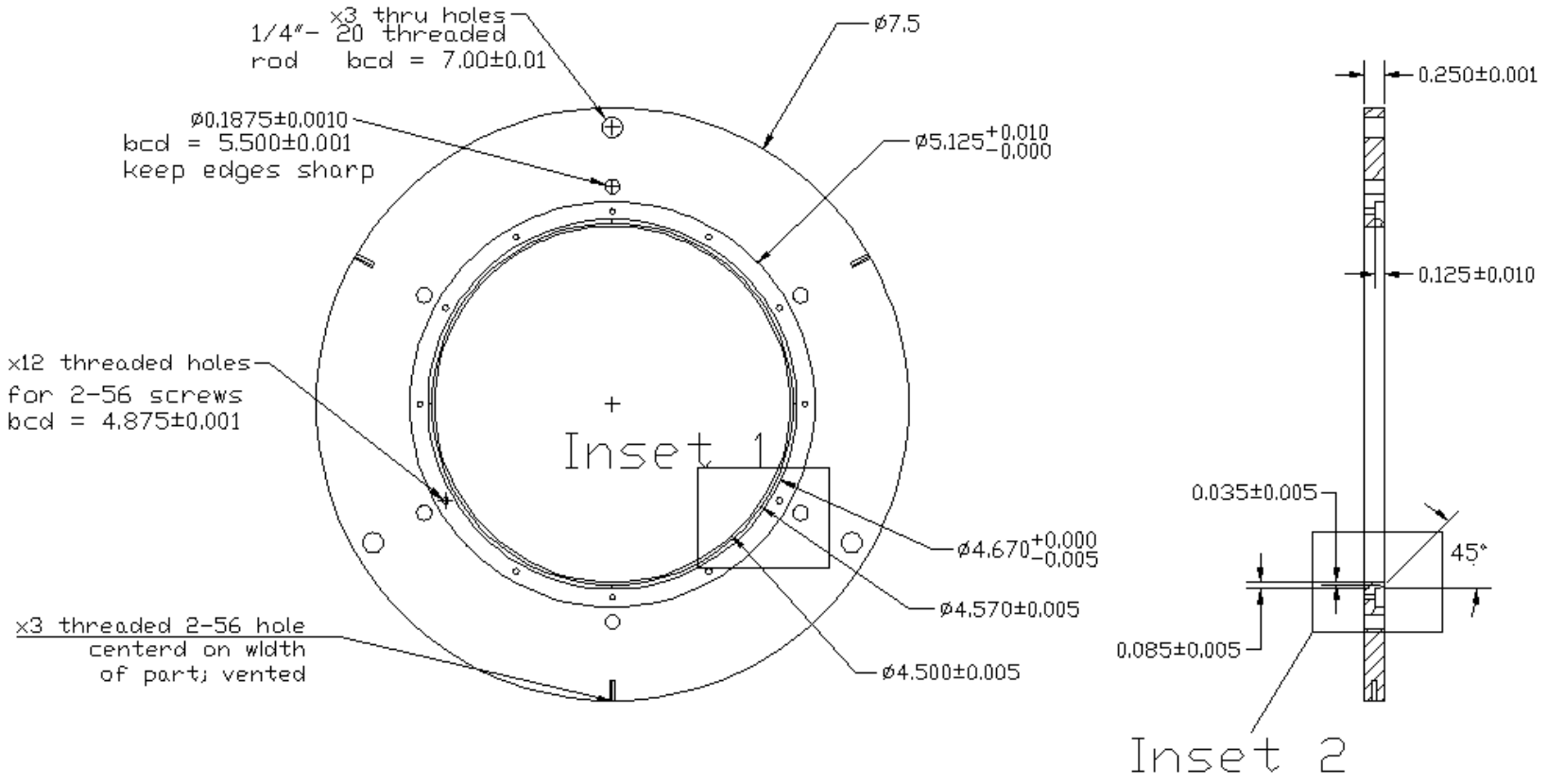

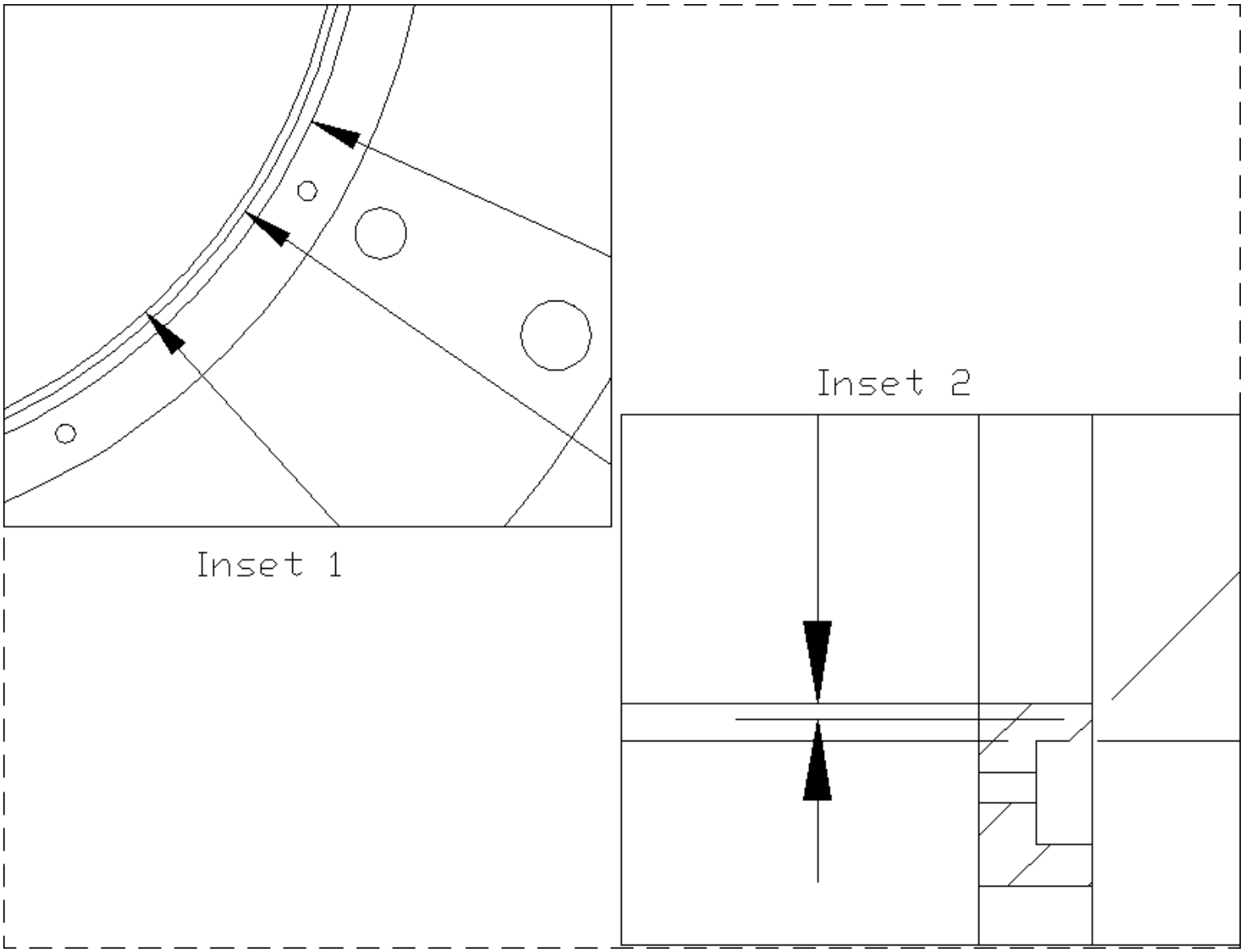
Inset 2
Inset 1

REFLECTRON GRID COMPRESSION PIECE – SMALL ELECTRODE

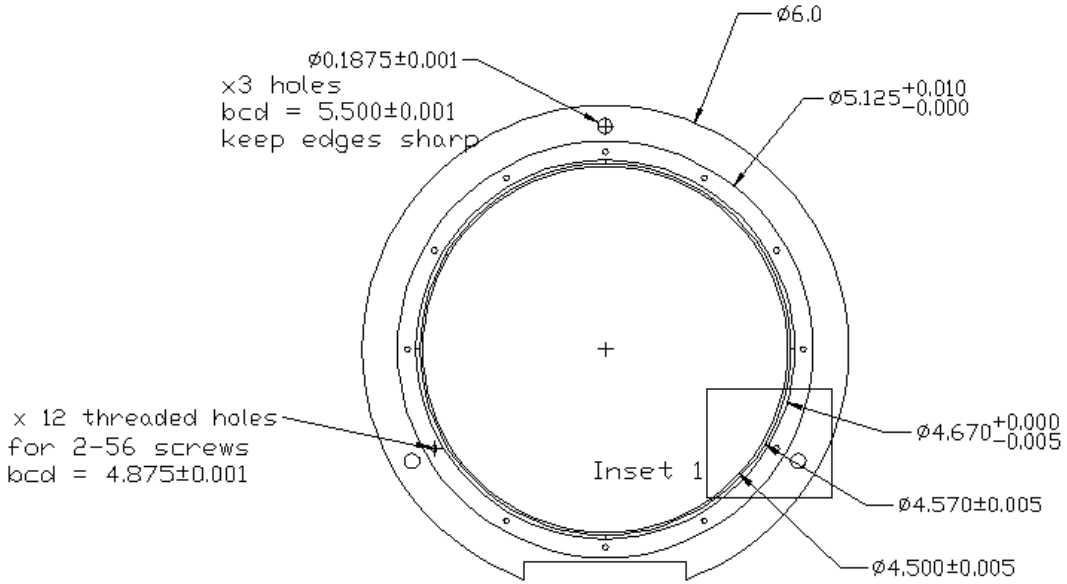

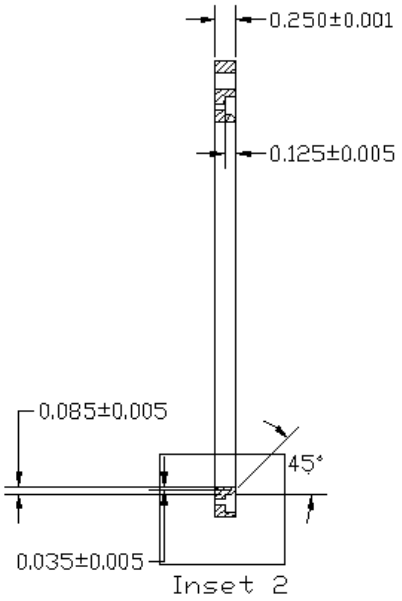

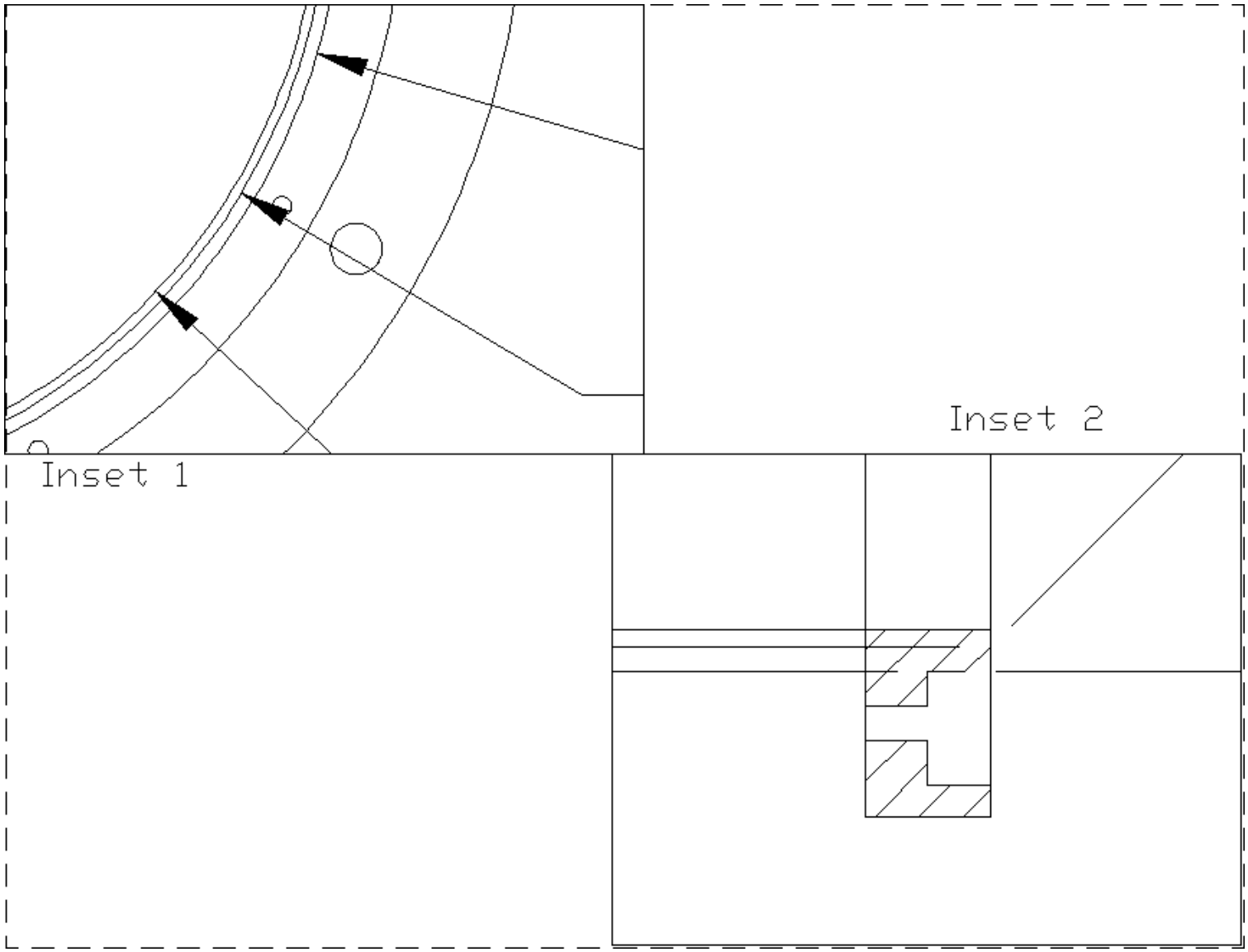
Inset 1
Inset 2

REFLECTRON GRID COMPRESSION PIECE – TO SET INSIDE LARGE & SMALL ELECTRODES

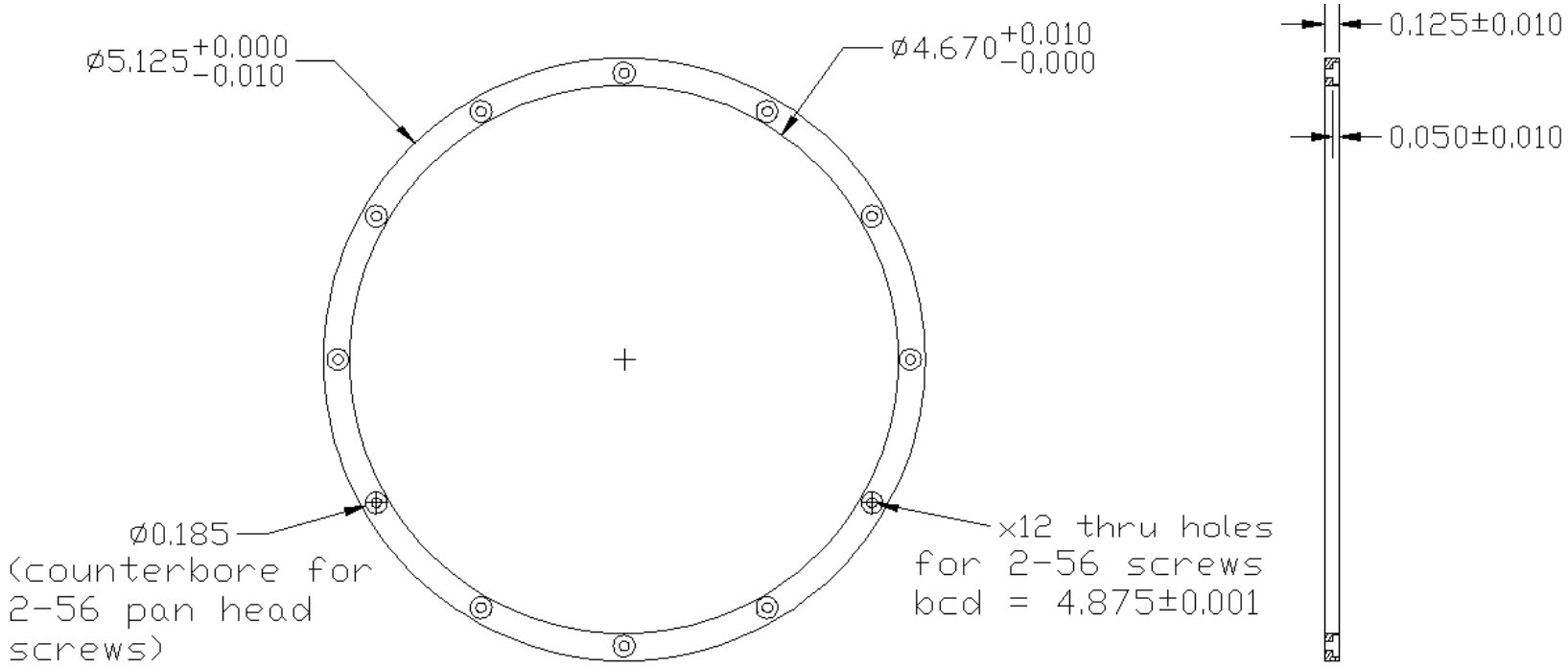

REFLECTRON STACK SUPPORT PIECE – DOUBLE CURVED PIECE

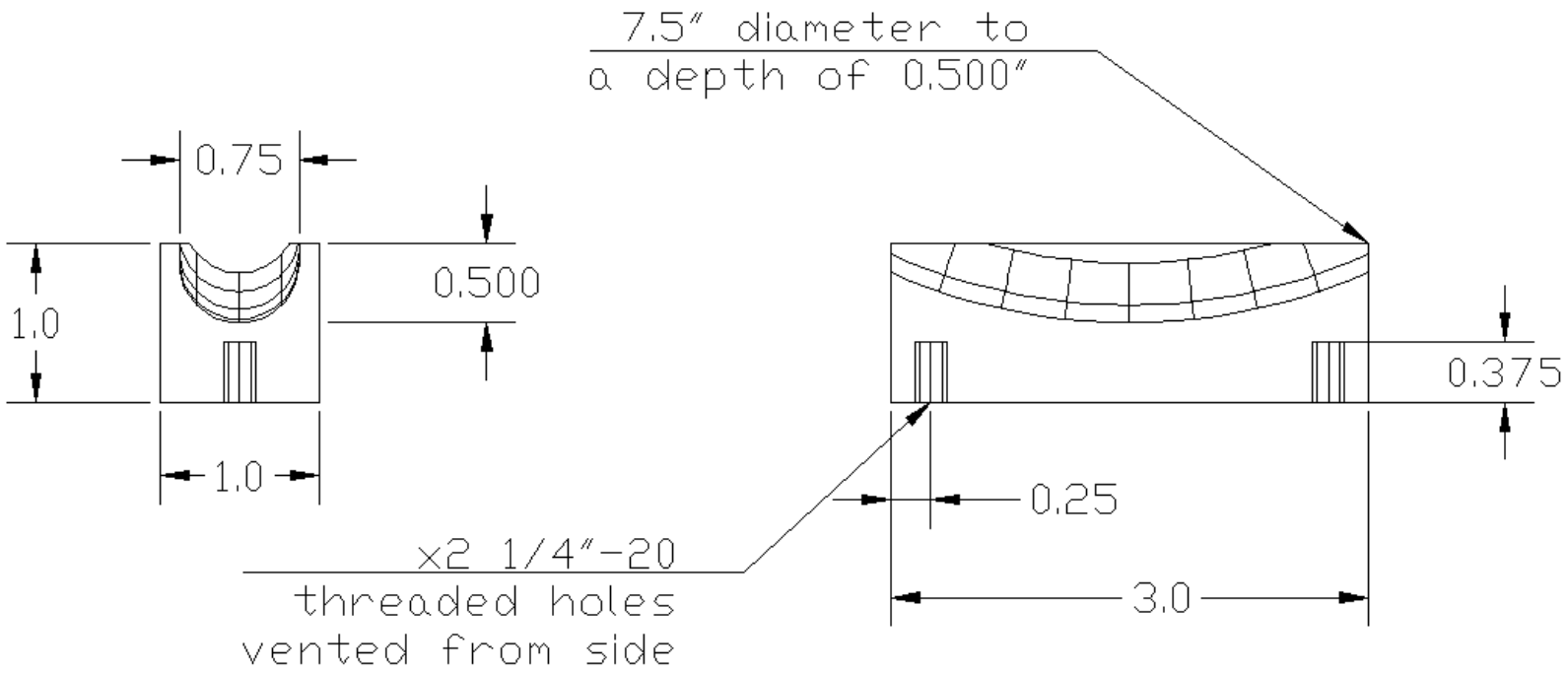

REFLECTRON STACK SUPPORT PIECE – MOUNTS ANGLE ADJUSTMENT PIECE TO FLANGE

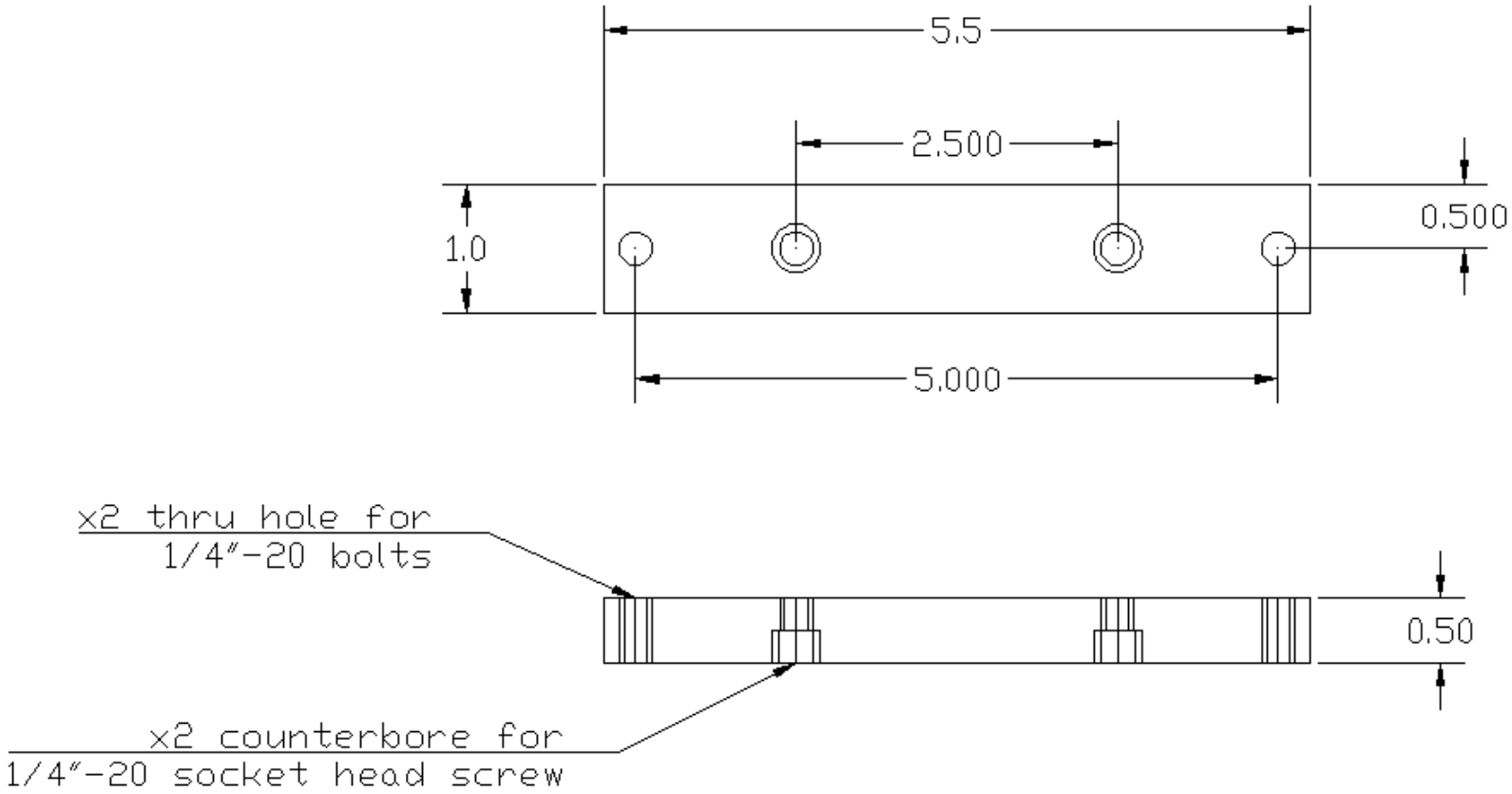

REFLECTRON STACK SUPPORT PIECE – ANGLE ADJUSTMENT PIECE

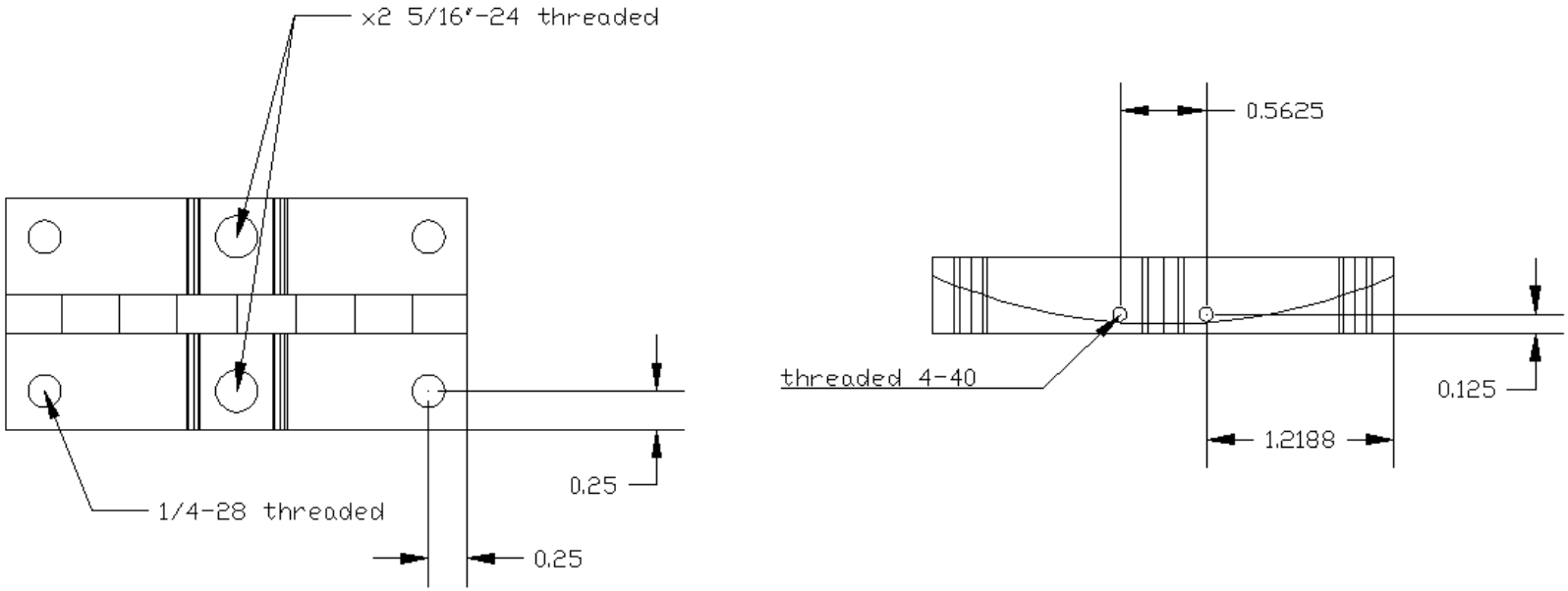

FOOT FOR BALL ENDED ¼”-28 SCREW

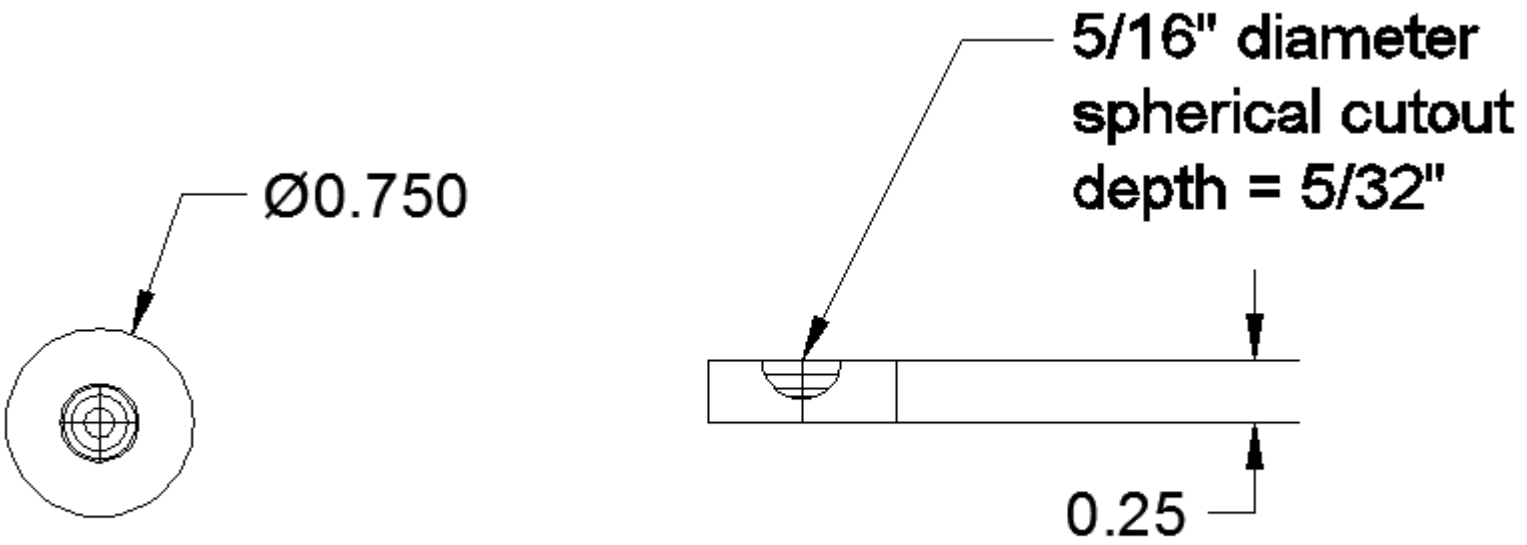

FULL ASSEMBLY OF BURLE DETECTOR MOUNT WITH ANGLE ADJUSTMENT

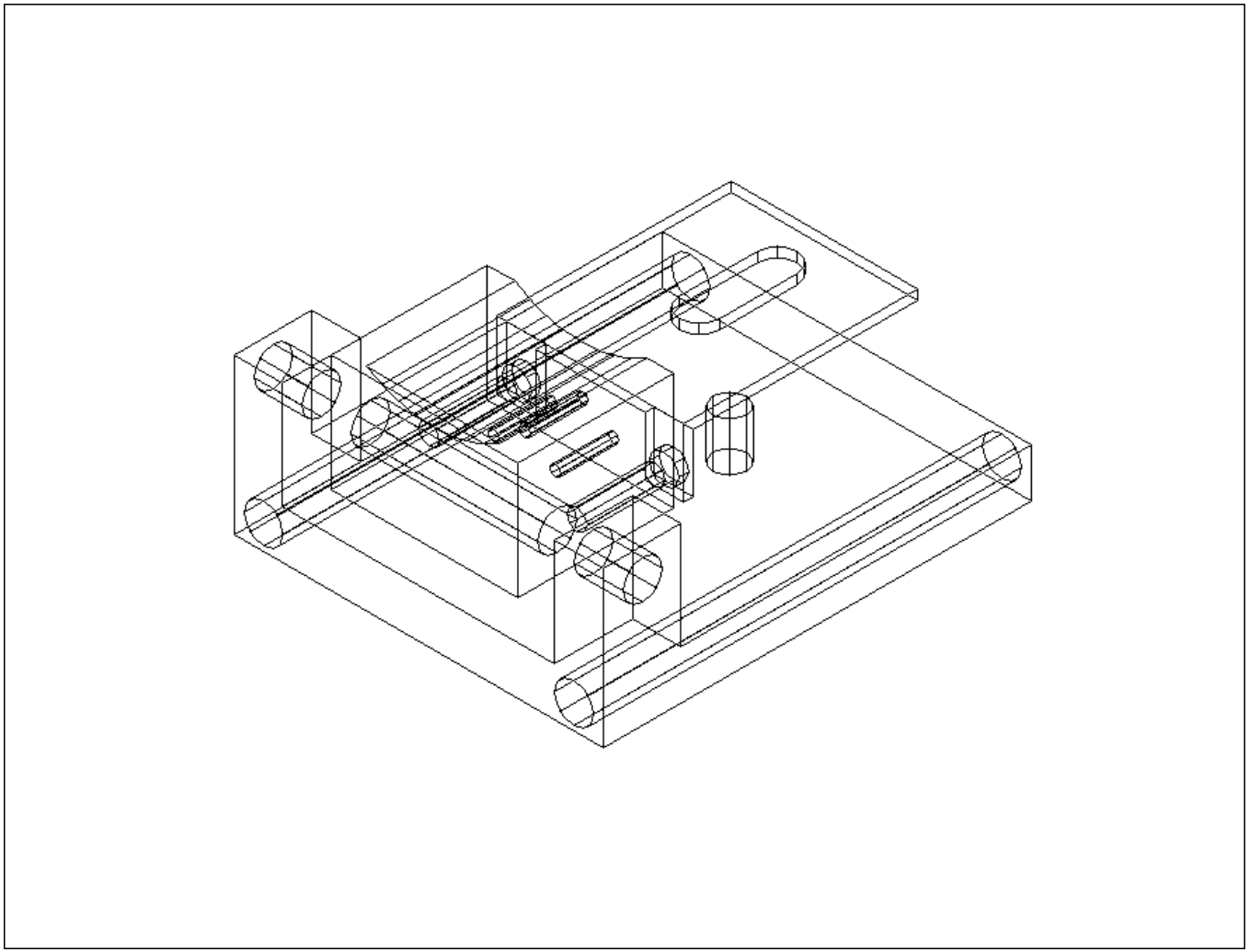

DETECTOR ASSEMBLY – ANGLE ADJUSTMENT

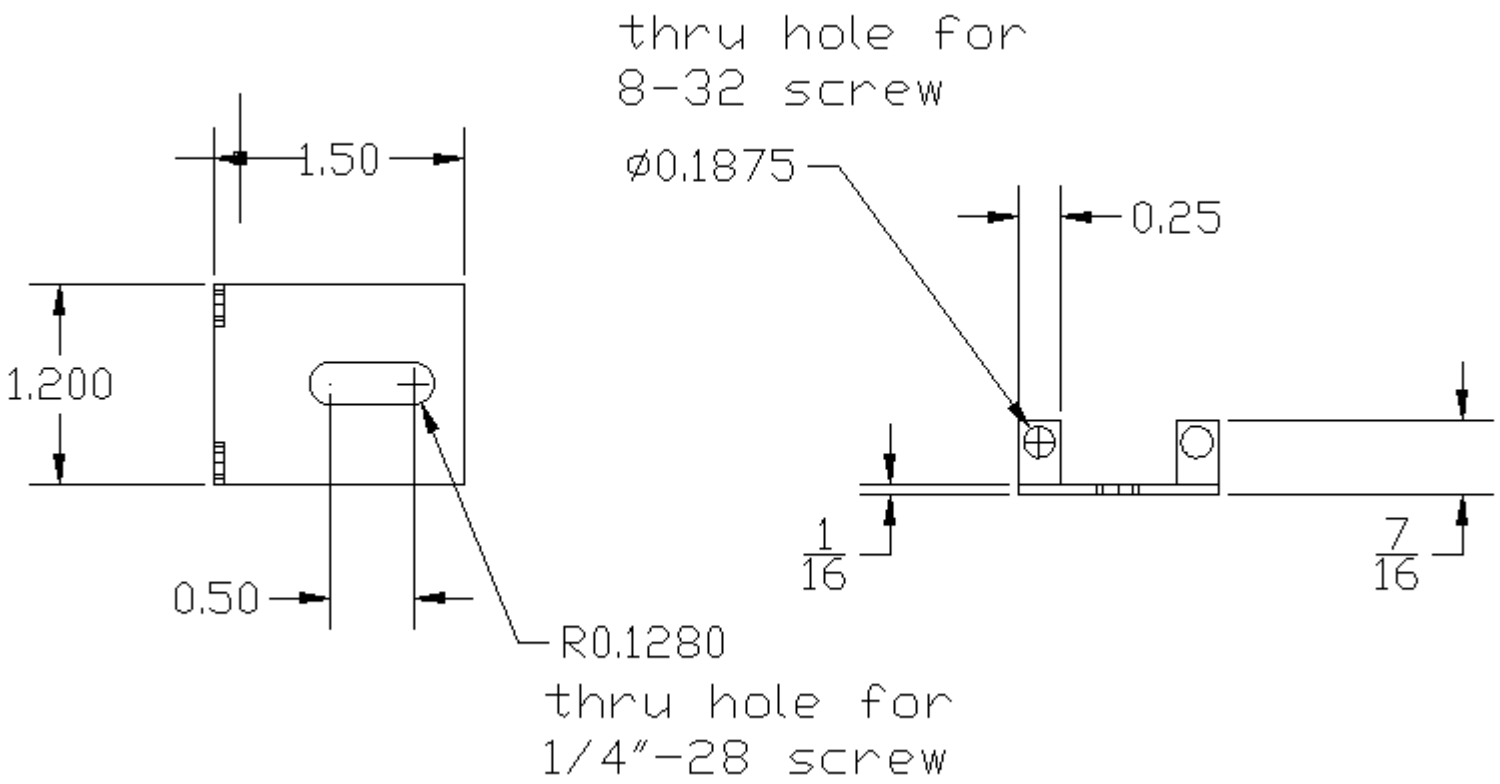

DETECTOR ASSEMBLY – SUPPORT PIECE FOR BURLE FAST-TOF DETECTOR

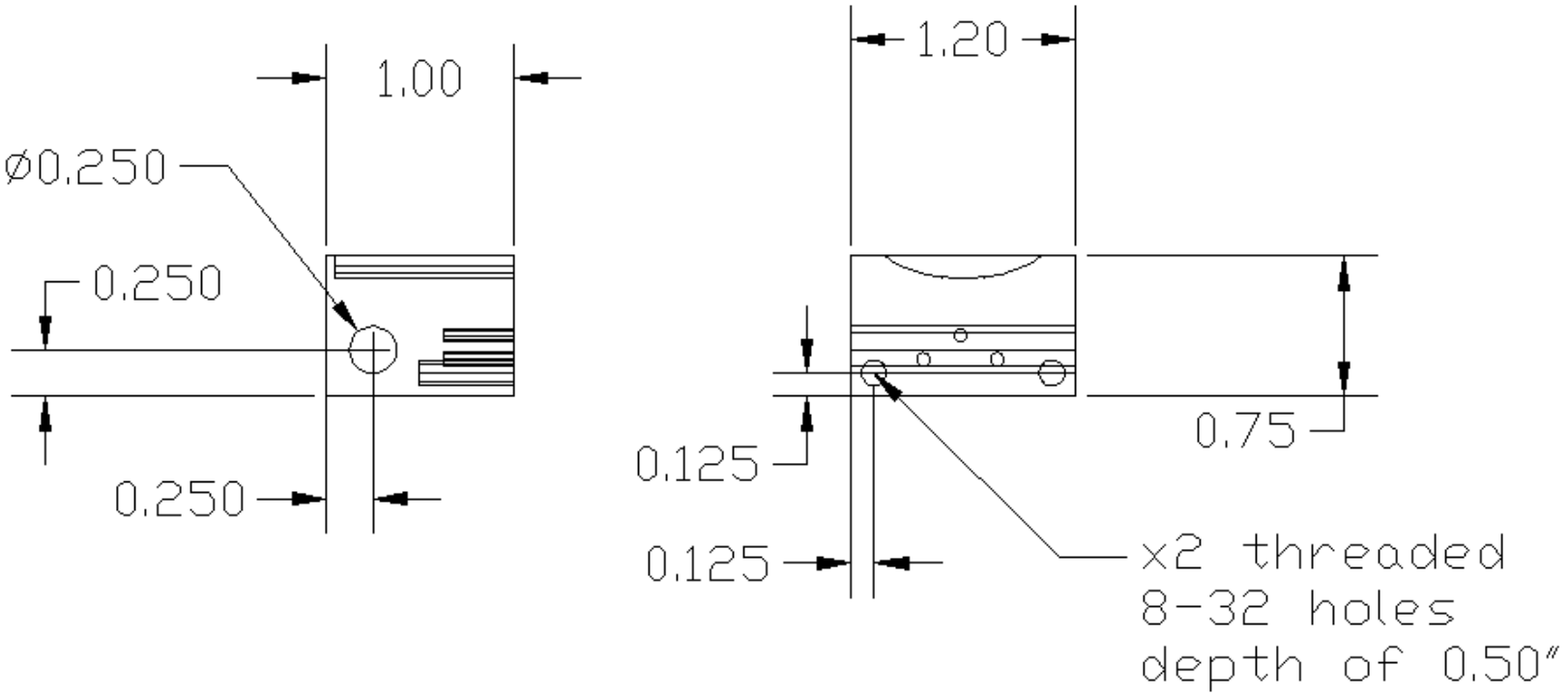

DETECTOR ASSEMBLY – BRACE TO MOUNT TO FLANGE

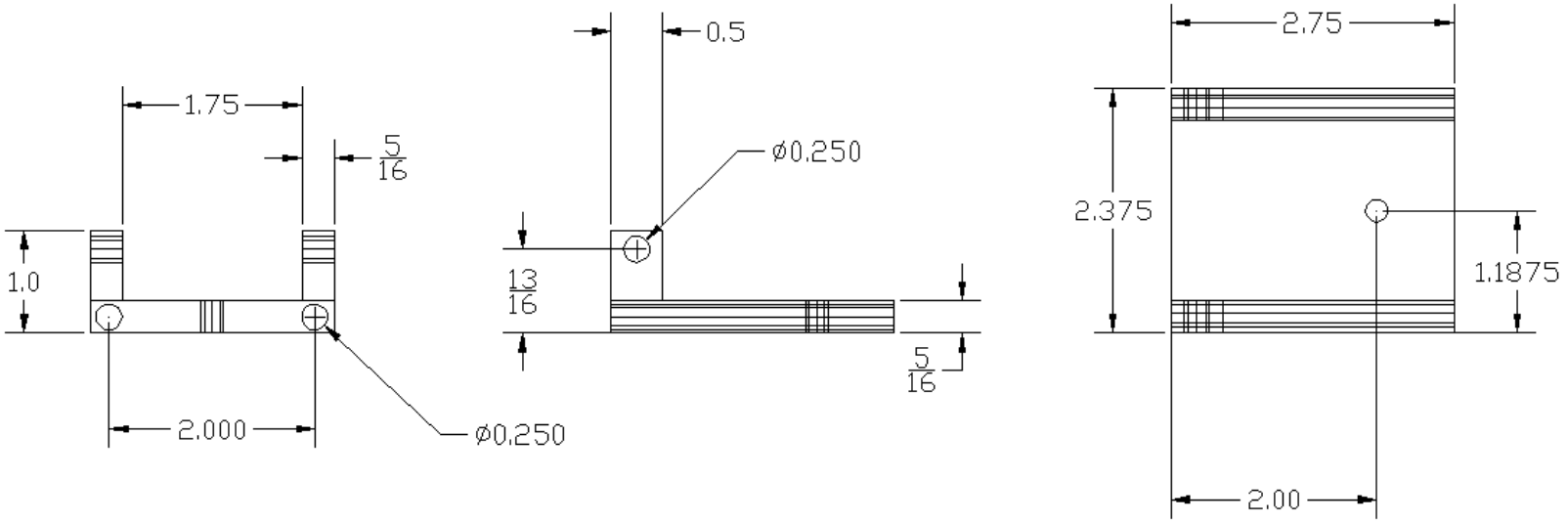

APPENDIX B

SIMION RENDERINGS

SIMION RENDERING OF THE ENTIRE INSTURMENT INCLUDING THE OPERATION OF SOURCE 2

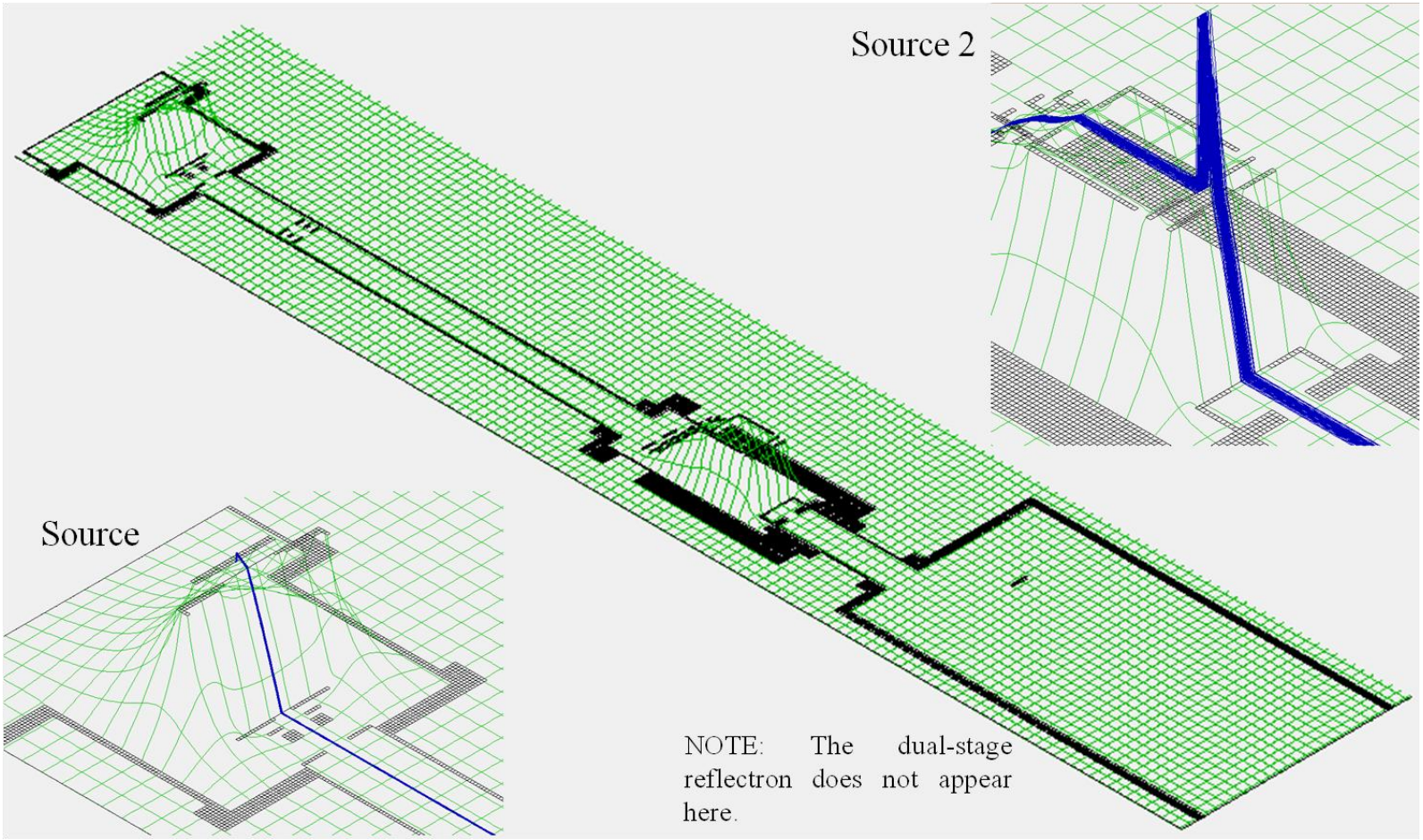

APPENDIX C

WIRING DIAGRAMS

DIAGRAM SHOWING THE WIRING OF THE DECELERATION LENS SYSTEM

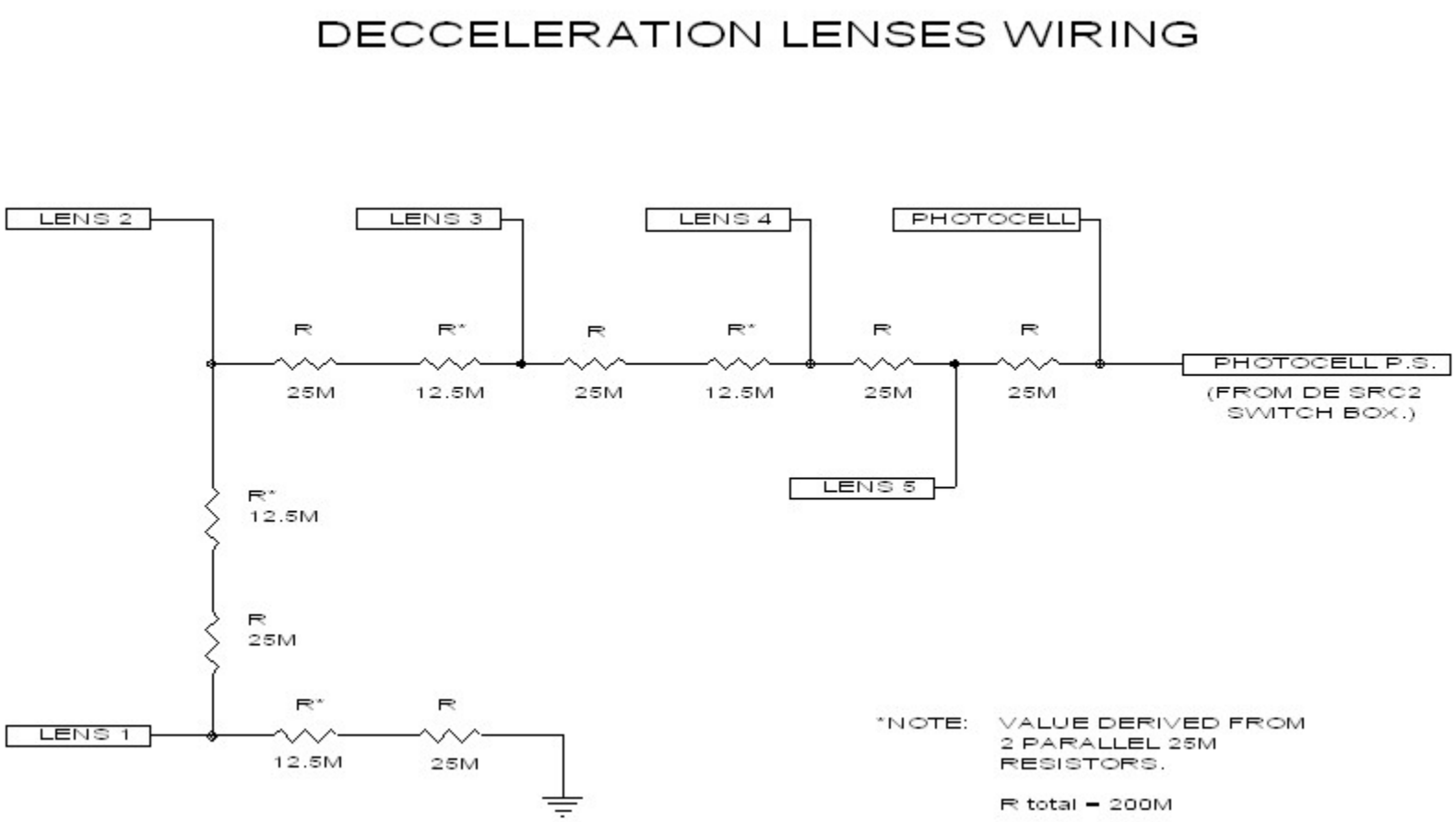

DIAGRAM SHOWING THE WIRING OF THE SOURCE

DELAYED EXTRACTION BOX

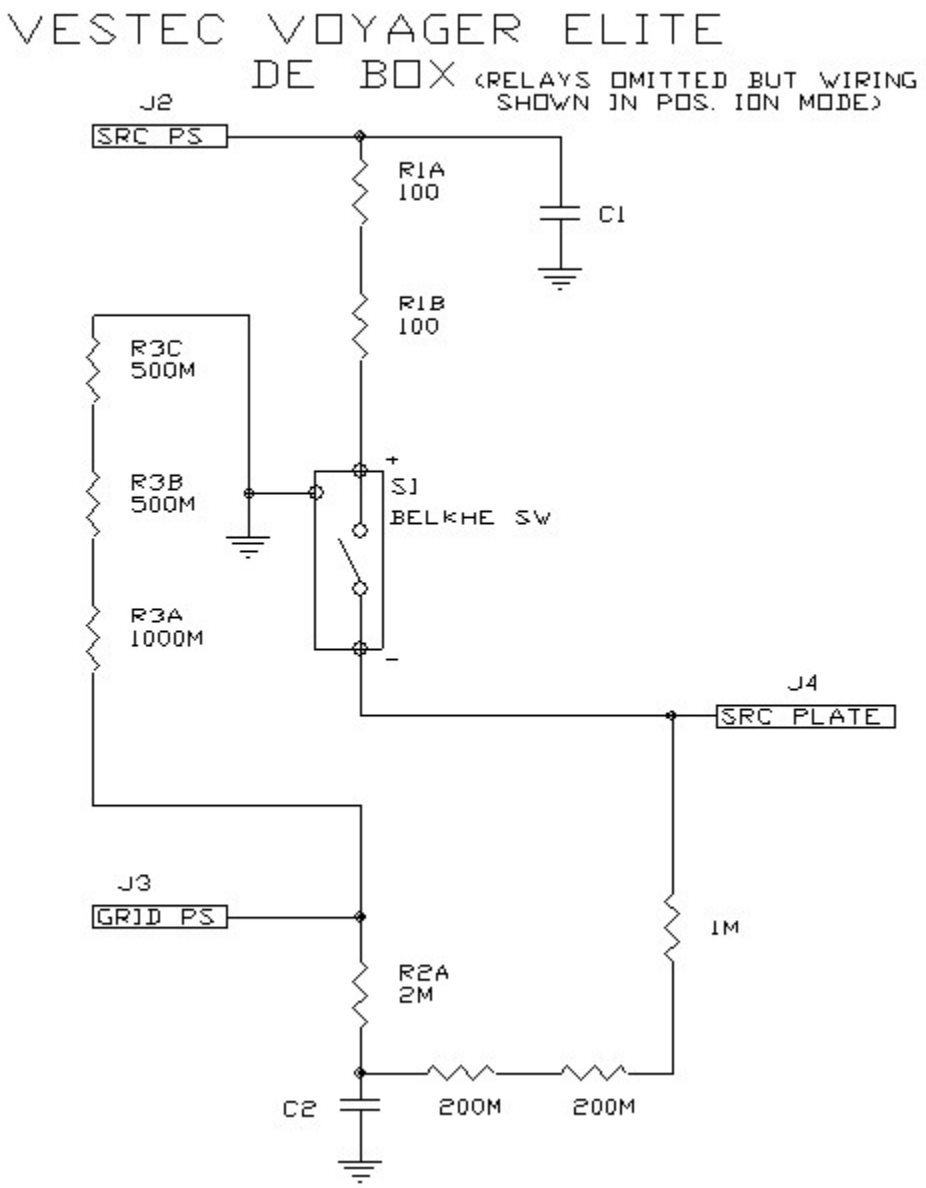

DIAGRAM SHOWING THE WIRING OF THE SOURCE 2

DELAYED EXTRACTION BOX

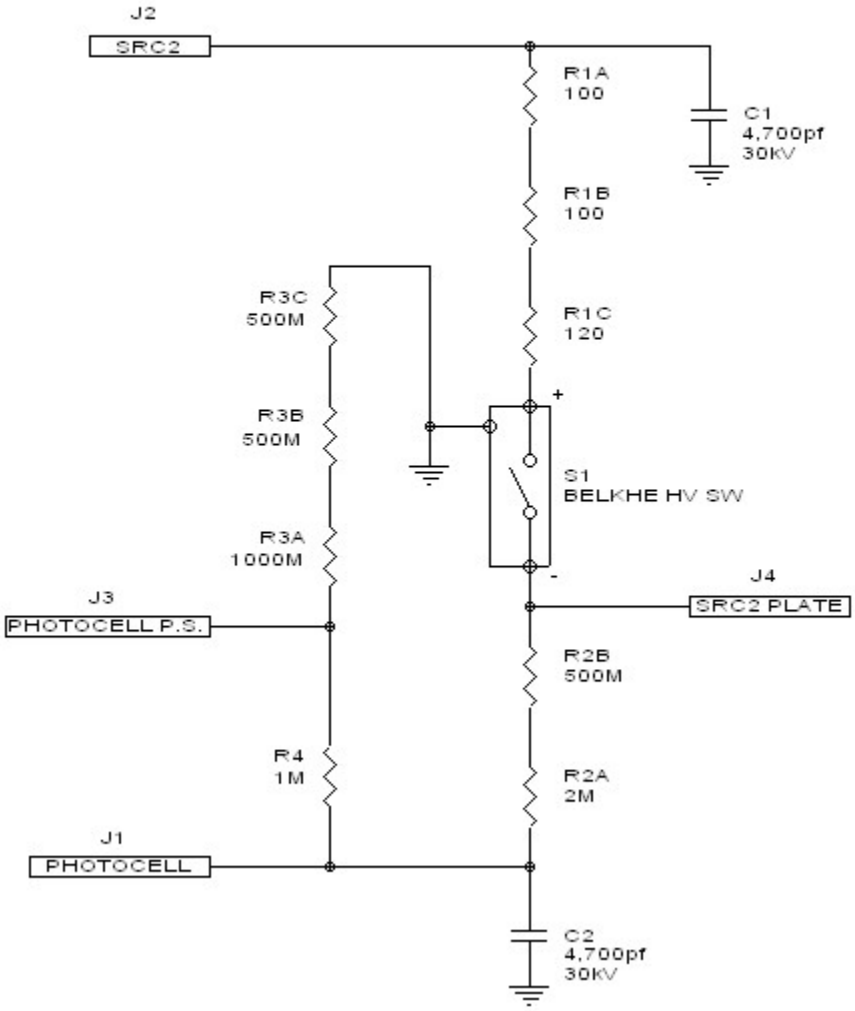

VITA

Kevin Lee Kmiec

Laboratory for Biological Mass Spectrometry
Department of Chemistry
Texas A&M University
Mail Stop 3255 TAMU
College Station, TX 77843

Phone: Office 979-845-0613
Fax: 979-845-9485
Email: KKmiec@chem.tamu.edu

EDUCATION

Ph.D. Chemistry August 2012
Department of Chemistry, Texas A&M University, College Station, TX

B.A. Chemistry (with Distinction) May 2006
Department of Chemistry, Hendrix College, Conway, AR

SELECTED PUBLICATIONS

1. B. J. Williams, Christopher K. Barlow, K. L. Kmiec, W. K. Russell, D. H. Russell Negative Ion Fragmentation of Cysteic Acid Containing Peptides: Cysteic Acid as a Fixed Negative Charge, J. Am. Soc. Mass Spectrom. 2011, 22, 1622-1630

2. B. J. Williams, K. L. Kmiec, W. K. Russell, D. H. Russell Effect of Cysteic Acid Position on the Negative Ion Fragmentation of Proteolytic Derived Peptides, J. Am. Soc. Mass Spectrom. 2011, 22, 31-37

3. K. L. Kmiec, J.G. Slaton, F.F. Fernandez-Lima, S. E. Tichy, W. K. Russell, D. H. Russell, How does Metal Ion Affinity and Binding Site Influence the Fragmentation of Peptide Ions?, J. Am. Soc. Mass Spectrom. Submitted

4. K. L. Kmiec, S. E. Tichy, D. H. Russell, Formation of x-type ions from Collision Induced Dissociation of Metal Cationized Peptides, In Preparation

5. K. L. Kmiec, C. M. Gamage, D. H. Russell, Fragmentation of Proline Containing Peptides via Collision Induced Dissociation and Photofragmentation TOF/TOF Mass Spectrometry, In Preparation